NLO Corrections to Production of Heavy Particles at Hadron Colliders

Davide Pagani

Max-Planck-Institut für Physik
(Werner-Heisenberg-Institut)

Technische Universität München

Max-Planck-Institut für Physik
(Werner-Heisenberg-Institut)

NLO Corrections to Production of Heavy Particles at Hadron Colliders

Davide Pagani

Vollständiger Abdruch der von der Fakultät für Physik
der Technischen Universität München zur Erlangung des akademischen Grades eines
Doktors der Naturwissenschaften (Dr. rer. nat.)
genehmigten Dissertation.

Vorsitzender:	Univ.-Prof. Dr. L. Oberauer.
Prüfer der Dissertation:	1. Hon.-Prof. Dr. W. F. L. Hollik
	2. Univ.-Prof. Dr. A. Ibarra

Die Dissertation wurde am 27.06.2013
bei der Technischen Universität München eingereicht und
durch die Fakultät für Physik am 17.09.2013 angenommen.

Zusammenfassung

In dieser Arbeit werden verschiedene Aspekte der Produktion schwerer Teilchen in Hadron-Hadron-Kollisionen beleuchtet. Speziell präsentieren wir Präzisionsvorhersagen unter Einschluss von Korrekturen der starken und elektroschwachen Wechselwirkung zur nächstführenden Ordnung der Störungsreihe.

Im ersten Teil dieser Arbeit wird die Ladungsasymmetrie des Top-Quarks untersucht. Speziell stellen wir eine Rechnung der elektroschwachen Beiträge des asymmetrischen Teils des Produktionswirkungsquerschnitts für Top-Quark-Paare zur Ordnung $\mathcal{O}(\alpha_s^2\alpha)$ und $\mathcal{O}(\alpha^2)$ vor. Numerisch wird besonders der Einfluss auf Vorhersagen der gemessenen Asymmetrie am Tevatron hervorgehoben. Die untersuchten elektroschwachen Beiträge können neben der QCD-induzierten Asymmetrie nicht vernachlässigt werden. Sie haben das gleiche Vorzeichen und vergrößern die Vorhersagen der Asymmetrie im Rahmen des Standard Models um etwa 20%. Dadurch wird die beobachtete Abweichung zwischen Vorhersage und Messung verringert.

Im zweiten Teil wird die Produktion von Squarks, den supersymmetrischen Partnern der Quarks, am Large Hadron Collider (LHC) untersucht. Wir diskutieren dabei die Berechnung von faktorisierbaren QCD-Korrekturen zur nächstführenden Ordnung der Störungsreihe, wobei die Produktion von Squark–Squark Paaren vollständig differenziell mit deren Zerfall kombiniert wird. Speziell wird die Kombination der Produktion mit zwei unterschiedlichen Zerfallsmöglichkeiten untersucht. Der Schwerpunkt liegt dabei auf Präzisionsvorhersagen für zwei experimentelle Signaturen, die für die Suche nach Supersymmetrie am LHC relevant sind. Bei der ersten Signatur konzentrieren wir uns auf den Einfluss von Strahlungskorrekturen in Produktion und Zerfall auf physikalisch wichtige differenzielle Verteilungen und auf inklusive experimentelle Suchen, wie sie von der ATLAS und der CMS Kollaboration durchgeführt werden. Bei der zweiten Signatur analysieren wir die Effekte auf Verteilungen, die für zukünftige Parameterbestimmung relevant werden können. Im Allgemeinen sollten die von uns untersuchten faktorisierbaren QCD-Korrekturen für eine präzise phänomenologische Vorhersage berücksichtigt werden. Insbesondere können diese Korrekturen nicht als im Phasenraum flach angenommen werden, und ein einfaches Multiplizieren von Vorhersagen zur führenden Ordnung mit einem globalen Faktor ist oft keine ausreichende Näherung.

Abstract

In this thesis we study specific aspects of the production of heavy particles at hadron colliders, with emphasis on precision predictions including next-to-leading order (NLO) corrections from the strong and electroweak interactions.

In the first part of the thesis we consider the top quark charge asymmetry. In particular, we discuss in detail the calculation of the electroweak contributions from the asymmetric part of the top quark pair production cross section at $\mathcal{O}(\alpha_s^2\alpha)$ and $\mathcal{O}(\alpha^2)$ and their numerical impact on predictions for the asymmetry measurements at the Tevatron. These electroweak contributions provide a non-negligible addition to the QCD-induced asymmetry with the same overall sign and, in general, enlarge the Standard Model predictions by a factor around 1.2, diminishing the deviations from experimental measurements.

In the second part of the thesis we consider the production of squarks, the supersymmetric partners of quarks, at the Large Hadron Collider (LHC). We discuss the calculation of the contribution of factorizable NLO QCD corrections to the production of squark–squark pairs combined at fully differential level with squark decays. Combining the production process with two different configurations for the squark decays, our calculation is used to provide precise phenomenological predictions for two different experimental signatures that are important for the search of supersymmetry at the LHC. We focus, for one signature, on the impact of our results on important physical differential distributions and on cut-and-count searches performed by the ATLAS and CMS collaborations. Considering the other signature, we analyze the effects from NLO QCD corrections and from the combination of production and decays on distributions relevant for parameter determination. In general, factorizable NLO QCD corrections have to be taken into account to obtain precise phenomenological predictions for the analyzed distributions and inclusive quantities. Moreover, these corrections cannot be considered flat in phase space; rescaling leading-order predictions by a global correction factor is in general not a viable approximation.

Publications

This thesis is based on the following articles and proceedings:

Articles

- W. Hollik and D. Pagani, *The electroweak contribution to the top quark forward-backward asymmetry at the Tevatron*, *Phys.Rev.* **D84** (2011) 093003, [arXiv:1107.2606].
- W. Hollik, J. M. Lindert, and D. Pagani, *NLO corrections to squark-squark production and decay at the LHC*, *JHEP* **1303** (2013) 139, [arXiv:1207.1071].
- W. Hollik, J. M. Lindert, and D. Pagani, *On cascade decays of squarks at the LHC in NLO QCD*, *Eur.Phys.J.* **C73** (2013) 2410, [arXiv:1303.0186].

Proceedings

- D. Pagani, *Top quark forward-backward asymmetry at the Tevatron: the electroweak contribution*, *PoS* **CORFU2011** (2011) 027, [arXiv:1205.6182].
- D. Pagani, *The electroweak contribution to top quark pair production: cross sections and asymmetries*, arXiv:1212.0808.

Contents

Chapter 1

Introduction

The Standard Model (SM) describes the electroweak and strong interactions of elementary particles. On the one hand, the electroweak sector unifies the electromagnetic and weak forces [1–4]. On the other hand, the strong sector provides, via Quantum Chromodynamics (QCD) [5–7], an explanation for both the hadronic bound states and the asymptotic freedom of strong interactions at high energies.

The predictions of the Standard Model are in very good agreement with almost all the measurements performed during the last 50 years at experiments with particle accelerators. Moreover, with the recent discovery [8,9] of a new particle in the searches for the Higgs boson [10–15] at the Large Hadron Collider (LHC), finally, all the particle content of the Standard Model has been experimentally detected. However, the SM cannot be the "theory of everything"; it does not include gravity and cannot describe the largest part of the matter and energy content in the Universe. New ingredients, the dark matter and the dark energy, have to be introduced to explain the astrophysical and cosmological data from the observable Universe. Thus, these phenomenological problems and also other theoretical problems, as, e.g., the hierarchy problem, suggest the presence of new physics "beyond the Standard Model" (BSM).

Although, until now, measurements at colliders have not shown any significant evidence of new physics dynamics, the information provided by this kind of experiments is a valuable input for the investigation of BSM models. At the LHC, colliding hadrons with higher luminosity and at higher energies than ever before, the evidence for new physics can be searched for, following two complementary strategies: testing Standard Model predictions with high precision, or trying to detect the direct production of non-standard particles.

From the theoretical side, the requirements are twofold. On the one hand, the accuracy of the calculations has to be further improved in order to match the increased experimental precision for the measurements of Standard Model processes. On the other hand, theoretical predictions for the production of non-standard particles must be extended from a theoretical to a realistic phenomenological level. As for the SM

case, calculations have to be either performed taking directly into account the particular experimental set-up or implemented consistently into event generators.

Both situations, improving the accuracy of SM predictions and providing realistic predictions for the experimental signatures emerging from non-standard processes, are treated in this thesis.

In the first part of the thesis we consider a SM process, the production of top quark pairs at hadron colliders, and we analyze in detail the top quark charge asymmetry as a specific quantity of high current interest.

The top quark, discovered in 1995 at the Tevatron [16,17], is the heaviest particle of the Standard Model. Due to its large mass, it decays before hadronization, producing a signature that is different from the signatures of the other quarks. At the Tevatron, its mass has been measured with a relative error smaller than 1% and is consistent with the value obtained from the analyses of electroweak precision observables for SM processes. Also, the measurements of cross sections, distributions, and branching ratios, performed at the Tevatron and now also at the LHC, are in very good agreement with the corresponding SM predictions. The situation is, however, very different for the top quark charge asymmetry.

At the Tevatron, due to the proton–antiproton initial state, this observable corresponds to a forward-backward asymmetry and is one of the few quantities that show a deviation around three standard deviations (3σ) from the SM predictions. Amongst the precisely measured observables, only the muon anomalous magnetic moment [18] and the LEP forward-backward asymmetry of bottom quarks at the Z resonance [19] show deviations of comparable size. In the case of the top quark asymmetry, the size of the deviation depends on the particular definition of this quantity; it was maximal (3.5σ) in the CDF analyses in early 2011 [20] for the definition in the rest frame of the top quark pairs and applying a cut $M_{t\bar{t}} > 450$ GeV on their invariant mass $M_{t\bar{t}}$. Hence, an accurate analysis of higher-order effects is necessary in order to correctly identify possible effects from BSM physics.

In the second part we consider one of the theoretically most favored BSM scenarios, supersymmetry [21]. We present higher-order calculations and corresponding phenomenological predictions for a specific class of processes predicted by the simplest supersymmetric extension of the SM, namely the Minimal Supersymmetric Standard Model (MSSM) [22, 23].

Supersymmetry, introducing a symmetry between fermions and bosons, naturally and elegantly solves the hierarchy problem, stabilizes the electroweak vacuum and leads to the unification of gauge couplings at higher energy scales. Moreover, assuming conservation of R-parity, the lightest supersymmetric particle (LSP) of the MSSM is stable and, if electrically uncharged, a promising candidate for dark matter.

In the MSSM, every SM particle has a supersymmetric partner and, in contrast to the SM, two Higgs doublets are present. Amongst the production processes in-

volving non-standard MSSM particles, those with the largest cross sections at hadron colliders involve colored supersymmetric particles, i.e., squarks and gluinos, which are respectively the superpartners of quarks and gluons. So far, these colored particles, like the remaining non-standard particles in the MSSM, have not been found yet. On the contrary, considering specific simplified MSSM scenarios, higher and higher lower bounds on squark and gluino masses have been set by the ATLAS and CMS collaborations [24–28]. With squarks and gluinos heavier than 1 TeV, as suggested by these bounds, the squark–squark production process has the largest cross section and could potentially give the most easily detectable signal. Thus, accurate and reliable predictions are necessary especially for this process. For this reason, we present a study of the effects from higher-order corrections to predictions for squark–squark production at the LHC. Specifically, we analyze their impact on the searches for colored supersymmetric particles performed by ATLAS and CMS collaborations and on possible techniques used for parameter determination in case of a discovery.

The outline of the thesis is as follows. In the first part, after a brief description of the theoretical basis and the open problems of the SM (chapter 2), and a review of important features of top quark phenomenology (chapter 3), we discuss in detail the top quark charge asymmetry (chapter 4). In particular, we focus on the calculation of the electroweak contributions to the forward-backward asymmetry at the Tevatron from $\mathcal{O}(\alpha_s^2\alpha)$ and $\mathcal{O}(\alpha^2)$ terms in the cross section [29], which, increasing the QCD prediction [30] by a factor ~ 1.2, diminish in general the deviations from experimental measurements. For example, in more recent CDF analyses with a larger data set [31], the inclusion of electroweak corrections contributed to reduce the deviation, in the region $M_{t\bar{t}} > 450$ GeV, to 2.5σ. First, we list and briefly describe the measurements performed at the Tevatron and the LHC. Second, we explain in detail the calculation of the electroweak contributions to the forward-backward asymmetry at the Tevatron. Third, we present numerical results and compare them with the experimental measurements. Finally, we briefly discuss the status of the charge asymmetry at the LHC, where, in contrast to the Tevatron, no deviation has been found, and we comment on the tension between these measurements and those at the Tevatron.

In the second part, after describing (chapter 5) basic phenomenological features of the MSSM, the status of the searches for colored supersymmetric particles at the LHC and the corresponding relevant higher-order calculations, we analyze squark–squark production combined with two different decay configurations, providing phenomenological results for two different experimental signatures.

In chapter 6 we present the calculation of the contribution of factorizable NLO QCD corrections to the on-shell production of squark–squark pairs, with squarks of the first two families, combined with subsequent squark decays at the fully differential level [32]. NLO QCD factorizable corrections can be seen as separate corrections to the production and the decays. Although separate NLO QCD corrections to production [33] and decay [34,35] have already been calculated, these results are not sufficient

to obtain corrections to differential distributions for the complete processes (production+decays). We have performed these calculations at fully differential level, treating independently all the chiralities and flavor configurations and using a different infrared and collinear regularization approach. We obtained predictions with the accuracy of factorizable NLO QCD corrections for observable experimental signatures, by generating and combining events from production and decays into events for the complete process and then clustering partons into jets, using the typical parameters and the jet-algorithm chosen by ATLAS and CMS experiments.

The numerical results obtained from this calculation are presented in chapter 7. In section 7.1, we consider both the squarks decaying into the lightest neutralino and analyze the contribution to the signature including only two jets and missing transverse energy. We show the size of NLO corrections for several differential distributions and different MSSM spectra, and the impact on cut-and-count searches performed by ATLAS and CMS on this signature [32].

In section 7.2 we consider one squark decaying directly into the lightest neutralino and a squark decaying via a particular electroweak decay chain, the so called "golden decay chain". Here we analyze a different signature containing two jets, two leptons, with opposite charge sign and same flavor (OS-SF), and missing transverse energy [36]. In this case, besides investigating the impact of NLO factorizable corrections on cut-and-count searches, we analyze if and how these corrections and the combination with squark–squark production can alter the efficiency of particular parameter determination techniques that have been proposed for the isolate "golden decay chain".

Chapter 2

The Standard Model of elementary particles

2.1 Theoretical description

The Standard Model of elementary particles is theoretically based on the general framework of quantum field theory (QFT). The dynamics of the Standard Model is described by a Lorentz invariant Lagrangian involving spin 1/2 fermions and spin 0 and 1 bosons. The interactions among the different fields are obtained by requiring gauge invariance under the group $SU(3)_C \otimes SU(2)_L \otimes U(1)_Y$ and introducing Yukawa interaction terms. Fermions represent the elementary constituents of matter; strong, weak and electromagnetic interactions are mediated by the vector bosons and all the masses of the particles originate from a non-vanishing vacuum expectation value (VEV) of one scalar field.

In the Standard Model the strong force, responsible for the formation and the interactions of baryons and mesons, is described by Quantum Chromodynamics (QCD), namely the $SU(3)_C$ gauge symmetry. The fermions of the Standard Model can be divided into two categories: the quarks q, interacting via the strong force, and the leptons l, which do not strongly interact. In QCD the color components of quarks are organized according to the fundamental representation (triplet) of the $SU(3)_C$ group. Interactions among quarks are mediated by gluons g, the gauge vector bosons of the $SU(3)_C$ group, expressed in the adjoint representation (octet). QCD interactions among quarks and gluons can be described by the following Lagrangian,

$$\mathcal{L}_{\mathrm{QCD}} = -\frac{1}{4} F_A^{\mu\nu} F^A_{\mu\nu} + \sum_{\text{quarks}} \bar{q}_a (i \not{D} - m_q)_{ab} q_b \,, \tag{2.1}$$

where

$$F^A_{\mu\nu} = \partial_\mu G^A_\nu - \partial_\nu G^A_\mu + g_s f^{ABC} G^A_\mu G^B_\nu \tag{2.2}$$

and

$$(D_\mu)_{ab} = \partial_\mu \delta_{ab} + i g_s (t^C G^C_\mu)_{ab} \,. \tag{2.3}$$

In the previous equations, indices with small latin letters denote colors in the triplet representation. Conversely, capital letters refer to the octet representation. The matrices t_A are the $SU(3)_C$ generators in the fundamental representation and f^{ABC} are the structure constants of this group. G^μ is the gluon field and g_s is the strong coupling. The Lagrangian in eq. (2.1) is renormalizable and the strong interaction is asymptotically free at high energies. Thus, besides predicting bound states as baryons and mesons, it can be used to perform perturbative calculations and obtain predictions for particle phenomenology at high-energy colliders[1].

The remaining part of the Standard Model gauge group, $SU(2)_L \otimes U(1)_Y$, describes and unifies the weak force, introduced to explain beta decays and the muon decay, and the electromagnetic force, which is described in the QFT language by Quantum Electrodynamics (QED). The Yang-Mills Lagrangian for this gauge group can be written as

$$\mathcal{L}_{SU(2)_L \otimes U(1)_Y} = -\frac{1}{4} W_i^{\mu\nu} W^i_{\mu\nu} - \frac{1}{4} B^{\mu\nu} B_{\mu\nu} \,, \tag{2.4}$$

where

$$W^i_{\mu\nu} = \partial_\mu W^i_\nu - \partial_\nu W^i_\mu + g_W \epsilon^{ijk} W^j_\mu W^k_\nu \tag{2.5}$$

and

$$B_{\mu\nu} = \partial_\mu B_\nu - \partial_\nu B_\mu \,. \tag{2.6}$$

The Levi-Civita symbol ϵ^{ijk} represents the structures constants of $SU(2)_L$, and the g_W coupling parametrizes the W interactions. The gauge bosons W^i are an adjoint representation of the $SU(2)_L$ group, so a triplet ($i = 1, 2, 3$). Non-abelian gauge theories do not allow mass terms for the gauge bosons, hence the three W^i vector bosons have to be massless. Such a model would be unable to reproduce the observed phenomenology of elementary particles; however, the $SU(2)_L \otimes U(1)_Y$ gauge symmetry can be spontaneously broken via the Higgs mechanism, yielding three massive vectors.

A complex $SU(2)_L$ doublet of scalar fields $\phi = (\phi^+,\ \phi^0)$, the so called Higgs doublet, is introduced and its dynamics is described by the Lagrangian

$$\mathcal{L}_{\text{Higgs}} = (D^\mu \phi)^\dagger (D_\mu \phi) - V(\phi) \,, \qquad V(\phi) = \lambda |\phi|^4 - \mu^2 |\phi|^2 \,. \tag{2.7}$$

The covariant derivative appearing in eq. (2.7),

$$D^\mu_{ij} = \delta_{ij} \partial^\mu + i g_W T_{ij} \cdot W^\mu + i Y \delta_{ij} g'_W B^\mu \,, \tag{2.8}$$

guarantees the gauge invariance for $\mathcal{L}_{\text{Higgs}}$ and introduces the interactions of ϕ with W^i and B bosons.

The term g'_W parametrizes the B interactions, $W \cdot T := W^1 T^1 + W^2 T^2 + W^3 T^3$ and T^A_{ij} are $SU(2)_L$ matrices in the fundamental doublet representation. These matrices represent the $SU(2)_L$ weak isospin algebra. The representation of $U(1)_Y$ is trivial

[1] Gauge-fixing terms and ghost interactions have to be included in order to perform calculations including loop effects.

and parametrized by Y, the weak hypercharge, which is equal to $+1/2$ for the Higgs doublet.

Including in the Lagrangian the potential $V(\phi)$ of eq. (2.7), the configuration of minimum energy $\langle\phi\rangle$ satisfies the condition

$$|\langle\phi\rangle| = \sqrt{\frac{\mu^2}{2\lambda}} := \frac{v}{\sqrt{2}} \tag{2.9}$$

and breaks the $SU(2)_L \otimes U(1)_Y$ gauge symmetry. Choosing a particular direction in the complex plane, the minimum energy configuration reduces the $SU(2)_L \otimes U(1)_Y$ symmetry into a $U(1)_{\text{em}}$ symmetry that will be identified as the QED gauge group. With the choice $\langle\phi\rangle := \frac{1}{\sqrt{2}}(0, v)$, the $U(1)_{\text{em}}$ is generated by the charge $Q = T^3 + Y$, which corresponds to the electrical charge.

With a non-vanishing VEV, it is useful to rewrite the Higgs doublet ϕ as

$$\phi = \frac{1}{\sqrt{2}} \begin{pmatrix} 0 \\ H + v \end{pmatrix}, \tag{2.10}$$

where H is a real scalar field[2]. Using this parametrization in eq. (2.7), the quadratic terms for the vector boson fields can be written as

$$\mathcal{L}_{\text{mass}} = \frac{v^2}{8}\left[(g_W W^3_\mu - g'_W B_\mu)(g_W W^{3\mu} - g'_W B^\mu) + 2g^2_W W^-_\mu W^{+\mu}\right], \tag{2.11}$$

with $W^\mu_\pm = (W^\mu_1 \mp i W^\mu_2)/\sqrt{2}$. The mass terms in eq. (2.11) can be diagonalized defining $(W^3_\mu,\ B_\mu) := R(\theta_W)(Z_\mu,\ A_\mu)$, where $R(\theta_W)$ is a $SO(2)$ rotation matrix with the angle θ_W given by the relation $\sin(\theta_W) = g'^2_W/(g'^2_W + g^2_W)$. In this way, the mass terms of the W and Z bosons are explicitly obtained,

$$\mathcal{L}_{\text{mass}} = \frac{g^2_W v^2}{4} W^+ W^- + \frac{(g^2_W + g'^2_W)v^2}{8} Z^2, \tag{2.12}$$

and the massless vector field A is identified as the photon field. The masses of the W and Z bosons are related to the weak coupling and the the vacuum expectation value v via the relations

$$m_W = v g_W/2, \qquad m_Z = m_W/\cos(\theta_W). \tag{2.13}$$

The remaining terms in $\mathcal{L}_{\text{Higgs}}$ correspond to the kinetic and mass term for the Higgs ($m_H = \sqrt{2}\mu = \sqrt{2\lambda}v$), the cubic and quartic self-coupling terms $-\lambda v H^3 - \lambda H^4/4$, and the interaction terms between the Higgs field and the gauge bosons.

[2]In this step a particular gauge, called unitary gauge, has been implicitly chosen. The remaining three degrees of freedom of ϕ, corresponding to the Goldstone bosons $(G^\pm, G^0)$ originating from the symmetry breaking, do not appear in the Higgs Lagrangian with this choice of gauge. However, these three unphysical states are important for the consistency of the theory; they yield the longitudinal components of $W^\pm$ and Z bosons, defined afterward in the text.

Gauge bosons and the Higgs boson interact also with quarks and leptons. The left-handed chiralities of these fermions are classified in weak isospin doublets, whereas the right-handed chiralities are singlets under $SU(2)_L$ group. The hypercharges Y are assigned in such a way that the correct electric charges $Q_f = T^3 + Y$ for the fermions are obtained. Both for quarks and leptons there are three left-handed doublets

$$Q_L := \begin{pmatrix} u_L \\ d_L \end{pmatrix}, \qquad \begin{pmatrix} c_L \\ s_L \end{pmatrix}, \qquad \begin{pmatrix} t_L \\ b_L \end{pmatrix}, \tag{2.14}$$

$$L_L := \begin{pmatrix} \nu_e \\ e_L \end{pmatrix}, \qquad \begin{pmatrix} \nu_\mu \\ \mu_L \end{pmatrix}, \qquad \begin{pmatrix} \nu_\tau \\ \tau_L \end{pmatrix}, \tag{2.15}$$

whereas the right component are present for all the quarks (u_R,d_R,c_R,s_R,t_R,b_R) but not for all the leptons (e_R, μ_R, τ_R). The three doublets naturally define three generations (or families) of fermions. Each one of the three families contains a quark and a lepton left-handed doublet and the corresponding right-handed components. Thus, all the fields of the SM and their quantum numbers can be summarized in Table 2.1 and Table 2.2.

The kinetic terms of the leptons and quarks, and their interactions with the four gauge bosons are described by the Lagrangian

$$\mathcal{L}_{\text{fermions}} = \sum_{3 \text{ families}} (i\bar{Q}_L \not{D} Q_L + i\bar{L}_L \not{D} L_L) + \sum_{\substack{\text{right-handed} \\ \text{fermions}}} (i\bar{q}_R \not{D} q_R)\,, \tag{2.16}$$

where, using mass eigenstates for the gauge fields, the covariant derivative is given for left-handed doublets as

$$D_\mu = \partial_\mu - i\frac{g_W}{\sqrt{2}}(W^+_\mu T^+_\mu + W^-_\mu T^-_\mu) - i\frac{g_W}{\cos(\theta_W)} Z_\mu (T^3 - \sin^2(\theta_W) Q_f) - ieA_\mu Q_f \tag{2.17}$$

and for right-handed fermions as

$$D_\mu = \partial_\mu - i\frac{g_W}{\cos(\theta_W)} Z_\mu (-\sin^2(\theta_W) Q_f) - ieA_\mu Q_f\,. \tag{2.18}$$

In eq. (2.17) $T^\pm$ are defined as $T^\pm = T^1 \pm T^2$, and the QED coupling e is identified as $e = g\sin(\theta_W)$.

Eq. (2.16) does not include Dirac mass terms $m\bar{\psi}\psi = m(\bar{\psi}_L\psi_R + \bar{\psi}_R\psi_L)$. Indeed these terms are not gauge invariant, since the left-handed components of fermions belong to $SU(2)_L$ doublets, whereas the right-handed components are $SU(2)_L$ singlets. However, for each family, gauge-invariant Yukawa interactions between fermions and the Higgs boson can be introduced,

$$\begin{aligned} \mathcal{L}_{\text{Yukawa}} = -\frac{y_d}{\sqrt{2}}\bar{Q}^a_L \phi_a d_R - \frac{y_u}{\sqrt{2}}\epsilon_{ab}\bar{Q}^a_L \phi^\dagger_b u_R - \frac{y_e}{\sqrt{2}}\bar{L}^a_L \phi_a e_R + \text{h.c.} \xrightarrow{EWSB} \\ \xrightarrow{EWSB} -m_u \bar{u}u\left(1 + \frac{H}{v}\right) - m_d \bar{d}d\left(1 + \frac{H}{v}\right) - m_e \bar{e}e\left(1 + \frac{H}{v}\right)\,. \end{aligned} \tag{2.19}$$

Names	Spin 1/2	$SU(3)_C$, $SU(2)_L$, $U(1)_Y$
quarks	$Q_L = (u_L, d_L)$	$(\mathbf{3}, \mathbf{2}, +\frac{1}{6})$
($\times$3 families)	u_R	$(\mathbf{3}, \mathbf{1}, +\frac{2}{3})$
	d_R	$(\mathbf{3}, \mathbf{1}, -\frac{1}{3})$
leptons	$L_L = (\nu, e_L)$	$(\mathbf{1}, \mathbf{2}, -\frac{1}{2})$
($\times$3 families)	e_R	$(\mathbf{1}, \mathbf{1}, -1)$

Names	Spin 0	$SU(3)_C$, $SU(2)_L$, $U(1)_Y$
Higgs	$\phi = (\phi^+, \phi^0)$	$(\mathbf{1}, \mathbf{2}, +\frac{1}{2})$

Table 2.1: Spin 1/2 and spin 0 fields in the Standard Model.

Names	Spin 1	$SU(3)_C$, $SU(2)_L$, $U(1)_Y$
gluon	g	$(\mathbf{8}, \mathbf{1}, 0)$
W bosons	W	$(\mathbf{1}, \mathbf{3}, 0)$
B boson	B	$(\mathbf{1}, \mathbf{1}, 0)$

Table 2.2: Spin 1 fields in the Standard Model.

As shown in eq. (2.19) using the unitary gauge, the electroweak symmetry breaking (EWSB) automatically generates mass terms for the fermions ($m_f = vy_f/\sqrt{2}$) and interaction terms between the fermions and the Higgs field, parameterized by couplings proportional to the fermion masses. In eq. (2.19) the index a indicates the components of the Higgs doublet ϕ and ϵ_{ab} is the Levi-Civita antisymmetric tensor.

Considering all the three families, the Yukawa terms can also introduce interactions between fermions of different generations with same quantum numbers, without spoiling gauge invariance. In this case, the Yukawa couplings y_f are non-diagonal y_f^{ij} matrices, with the indices i and j referring to the three families. For quarks, this generalization is equivalent to defining diagonal y_u^{ij} and y_d^{ij} matrices and rotating all the left-handed down- and up-type quarks via two unitary matrices: $u_L^i \to U_u^{ij} u_L^j$ and $d_L^i \to U_d^{ij} d_L^j$. The interactions of quarks with the gluon, the photon and the Z boson are unaltered by these rotations. Conversely, W boson interactions allow for changes of generations that are parametrized by the unitary Cabibbo-Kobayashi-Maskawa (CKM) matrix $V_{CKM} = U_u^\dagger U_d$. This matrix is complex and can be parametrized via three real angles and one complex phase, which yields the only source of CP violation in the Standard Model.

In the case of the leptons, the situation is different; in the original Standard Model neutrinos are considered massless, so we can define arbitrarily $U_\nu := U_e$. Thus, leptons do not present interactions with other leptons of a different generation.

2.2 Open problems

The Standard Model, briefly described in the previous section, is a renormalizable quantum field theory that depends on 18 parameters:

- 9 fermion masses (6 for quarks and 3 for leptons),
- 3 angles and 1 phase of the CKM matrix,
- 3 parameters for electroweak interactions, e.g. : $\alpha = e^2/(4\pi)$, g_W and m_Z,
- the Higgs mass m_H,
- the strong coupling $\alpha_s = g_s^2/(4\pi)$.

At present, almost all the measurements at experiments with particle accelerators seem to be consistent with the predictions of the Standard Model. Thus, 18 parameters are sufficient to explain thousands of experimental data and a plethora of different phenomena. Only few deviations, not much larger than 3σ, between experimental measurements and SM predictions have been observed: the muon anomalous magnetic moment [18], the LEP forward-backward asymmetry of bottom quarks at the Z resonance [19] an the forward backward asymmetry of top quark at the Tevatron, which is discussed in detail in chapter 4.

However, besides these deviations, we already know that the Standard Model cannot be the "theory of everything" and presents some theoretical and phenomenological problems:

- First of all, the Standard Model does not include gravity and thus it cannot explain all the phenomena in our universe. Gravity introduces a new scale, the Planck scale $\Lambda_{\text{Planck}} \sim 10^{19}$ GeV, however, also assuming the validity of of the Standard Model up to this scale seems to be "unnatural". Indeed, in this way no new physics dynamics would be present in the $10^3 - 10^{19}$ GeV energy scale range. Moreover, the large difference between the electroweak and Planck scale, known also as the "hierarchy problem", is connected to another problem of the Standard Model: the fine tuning of Higgs parameters. In the definition of Higgs mass at one loop level, every fermion loop contributes with a term

$$\Delta m_H^2 = -\frac{|y_f|}{8\pi}\Lambda^2_{\text{Planck}}\,, \tag{2.20}$$

  where Λ_{Planck} is used as natural cut-off to regulate ultraviolet (UV) divergences. Thus, due to the quadratic divergence, the UV counterterms should be fine tuned at the $\mathcal{O}(10^{-30})$ accuracy in order to yield, after the cancellation of the divergences, the right value of m_H.

- A necessary condition for the renormalizability of a Lagrangian in quantum field theory is the absence of anomalies, i.e., symmetries that are valid in classical field theory but not at the quantum level. Anomalies typically appear in chiral gauge theories and the Standard Model, due to the $SU(2)_L$ group, belongs to this class of theories. However, in the Standard Model the anomalies automatically cancel, once all the leptons and quarks of one generation are taken into account. Ignoring the mixing induced by V_{CKM}, the Standard Model, with also only one or two generations, is renormalizable. Conversely, excluding one particle in one of the three generations, the renormalizability is lost. Thus, the particle content of any generation is not only necessary to explain the observed phenomenology, but also to guarantee the renormalizability of the theory. In the Standard Model, however, the cancellation of the anomalies appears to be accidental and not motivated by other theoretical arguments.

- The value of the 18 parameters of the Standard Model are input quantities that cannot be explained by the theory itself. Moreover, the values of the Yukawa couplings, i.e. the masses of the fermions, are very different, ranging from ~ 500 keV for the electron up to ~ 170 GeV for the top quark. Also the entries of the CKM matrix are not all of the same order, e.g., they suppress transitions of the top quark into a strange or down quark. Finally, also the gauge couplings do not seem to unify to the same value at any high-energy scale, as expected in a Grand Unified Theory (GUT).

- In principle also QCD interactions can introduce CP violation; indeed in the Lagrangian of the Standard Model a term

$$\mathcal{L}_{\text{strong}-\text{CP}} = \frac{\theta g_s^2}{32\pi^2} F_{\alpha\beta}\tilde{F}_{\alpha\beta}\,, \tag{2.21}$$

  where $F_{\alpha\beta} := \frac{1}{2}\epsilon_{\alpha\beta\gamma\delta}F^{\gamma\delta}$, can be added without violating gauge invariance. The term $\mathcal{L}_{\text{strong}-\text{CP}}$ can be written as a total derivative and does not introduce modification in perturbative calculations. However, it induces non-perturbative effects such as an electric dipole moment for the neutron. Measurements indicate that this quantity is extremely small, constraining θ to unnaturally small values. This is another parameter that must be fine-tuned in order to have a phenomenologically valid theory.

- Besides the previous pure theoretical problems, there are also important phenomena that cannot be explained by the Standard Model. Various aspects of galaxy dynamics, as e.g. the galaxy rotation curves, and the anisotropies of the cosmic microwave background (CMB) indicate that our universe is not composed only

by ordinary matter. This issue is known as the dark matter (DM) problem; a new kind of matter, the dark matter, has to be introduced to explain these phenomena. Dark matter is supposed to be electrically uncharged and only weakly or gravitationally interacting. According to recent measurements [37], it constitutes 84.5% of all the matter in the universe and 26.8% of the total energy. The remaining part of the energy is given by the dark energy, which also cannot be explained within the Standard Model and it is responsible for the accelerating expansion of the universe. Moreover, even the larger amount of matter with respect to antimatter in the observable universe cannot be explained by Standard Model and General Relativity alone.

- Observing the flux of neutrinos coming from the sun and from the atmosphere, oscillations amongst different flavors have been found. In order to explain these oscillations, neutrinos have to be massive, but they are massless and purely left-handed in the Standard Model. Still, right-handed neutrino components can be added and the masses can be originated via the Yukawa interactions with the Higgs, as for the other fermions. The Yukawa interactions would constitute also the only interaction terms for the right-handed neutrino components, which are singlets of the $SU(3)_C$ and $SU(2)_L$ groups and have hypercharges equal to zero. In this way, despite the fact that no right-handed neutrino has been observed yet, this model is not phenomenologically excluded, thanks to the extremely small interactions of right-handed neutrinos with the other particles. The mass terms, however, would introduce another hierarchy problem, since their values (m_ν) have to be much smaller than the ones of all the other particles in the Standard Model, $m_{\nu_i} < 1$ eV [37].

Chapter 3

The top quark

3.1 The top quark, a special quark

The top quark was discovered at the Tevatron in 1995 [16, 17], but particle physicists had been searching for it for at least 20 years. Indeed, after the discoveries of the τ lepton at SLAC-LBL in 1975 [38] and of the bottom quark at Fermilab in 1977 [39], the necessity of a third new particle was clear.

Without the top quark, the new incomplete third generation including the bottom quark and the τ lepton would have introduced anomalies and consequently spoiled the renormalizability of the Lagrangian describing the dynamics of elementary particles. Besides this pure theoretical argument, the existence of the top quark was also predicted at a later stage from limits on Flavor-Changing Neutral Current (FCNC) decays of the bottom and from the observation of B_d^0 and $\bar{B}_d^0$ oscillation [40]. Furthermore, with the measurements of the forward-backward asymmetry in $e^+e^- \to b\bar{b}$ production at PETRA [41], it was also possible to determine the weak isospin of the bottom quark ($T^3 = -1/2$) and thus infer the isospin of the top quark ($T^3 = +1/2$).

Hence, already before its discovery, the top quark was expected to be an up-type quark and the part of the SM Lagrangian, after EWSB, describing its electroweak and strong interaction was supposed to be:

$$\begin{aligned}\mathcal{L}_{\text{top}} = \; & \bar{t}(i\partial\!\!\!/ - m_t)t + g_s\bar{t}T^a\gamma^\mu t G_\mu^a + eQ_t\bar{t}\gamma^\mu t A_\mu + \\ & \frac{g_W}{\sqrt{2}}V_{CKM}^{ti}\bar{t}\gamma^\mu P_L d_i W_\mu + \frac{g_W}{2\cos\theta_W}\bar{t}\gamma^\mu(V_t - A_t\gamma^5)tZ_\mu + \frac{y_t}{\sqrt{2}}H\bar{t}t\,. \end{aligned} \tag{3.1}$$

In eq. (3.1) the first line contains the dynamic and mass term and the QCD and QED interaction terms. The second line contains the chiral and flavor-changing charged weak (W boson) interaction term with down-type quarks $d_i, (i = d, s, b)$, the flavor-conserving and parity violating neutral weak (Z boson) interaction term and the Yukawa interaction term with the Higgs field. The parameters V_t and A_t are respectively the vector and axial coupling of the Z boson with the top quark.

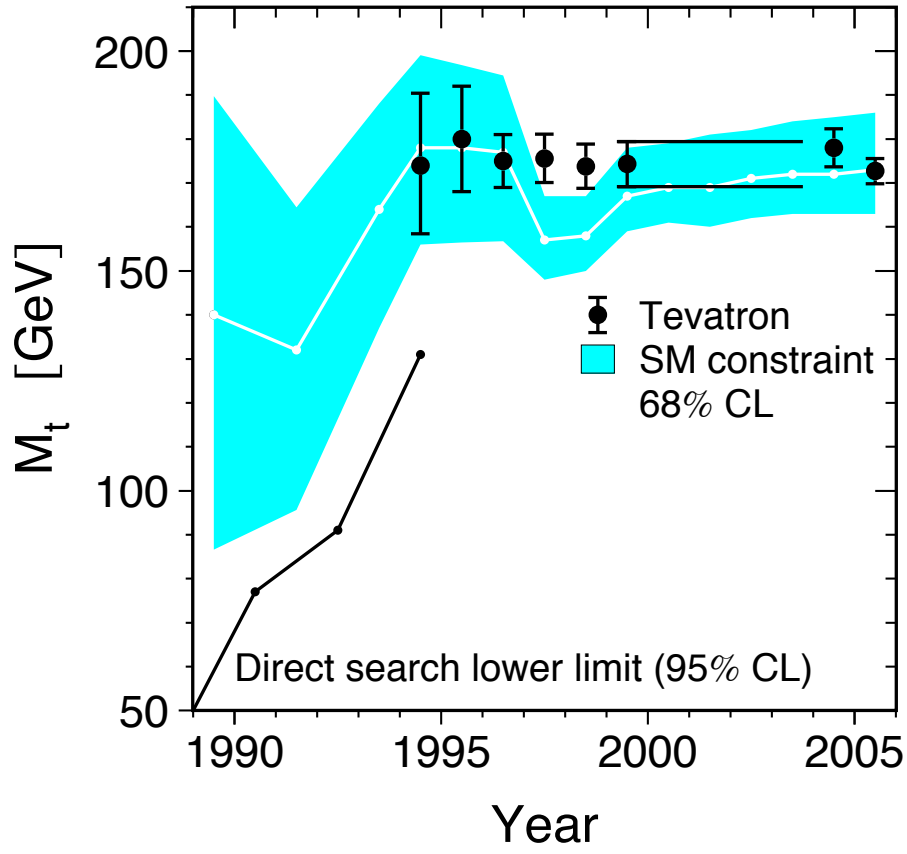

Figure 3.1: Evolution of the range allowed by electroweak-precision-observable analyses for the top quark mass value. Plot taken from [19].

Before the discovery of the top quark via direct production, new physical processes involving the production of the other particles of the SM as, e.g. the W and Z bosons, had been observed and the precision of the corresponding measurements increased during the years. In order to compare theoretical predictions with experimental measurements, leading-order (LO) approximations were not sufficiently precise anymore and effects induced by loop corrections had to be included. Using eq. (3.1) and the remaining part of the SM Lagrangian, it was possible, e.g. with production processes at the Z resonance [19], to estimate the effect of the top quark in loop corrections and so determine via electroweak precision observables (EWPO) the allowed region for the value of its mass. In Figure 3.1 taken from [19] the blue band, around the central value line in white, shows how the allowed region for m_t, obtained from the analysis

of EWPO, evolved during the years. The discovery of the top quark at the Tevatron, with a measured mass (black dots with error bars) compatible with the predictions, was a tremendous success of the SM and, in general, of quantum field theory.

With the previous colliders the expected discovery failed, because the top quark was too heavy to be produced. Its mass, $m_t = 173.5 \pm 0.6 \pm 0.8$ GeV according to the most recent world average value [42], is much larger than the masses of the others particles of the Standard Model and especially of the other quarks. The top quark has almost the same mass of a Rhenium atom; the bottom quark, the second heaviest quark, is $\sim$ 40 times lighter and the up quark, the lightest quark, is $\sim$ 10000 times lighter. Due to its large mass, the phenomenology of the top quark is completely different from the other quarks in the SM. For example, the top quark does not produce a single jet; it decays before hadronization, allowing to measure its properties as a "bare quark". Consequently, ad hoc experimental techniques have been developed to analyze its signature at colliders. Also, theoretical calculations had to tackle new challenging problems, in order to provide reliable predictions. For example, it was necessary to calculate, for the first time, radiative QCD corrections to processes involving colored massive particles.

Furthermore, the large value of m_t gives a special role in the context of BSM theory to the top quark. On the one hand, the tree-level coupling with the Standard Model Higgs $y_t \sim \sqrt{2} m_t/v \sim 1$ is large and hence the proximity of the top quark mass to v suggests that the top quark is naturally related to the electroweak symmetry breaking mechanism. Also, having the largest mass among the quarks, the term proportional to m_t^2 is the dominant contribution to the quadratic divergences of eq. (2.20), which emerge from the quark loop corrections to the Higgs mass. On the other hand, new particles in BSM models could be massive but lighter than the top quark and thus they could be directly produced in its decay. All these features of top quark physics are summarized in the following introductory sections 3.2 and 3.3, which have been written according to [42–48], where many more details can also be found.

3.2 Top quark properties

The top quark decays almost entirely into a positively charged W boson and a down-type quark ($t \to W^+ q$) via electroweak interactions. The measured value for the decay width, $\Gamma_t = 2.0^{+0.7}_{-0.6}$ GeV [42], is in agreement with the NLO QCD prediction

$$\Gamma_t^{NLO} = \frac{|V_{CKM}^{tq}|^2 m_t^3}{16\pi v^2}(1-r)^2(1+2r)\left[1 - \frac{2\alpha_s}{3\pi}\left(\frac{2\pi^2}{3} - \frac{5}{2}\right)\right], \quad r = \frac{m_W^2}{m_t^2}. \tag{3.2}$$

Numerically, $\Gamma_t^{NLO} = 1.3 - 1.4$ and the exact value depends on the constants entering eq. (3.2). NNLO QCD and NLO electroweak corrections and also effects from an off-shell W boson have been calculated; they shift the value of Γ_t by only a few percent [49–55]. The value of Γ_t, being larger than the QCD scale Λ_{QCD}, determines important

features of the phenomenology of the top quark. This quark does not form $t\bar{q}$ or tqq' bound states, since it electroweakly decays before hadronization. Thus, the top quark does not appear as a single jet in detectors; its signatures involve jets and possibly leptons and missing transverse energy. On the one hand, this kind of signature allows to measure its mass and spin structure, on the other hand, it can mimic the same signature emerging from decays of non-standard particles as, e.g., squarks of the third generation.

As said before, the top quark decays almost entirely into a W boson and a down-type quark. Since $|V_{CKM}^{tb}|$ is much larger than $|V_{CKM}^{td}|$ and $|V_{CKM}^{ts}|$, the largest part of $\Gamma(t \to W^+q)$ originates from the $t \to W^+b$ decay. According to [44], $\mathrm{BR}(t \to W^+b) = 0.998$, $\mathrm{BR}(t \to W^+s) = 1.9 \times 10^{-3}$ and $\mathrm{BR}(t \to W^+d) \sim 10^{-4}$, where the value of $\mathrm{BR}(t \to W^+b)$ is in agreement with recent measurements [56].

However, the classification of the different experimental signatures emerging from top quarks is determined by the W boson decay products, which can be either a lepton and a neutrino ($W^+ \to l^+\nu$) or a down-type and an up-type quark ($W^+ \to \bar{q}q'$). Neglecting the sub-leading decays $t \to Wq$ with $q \neq b$, the SM predictions for the branching ratios of the relevant decays [44], in agreement with the measured values, are:

$$BR(t \to bl^+\nu) = 0.108 \quad (l = e, \mu, \tau) \ , \qquad BR(t \to b\bar{q}q') = 0.337 \times |V_{CKM}^{qq'}|^2. \quad (3.3)$$

Typically, neutrinos cannot be detected at colliders, but they appear as a missing transverse energy ($\not{E}_T$) component in the total momentum of the final-state particles produced in a process. Hence, according to eq. (3.3), $\sim 1/3$ of the top quark decays gives the signature b-jet+lepton+$\not{E}_T$ (+X) and $\sim 2/3$ of them give the signature b-jet+2 jets(+X).

In the top sector, the mass m_t is the physical parameter known with the highest precision. At the Tevatron and the LHC, it has been obtained comparing lepton and jet template distributions for different values of m_t with experimental results. Also more advanced techniques have been developed, however based on kinematical distributions for which the additional jets radiated in the production of the top quark lead always to non-trivial problems for the reconstruction of the top quark kinematic. With these methods, it has been possible to achieve an accuracy of the order of 1 GeV in the measurements. It is difficult or maybe even impossible, due to a theoretical problem, to substantially lower the accuracy of the measurement using these methods. The mass, measured from kinematical distribution, is supposed to be the pole mass, a quantity that, due to the non-perturbative nature of QCD at low energy, has an intrinsic ambiguity of order Λ_{QCD} in its definition. This problem can be avoided measuring $m_t^{\overline{\mathrm{MS}}}(\mu)$ for which this problem is not present[1]. The relation between m_t and $m_t^{\overline{\mathrm{MS}}}(\mu)$

[1]The renormalization in the $\overline{\mathrm{MS}}$ scheme consists in the following steps: regularize the UV divergences via dimensional regularization, eliminate the terms proportional to $\Delta = 2/\epsilon - \gamma_E + \log(4\pi)$ and finally set the regularization scale equal to the renormalization scale.

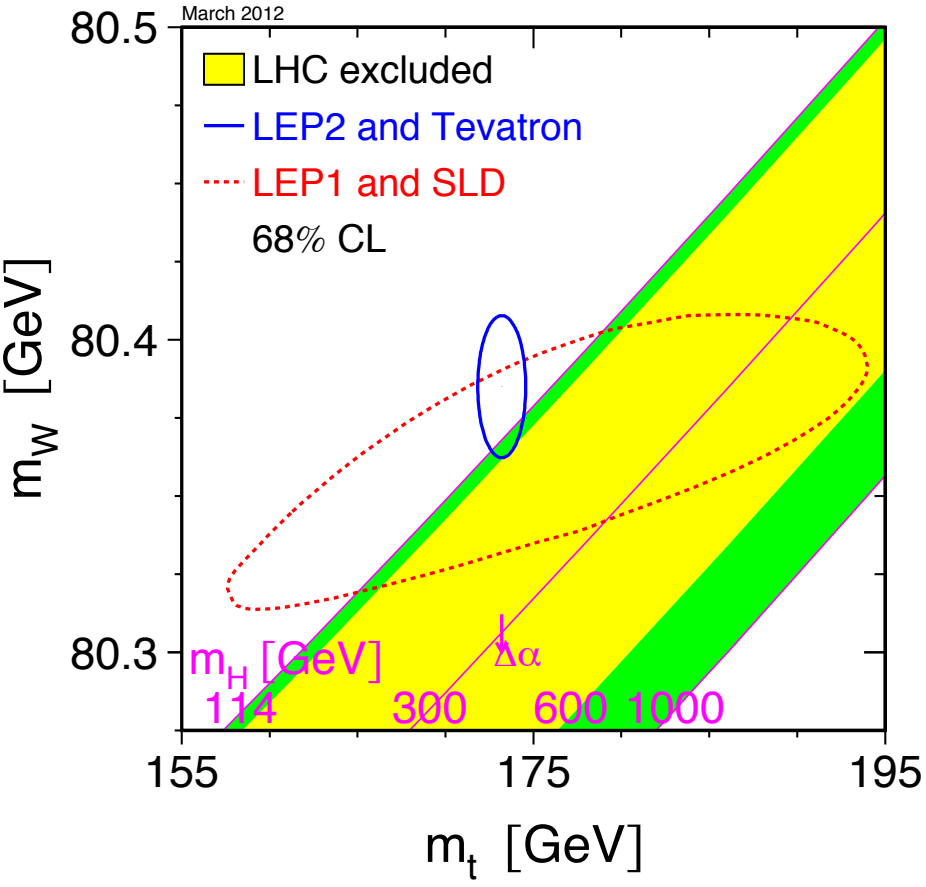

Figure 3.2: m_W as function of m_t for various values of m_h. The blue circle delimits the area allowed by direct measurements of m_W and m_t, the red circle delimits the area allowed by EWPO. The yellow region represents the exclusions from the LHC before the Higgs discovery. This plot is an updated version of the analogous one in [19], and it is provided by the LEP Electroweak Working Group at `http://lepewwg.web.cern.ch/LEPEWWG`.

is known up to $\mathcal{O}(\alpha_s^3)$ and the difference between the two masses is ~ 10 GeV. The value of $m_t^{\overline{\text{MS}}}(\mu)$ can be extracted, e.g, from measurements of the total cross section of top pair production. Studies in this direction have already been performed (see [42,57] for a more detailed discussion and further references).

The precise determination of the top quark mass is an important input for SM tests. The electroweak corrections involved in the prediction of many observables contain, as the dominant contribution, terms depending on the mass of the top quark. The

same electroweak global fits used to determine the expected value of the top quark mass, before its discovery, have also been used to predict the mass of the Higgs. The prediction for the Higgs mass value strongly depends on the values of m_t ad m_W, as shown in Figure 3.2, where this dependence has been plotted in the $m_t - m_W$ plane together with the value of m_t and of m_W obtained from direct measurements (blue circle) and from EWPO analyses (red circle). Now that the Higgs boson has eventually been discovered [8,9], it is possible to test the validity of the SM using also the measured Higgs mass as input parameter in fits based on EWPO. As shown, e.g., in [58], a good consistency has been found in this kind of global fits.

Also, the precise knowledge of the top quark mass is important to determine the energy scale up to which the SM Higgs potential is stable [59, 60], indeed this scale strongly depends on the top quark mass. As can be seen in Figure 3.3 taken from [61], an error of ~ 1 GeV on m_t implies an error of about one order of magnitude on the instability scale of the Higgs potential.

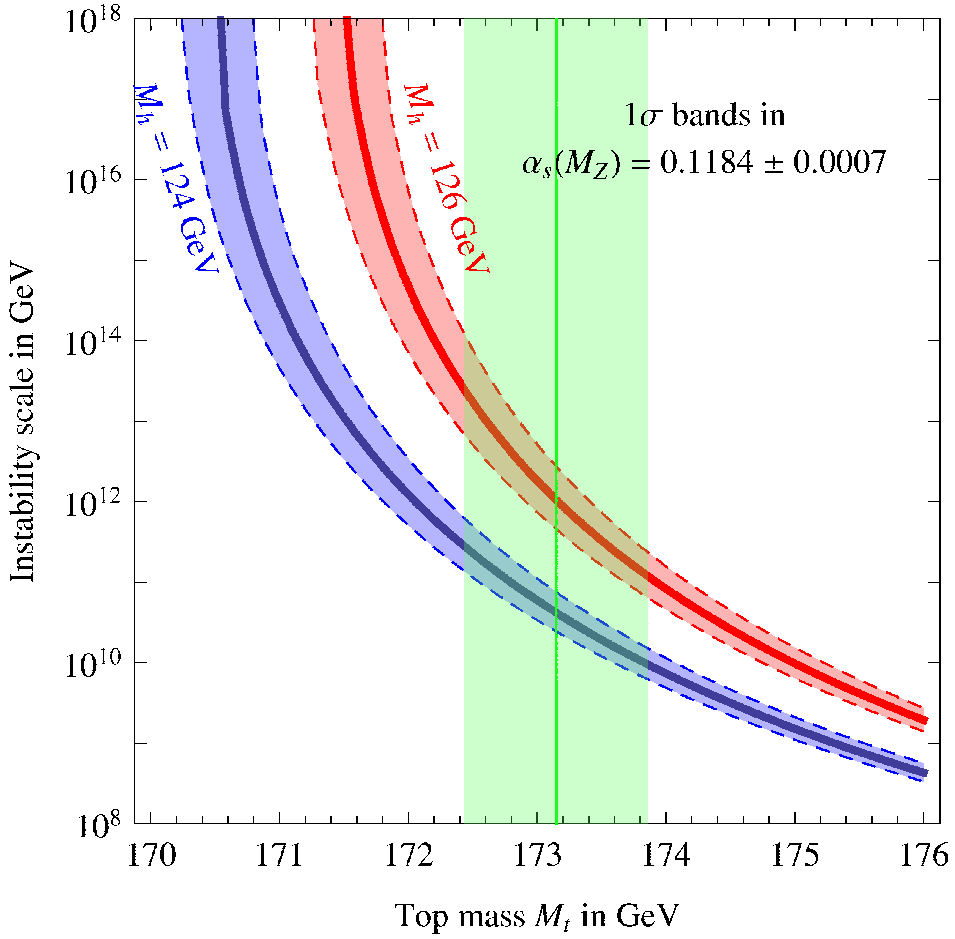

Figure 3.3: Instability scale for the Higgs potential as function of the mass of the top quark for two values of the Higgs mass. Plot taken from [61].

The possibility of studying the top quark as a bare quark allows also to investigate its spin structure, unaffected by hadronization effects. Actually, the top quark itself analyzes its spin structure through the pure left-handed interactions with the W boson and the bottom quark. Under the assumption $m_b = 0$, the bottom quark emerging from the top quark decay has always left-handed helicity. Due to angular momentum conservation in the top quark center-of-mass system, the W boson can be longitudinally or left-handed polarized but not right-handed polarized. Specifically, a fraction $F_0 \sim 70\%$ of W bosons from top decays is longitudinally polarized and the remaining part $F_L \sim 30\%$ is left-handed polarized. This picture is qualitatively unaltered by the inclusion of radiative corrections, and a non-vanishing bottom quark mass induces only effects $\mathcal{O}(m_b^2/m_W^2)$. In the SM, the longitudinal component of the W boson originates, after EWSB, from the charged component of the Higgs doublet. Thus, the analysis of the polarization of the W boson emerging from top quark decays can be used to investigate the EWSB mechanism. However, the helicity of the W boson cannot be directly measured, but, analyzing W boson decay products, the values of F_0 and F_L can be extracted. The measured values are in good agreement with the SM theoretical predictions [62]. Interesting information on the spin of the top quark can also be obtained by studying directly the angular distributions of the decay products of the top quark in respect to its polarization vector (see discussion in [44]).

Due to its large mass and the large uncertainty on the measured value of its total decay width, the top quark can also accommodate new decay modes, with branching ratios of the order of a few percent, involving new non-standard particles. In the following we list some interesting cases.
Theories with an extended Higgs sector can present flavor-changing decays into charged Higgs, $t \to H^+ b$. The MSSM[2], e.g., belongs to this class of models and includes, in scenarios with $m_t > m_{\tilde{t}_1}$, also the flavor conserving decay $t \to \tilde{t}\tilde{\chi}^0$.
In the SM, due to the Glashow-Iliopoulos-Maiani (GIM) mechanism [63], FCNC decays are extremely suppressed (BR $< 10^{-12}$) and not detectable at the LHC. In some BSM models the branching ratios of this kind of decays can be increased to values possibly measurable at the LHC.
Finally, BSM theories can affect the purely left-handed SM Wtb coupling also if new particles are heavier than the top quark and do not appear as top quark decay products. ATLAS and CMS have already investigated these possible deviations and set limits on their size, see e.g. [64].

[2]The MSSM and its particle content are introduced and discussed in chapter 5, as introduction to the calculation of squark–squark production and decay presented in chapter 6.

3.3 Top quark production at hadron colliders

At hadron colliders, the top quark can be produced in association with a quark or a W boson via electroweak interactions (single top production) and in pairs, together with an antitop quark, via strong or electroweak interactions. The first top quark pair production events were detected in 1995 at the Tevatron and led to the discovery of the top quark. In contrast, the evidence for single top production was only established in 2006 [65–67]. At the LHC, both processes have already been measured.

The theoretical predictions for top quark pair and single top quark production are known at almost the same order of accuracy in perturbation theory. Conversely, the experimental measurements of single top quark production cross sections are less accurate than the ones of top quark pair production. Indeed, the separation between signal and background is much more difficult for the former case.

The basic features of single top quark production are discussed in subsection 3.3.1, whereas in subsection 3.3.2 we present the phenomenology of top quark pair production at hadron colliders. In this second case, effects of radiative corrections, especially for the electroweak case, are discussed in detail.

3.3.1 Single top quark production

In the SM, the top quark can be singly produced via three different partonic processes:

- s-channel: $qq' \to W \to \bar{b}t$, illustrated in Figure 3.4(a),
- t-channel: $qb \to q'$, illustrated in Figure 3.4(b),
- Wt production: $bg \to Wt$, illustrated in Figure 3.4(c).

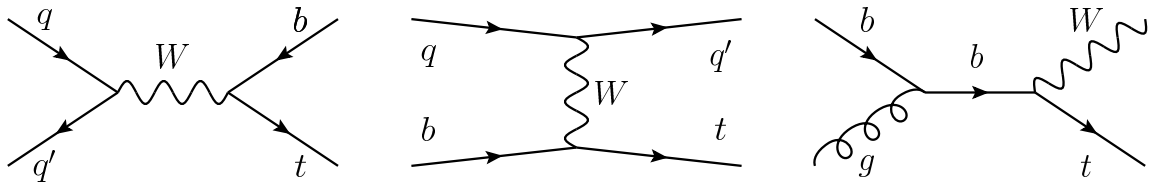

Figure 3.4: Illustrative tree-level diagrams for: s-channel, t-channel and Wt production.

As can be seen in Figure 3.4, the three process classes involve, in different ways, the electroweak Wtb coupling. Thus, the cross section of single top production can be used to test the structure of the Wtb coupling and directly measure the value of $|V_{CKM}^{tb}|$. In Table 3.1 the values, taken from [44], of the predictions for total cross sections of single (anti)top production are listed for the Tevatron and the LHC at 14 TeV. These results

cross section (pb)	s-channel	t-channel	Wt production
Tevatron: $\sigma_t + \sigma_{\bar{t}}$	0.54 ± 0.04	1.15 ± 0.07	0.14 ± 0.03
LHC: σ_t	7.8 ± 0.7	150 ± 6	44 ± 5
LHC: $\sigma_{\bar{t}}$	4.3 ± 0.3	92 ± 4	44 ± 5

Table 3.1: Cross sections for single (anti)top production at the Tevatron and the LHC at 14 TeV.

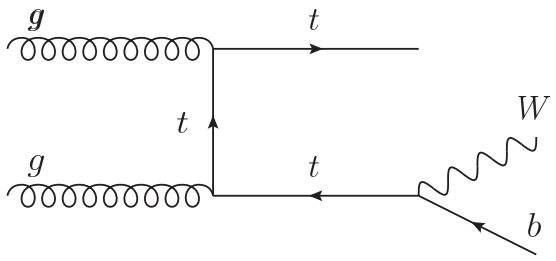

Figure 3.5: Real radiation of a b-quark.

include NLO QCD corrections [68,69] and partly corrections beyond NLO [70,71].[3] As can be seen in Table 3.1 the three channels have a different phenomenological impact at the Tevatron and the LHC.

Here, we do not discuss in detail the phenomenology and the calculation of higher-order corrections for single top quark production. However, we want to point out that the calculation of NLO corrections to Wt production involves a technical problem that is very common for supersymmetric processes and is present also in the calculation discussed in chapter 6. The diagram in Figure 3.5 contributes to NLO QCD corrections of Wt production, but part of its contribution is also included in the LO cross section of top quark pair production (described in the next subsection). Indeed, the diagram in Figure 3.5 represents the real radiation of a b-quark in Wt production, but it can also be viewed as the production of a top quark pair with the antitop quark decaying into a W boson and a b-quark. In order to avoid double counting of the same terms in the two different processes, at least the contribution from phase-space configurations with on-shell antitop must be subtracted in the single top calculation.

Different strategies can be used to perform this subtraction and many details can be found in section 6.4.3 for the case of the calculation of quark radiation from squark–squark production. This process contributes to NLO QCD corrections to squark–squark production, but at the tree level, in analogy to the case of single top quark production, some diagrams can be viewed as squark–gluino production with a gluino decaying into a squark and a quark. Thus, also in this case at least the contribution from phase space configurations with an on-shell gluino must be subtracted in the quark radiation from squark-squark production.

[3] See [44] for more details about approximation used in the predictions.

Considering BSM models, single top quark production is also a promising channel for the identification of possible new physics effects. In theories containing a W' state[4], the cross section for the s-channel process is enhanced and the distribution of the invariant mass for the top and bottom quark in the final state presents a resonance peak around the W' mass (see [72] and references therein). Moreover, the top quark could be produced in association with other particles, e.g., a charged Higgs boson in theories with an extended Higgs sector [73]. FCNC interactions allow also tX final states, where X can be a neutral Z or Higgs boson, a gluon or a photon [74]. Finally, as in the case of the top quark decay, with this process possible deviations from the SM Wtb coupling can be studied.

3.3.2 Top quark pair production

Top quark pair production consists in the inclusive production of a top and an antitop quark. The corresponding experimental signatures are determined by the possible configurations for the top and antitop quark decay modes. As said in section 3.2, the decay modes of the top quark are characterized by the decay modes of the W boson. Its branching ratio into a lepton and a neutrino is approximately 1/3 and its branching ratio into jets is around 2/3. Consequently, three classes of signatures, as illustrated in Figure 3.6, are possible for top quark pair production:

- *all-hadronic*, branching ratio $\sim 4/9$,
  signature: 2 b-jets + 4 jets $(+X)$,
- *semi-leptonic*, branching ratio $\sim 4/9$,
  signature: 2 b-jets + 2 jets + 1 lepton+ $\not{E}_T$ $(+X)$,
- *dileptons*, branching ratio $\sim 1/9$,
  signature: 2 b-jets + 2 leptons $+\not{E}_T$ $(+X)$.

In the experimental analyses the contribution of tau leptons is typically discarded, thus the semileptonic and dileptons branching ratios are reduced. The all-hadronic channel gives the largest contribution, 46% of the top quark pair cross section, but its background contains large QCD contributions from multijet production. The dilepton channel has a very clean signature, but, excluding tau leptons, only 5% of the top quark pair events present this signature. The semi-leptonic channel is a good compromise between the clearness of the signal and the size of the branching ratio, BR $\sim$ 30%. Thus, in the experimental analyses, this signature is generally preferred.

We now turn to the description of the partonic subprocesses that yield top quark pair production and their contributions at different orders of perturbation theory. In Figure 3.7, SM tree-level diagrams for the corresponding partonic subprocesses at

[4] W' are BSM gauge bosons arising from an additional $SU(2)$ symmetry group.

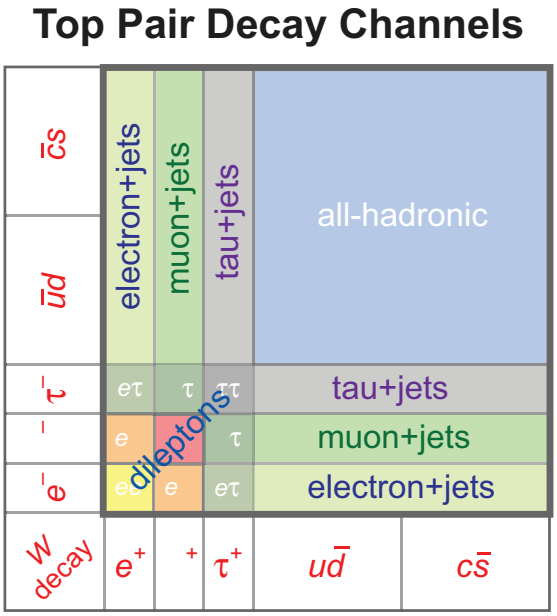

Figure 3.6: Different signatures emerging from top quark pair production. Figure taken from [48].

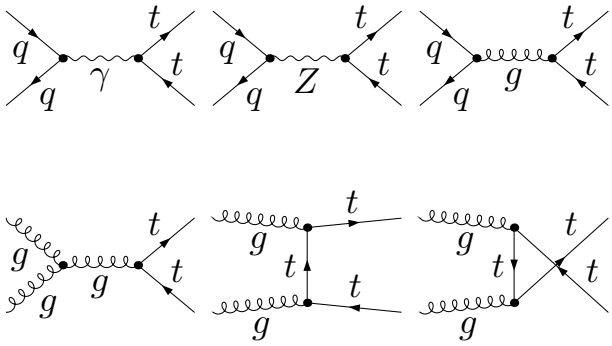

Figure 3.7: Electroweak and QCD Born diagrams for $t\bar{t}$ production.

hadron colliders are shown. The first line of diagrams contribute to the $q\bar{q} \to t\bar{t}$ process, the second line to the $gg \to t\bar{t}$ process. The $q\bar{q}$ initial state presents an $\mathcal{O}(\alpha_s)$ diagram, $q\bar{q} \to g \to t\bar{t}$, and two $\mathcal{O}(\alpha)$ diagrams, $q\bar{q} \to \gamma \to t\bar{t}$ and $q\bar{q} \to Z \to t\bar{t}$. The interference between $\mathcal{O}(\alpha_s)$ and $\mathcal{O}(\alpha)$ diagrams is zero due to the different color structure: the gluon in the propagator of $q\bar{q} \to g \to t\bar{t}$ is a color octet, whereas the photon or the Z boson in the propagator of $q\bar{q} \to \gamma, Z \to t\bar{t}$ is a color singlet. Thus, $\mathcal{O}(\alpha)$ diagrams contribute only starting from $\mathcal{O}(\alpha^2)$ in the cross section. In principle also an s-channel diagram with a Higgs boson and a t-channel diagram with a W boson are possible. The interference of the W boson t-channel diagram with $q\bar{q} \to g \to t\bar{t}$ is

$\sigma_{t\bar{t}}$ (pb)	Tevatron	LHC 7 TeV	LHC 14 TeV
NLO	$5.79^{+0.79+0.33}_{-0.80-0.22}$	133^{+21+7}_{-19-7}	$761^{+105+26}_{-101-27}$
NLO+NNLL	$6.30^{+0.19+0.31}_{-0.19-0.23}$	149^{+7+8}_{-7-8}	821^{+40+24}_{-42-31}

Table 3.2: Cross sections at NLO and NLO+NNLL for top quark pair production at the Tevatron and at the LHC.

non-vanishing, but suppressed either by $|V^{qt}_{CKM}|$ for $q \neq b$ or by the PDF luminosity for $q = b$. The contribution of the Higgs s-channel diagram to $\mathcal{O}(\alpha^2)$ is suppressed by the small coupling of the Higgs with the quarks in the initial state. Thus, the $\mathcal{O}(\alpha^2)$ contributions can be safely neglected in predictions for cross sections and differential distributions. This will appear clearer after the discussion of the size of QCD radiative corrections and their associated theoretical errors.

Top quark pair production is, first of all, a "QCD process". At LO, $\mathcal{O}(\alpha_s^2)$, $t\bar{t}$ production originates via strong interactions from $q\bar{q} \to t\bar{t}$ and $gg \to t\bar{t}$ processes. The contribution of these two processes are different at the Tevatron and the LHC. The $q\bar{q}$ and gg initial states respectively yield circa 85% and 15% of the total cross section at the Tevatron and, e.g., 10% and 90% at the LHC 14 TeV. This difference is due to PDFs; increasing the energy in the hadronic center-of-mass system, their contributions arise from smaller values of the variable x for the parton momentum. In this region the gluon PDF is larger than the valence quark PDFs. In addition, $p\bar{p}$ allows both the quark and the antiquark in the initial state to be a valence quark, whereas with pp there is no valence antiquark in the initial state. The $q\bar{q}$ and gg initial states present different distributions and top quark polarizations. Thus, these differences appear also comparing LHC and Tevatron predictions at the hadronic level.

Also the dominant radiative corrections are, in general, generated by QCD interactions. The NLO QCD corrections, $\mathcal{O}(\alpha_s^3)$, have to be taken into account to obtain a realistic phenomenological description. The K-factor, i.e. the ratio between the cross-section at NLO and LO, is $\sim 1.25(1.50)$ at the Tevatron(LHC 14 TeV). Moreover, the NLO corrections, which include also a contribution from the qg and $\bar{q}g$ initial state, reduce the errors due to the variation of the renormalization and factorization scale.

These errors, including Next-to-Next-to-Leading-Logarithm (NNLL) corrections, can be further reduced. In Table 3.2 the NLO and NLO+NNLL results presented in [75] are listed. The first error refers to scale uncertainties, the second comes from PDFs[5]. As can be seen in Table 3.2, the error due to scale variation strongly decreases once NNLL corrections are taken into account. Several groups have performed NLO+NNLL calculations [76–80], using different technical approaches. In Figure 3.8, the predictions obtained by these groups for the total cross section at NLO, NLO+NNLL and at approximated Next-to-Next-to-Leading-Order (NNLO)[6] accuracy are compared to the

[5]See [75] for more details on the procedure used to obtain the errors.

[6]See [77, 79, 82, 83] for the definitions of the approximate NNLO.

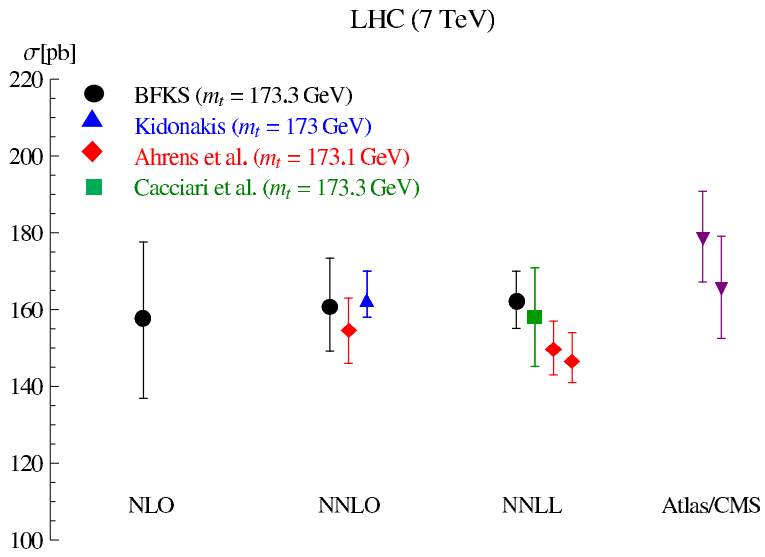

Figure 3.8: Comparison between different predictions (NLO, NNLL and approximated NNLO) and the values of the total cross section measured by ATLAS and CMS at the LHC with $\sqrt{S} = 7$ TeV. Plot taken from [81].

values measured by ATLAS and CMS at 7 TeV. In the error band PDF errors are not included, still, the different theoretical predictions and the experimental measurements are in good agreement.

Also the total cross section at full NNLO accuracy [84–86], NLO factorizable corrections[7] including the decay in narrow-width approximation [87,88] and non-factorizable corrections have been calculated [89]. Now, also the complete NLO corrections including leptonic decays [90,91] are known.

It is worth to note that, especially at LHC 14 TeV, the cross section of single top quark production is smaller than the cross section of top quark pair production, but not as much as one could expect from their different leading perturbative orders: $\mathcal{O}(\alpha^2)$ for single top quark production and $\mathcal{O}(\alpha_s^2)$ for top quark pair production. Indeed, in single top quark production a larger phase-space volume is available and thus the cross section is enhanced.

Besides pure QCD effects, also electroweak interactions induce corrections to top quark pair production [92–96]. The size of these corrections and their phenomenological impact strongly depend on the particular physical observable under consideration. In this section we discuss total cross sections and differential distributions, the charge asymmetry is discussed in detail in section 4.2. The following paragraphs are taken

[7] A definition of the terms *factorizable* and *non-factorizable* will be given in the context of squark-squark production and decay in section 6.2.2 and in appendix A. The same arguments apply also to the case of top quark pair production and decays.

from [97].

The weak $\mathcal{O}(\alpha_s^2\alpha)$ corrections to the total cross section have been calculated for the first time in [92] and later at differential level in [93] and including polarization and spin correlations in [94]. Also, in a very recent publication [98], new numerical results, based on calculations in [93], have been presented using updated PDFs and input parameters, as e.g. the Higgs mass. At this order, the $gg \to t\bar{t}(+X)$ process contributes only via electroweak loop corrections. The $q\bar{q} \to t\bar{t}(+X)$ process contributes with loop corrections and also with real gluon radiation via the interference of $q\bar{q} \to Z \to t\bar{t}g$ and $q\bar{q} \to g \to t\bar{t}g$ diagrams. With the Higgs mass of about 126 GeV, weak corrections amount to -2% of the LO cross section, for the LHC at 14 TeV, and few permille for the Tevatron. These effects are small, especially if compared with the aforementioned theoretical errors from PDFs and the scale variation in QCD corrections.

As said before, the total cross section at the LHC gets the dominant contribution from the gg initial state, whereas at the Tevatron the $q\bar{q}$ initial-state contribution is larger than in the gg case. Conversely, the tail of the distributions involving a very hard top is dominated, for both the colliders, by the $q\bar{q}$ initial state. Indeed, very hard tops can be produced only with high partonic center-of-mass energies, for which the $q\bar{q}$ PDFs luminosity is larger than for gg. In this regime, especially for the dominant $q\bar{q} \to t\bar{t}(+X)$ process, Sudakov logarithms enhance the size of relative electroweak corrections. These logarithms always arise in the calculation of electroweak loop corrections and, at NLO, they correspond to terms $\mathcal{O}(\alpha \log^2(M^2/\hat{s}))$, where $\hat{s}$ is the total energy of the partonic process in its center-of-mass frame and $M = M_W, M_Z$. In the p_T distribution for the LHC at 14 TeV, e.g., $\mathcal{O}(\alpha_s^2\alpha)$ weak corrections reach -20% for p_T around 2 TeV. This effect is larger than the PDF and scale variation uncertainties. However, the absolute value of the differential cross section in the tail is six orders of magnitude smaller than in the peak region, so a very high luminosity is necessary to compare the effects of these corrections with experimental data. In [93] a similar quantity is discussed: the relative weak corrections to the LO cross section with a cut $p_T > p_T^{\text{cut}}$ applied. For $p_T^{\text{cut}} < 2$ TeV these corrections are larger than the statistical uncertainty estimated for an integrated luminosity of 200 fb^{-1}. It seems that it will be possible to test experimentally the effects from the discussed weak radiative corrections. The same arguments apply to the LHC at 7 and 8 TeV and the Tevatron, but the luminosity accumulated in these runs is not enough for a comparison with data [99].

The remaining part of the $\mathcal{O}(\alpha_s^2\alpha)$ electroweak contribution, the QED corrections [95], involves only diagrams with QED and QCD interactions. The $gg \to t\bar{t}(+X)$ process contributes, as in the weak case, only with loop corrections, the $q\bar{q} \to t\bar{t}(+X)$ process with loop corrections, real gluon radiation and also real photon radiation. In $q\bar{q} \to t\bar{t}(+X)$, boxes and the interference of the initial-state and final-state radiation do not contribute to the inclusive total cross section. Oppositely, as we will see in detail in section 4.2, the non vanishing terms do not contribute to the asymmetric cross section. The QED $\mathcal{O}(\alpha_s^2\alpha)$ of $q\bar{q} \to t\bar{t}(+X)$ can be divided, on a diagrammatic

basis, into corrections to the total cross section and corrections to the charge asymmetry. Moreover, also the $\gamma g \to t\bar{t}$ process is present at this order and, at the LHC 14 TeV, constitutes the dominant contribution to the QED corrections. Unfortunately, MRST2004QED [100] is at the moment the only PDF set[8] that provides a photon distribution and allows in general to perform consistent calculations of electroweak corrections at hadron colliders.

The QED corrections to the total cross section, as in the weak case, are small: -2% for the Tevatron and 1% for the LHC at 14 TeV. Corrections to distributions, again, are enhanced in regions involving a very hard top, but here they are reduced by the positive contribution of $\gamma g \to t\bar{t}$. As illustrative comparison, in the p_T distribution they sum up to -4% for $p_T = 2$ TeV.

In [96] NLO QCD results are combined with both QED and weak $\mathcal{O}(\alpha_s^2\alpha)$ corrections and also with contributions from $\mathcal{O}(\alpha_s\alpha)$, $\mathcal{O}(\alpha^2)$ and $\mathcal{O}(\alpha_s\alpha^2)$. In conclusion, electroweak corrections are in general much smaller than QCD effects. They are larger only in phase-space regions not easily accessible by experimental measurements. As it will be discussed in section 4.2, the situation is very different for the charge asymmetry.

The top quark pair production is also a promising channel for the identification of new physics effects. In the following we list some interesting BSM scenarios for which this process has a relevant role. In this contest, the clearest evidence of a new particle X can be obtained from its direct production and subsequent decay into a top quark pair, $X \to t\bar{t}$. The particle X can be, e.g., a Z' boson[9] or a Kaluza–Klein gluon excitation. Unfortunately, the potential clear signal has led, until now, only to lower bounds beyond 1 TeV for the mass of the resonant particle, see [102,103] and references therein.

In some BSM theories, as, e.g., supersymmetric extension of the SM, a partner T of the top quark with the same quantum numbers and possibly different spin is present. In the case $m_T > m_t$, it can decay into a top quark and SM particles. The production of $T\bar{T}$ pairs at the LHC could result in a signature equal to $t\bar{t}$ plus other SM particles emerging from T decay. However, the additional particles emerging in the T decays can also be stable undetectable particles appearing as $\not{E}_T$ in the detector, as, e.g., in the MSSM the lightest neutralino $\tilde{\chi}_1^0$ emerging from the decay of a top squark ($\tilde{t} \to t\tilde{\chi}_1^0$). In this case, for values of m_T close to m_t, $T\bar{T}$ and $t\bar{t}$ are experimentally undistinguishable. This is an example of how, in contrast to the scenarios discussed before, $t\bar{t}$ production can be background of BSM signatures. Jets, leptons and $\not{E}_T$ are the typical content of signatures, as it will be explained in section 5.3.1, emerging from production of supersymmetric particles or, in general, BSM particles, and the $t\bar{t}$ production can mimic this signature. Moreover for some channels, $t\bar{t}$ production is a

[8] NNPDF collaboration announced (Rencontres de Moriond: QCD and High Energy Interactions La Thuile, March 9-16, 2013) that soon a new set of PDFs including electroweak effects and the photon distribution will be publicly available. See also [101].

[9] Z' are BSM gauge bosons arising from an additional $U(1)$ symmetry group.

background to Higgs production. Thus, both as background to new physics searches or as signal for new physics effects, the prediction of top quark pair production have to be known with high accuracy.

Chapter 4

The top quark forward-backward asymmetry

As explained in the previous sections, many theoretical motivations suggest that BSM effects could be naturally observed in top quark phenomenology. However, no hint for new physics, i.e. significant deviations between SM theoretical predictions and experimental results, has appeared for the physical observables discussed so far: decay widths, branching ratios and cross sections for top quark pair and single top production.

In 2010, at the Tevatron, the CDF collaboration performed the measurement of the top quark forward-backward asymmetry A_{FB}, i.e., the relative difference between the number of top quarks produced in the "forward direction" (the direction of the proton) and the number of top quarks produced in the "backward direction" (the direction of the antiproton). Given the CP-invariant $p\bar{p}$ initial state, the forward-backward asymmetry is equivalent to the charge asymmetry, i.e., the relative difference between the number of top and antitop quarks produced in the "forward direction".

Various definitions of the asymmetry are possible. They differ by just the precise definition of "forward" and "backward", but they can be in general written as

$$A = \frac{\sigma_+ - \sigma_-}{\sigma_+ + \sigma_-} \ , \tag{4.1}$$

where the denominator is the total cross section and the numerator is the difference of the two complementary forward σ_+ and backward σ_- cross sections. The directions are typically determined via the rapidity of the top and antitop quark, y_t and $y_{\bar{t}}$, defined as

$$y_t = \frac{1}{2}\log\left(\frac{E_t + p_t^z}{E_t - p_t^z}\right) , \qquad y_{\bar{t}} = \frac{1}{2}\log\left(\frac{E_{\bar{t}} + p_{\bar{t}}^z}{E_{\bar{t}} - p_{\bar{t}}^z}\right) . \tag{4.2}$$

In eq. (4.2), E_t and $E_{\bar{t}}$ are respectively the energy of the top and the antitop quark and p_t^z and $p_{\bar{t}}^z$ are their three-momentum components parallel to the beam axis and oriented in the direction of the proton beam.

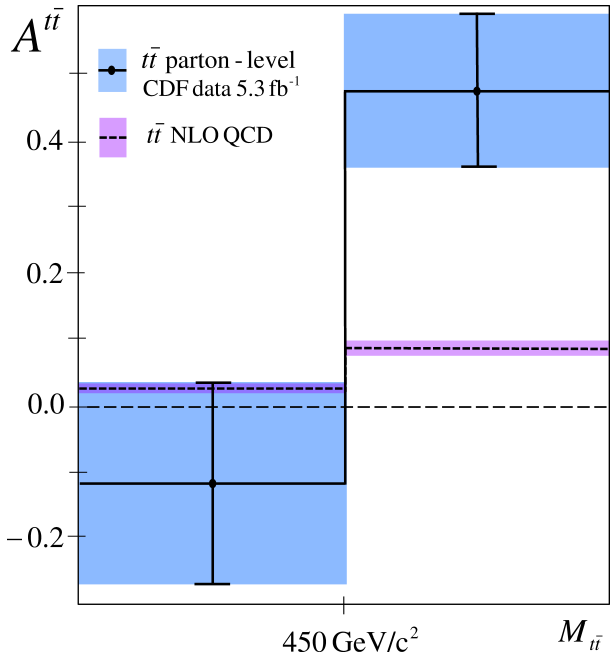

Figure 4.1: Comparison between predictions for $A_{FB}^{t\bar{t}}$ (see eq. (4.4)) at NLO QCD, in the two regions $M_{t\bar{t}} > 450$ GeV and $M_{t\bar{t}} < 450$ GeV, and the corresponding values measured by CDF with 5.3 fm^{-1} luminosity. Plot taken from [20].

Using the definitions $\sigma_+ = \sigma(\Delta y > 0)$ and $\sigma_- = \sigma(\Delta y < 0)$, where $\Delta y = y_t - y_{\bar{t}}$, CDF found a 3.5σ deviation in the high-invariant-mass region $M_{t\bar{t}} > 450$ GeV between the measured value and the corresponding theoretical prediction at NLO QCD accuracy [20]. This deviation has triggered an intense theoretical activity into two different directions.

On the one hand, the effects of SM radiative corrections beyond NLO QCD corrections have been investigated, on the other hand, new BSM models have been created and/or tested to explain this deviation. Both the DØ and CDF collaborations repeated the analyses increasing the data set and studying the dependence of the asymmetry on cuts or additional kinematic variables. The increment of the precision of the theoretical prediction and of the experimental measurements has decreased the size of the deviation to 2.5σ; still, this anomaly remains at the moment one of the most promising hints for possible BSM effects.

The LHC, colliding protons with protons, does not present a "forward" and "backward" direction and the measurement of the same quantity would be zero due to the symmetric initial state. Analogue central asymmetries, defined according to the general form of eq. (4.1), have been used at the LHC, but no deviation from SM predictions has been measured so far.

In section 4.1 the various measurements for the different definitions used at the Tevatron and the LHC are listed. In section 4.2 the charge asymmetry is discussed from

a theoretical point of view for the Tevatron case, where it corresponds to a forward-backward asymmetry. The calculation of the electroweak contribution is explained in details. The numerical results are presented in section 4.3 and compared to the measured values. The differences between the charge asymmetry at the Tevatron and the LHC are discussed in section 4.4. The general features of BSM models that might eliminate the deviation between SM predictions and experimental measurements are briefly described in section 4.5.

4.1 Measurements

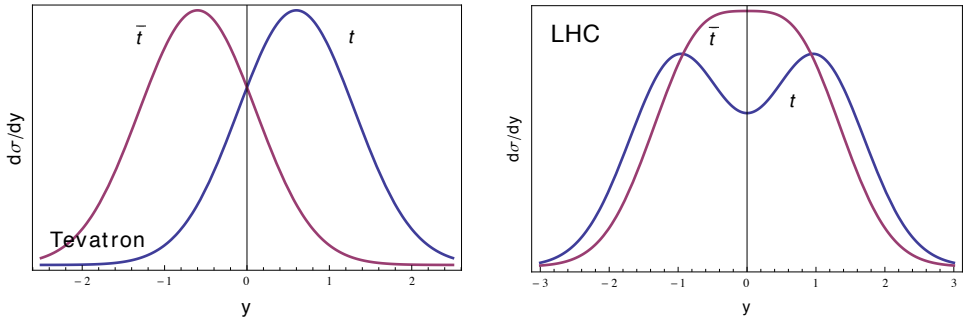

(a) (b)

Figure 4.2: Distribution in rapidity for top and antitop quarks at the Tevatron and the LHC. Plot taken from [104].

The qualitative behavior of the rapidity distributions of top and antitop quarks is shown in Figure 4.2(a) for the Tevatron and in Figure 4.2(b) for the LHC. At the Tevatron, top quarks are preferably produced in the "forward" direction and antitop quarks in the "backward" direction. At the LHC, the distributions are forward-backward symmetric, but the antitop quark distribution is more "central" than the top quark distribution. In order to measure these two different phenomenological behaviors, which have the same physical origin, different asymmetry definitions have been used at the Tevatron and the LHC. At the Tevatron the following charge asymmetry definitions, equivalent to a forward-backward asymmetry, have been used:

$$A_{FB}^{p\bar{p}} = \frac{\sigma(y_t > 0) - \sigma(y_t < 0)}{\sigma(y_t > 0) + \sigma(y_t < 0)} = \frac{\sigma(y_t > 0) - \sigma(y_{\bar{t}} > 0)}{\sigma(y_t > 0) + \sigma(y_{\bar{t}} > 0)} \tag{4.3}$$

and

$$A_{FB}^{t\bar{t}} = \frac{\sigma(\Delta y > 0) - \sigma(\Delta y < 0)}{\sigma(\Delta y > 0) + \sigma(\Delta y < 0)} \,. \tag{4.4}$$

As already said, Δy is the difference between the rapidity y_t and $y_{\bar{t}}$ of the top and antitop quarks, where the direction of the beam axis is defined by the proton beam.

Δy (not y_t) is invariant under a boost along the beam axis, thus it has the same value in the partonic and in the hadronic rest frame. Conversely, at the LHC a central charge asymmetry is used

$$A_C^{t\bar{t}} = \frac{\sigma(\Delta|y| > 0) - \sigma(\Delta|y| < 0)}{\sigma(\Delta|y| > 0) + \sigma(\Delta|y| < 0)} , \tag{4.5}$$

where $\Delta|y| = |y_t| - |y_{\bar{t}}|$.

In order to measure these quantities, the (anti)top momentum must be reconstructed. This can be avoided measuring similar asymmetries that do not involve the top quark momenta in their definitions, but the momenta of the leptons emerging in the decays:

$$A_{FB}^{l} = \frac{\sigma(q_l y_l > 0) - \sigma(q_l y_l < 0)}{\sigma(q_l y_l > 0) + \sigma(q_l y_l < 0)} , \tag{4.6}$$

$$A_{FB}^{ll} = \frac{\sigma(\Delta\eta > 0) - \sigma(\Delta\eta < 0)}{\sigma(\Delta\eta > 0) + \sigma(\Delta\eta < 0)} , \tag{4.7}$$

$$A_{C}^{ll} = \frac{\sigma(\Delta|\eta| > 0) - \sigma(\Delta|\eta| < 0)}{\sigma(\Delta|\eta| > 0) + \sigma(\Delta|\eta| < 0)} . \tag{4.8}$$

A_{FB}^{l} is used at the Tevatron with the semi-leptonic signature. y_l is the rapidity of the lepton, defined in analogy with eq. (4.2) for the case of the lepton, and q_l is its charge. A_{FB}^{ll} and A_C^{ll} are respectively used at the Tevatron and the LHC with the dileptonic signature and depend on $\Delta\eta = \eta_{l^+} - \eta_{l^-}$ and $\Delta|\eta| = |\eta_{l^+}| - |\eta_{l^-}|$. The variables η_{l^+} and η_{l^-} are the pseudorapidity of the positive and negative lepton, defined as

$$\eta_{l^+} = \frac{1}{2}\log\left(\frac{|\vec{p}_{l^+}| + p_{l^+}^z}{|\vec{p}_{l^+}| - p_{l^+}^z}\right) , \qquad \eta_{l^-} = \frac{1}{2}\log\left(\frac{|\vec{p}_{l^-}| + p_{l^-}^z}{|\vec{p}_{l^-}| - p_{l^-}^z}\right) . \tag{4.9}$$

In eq. (4.9), $\vec{p}_{l^+}$ and $\vec{p}_{l^-}$ are respectively the three-momenta of l^+ and l^-; $p_{l^+}^z$ and $p_{l^-}^z$ are their components parallel to the beam axis and oriented in the direction of the proton beam.

Practically, in the experiments, the number of events from the phase-space regions defined by σ_+ and σ_- are simply counted. However, asymmetries are dimensionless quantities; if experimental cuts are consistently taken into account, the definitions listed before are equal to definitions in which cross sections are replaced by the number of events. We list in Table 4.1 and Table 4.2. the values measured at the Tevatron and the LHC for the asymmetries defined above. The values are taken from [31, 105]; a list of the previous measurements and their deviations from theoretical predictions can be found in [106]. The measurements of $A_{FB}^{p\bar{p}}$ was performed by CDF only in the 5.3 fm^{-1} analysis, in the new analyses this quantity has not been measured anymore. However, some theoretical arguments can be easily explained using this particular definition and thus we include it.

asymmetry	value (%)	signature	$\mathcal{L}$ (fb^{-1})	experiment
$A_{FB}^{p\bar{p}}$	15.5 ± 5.5	lepton+jets	5.3	CDF
$A_{FB}^{t\bar{t}}$	16.4 ± 4.5	lepton+jets	9.4	CDF
$A_{FB}^{t\bar{t}}$	19.6 ± 6.5	lepton+jets	5.4	DØ
$A_{FB}^{t\bar{t}}$	42 ± 16	dilepton	8.7	CDF
$A_{FB}^{t\bar{t}}(\lvert\Delta y\rvert < 1)$	10.1 ± 4.7	lepton+jets	9.4	CDF
$A_{FB}^{t\bar{t}}(\lvert\Delta y\rvert > 1)$	39.2 ± 10.2	lepton+jets	9.4	CDF
$A_{FB}^{t\bar{t}}(M_{t\bar{t}} < 450$ GeV)	8.4 ± 5.3	lepton+jets	9.4	CDF
$A_{FB}^{t\bar{t}}(M_{t\bar{t}} > 450$ GeV)	29.5 ± 6.6	lepton+jets	9.4	CDF
A_{FB}^{l}	6.6 ± 2.5	lepton+jets	8.7	CDF
A_{FB}^{l}	5.8 ± 5.3	dilepton	5.4	DØ
A_{FB}^{ll}	5.3 ± 8.4	dilepton	5.4	DØ

Table 4.1: Forward-backward asymmetries and lepton asymmetries measurements at the Tevatron.

asymmetry	value (%)	signature	$\mathcal{L}$ (fb^{-1})	experiment
A_C	-1.9 ± 3.7	lepton+jets	1.04	ATLAS
A_C	0.4 ± 1.5	lepton+jets	5.0	CMS
A_C	5.7 ± 2.8	dilepton	4.7	ATLAS
A_C	2.9 ± 2.8	combined	5.0 & 1.04	ATLAS
A_C^{ll}	2.3 ± 1.4	dilepton	4.7	ATLAS

Table 4.2: Charge asymmetries measurements at the LHC 7 TeV.

4.2 Calculation of $\mathbf{A_{FB}}$

At leading order, as we said in section 3.3.2, the production of $t\bar{t}$ pairs in $p\bar{p}$ collisions originates from the partonic processes $q\bar{q} \to t\bar{t}$ and $gg \to t\bar{t}$ via the strong interaction. The denominator in the r.h.s. of eq. (4.1), i.e., the integrated cross section, receives a contribution from LO, at $\mathcal{O}(\alpha_s^2)$, whereas the numerator is equal to zero at this order. The asymmetric cross section, the numerator of A, starts to contribute at $\mathcal{O}(\alpha_s^3)$. The arguments explained in this section apply to the charge asymmetry definitions used at the Tevatron, i.e. the forward-backward asymmetries defined in eq. (4.3) and eq. (4.4). In general they can be extended also to the charge asymmetry used at the LHC, eq. (4.5), the few differences are explained in section 4.4.

The numerator of A_{FB} starts at $\mathcal{O}(\alpha_s^3)$, however it gets contributions only from partonic subprocesses $q\bar{q} \to t\bar{t}(g)$, $qg \to t\bar{t}q$ and $\bar{q}g \to t\bar{t}\bar{q}$ with $q = u, d$. Indeed, in

order to give a contribution to the top quark forward-backward asymmetry, a partonic subprocess must satisfy two conditions [107]:

- The partonic subprocess $p_1 p_2 \to t\bar{t}(+X)$ is asymmetric in its reference frame.
- The parton luminosity of the initial state $p_1 p_2$, from the two hadrons h_1 and h_2, does not cancel the asymmetric contribution at the parton level.

The first condition depends on results obtained via a perturbative calculation for the hard process. The second condition depends on how the non-perturbative structure of the proton is described, i.e. the assumptions used for the determination of the PDFs.

The $gg \to t\bar{t}(g)$ process cannot satisfy the first condition. With two gluons in the initial state no "forward" or "backward" direction is defined in the partonic rest frame. The $q\bar{q} \to t\bar{t}(g)$ process, with two different particles in the initial state, exhibits a direction and can be asymmetric. However, not all the $q\bar{q}$ initial states satisfy the second condition.

We show now what the second condition implies. The partonic subprocesses $p_1 p_2 \to t\bar{t}(+X)$ can be generated with $p_1(p_2)$ coming from the first(second) hadron $h_1(h_2)$ or from $h_2(h_1)$. Considering the case of $A_{FB}^{p\bar{p}}$, if a partonic $p_1 p_2 \to t\bar{t}(+X)$ event in a given kinematic configuration contributes to $\sigma(y_t > 0)$ in the $h_1(h_2)$ case, it contributes with the same partonic weight also to $\sigma(y_t < 0)$ in the $h_2(h_1)$ case. Thus, the total contribution to $A_{FB}^{p\bar{p}}$ is non-vanishing only if the weight coming from the parton distributions in the two cases is different, i.e., if

$$f_{p_1,h_1}(x_1) f_{p_2,h_2}(x_2) \neq f_{p_1,h_2}(x_1) f_{p_2,h_1}(x_2)\,, \tag{4.10}$$

where $f_{p_i,h_j}(x_i)$ is the parton distribution of the parton p_i in the hadron h_j. The same discussion applies also to different definitions of the forward-backward asymmetry like, e.g., $A_{FB}^{t\bar{t}}$, but cannot be extended to the charge asymmetry definitions used at the LHC.

Equation (4.10) tells us that at the Tevatron, where $h_1 = p$ and $h_2 = \bar{p}$, only initial states with at least one of the two partons p_1 and p_2 equal to (anti)quark up or (anti)quark down can produce an asymmetric contribution. Indeed, only valence quarks have different PDFs in protons and antiprotons. Again, we want to stress that this last statement is completely independent of the assumptions made for the partonic calculation, it relies only on the way the proton structure is described by PDFs. For instance, a very small but non-vanishing contribution from the $s\bar{s}$ initial state can be generated with PDF sets, as e.g. MSTW08 [108] and NNPDF [109], in which $f_s \neq f_{\bar{s}}$. Looking at eq. (4.10), it is also clear that at the LHC, where $h_1 = h_2$, the second condition, as expected, is never satisfied.

Before describing the structure of the $\mathcal{O}(\alpha_s^3)$ contribution to the asymmetric part of A_{FB}, we analyze the perturbative expansion of A_{FB} in order to identify which are the

leading terms. If we start considering only QCD interactions, writing the numerator and the denominator of A_{FB} in powers of α_s, we obtain

$$\begin{aligned} A_{FB} = \frac{N}{D} &= \frac{\alpha_s^3 N_1 + \alpha_s^4 N_2 + \cdots}{\alpha_s^2 D_0 + \alpha_s^3 D_1 + \cdots} = \\ &= \frac{\alpha_s}{D_0}(N_1 + \alpha_s(N_2 - N_1 D_1/D_0)) + \cdots . \end{aligned} \tag{4.11}$$

The terms up to one-loop (D_0, D_1, N_1) have been respectively calculated in [110–115], [87, 116–118] and [30], whereas only some parts of N_2 are currently known [119–121]. The inclusion of the term $N_1 D_1/D_0$ without the term N_2 is questionable, indeed it would decrease by $\sim 30\%$ the predicted value, when N_2 could in principle be of the same order or even bigger than $N_1 D_1/D_0$. Moreover, according to [119], an approximate calculation suggests that the inclusion of both terms should not sensitively change our result. We chose to use only the lowest order cross section in the denominator and the $\mathcal{O}(\alpha_s^3)$ term in the numerator for the numerical evaluation presented in section 4.3. Besides the strong interaction, the electroweak interaction gives rise to further contributions to the $t\bar{t}$ forward-backward asymmetry, through photon and Z exchange at the tree level as well as through interference between QCD and electroweak amplitudes at one-loop order (including real radiation corrections) in both interactions. Although smaller in size, they are not negligible, and a careful investigation is an essential ingredient for an improved theoretical prediction.

Taking into account electroweak interactions and expanding N and D in powers of α_s and α, A_{FB} yields the following expression,

$$\begin{aligned} A_{FB} = \frac{N}{D} &= \frac{\alpha^2 \tilde{N}_0 + \alpha_s^3 N_1 + \alpha_s^2 \alpha \tilde{N}_1 + \alpha_s^4 N_2 + \cdots}{\alpha^2 \tilde{D}_0 + \alpha_s^2 D_0 + \alpha_s^3 D_1 + \alpha_s^2 \alpha \tilde{D}_1 + \cdots} = \\ &= \alpha_s \frac{N_1}{D_0} + \alpha \frac{\tilde{N}_1}{D_0} + \frac{\alpha^2}{\alpha_s^2} \frac{\tilde{N}_0}{D_0} + \cdots . \end{aligned} \tag{4.12}$$

In the second line of eq. (4.12) the three leading terms, excluding the incomplete $\mathcal{O}(\alpha_s^2)$ of A_{FB}, are explicitly shown. In the following we discuss the evaluation of these three terms as presented in [29]. The term D_0 is simply the total LO cross section divided by α_s^2. The first term involving N_1 was calculated in [30], conversely the second and the third terms, of electroweak origin, had been treated only marginally before [29]. Whereas the third term $\sim \tilde{N}_0$ had not been considered at all, the contribution from the second term $\sim \tilde{N}_1$ had been obtained in [30], in an approximate way, by a rescaling of the leading QCD contribution with coupling constants and group factors.

The relevant tree-level diagrams for the partonic subprocesses $q\bar{q} \to t\bar{t}$ and $gg \to t\bar{t}$ have already been shown in Figure 3.7. The squared terms $|\mathcal{M}_{q\bar{q}\to g\to t\bar{t}}|^2$ and $|\mathcal{M}_{gg\to t\bar{t}}|^2$ yield the term D_0 from the LO cross section; the $\mathcal{O}(\alpha^2)$ terms arise from $|\mathcal{M}_{q\bar{q}\to\gamma\to t\bar{t}} +$

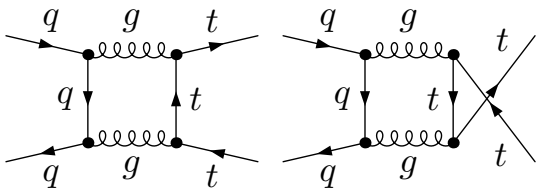

Figure 4.3: QCD box diagrams.

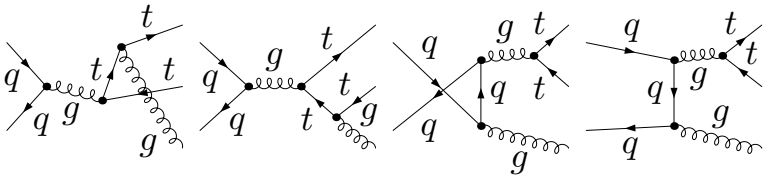

Figure 4.4: Real emission of gluons at $\mathcal{O}(\alpha_s^3)$.

$\mathcal{M}_{q\bar{q}\to Z\to t\bar{t}}|^2$, which generate a purely electroweak asymmetric differential cross section, in the partonic center-of-mass system given by

$$\frac{d\sigma_{\text{asym}}}{d\cos\theta} = 2\pi\alpha^2\cos\theta\left(1-\frac{4m_t^2}{s}\right)\left[\kappa\frac{Q_qQ_tA_qA_t}{(s-M_Z^2)}+2\kappa^2A_qA_tV_qV_t\frac{s}{(s-M_Z^2)^2}\right], \quad (4.13)$$

$$\kappa = \frac{1}{4\sin^2(\theta_W)\cos^2(\theta_W)}, \qquad V_q = T_q^3 - 2Q_q\sin^2(\theta_W), \qquad A_q = T_q^3,$$

where s is the squared center-of-mass energy in the parton reference frame, θ is the top quark scattering angle, also in the partonic center-of-mass system. Q_q and Q_t are the charges of the parton q and of the top quark and A_q, A_t and V_q, V_t are their axial and vectorial couplings to the Z boson. In A_{FB} this leads to the term $\tilde{N}_0$ of eq. (4.12). The complementary symmetric cross section provides the $\tilde{D}_0$ term in the denominator, which does not contribute in the order under consideration. As mentioned before, the interference of $q\bar{q}\to\gamma, Z\to t\bar{t}$ and $q\bar{q}\to g\to t\bar{t}$ is zero because of the color structure, so $\mathcal{O}(\alpha_s\alpha)$ terms appear neither in the numerator nor in the denominator.

The $\mathcal{O}(\alpha_s^3)$ terms that contribute to N arise from four classes of partonic processes: $q\bar{q}\to t\bar{t}$, $q\bar{q}\to t\bar{t}g$, $qg\to t\bar{t}q$ and $\bar{q}g\to t\bar{t}\bar{q}$. In the first case the origin is the interference of QCD one-loop and Born amplitudes; the other processes correspond to real particle emissions. All one-loop vertex corrections and self-energies do not generate any asymmetric term, hence, among the virtual corrections, only the box diagrams (Figure 4.3) are relevant. These box integrals are free of ultraviolet and collinear divergences, but they involve infrared (IR) singularities which are cancelled after adding the integrated real gluon emission contribution $q\bar{q}\to t\bar{t}g$, shown in Figure 4.4. For the corresponding relevant gluon-radiation part only the interference of initial- and final-state gluon radiation, yielding another asymmetric cross section, has to be taken into account. The processes of real quark radiation $qg\to t\bar{t}q$ and $\bar{q}g\to t\bar{t}\bar{q}$ yield contributions to A_{FB},

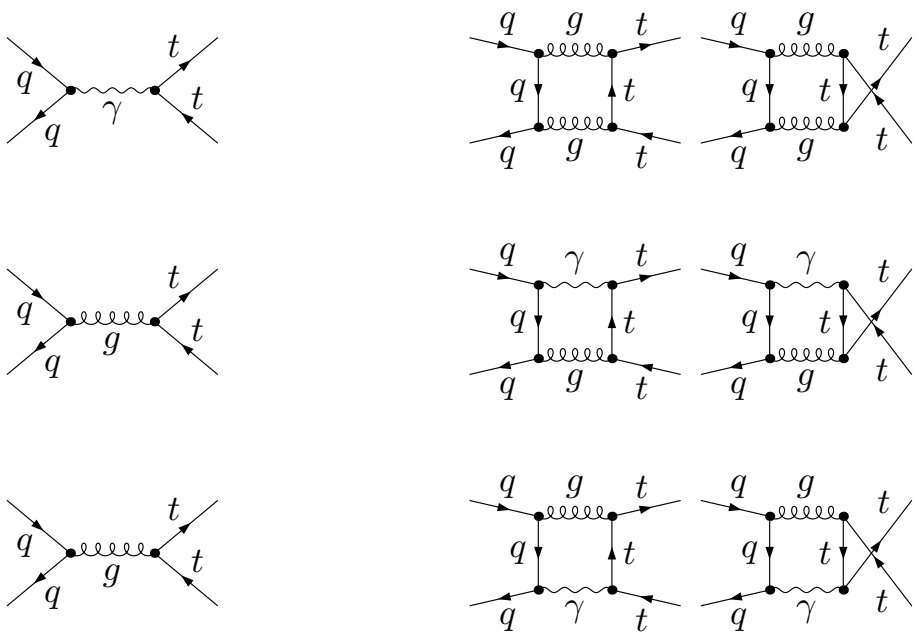

Figure 4.5: Different ways of QED–QCD interference at $\mathcal{O}(\alpha_s^2\alpha)$.

which are numerically negligible for A_{FB} at the Tevatron [30].

In order to analyze the electroweak $\mathcal{O}(\alpha_s^2\alpha)$ terms, it is useful to separate the QED contributions involving photons from the weak contributions with Z bosons. In the QED sector we obtain the $\mathcal{O}(\alpha_s^2\alpha)$ contributions to N from three classes of partonic processes: $q\bar{q} \to t\bar{t}$, $q\bar{q} \to t\bar{t}g$ and $q\bar{q} \to t\bar{t}\gamma$. The first case is the virtual-photon contribution, which can be obtained from the QCD analogue, namely the $\mathcal{O}(\alpha_s^3)$ interference of box and tree-level amplitudes, by substituting successively each one of the three internal gluons by a photon, as displayed in Figure 4.5.

The essential differences between the calculation of the $\mathcal{O}(\alpha_s^3)$ and of QED $\mathcal{O}(\alpha_s^2\alpha)$ terms are the coupling constants and the appearance of the $SU(3)_C$ generators in the strong vertices. Summing over color in the final state and averaging in the initial state we find for the virtual contributions to the asymmetric cross section the following ratio,

$$\begin{aligned}\frac{\overline{|\mathcal{M}^{t\bar{t}}|}^2_{\mathcal{O}(\alpha_s^2\alpha),\text{asym}}}{\overline{|\mathcal{M}^{t\bar{t}}|}^2_{\mathcal{O}(\alpha_s^3),\text{asym}}} &= \frac{\overline{2Re\big(\mathcal{M}^{t\bar{t}}_{\mathcal{O}(\alpha)}\mathcal{M}^{t\bar{t}\,*}_{\mathcal{O}(\alpha_s^2)}\big)}_{\text{asym}} + 2Re\overline{\big(\mathcal{M}^{t\bar{t}}_{\mathcal{O}(\alpha_s)}\mathcal{M}^{t\bar{t}\,*}_{\mathcal{O}(\alpha_s\alpha)}\big)}_{\text{asym}}}{\overline{2Re\big(\mathcal{M}^{t\bar{t}}_{\mathcal{O}(\alpha_s)}\mathcal{M}^{t\bar{t}\,*}_{\mathcal{O}(\alpha_s^2)}\big)}_{\text{asym}}} = \\ &= \frac{F^{t\bar{t}}_{QED}(\alpha_s,\alpha,Q_t,Q_q)}{F^{t\bar{t}}_{QCD}(\alpha_s)}\,, \end{aligned} \tag{4.14}$$

that can be expressed in terms of two factors $F^{t\bar{t}}_{QED}$ and $F^{t\bar{t}}_{QCD}$, depending only on

coupling constants and color traces,

$$\begin{aligned} F_{QCD}^{t\bar{t}} &= \frac{g_s^6}{9}\delta_{AD}\delta_{BF}\delta_{EC}Tr(t^At^Bt^C)\Big[\frac{1}{2}Tr\big(t^Dt^Et^F\big)+\frac{1}{2}Tr\big(t^Dt^Ft^E\big)\Big] = \\ &= \frac{g_s^6}{16\cdot 9}d^2\,, \qquad (4.15a) \\ F_{QED}^{t\bar{t}} &= n_{t\bar{t}}\Big[\frac{g_s^4e^2Q_qQ_t}{9}\delta_{AC}\delta_{BD}Tr(t^At^B)Tr(t^Ct^D)\Big] = \\ &= \frac{6g_s^4e^2}{9}Q_tQ_q\,. \qquad (4.15b) \end{aligned}$$

$F_{QCD}^{t\bar{t}}$ contains two different color structures and the result depends on $d^2 = d^{ABC}d_{ABC} = \frac{40}{3}$, which arises from $Tr(t^At^Bt^C) = \frac{1}{4}(if^{ABC}+d^{ABC})$. $F_{QED}^{t\bar{t}}$ instead depends on the charges of the incoming quarks (Q_q) and of the top quark (Q_t), together with $n_{t\bar{t}} = 3$ corresponding to the three photon insertions illustrated in Figure 4.5.

In a similar way, also the real radiation processes $q\bar{q}\to t\bar{t}g$ and $q\bar{q}\to t\bar{t}\gamma$ (Figures 4.6 and 4.7) can be evaluated starting from the result obtained for $q\bar{q}\to t\bar{t}g$ in the QCD case and substituting successively each gluon by a photon, yielding the ratios

$$\frac{\overline{|\mathcal{M}^{t\bar{t}g}|}^2_{\mathcal{O}(\alpha_s^2\alpha),\text{asym}}}{\overline{|\mathcal{M}^{t\bar{t}g}|}^2_{\mathcal{O}(\alpha_s^3),\text{asym}}} = \frac{\overline{2Re\big(\mathcal{M}^{t\bar{t}g}_{\mathcal{O}(\alpha\sqrt{\alpha_s})}\mathcal{M}^{t\bar{t}g\;*}_{\mathcal{O}(\alpha_s\sqrt{\alpha_s})}\big)}_{\text{asym}}}{\overline{\big|\mathcal{M}^{t\bar{t}g}_{\mathcal{O}(\alpha_s\sqrt{\alpha_s})}\big|^2}_{\text{asym}}} = \frac{F_{QED}^{t\bar{t}g}(\alpha_s,\alpha,Q_t,Q_q)}{F_{QCD}^{t\bar{t}g}(\alpha_s)}\,, \qquad (4.16)$$

$$\frac{\overline{|\mathcal{M}^{t\bar{t}\gamma}|}^2_{\mathcal{O}(\alpha_s^2\alpha),\text{asym}}}{\overline{|\mathcal{M}^{t\bar{t}g}|}^2_{\mathcal{O}(\alpha_s^3),\text{asym}}} = \frac{\overline{\big|\mathcal{M}^{t\bar{t}\gamma}_{\mathcal{O}(\alpha_s\sqrt{\alpha})}\big|}^2_{\text{asym}}}{\overline{\big|\mathcal{M}^{t\bar{t}g}_{\mathcal{O}(\alpha_s\sqrt{\alpha_s})}\big|^2}_{\text{asym}}} = \frac{F_{QED}^{t\bar{t}\gamma}(\alpha_s,\alpha,Q_t,Q_q)}{F_{QCD}^{t\bar{t}g}(\alpha_s)}\,. \qquad (4.17)$$

$F_{QCD}^{t\bar{t}g}$, $F_{QED}^{t\bar{t}g}$ and $F_{QED}^{t\bar{t}\gamma}$ are related to $F_{QCD}^{t\bar{t}}$, $F_{QED}^{t\bar{t}}$ in the following way,

$$\begin{aligned} F_{QCD}^{t\bar{t}g} &= F_{QCD}^{t\bar{t}}, & F_{QED}^{t\bar{t}g} &= \frac{2}{3}F_{QED}^{t\bar{t}}\,, \qquad (4.18) \\ F_{QED}^{t\bar{t}\gamma} &= \frac{1}{3}F_{QED}^{t\bar{t}}, & F_{QED}^{t\bar{t}} &= F_{QED}^{t\bar{t}g}+F_{QED}^{t\bar{t}\gamma}\,. \end{aligned}$$

This guarantees the cancellation of the IR singularities stemming from the virtual contributions.

The $\mathcal{O}(\alpha_s^2\alpha)$ asymmetric term from $q\bar{q}\to t\bar{t}g$ comes from the interference of $q\bar{q}\to g\to t\bar{t}g$ (Figure 4.4) and $q\bar{q}\to\gamma\to t\bar{t}g$ (Figure 4.6). It can be obtained from the corresponding QCD result with the replacement of one gluon by a photon and inserting the right couplings, as done in the case of $q\bar{q}\to t\bar{t}$. The only difference is the number of gluons to be replaced: in the $q\bar{q}\to t\bar{t}g$ case they are only two instead of three as for the virtual photon contributions.

The $\mathcal{O}(\alpha_s^2\alpha)$ asymmetric term from $q\bar{q}\to t\bar{t}\gamma$ comes from the $q\bar{q}\to g\to t\bar{t}\gamma$ diagrams in Figure 4.7, and again it can be obtained from the corresponding QCD

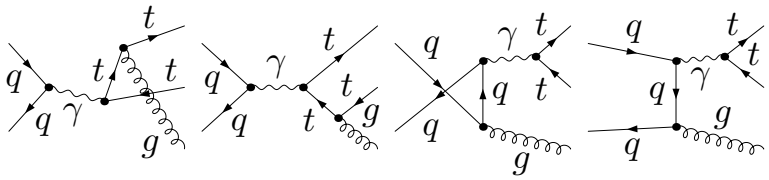

Figure 4.6: Real gluon emission from photon-exchange diagrams.

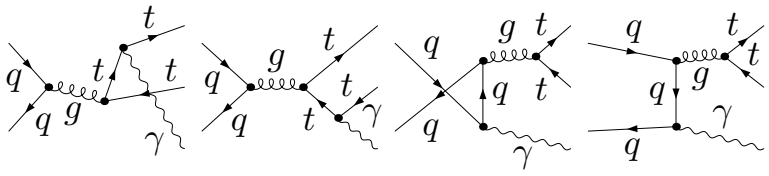

Figure 4.7: Real photon emission from gluon-exchange diagrams.

result for the gluon-radiation process $q\bar{q} \to t\bar{t}g$. Here we have a one-to-one relation between the QED and QCD diagrams.

Finally, we can relate the QED contribution to the asymmetric term $\tilde{N}_1$ in eq. (4.12) to the $\mathcal{O}(\alpha_s^3)$ QCD term N_1 for a given quark species $q\bar{q} \to t\bar{t} + X$ in the following way,

$$R_{QED}(Q_q) = \frac{\alpha \tilde{N}_1^{QED}}{\alpha_s N_1} = \frac{F_{QED}^{t\bar{t}}}{F_{QCD}^{t\bar{t}}} = Q_q Q_t \frac{36}{5} \frac{\alpha}{\alpha_s}\,. \tag{4.19}$$

Now we consider the weak contribution to $\tilde{N}_1$. It can be depicted by the same diagrams as for $q\bar{q} \to t\bar{t}g$ and $q\bar{q} \to t\bar{t}$ in the QED case, but with the photon now substituted by a Z boson (Figure 4.8 and Figure 4.9), involving massive box diagrams.

The result cannot be expressed immediately in a simple factorized way. We performed the explicit calculation including also the contribution from real gluon radiation with numerical integration over the hard gluon part.

Basically also Z boson radiation, $q\bar{q} \to t\bar{t}Z$, can contribute at the same order. As our calculation has shown, it yields only a tiny effect of 10^{-5} in A_{FB} and thus may be safely neglected. The same applies to $u\bar{d} \to t\bar{t}W^+$ as well as to Higgs boson radiation. For these processes with an additional heavy particle in the final state, the phase-space volume is reduced, thus the contribution is much smaller.

Weak one-loop contributions to the $q\bar{q}g$ and $t\bar{t}g$ vertices induce also axial vector form

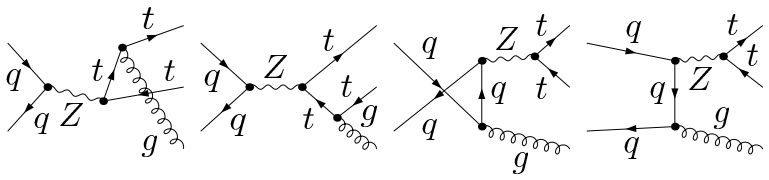

Figure 4.8: Real gluon emission from Z-exchange diagrams.

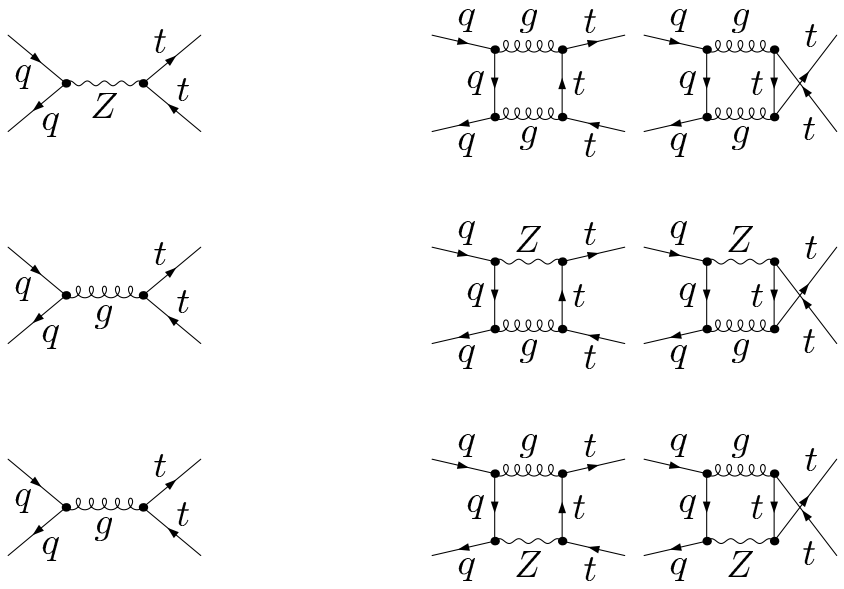

Figure 4.9: Different ways of weak–QCD interference at $\mathcal{O}(\alpha_s^2\alpha)$.

factors, which, however, yield vanishing interference terms with the Born amplitude for the asymmetric cross section at $\mathcal{O}(\alpha_s^2\alpha)$ and are thus irrelevant. Indeed, the two vertices can be written as

$$i\Lambda_\mu^a = -ig_s t^a \frac{\alpha}{4\pi}\left[\gamma_\mu F_V + \gamma_\mu\gamma_5 G_A + \frac{(p-p')_\mu}{2m_q} F_M + (p+p')_\mu\gamma_5 G_E\right], \tag{4.20}$$

where p and p' are the momenta of q and $\bar{q}$ (t and $\bar{t}$). In the interference with tree-level diagrams, the contributions from terms proportional to G_E and G_A vanish since the trace of one γ_5 and four(three) γ matrixes is imaginary(zero). The $\gamma^\mu F_V$ term does not contribute to A_{FB}, otherwise also $\mathcal{O}(\alpha_s^2)$ cross section would be asymmetric. In the calculation presented in [92] it can be seen that also the term proportional to F_M vanishes in the A_{FB} calculation.

4.3 Numerical results

The following numerical analysis is based on the analytical evaluation of the required symmetric and asymmetric parts of the partonic cross sections and semi-numerical phase-space integration for the radiation processes applying phase-space slicing[1], with support of *FeynArts* [122] and *FormCalc* [123].

[1]More details on the phase-space slicing approach can be found in section 6.4.2. The calculation discussed there involves also the other possible divergences arising in the calculation of NLO corrections for the production of heavy particle, i.e., the initial-state collinear divergences. Moreover, also renormalization of UV divergences is necessary. Thus, the calculation performed here is technically

In order to obtain results at the hadronic level, we convolute the partonic contributions, discussed in detail in the previous section, with the corresponding parton luminosities. For any subprocess $ij \to t\bar{t}(+X)$, we express the contribution $d\sigma_{ij\to t\bar{t}(+X)}$ to the hadronic production cross section as

$$d\sigma_{ij\to t\bar{t}(+X)} \;=\; \int_{\tau_0}^{1} d\tau\, \mathcal{L}_{ij}(\tau)\, d\hat{\sigma}_{ij\to t\bar{t}(+X)}(\tau)\,. \tag{4.21}$$

In eq. (4.21), $d\hat{\sigma}_{ij\to t\bar{t}(+X)}$ is the partonic cross section and the term $\mathcal{L}_{ij}(\tau)$ is the parton luminosity defined as

$$\mathcal{L}_{ij}(\tau) = \frac{1}{1+\delta_{ij}} \int_{\tau}^{1} \frac{dx}{x} \left[f_{i,p}(x,\mu_F)\, f_{j,\bar{p}}\Big(\frac{\tau}{x},\mu_F\Big) \;+\; f_{j,p}(x,\mu_F)\, f_{i,\bar{p}}\Big(\frac{\tau}{x},\mu_F\Big)\right], \tag{4.22}$$

where $f_{i,p}(x,\mu_F)$ and $f_{i,\bar{p}}(x,\mu_F)$ are respectively the PDFs of the parton i inside the proton and the antiproton at the scale μ_F and with momentum fraction x. τ denotes the ratio between the squared center-of-mass energies of the partonic and hadronic processes, $\tau = s/S$, and the kinematical production threshold corresponds to $\tau_0 = (2m_t)^2/S$.

For the $\mathcal{O}(\alpha_s^3)$ and $\mathcal{O}(\alpha_s^2\alpha)$ contributions to the numerator of A_{FB}, the soft part of the gluon and photon real radiation ($E_g, E_\gamma < \Delta E$) is calculated analytically, the hard part ($E_g, E_\gamma > \Delta E$) numerically. The soft emission of a gluon in the asymmetric contribution originating from $\mathcal{O}(\alpha_s)$ corrections, $\alpha_s^3 N_1$, is evaluated by multiplying the LO contribution with a soft-gluon factor C_{QCD}^{soft} dependent on the kinematics of the top and antitop quark,

$$\begin{aligned} C_{QCD}^{\text{soft}} \;=\; & -\frac{5}{6}\frac{\alpha_s}{\pi}\Bigg[2\log\left(\frac{2\Delta E}{\lambda}\right)\log\left(\frac{m_t^2-u}{m_t^2-u}\right) \\ & + \mathrm{Li}_2\left(1-\frac{s(1+\beta)}{2(m_t^2-t)}\right) + \mathrm{Li}_2\left(1-\frac{s(1-\beta)}{2(m_t^2-t)}\right) \\ & - \mathrm{Li}_2\left(1-\frac{s(1+\beta)}{2(m_t^2-u)}\right) - \mathrm{Li}_2\left(1-\frac{s(1-\beta)}{2(m_t^2-u)}\right)\Bigg]. \end{aligned} \tag{4.23}$$

In eq. (4.23) $\beta = \sqrt{1-4m_t^2/s}$ and s, t and u are the usual Mandelstam variables for the partonic subprocesses. Infrared divergences are regulated by a finite gluon mass λ. Equation (4.23) has been obtained using the soft photon factor formulae listed in [124] and introducing the correct color factor and couplings. Combining this contribution with the loop corrections, the dependence on λ is analytically canceled. The remaining dependence on the phase-space slicing parameter ΔE is canceled combining also the contribution from real radiation of gluons $E_g > \Delta E$. In Figure 4.10 a numerical test of the independence on ΔE for the $\mathcal{O}(\alpha_s^3)$ hadronic contribution of $u\bar{u}$ to N of $A_{FB}^{t\bar{t}}$ is shown as illustration.

easier: only soft divergences need to be regularized and only soft and hard region have to be divided with the phase-space slicing.

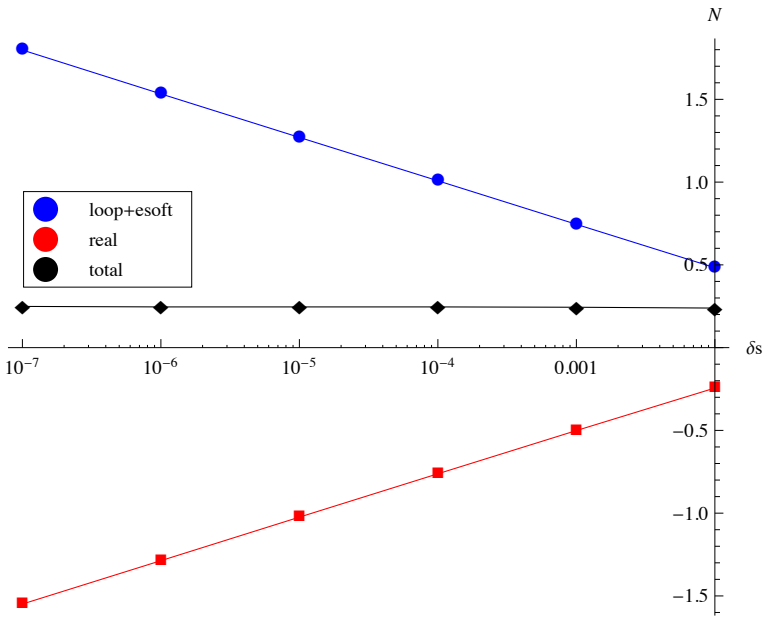

Figure 4.10: $\mathcal{O}(\alpha_s^3)$ contribution of $u\bar{u}$ to N of $A_{FB}^{t\bar{t}}$, $\mu = 2m_t$. In the simulations we used the soft phase-space slicing parameter $\Delta E = \delta_s \hat{s}$, in the plot the results under the variation of δ_s are shown.

The antisymmetric contribution originating from $\mathcal{O}(\alpha_s^2\alpha)_{QED}$ corrections, $\alpha_s^2\alpha\tilde{N}_1^{QED}$, is calculated multiplying the $\mathcal{O}(\alpha_s^3)$ result, $\alpha_s^3 N_1$, by the $R_{QED}(Q_q)$ factor defined in eq. (4.19). In addition, we checked the results repeating the calculation with the phase-space slicing approach, starting from the $t\bar{t}$, $t\bar{t}g$ and $t\bar{t}\gamma$ diagrams. The soft emission of a photon or a gluon contributing to the asymmetric $\mathcal{O}(\alpha_s^2\alpha)_{QED}$ can again be expressed as the LO contribution multiplied by a soft factor C_{QED}^{soft} depending on the kinematics of the top and antitop quark. According to eq. (4.18), $C_{QED}^{\text{soft}} = R_{QED}(Q_q)C_{QCD}^{\text{soft}}$. We found perfect compatibility between the two approaches.

The calculation of the $\mathcal{O}(\alpha_s^2\alpha)_{\text{weak}}$ contribution to the numerator of the asymmetry is also performed with the phase-space slicing method. In this case we have four contributions:

- interference of $q\bar{q} \to Z \to t\bar{t}$ with gluon–gluon boxes V_{gg} (first line of Figure 4.9),
- interference of $q\bar{q} \to g \to t\bar{t}$ with gluon–Z boxes V_{gZ} (second and third line of Figure 4.9),
- real emission of a hard gluon H_g (interference of the diagrams in Figure 4.4 and Figure 4.8),
- soft emission of a gluon S_g (interference of the diagrams in Figure 4.4 and Figure 4.8).

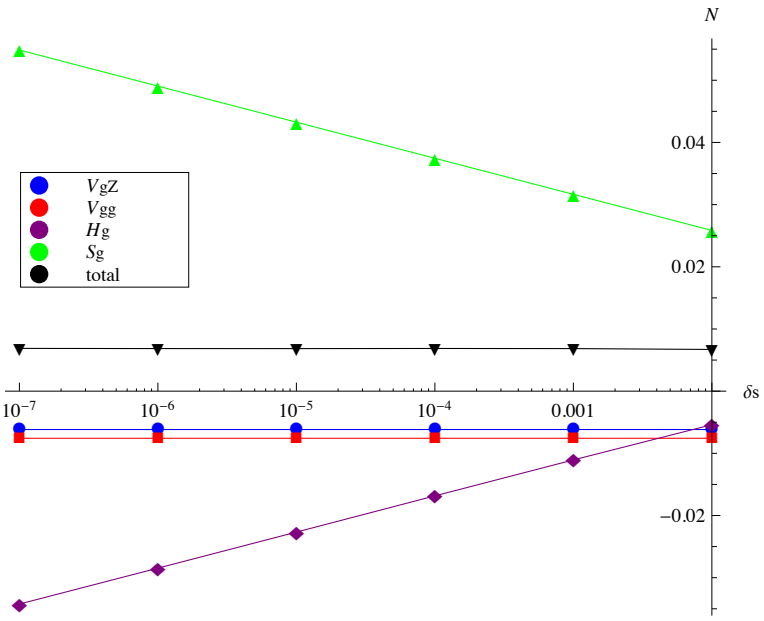

Figure 4.11: $\mathcal{O}(\alpha_s^2\alpha)_{\text{weak}}$ contributions of $u\bar{u}$ to N of $A_{FB}^{t\bar{t}}$, $\mu = 2m_t$. In the simulations we used the soft phase-space slicing parameter $\Delta E = \delta_s \hat{s}$, in the plot results under the variation of δ_s are shown.

We expect to express the soft-gluon radiation as a soft-gluon factor multiplying the cross section originating from the same diagrams without gluon emission, as for $\mathcal{O}(\alpha_s^3)$ and $\mathcal{O}(\alpha_s^2\alpha_s)$. However, due to the color structure, $2Re(\mathcal{M}^*_{q\bar{q}\to Z\to t\bar{t}}\mathcal{M}_{q\bar{q}\to g\to t\bar{t}})$ is zero. In order to use the *FormCalc* environment, we express S_g via a similar process that presents the same kinematic structure for the matrix elements, but different couplings and color factors. If we consider $q\bar{q} \to t\bar{t}\gamma$, the $\mathcal{O}(\alpha^3)$ interference of initial- and final-state radiation of a photon from respectively a Z- and photon- mediated diagram has exactly the same kinematic structure of the process we want to calculate. Moreover, it can be expressed in the soft limit (S_γ) with $2Re(\mathcal{M}^*_{q\bar{q}\to Z\to t\bar{t}}\mathcal{M}_{q\bar{q}\to\gamma\to t\bar{t}})$ and a soft photon factor that again can be calculated using formulae in [124]. The ratio between the contribution from the interference of diagrams in Figure 4.4 and Figure 4.8 and this $\mathcal{O}(\alpha^3)$ term just discussed is $R_{g-\gamma} = \frac{2}{9}(\frac{\alpha_s}{\alpha Q_q Q_t})^2$. Thus, the contribution of S_g to the numerator of the asymmetry can be calculated using S_γ and multiplying the results by $R_{g-\gamma}$. In Figure 4.11, a numerical test of the independence of ΔE for the $\mathcal{O}(\alpha_s^2\alpha)_{\text{weak}}$ contribution of $u\bar{u}$ to N of $A_{FB}^{t\bar{t}}$ is shown as an illustration.

In the numerical analyses, we chose MRST2004QED parton distributions [100] for NLO calculations and MRST2001LO for LO [125], using thereby $\alpha_s(\mu)$ provided by MRST2004QED also for the evaluation of the cross sections at LO (a similar strategy was employed in [96]). As said in section 3.3.2, this PDF set is, at the moment, the

σ(pb)	$\mu = m_t/2$	$\mu = m_t$	$\mu = 2m_t$
$u\bar{u}$	6.245	4.454	3.355
$d\bar{d}$	1.112	0.777	0.575
$s\bar{s}$	1.37×10^{-2}	9.60×10^{-3}	0.706×10^{-2}
$c\bar{c}$	2.24×10^{-3}	1.69×10^{-3}	1.32×10^{-3}
gg	0.617	0.378	0.248
$p\bar{p}$	7.990	5.621	4.187

Table 4.3: Integrated cross sections at $\mathcal{O}(\alpha_s^2)$ from the various partonic channels.

only one including the QED effects for the DGLAP[2] evolution. The same value μ is used also for the factorization scale. The numerical results are presented with three different choices for the scale: $\mu = m_t/2, m_t, 2m_t$. The other input parameters are taken from [126].

The results for the cross sections from the individual partonic channels and their sum, yielding the denominator of A_{FB}, are listed in Table 4.3. The various asymmetric terms entering the numerator of either of the two variants $A_{FB}^{t\bar{t}}$ and $A_{FB}^{p\bar{p}}$ are collected in Table 4.4, and the corresponding contributions to the asymmetry in Table 4.5.

As already mentioned, the QED part was obtained in two different ways, based on a diagrammatic calculation and on the use of eq. (4.19). Specifically, the $\mathcal{O}(\alpha_s^2\alpha)_{QED}$ contributions have been obtained multiplying $\mathcal{O}(\alpha_s^3)$ terms by the following numbers

$$\begin{aligned} R_{QED}^{u\bar{u}}(Q_u) &= (0.192, 0.214, 0.237)\,, \\ R_{QED}^{d\bar{d}}(Q_d) &= (-0.096, -0.107, -0.119)\,. \end{aligned} \tag{4.24}$$

The results for the weak part are obtained exclusively from the diagrammatic calculation.

The ratio R_{EW} of the total $\mathcal{O}(\alpha_s^2\alpha)+\mathcal{O}(\alpha^2)$ and $\mathcal{O}(\alpha_s^3)$ contributions to the numerator N of the asymmetry eq. (4.12) gives an illustration of the impact of the electroweak induced asymmetry relative to the QCD asymmetry. The values obtained numerically for $\mu = (m_t/2, m_t, 2m_t)$ for the two definitions of A_{FB} are

$$\begin{aligned} R_{EW}^{t\bar{t}} &= \frac{N_{\mathcal{O}(\alpha_s^2\alpha)+\mathcal{O}(\alpha^2)}^{t\bar{t}}}{N_{\mathcal{O}(\alpha_s^3)}^{t\bar{t}}} = (0.190, 0.220, 0.254), \\ R_{EW}^{p\bar{p}} &= \frac{N_{\mathcal{O}(\alpha_s^2\alpha)+\mathcal{O}(\alpha^2)}^{p\bar{p}}}{N_{\mathcal{O}(\alpha_s^3)}^{p\bar{p}}} = (0.186, 0.218, 0.243). \end{aligned} \tag{4.25}$$

This shows that the electroweak contribution provides a non-negligible additional part to the QCD-based asymmetric cross section with the same overall sign, thus enlarging

[2]The Dokshitzer-Gribov-Lipatov-Altarelli-Parisi (DGLAP) differential equations describe the dependence of the parton distribution functions on the factorization scale.

(a) $A_{FB}^{t\bar{t}}$

N(pb)		$\mu = m_t/2$	$\mu = m_t$	$\mu = 2m_t$
$\mathcal{O}(\alpha_s^3)$	$u\bar{u}$	0.560	0.354	0.234
$\mathcal{O}(\alpha_s^3)$	$d\bar{d}$	9.25×10^{-2}	5.76×10^{-2}	3.76×10^{-2}
$\mathcal{O}(\alpha_s^2\alpha)_{QED}$	$u\bar{u}$	0.108	0.0759	0.0554
$\mathcal{O}(\alpha_s^2\alpha)_{QED}$	$d\bar{d}$	-8.9×10^{-3}	-6.2×10^{-3}	-4.5×10^{-3}
$\mathcal{O}(\alpha_s^2\alpha)_{\text{weak}}$	$u\bar{u}$	1.25×10^{-2}	0.89×10^{-2}	0.66×10^{-2}
$\mathcal{O}(\alpha_s^2\alpha)_{\text{weak}}$	$d\bar{d}$	-3.6×10^{-3}	-2.5×10^{-3}	-1.8×10^{-3}
$\mathcal{O}(\alpha^2)$	$u\bar{u}$	1.47×10^{-2}	1.30×10^{-2}	1.17×10^{-2}
$\mathcal{O}(\alpha^2)$	$d\bar{d}$	1.8×10^{-3}	1.6×10^{-3}	1.4×10^{-3}

(b) $A_{FB}^{p\bar{p}}$

N(pb)		$\mu = m_t/2$	$\mu = m_t$	$\mu = 2m_t$
$\mathcal{O}(\alpha_s^3)$	$u\bar{u}$	0.373	0.236	0.155
$\mathcal{O}(\alpha_s^3)$	$d\bar{d}$	5.97×10^{-2}	3.72×10^{-2}	2.42×10^{-2}
$\mathcal{O}(\alpha_s^2\alpha)_{QED}$	$u\bar{u}$	7.15×10^{-2}	5.06×10^{-2}	3.67×10^{-2}
$\mathcal{O}(\alpha_s^2\alpha)_{QED}$	$d\bar{d}$	-5.7×10^{-3}	-4.0×10^{-3}	-2.9×10^{-3}
$\mathcal{O}(\alpha_s^2\alpha)_{\text{weak}}$	$u\bar{u}$	8.2×10^{-3}	5.8×10^{-3}	4.2×10^{-3}
$\mathcal{O}(\alpha_s^2\alpha)_{\text{weak}}$	$d\bar{d}$	-2.3×10^{-3}	-1.6×10^{-3}	-1.1×10^{-3}
$\mathcal{O}(\alpha^2)$	$u\bar{u}$	9.1×10^{-3}	8.0×10^{-3}	7.1×10^{-3}
$\mathcal{O}(\alpha^2)$	$d\bar{d}$	1.1×10^{-3}	1.0×10^{-3}	0.9×10^{-3}

Table 4.4: The various contributions to the asymmetric cross section N of $A_{FB}^{t\bar{t}}$ and $A_{FB}^{p\bar{p}}$.

the Standard Model prediction for the asymmetry The electroweak $\mathcal{O}(\alpha_s^2\alpha)$ contribution of $u\bar{u} \to t\bar{t}$ to the asymmetry is even bigger than the $\mathcal{O}(\alpha_s^3)$ contribution of $d\bar{d} \to t\bar{t}$.

The results in eq. (4.25) are larger than the previous estimate of 0.09 given in [30]. Afterwards, the authors of [30] have reevaluated the mixed EW–QCD contribution to A_{FB} and found it in agreement with our results [127]. We have also estimated the influence of the choice of parton distributions. Turning off the QED evolution leads only to marginal modification. Indeed, the difference between the calculation of the QCD part in the numerator of $A_{FB}^{t\bar{t}}$ using MRST2004QED and MRST2004[3] [128] is smaller than 1% of the result obtained with MRST2004QED. It is interesting to note that the $\mathcal{O}(\alpha_s^2\alpha)$ contributions to the numerator of the asymmetry (Table 4.4) depend on the scale μ, but, once the results are divided by D (Table 4.5), they seem to be independent. Both the weak and QED part of $\alpha\tilde{N}_1/D_0$ clearly do not depend on the renormalization

[3]This set of PDFs comes from the same input data of MRST2004QED, but it does not include the QED evolution.

(a) $A_{FB}^{t\bar{t}}$

$A_{FB}^{t\bar{t}}$		$\mu = m_t/2$	$\mu = m_t$	$\mu = 2m_t$
$\mathcal{O}(\alpha_s^3)$	$u\bar{u}$	7.01%	6.29%	5.71%
$\mathcal{O}(\alpha_s^3)$	$d\bar{d}$	1.16%	1.03%	0.92%
$\mathcal{O}(\alpha_s^2\alpha)_{QED}$	$u\bar{u}$	1.35%	1.35%	1.35%
$\mathcal{O}(\alpha_s^2\alpha)_{QED}$	$d\bar{d}$	-0.11%	-0.11%	-0.11%
$\mathcal{O}(\alpha_s^2\alpha)_{\text{weak}}$	$u\bar{u}$	0.16%	0.16%	0.16%
$\mathcal{O}(\alpha_s^2\alpha)_{\text{weak}}$	$d\bar{d}$	-0.04%	-0.04%	-0.04%
$\mathcal{O}(\alpha^2)$	$u\bar{u}$	0.18%	0.23%	0.28%
$\mathcal{O}(\alpha^2)$	$d\bar{d}$	0.02%	0.03%	0.03%
tot	$p\bar{p}$	9.72%	8.93%	8.31%

(b) $A_{FB}^{p\bar{p}}$

$A_{FB}^{p\bar{p}}$		$\mu = m_t/2$	$\mu = m_t$	$\mu = 2m_t$
$\mathcal{O}(\alpha_s^3)$	$u\bar{u}$	4.66%	4.19%	3.78%
$\mathcal{O}(\alpha_s^3)$	$d\bar{d}$	0.75%	0.66%	0.59%
$\mathcal{O}(\alpha_s^2\alpha)_{QED}$	$u\bar{u}$	0.90%	0.90%	0.90%
$\mathcal{O}(\alpha_s^2\alpha)_{QED}$	$d\bar{d}$	-0.07%	-0.07%	-0.07%
$\mathcal{O}(\alpha_s^2\alpha)_{\text{weak}}$	$u\bar{u}$	0.10%	0.10%	0.10%
$\mathcal{O}(\alpha_s^2\alpha)_{\text{weak}}$	$d\bar{d}$	-0.03%	-0.03%	-0.03%
$\mathcal{O}(\alpha^2)$	$u\bar{u}$	0.11%	0.14%	0.17%
$\mathcal{O}(\alpha^2)$	$d\bar{d}$	0.01%	0.02%	0.02%
tot	$p\bar{p}$	6.42%	5.92%	5.43%

Table 4.5: Individual and total contributions to $A_{FB}^{t\bar{t}}$ and $A_{FB}^{p\bar{p}}$.

scale, so the independence on μ would mean independence of the factorization scale. Even using two different sets of PDFs, it seems that the dependences of N and D on μ_f cancel in the ratio N/D.

The final result for the two definitions of A_{FB} can be summarized as follows,

$$\begin{aligned} A_{FB}^{t\bar{t}} &= (9.7, 8.9, 8.3)\%\,, \\ A_{FB}^{p\bar{p}} &= (6.4, 5.9, 5.4)\%\,. \end{aligned} \tag{4.26}$$

Figure 4.12 displays the theoretical prediction versus the experimental measurement of CDF in the lepton+jets signature listed in Table 4.1. The prediction is inside the 2σ range for both $A_{FB}^{t\bar{t}}$ and $A_{FB}^{p\bar{p}}$. Also for the DØ measurement in the lepton+jets signature, the deviation is smaller than 2σ. However, the CDF measurement in the dilepton channel shows a 2σ deviation from the predicted value.

It is important to note that in Figure 4.12 the blue bands indicating the dependence of the prediction on the scale variation do not account for all the theoretical

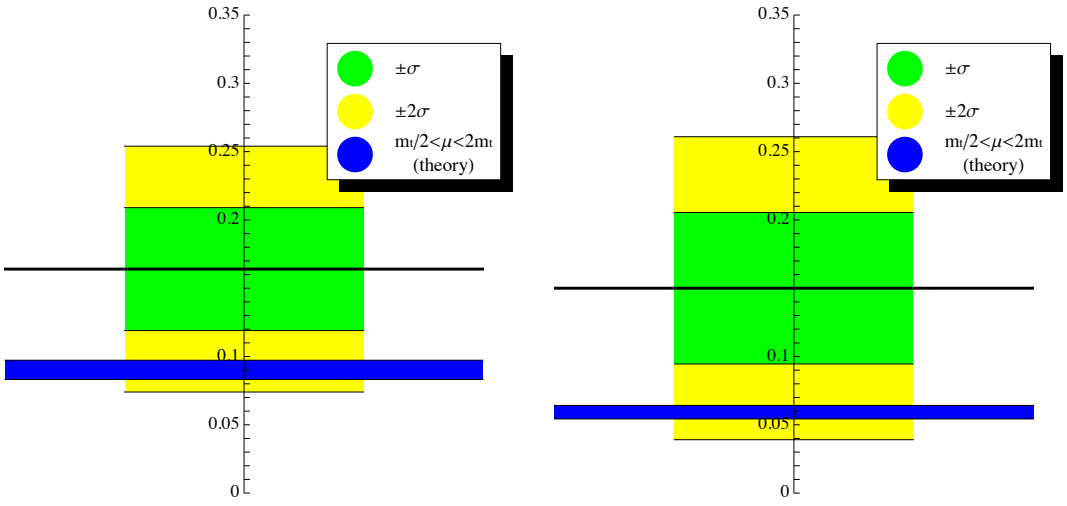

(a) $A_{FB}^{t\bar{t}}$ (b) $A_{FB}^{p\bar{p}}$

Figure 4.12: Theory (blue) and experimental data (black: central value, green: 1σ, yellow: 2σ).

uncertainties. For example, the $\mathcal{O}(\alpha_s^4)$ term in N is missing and we did not include the $\mathcal{O}(\alpha_s^3)$ part in D. Including this $\mathcal{O}(\alpha_s^3)$ term for the cross section in D, as said in the previous section, would decrease the asymmetry by about 30%, which indicates the size of the NLO terms in the asymmetry. In a conservative spirit one can consider this as an uncertainty from the incomplete NLO calculation for the asymmetry (see also the discussion in [30]).

We have performed our analysis also for applying two different types of cuts, one on the $t\bar{t}$ invariant mass $M_{t\bar{t}}$ and the other one on the rapidity: $M_{t\bar{t}} > 450$ GeV and $|\Delta y| > 1$. The cross section values for these cuts at LO are given in Table 4.6. The various terms of the asymmetric cross section contributing to N, as discussed above in the case without cuts, are now calculated for $A_{FB}^{t\bar{t}}$ for both cases $M_{t\bar{t}} > 450$ GeV and $|\Delta y| > 1$. The corresponding contributions to the asymmetry $A_{FB}^{t\bar{t}}$ are the entries of Table 4.7. Here, we see that $\mathcal{O}(\alpha_s^2\alpha)$ contributions show a small dependence on μ_f that in the cases without cuts applied (Table 4.5) was smaller than the numerical error and thus completely hidden.

σ(pb)	$\mu = m_t/2$	$\mu = m_t$	$\mu = 2m_t$
$p\bar{p}(M_{t\bar{t}} > 450$ GeV)	3.113	2.148	1.573
$p\bar{p}(\lvert\Delta y\rvert > 1)$	1.846	1.276	0.937

Table 4.6: Cross sections with cuts at $\mathcal{O}(\alpha_s^2)$.

(a) $A_{FB}^{t\bar{t}}(M_{t\bar{t}} > 450$ GeV)

$A_{FB}^{t\bar{t}}$		$\mu = m_t/2$	$\mu = m_t$	$\mu = 2m_t$
$\mathcal{O}(\alpha_s^3)$	$u\bar{u}$	10.13%	9.10%	8.27%
$\mathcal{O}(\alpha_s^3)$	$d\bar{d}$	1.44%	1.27%	1.14%
$\mathcal{O}(\alpha_s^2\alpha)_{QED}$	$u\bar{u}$	1.94%	1.95%	1.96%
$\mathcal{O}(\alpha_s^2\alpha)_{QED}$	$d\bar{d}$	-0.14%	-0.14%	-0.14%
$\mathcal{O}(\alpha_s^2\alpha)_{\text{weak}}$	$u\bar{u}$	0.28%	0.28%	0.28%
$\mathcal{O}(\alpha_s^2\alpha)_{\text{weak}}$	$d\bar{d}$	-0.05%	-0.05%	-0.05%
$\mathcal{O}(\alpha^2)$	$u\bar{u}$	0.26%	0.33%	0.41%
$\mathcal{O}(\alpha^2)$	$d\bar{d}$	0.03%	0.03%	0.04%
tot	$p\bar{p}$	13.90%	12.77%	11.91%

(b) $A_{FB}^{t\bar{t}}(|\Delta y| > 1)$

$A_{FB}^{t\bar{t}}$		$\mu = m_t/2$	$\mu = m_t$	$\mu = 2m_t$
$\mathcal{O}(\alpha_s^3)$	$u\bar{u}$	15.11%	13.72%	12.41%
$\mathcal{O}(\alpha_s^3)$	$d\bar{d}$	2.28%	2.02%	1.84%
$\mathcal{O}(\alpha_s^2\alpha)_{QED}$	$u\bar{u}$	2.90%	2.94%	2.94%
$\mathcal{O}(\alpha_s^2\alpha)_{QED}$	$d\bar{d}$	-0.22%	-0.22%	-0.22%
$\mathcal{O}(\alpha_s^2\alpha)_{\text{weak}}$	$u\bar{u}$	0.25%	0.25%	0.26%
$\mathcal{O}(\alpha_s^2\alpha)_{\text{weak}}$	$d\bar{d}$	-0.09%	-0.09%	-0.08%
$\mathcal{O}(\alpha^2)$	$u\bar{u}$	0.35%	0.45%	0.55%
$\mathcal{O}(\alpha^2)$	$d\bar{d}$	0.04%	0.05%	0.06%
tot	$p\bar{p}$	20.70%	19.12%	17.75%

Table 4.7: Individual and total contributions to the asymmetries applying cuts: $A_{FB}^{t\bar{t}}(M_{t\bar{t}} > 450$ GeV) and $A_{FB}^{t\bar{t}}(|\Delta y| > 1)$.

The asymmetry with cuts is the total result,

$$\begin{aligned} A_{FB}^{t\bar{t}}(M_{t\bar{t}} > 450 \text{ GeV}) &= (13.9, 12.8, 11.9)\%\,, \\ A_{FB}^{t\bar{t}}(|\Delta y| > 1) &= (20.7, 19.1, 17.5)\%\,. \end{aligned} \tag{4.27}$$

Figure 4.13 displays the theoretical prediction versus data for $A_{FB}^{t\bar{t}}$ with cuts. The Standard Model prediction is at 2σ for the $|\Delta y| > 1$ cut and it is at 2.5σ for the invariant mass cut $M_{t\bar{t}} > 450$ GeV.

With higher invariant masses, and thus PDFs sampled at higher Bjorken x values, the relative differences between $u\bar{u}$ and $d\bar{d}$ luminosities increase. Indeed, a comparison between Table 4.7(a) and Table 4.5(a) shows that the ratio of the QCD contribution to the $u\bar{u} \to t\bar{t}$ and $d\bar{d} \to t\bar{t}$ subprocesses is larger with the $M_{t\bar{t}} > 450$ GeV cut. Thus, the relative impact of negative $\mathcal{O}(\alpha_s^2\alpha)$ corrections from $d\bar{d}$ is reduced, leading to a

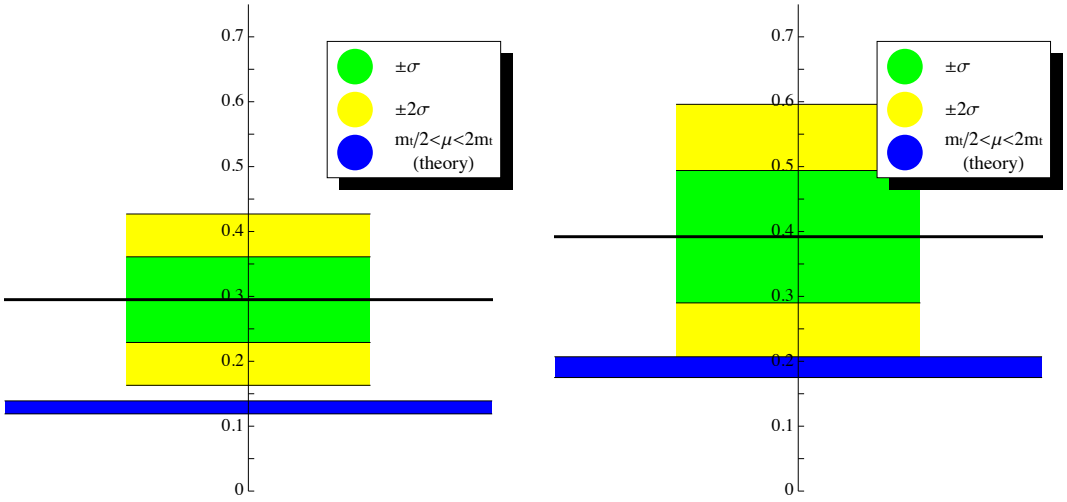

(a) $A_{FB}^{t\bar{t}}(M_{t\bar{t}} > 450\ \text{GeV})$ (b) $A_{FB}^{t\bar{t}}(|\Delta y| > 1)$

Figure 4.13: Theory (blue) and experimental data (black: central value, green: 1σ, yellow: 2σ).

slight increase of $R_{EW}^{t\bar{t}}$:

$$\begin{aligned} R_{EW}^{t\bar{t}}(M_{t\bar{t}} > 450\ \text{GeV}) &= (0.200, 0.232, 0.266)\,, \\ R_{EW}^{t\bar{t}}(|\Delta y| > 1) &= (0.191, 0.216, 0.246)\,. \end{aligned} \tag{4.28}$$

We want to stress again that, in contrast to R_{EW}, R_{QED} does not depend on the precise definition of the asymmetry and on the applied cuts. It depends only on the charge of the initial-state partons and the renormalization scale used in the calculation. In the publications based also on [29], eq. (4.19) has been widely used to evaluate the electroweak contribution to A_{FB}.

In order to compare the other measurements listed in Table 4.1 with the SM theoretical predictions, we will refer to the values listed in [129]. Although different sets of PDFs have been used in the numerical evaluation, the theoretical framework in [129] is exactly the same of [29] and, as stated by the authors, the results for the individual contributions are in very good agreement with our values in Table 4.4(a).

The theoretical prediction for $A_{FB}^{t\bar{t}}$ in the phase-space regions $M_{t\bar{t}} \leq 450$ GeV and $|\Delta y| \leq 1$ are:

$$\begin{aligned} A_{FB}^{t\bar{t}}(M_{t\bar{t}} \leq 450\ \text{GeV}) &= (5.9, 6.2, 6.6)\%, \\ A_{FB}^{t\bar{t}}(|\Delta y| \leq 1) &= (5.8, 6.1, 6.5)\%\,. \end{aligned} \tag{4.29}$$

These predictions are within 1σ deviations of the experimental results. Thus, the different deviations for low and high invariant mass and rapidity regions suggested to analyze the dependence of the asymmetry on $M_{t\bar{t}}$ and $|\Delta y|$.

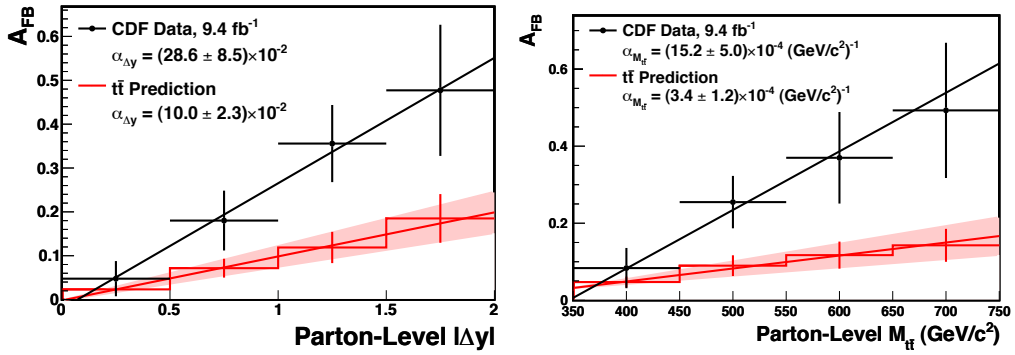

(a) $A_{FB}^{t\bar{t}}(|\Delta y|)$ (b) $A_{FB}^{t\bar{t}}(M_{t\bar{t}})$

Figure 4.14: Comparison between measured values and SM theoretical predictions for $A_{FB}^{t\bar{t}}(|\Delta y|)$ and $A_{FB}^{t\bar{t}}(M_{t\bar{t}})$. Plot taken from [31].

The theoretical prediction for

$$A_{FB}^{t\bar{t}}(|\Delta y|) = \frac{d\sigma(\Delta y > 0)/d|\Delta y| - d\sigma(\Delta y < 0)/d|\Delta y|}{d\sigma(\Delta y > 0)/d|\Delta y| + d\sigma(\Delta y < 0)/d|\Delta y|} \tag{4.30}$$

and

$$A_{FB}^{t\bar{t}}(M_{t\bar{t}}) = \frac{d\sigma(\Delta y > 0)/dM_{t\bar{t}} - d\sigma(\Delta y < 0)/dM_{t\bar{t}}}{d\sigma(\Delta y > 0)/dM_{t\bar{t}} + d\sigma(\Delta y < 0)/dM_{t\bar{t}}} \tag{4.31}$$

can be safely approximated as a linear dependence respectively in $|\Delta y|$ and $M_{t\bar{t}}$ with slopes $\alpha_{\Delta y}$ and $\alpha_{M_{t\bar{t}}}$.

In [31] the CDF collaboration compared, as shown in Figure 4.14, the measured value and the SM predictions, including EW contributions, for these two parameters, $\alpha_{\Delta y}$ and $\alpha_{M_{t\bar{t}}}$. The measured values are extracted, in both cases, by fitting four points obtained binning the phase space. The theoretical values are also obtained from the fit of the corresponding SM predictions for the four bins, where the errors are estimated again by varying the renormalization scale. As can be seen from Figure 4.14(a) and Figure 4.14(b), the measured and predicted slopes differ by slightly more than 2σ.

In conclusion, the deviation of 3.5σ for $A_{FB}^{t\bar{t}}(M_{t\bar{t}} > 450$ GeV), found by CDF in the first analysis [20], has decreased to 2.5σ taking also into account the effect of electroweak corrections and increasing the data set. Still, as just mentioned, a 2σ deviation between the predicted and measured dependence of A_{FB} on $M_{t\bar{t}}$ remains.

4.4 The charge asymmetry at the LHC

As said in section 4.2, most of the theoretical arguments described for the case of A_{FB} are valid also for the charge asymmetry at the LHC, called also central asymmetry, A_C, due its definition in eq. (4.5). However, the two conditions that, as explained in section 4.2, a partonic subprocess must satisfy in order to generate an asymmetric

contribution, cannot be extended to the case of A_C. First of all, in order to generate a central asymmetry, the differential distributions in y_t and $y_{\bar{t}}$ must be different at the partonic level in the partonic rest frame. Without this condition, summing over the two configurations (first parton from the first proton or first parton from the second proton) or boosting to the laboratory frame clearly cannot induce a central asymmetry. If the two distributions are asymmetric, $d\hat{\sigma}/dy_t \neq d\hat{\sigma}/dy_{\bar{t}}$, a central asymmetry is not automatically generated. Indeed, if they are antisymmetric, i.e. $d\hat{\sigma}/dy_t = d\hat{\sigma}/d(-y_{\bar{t}})$, the sum over the two configurations (first parton from the first proton or first parton from the second proton) can in principle lead to the condition $d\sigma/dy_t = d\sigma/dy_{\bar{t}}$ at the hadronic level. If the distributions are antisymmetric, it is necessary that the PDFs in the proton for the two partons in the initial state are different ($f_{p_1} \neq f_{p_2}$), thereby boosting in different ways the top and the antitop quark. Since the partonic contributions that we discussed in section 4.1 are indeed antisymmetric, the condition $f_{p_1} \neq f_{p_2}$ must be true and again the $q\bar{q}$ initial state contribute to eq. (4.5) only if $q = u, d$.

Besides the different definitions for the charge asymmetry, A_{FB} and A_C, the main difference between the Tevatron and the LHC is the total energy in the center of mass and thus the luminosities for the various partonic subprocesses. At the LHC with 7 TeV, 85% of the cross section originates from the gg initial state, which is symmetric. This subprocess contributes to the denominator of A_C but not to the numerator, so it suppresses the value of A_C. This effect is further enhanced at 8 TeV and even more at 14 TeV. With the increment of the gluon PDF value, also the contribution of the qg and $\bar{q}g$ initial states becomes non-negligible; it can be of the order of 10% of the $q\bar{q}$ contribution. The precise value depends on the total energy and, possibly, on applied $M_{t\bar{t}}$ cuts.

A detailed study of the SM predictions, including electroweak contributions, for A_C at the LHC has been presented in [129]. There, in addition to the contributions discussed in the previous section, the $\mathcal{O}(\alpha_s^3)$ and $\mathcal{O}(\alpha_s^2\alpha)_{QED}$ contribution from qg and $\bar{q}g$ initial states are also taken into account. In analogy to the $q\bar{q}$ initial state, the $\mathcal{O}(\alpha_s^2\alpha)_{QED}$ contribution from the qg and $\bar{q}g$ initial states can be obtained multiplying the $\mathcal{O}(\alpha_s^3)$ results by a factor $R^{qg}_{QED}(Q_q)$,

$$R^{qg}_{QED}(Q_q) = Q_q Q_t \frac{24}{5}\frac{\alpha}{\alpha_s}\,. \tag{4.32}$$

In the case of A_C the ratios R_{EW} of the central values of QCD and QCD+EW predictions are between 1.15 and 1.20, depending on the total energy and on the applied cuts, and thus they are smaller than in the case of A_{FB}. The measurements of A_C listed in Table 4.2 are in agreement with the QCD+EW predictions for the LHC at 7 TeV presented in [129], $A_C^{t\bar{t}} = 1.23\ (5)\ \%$.

We want to stress here that, especially at the Tevatron, the impact of the electroweak corrections on the asymmetry is much larger than in the case of the cross section. The first obvious reason is the different leading perturbative order for the

two cases: $\mathcal{O}(\alpha_s^2)$ for the total cross section and $\mathcal{O}(\alpha_s^3)$ for the antisymmetric cross section. The second reason is more subtle. Excluding the trigluon interactions, the diagrams that contribute to the total cross section at the $\mathcal{O}(\alpha_s^3)$ (vertex corrections and self energies) are in one-to-one relation with the diagrams that contribute to the $\mathcal{O}(\alpha_s^2\alpha)_{QED}$. In the antisymmetric contribution the situation is different. Here, the diagrams in $\mathcal{O}(\alpha_s^2\alpha)_{QED}$ are three times the diagrams of $\mathcal{O}(\alpha_s^3)$. This is reflected by the parameter $n_{t\bar{t}} = 3$ used in section 4.2 and illustrated in Figure 4.5.

At present, no deviation larger than 3σ is visible both for the A_{FB} measured at the Tevatron and A_C measured at the LHC. However, all the measured values for A_{FB} are larger than the SM predictions, whereas the A_C measurements are, at least for the lepton+jets signatures, a bit lower than the SM predictions and in very good agreement with them (1σ deviations). In [130, 131] it has been proposed and shown that the forward-backward and central asymmetry can be written as

$$\begin{aligned} A_{FB} &= A_u F_u + A_d F_d \,, \\ A_C &= A'_u F'_u D_u + A'_d F'_d D_d \,, \end{aligned} \tag{4.33}$$

where $A_u \sim A'_u$ and $A_d \sim A'_d$, when A_{FB} and A_C are measured in fixed bins for $M_{t\bar{t}}$ and for the longitudinal velocity of the $t\bar{t}$ system. The terms $A_u^{(\prime)}$ and $A_d^{(\prime)}$ are the contributions to the asymmetry from $u\bar{u}$ and $d\bar{d}$ initial states, considering only $u\bar{u}$ or $d\bar{d}$ in the calculation of the asymmetry. $F_u^{(\prime)}$ and $F_d^{(\prime)}$ are the relative fractions of $u\bar{u}$ and $d\bar{d}$ initial-state events, and they weight the $A_u^{(\prime)}$ and $A_d^{(\prime)}$ contributions. D_u and D_d are "dilution" factors that correct, at the LHC, the contribution from the rest frame of the partonic center of mass to the laboratory frame. For A_{FB}, defined with the boost invariant quantity Δy, these factors are clearly not necessary. Thus, according to eq. (4.33), in principle it is possible to compare measurements at the Tevatron and at the LHC.

For completeness we report also the SM predictions for A_{FB}^l, A_{FB}^{ll} and A_C^{ll} of [129], where all the factorizable QCD corrections to production and decay of top quark pairs and EW corrections to the production have been calculated. The predicted values at QCD+EW accuracy are, without including experimental cuts,

$$A_{FB}^l = 3.6\ (2)\ \%\,, \quad A_{FB}^{ll} = 4.8\ (4)\ \%\,, \quad A_C^{ll} = -0.25\ (1)\ \%\,. \tag{4.34}$$

These values are, in general, in good agreement with the corresponding experimental measurements listed in Table 4.1 and Table 4.2.

4.5 Asymmetries and BSM theories

In this section we briefly discuss the general features of BSM models that might explain the deviations between SM theoretical predictions and experimental measurements of the asymmetries.

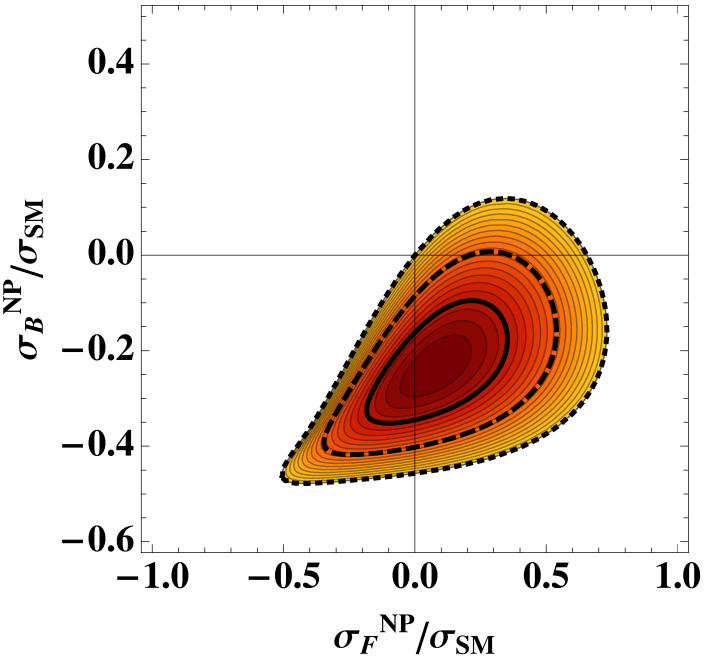

Figure 4.15: Fit of σ_F^{NP} and σ_B^{NP}. The dashed contours correspond to 1σ, 2σ and 3σ regions. Figure taken from [132].

We want to remind that, at the moment, only the measurements of the forward-backward asymmetry at the Tevatron present deviations from SM predictions and, anyway, they are smaller than 3σ. In addition, a large error is associated to the experimental values and the theoretical predictions are, for the asymmetry, at LO accuracy for QCD. Thus, improvements in the precision of SM theoretical predictions and in the experimental analyses[4] could solve this tension.

However, apart from the measurement of $A_{FB}^{t\bar{t}}$ in the high-invariant-mass region, these deviations did not decrease with larger data sets, so it is worth to check possible explanations from new physics effects. The SM is in good agreement with the measurements of the total and differential cross sections of top quark pair production. Thus, the new models, that are candidates to explain the deviations for the asymmetry, must not spoil this agreement between theory and experiment.

We can in general denote the contribution from new physics (NP) to the forward cross section of top quark pair production as σ_F^{NP} and the contribution to the backward cross section as σ_B^{NP} [132]. Figure 4.15 shows the results of the fit of these two quantites from $A_{FB}^{t\bar{t}}$ measurements, taking into account the constraints from the inclusive cross section measurements. It is important to note that σ_F^{NP} and σ_B^{NP} can originate from NP amplitudes squared or interfering with the SM amplitudes. However, only the latter

[4]The Tevatron has been shut down, so only more sophisticated analyses can be performed for A_{FB}, but new data cannot be taken.

case allows negative contributions. Thus, Figure 4.15 suggests that the interference between SM and NP diagrams should be non-vanishing.

According to [132], where many more details can be found, two main categories of models, can be classified via the structure of the Feynman diagrams contributing to top quark pair production:

- models originating vector octet s-channel diagrams,
- models originating t-channel diagrams.

In the first class of models the propagator in the s-channel diagram must be colored otherwise the interference with the SM s-channel $q\bar{q} \to g \to t\bar{t}$ colored diagrams would be zero. Moreover, both the interactions with the top quark pair and the $q\bar{q}$ initial state must have an axial component in order to generate an asymmetric term. Conversely, in the second class of models, particles in the t-channel propagator do not need to be colored. The new interactions can violate or conserve the flavor structure. In addition, new invisible particles could be generated. In [134] it has been shown that NP models giving positive contribution to A_{FB} can be consistent with LHC results for A_C. However, it is important that the $u\bar{u}$ and $d\bar{d}$ contributions are of different sign, so that the different ratios at the Tevatron and the LHC between the $u\bar{u}$ and $d\bar{d}$ luminosities can produce total contributions with different sign in the two cases.

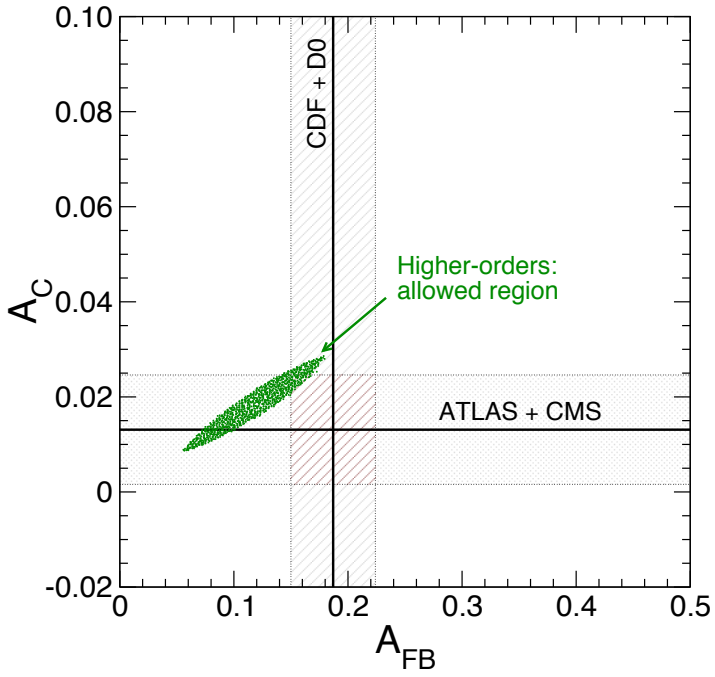

Figure 4.16: Correlation between A_{FB} and A_C obtained estimating higher-order corrections. The bands around central values, in the experimental measurements, correspond to 1σ deviations. Plot taken from [133].

In [133] it is shown that many of these models and their parameter regions are excluded, once also the compatibility with measurements of the total cross section, the tail in the $M_{t\bar{t}}$ distribution at the LHC, and the top quark polarization are taken into account. It has been argued [133] that the calculation of N_2 in eq. (4.11), giving a prediction at NLO QCD accuracy for A_{FB} and A_C, could be not sufficient for a complete explanation of the values measured at the Tevatron and the LHC. Figure 4.16, from [133], shows in green the prediction for A_{FB} and A_C obtained from eq. (4.33) rescaling the $A_u^{(\prime)}$ and $A_d^{(\prime)}$ NLO QCD predictions by a common factor. Indeed, NNLO QCD contributions to the asymmetry, as NLO, do not depend at parton level on the flavor of the initial state. It seems that SM predictions could be compatible with measurements within 1σ deviation, but they cannot cross their central values.

In conclusion, the top quark charge asymmetry remains an interesting anomaly in collider physics at the moment and further studies will be performed both from the experimental and theoretical side.

Chapter 5

The Minimal Supersymmetric Standard Model (MSSM)

5.1 Supersymmetry and the Standard Model

Supersymmetry (SUSY) [21] is a symmetry that, relating fermions and bosons, combines in the only possible non-trivial way the Poincaré space-time symmetry and internal symmetries of Lagrangians in QFT [135]. According to the Coleman-Mandula theorem [136], it is impossible to combine the Poincaré algebra and an internal symmetry algebra into a larger algebra different from the trivial direct product of the previous two; non-trivial combinations would lead to the non-analyticity of the S-matrix.

Supersymmetry in some sense eludes this theorem, by introducing anti-commutation relations for the spinorial generators $Q_i,\ i = 1 \dots N$, for the transformations of bosons into fermions and fermions into bosons,

$$Q_i|\text{boson}\rangle = |\text{fermion}\rangle\,, \qquad Q_i|\text{fermion}\rangle = |\text{boson}\rangle\,. \tag{5.1}$$

In the simplest case, $N = 1$, the general structure of the superalgebra is determined by the following relations[1],

$$\begin{aligned} &\{Q, Q^\dagger\} = P^\mu \sigma_\mu\,, \\ &\{Q, Q\} = \{Q^\dagger, Q^\dagger\} = 0\,, \\ &[P, Q] = [P, Q^\dagger] = 0\,, \\ &[M_{\mu\nu}, Q] = i\sigma_{\mu\nu} Q\,, \end{aligned} \tag{5.2}$$

and by the usual relations among the generators of the Poincaré algebra.

In eq. (5.2) P^μ are the generators of translations in space-time and $M_{\mu\nu}$ are the Lorentz generators of boosts and spatial rotations; σ^μ are the Pauli matrices, with

[1] For an easier reading, in eq. (5.2) we dropped the spinorial indices of Q, σ^μ and $\sigma^{\mu\nu}$.

Names	spin 0	spin 1/2	$SU(3)_C$, $SU(2)_L$, $U(1)_Y$
(s)quarks	$\tilde{Q}_L = (\tilde{u}_L, \tilde{d}_L)$	$Q_L = (u_L, d_L)$	$(\mathbf{3}, \mathbf{2}, +\frac{1}{6})$
($\times$3 families)	$\tilde{u}_R$	u_R	$(\mathbf{3}, \mathbf{1}, +\frac{2}{3})$
	$\tilde{d}_R$	d_R	$(\mathbf{3}, \mathbf{1}, -\frac{1}{3})$
(s)leptons	$\tilde{L}_L = (\tilde{\nu}\ \tilde{e}_L)$	$L_L = (\nu, e_L)$	$(\mathbf{1}, \mathbf{2}, -\frac{1}{2})$
($\times$3 families)	$\tilde{e}_R$	e_R	$(\mathbf{1}, \mathbf{1}, -1)$
Higgs(inos)	$H_u = (H_u^+, H_u^0)$	$\tilde{H}_u = (\tilde{H}_u^+, \tilde{H}_u^0)$	$(\mathbf{1}, \mathbf{2}, +\frac{1}{2})$
	$H_d = (H_d^0, H_d^-)$	$\tilde{H}_d = (\tilde{H}_d^0, \tilde{H}_d^-)$	$(\mathbf{1}, \mathbf{2}, -\frac{1}{2})$

Table 5.1: Field content of the chiral supermultiplets of the MSSM.

Names	spin 1/2	spin 1	$SU(3)_C$, $SU(2)_L$, $U(1)_Y$
gluino, gluon	$\tilde{g}$	g	$(\mathbf{8}, \mathbf{1}, 0)$
winos, W bosons	$\tilde{W}^{\pm}\ \ \tilde{W}^0$	$W^{\pm}\ \ W^0$	$(\mathbf{1}, \mathbf{3}, 0)$
bino, B boson	$\tilde{B}$	B	$(\mathbf{1}, \mathbf{1}, 0)$

Table 5.2: Field content of the vector supermultiplets of the MSSM.

σ^0 equal to the unity matrix, and $\sigma^{\mu\nu} = (\sigma^\mu\sigma^\nu - \sigma^\nu\sigma^\mu)/2$. Also, the supersymmetry generators Q_i commute with the generators of any internal symmetry.

The representations of the supersymmetry algebra are called supermultiplets and contain both fermions and bosons. The members of a multiplet share the same quantum numbers of the gauge groups and, since P^2 is a Casimir operator, have the same mass. Moreover, every supermultiplet contains the same number of fermionic and bosonic degrees of freedom. As said, several generators $Q_i,\ i = 1 \ldots N$, can in general be introduced in the superalgebra. However, for $N > 1$, chiral fermions and parity violation are not allowed in four dimensions. Thus, such models cannot easily reproduce the phenomenology of the Standard Model.

The two simplest representations of $N = 1$ supersymmetry are called chiral multiplets and vector multiplets. The chiral multiplet consists in a spin 1/2 chiral fermion with two degrees of freedom and two real scalars, whereas the vector multiplet contains a massless spin-1 real vector and a massless Majorana spin 1/2 fermion with two degrees of freedom.

The minimal supersymmetric extension of the Standard Model is given by the so called Minimal Supersymmetric Standard Model (MSSM) [22, 23]. In this model the field content of the Standard Model is embedded in chiral and vector supermultiplets.

The chiral multiplets, also called scalar or matter multiplets, include the fermions of the Standard Model and the Higgs complex doublets, as shown in Table 5.1. The vector multiplets, also called gauge multiplets, include the gauge bosons of the Standard

Model, as shown in Table 5.2.

Every left- and right-handed component of a fermion of the Standard Model forms a chiral multiplet with its scalar superpartner, which is named, in obvious notation, sfermion, squark, slepton, etc. Each gauge boson forms a vector multiplet with its fermionic superpartner, which is generically called gaugino. In particular, the superpartners of W and B gauge bosons, and gluons are respectively called wino, bino and gluino.

An important new feature of the MSSM is the presence of two Higgs complex doublets, whereas the Standard Model has only one doublet. Supersymmetry relations impose constraints on the possible terms appearing in the Lagrangian, e.g., they do not allow to generate, with only a single Higgs doublet, the masses for both up- and down-type quarks. Moreover, the presence of only one doublet ($Y = +1/2$ or $Y = -1/2$) would lead to anomalies and, consequently, to a non-renormalizable theory. In addition, each one of the complex scalar Higgs components forms a chiral multiplet with a complex chiral fermion, called Higgsino.

If supersymmetry is realized in nature, however, it must be a broken symmetry. Without supersymmetry breaking, particles and their superpartners would have equal masses. Thus, also most of the non-standard MSSM particles should have already been experimentally detected. On the other hand, supersymmetry solves naturally the fine-tuning problem of Higgs parameters. For instance, loop corrections to the Higgs mass involving squarks cancel exactly the quadratic divergences of eq. (2.20) originating from quark loops. Thus, a possible supersymmetry breaking mechanism should not spoil this property.

The solution to this problem is provided by the so called soft supersymmetry breaking terms. The general Lagrangian of the MSSM can be written as

$$\mathcal{L}_{\text{MSSM}} = \mathcal{L}_{\text{SUSY}} + \mathcal{L}_{\text{soft}} \,, \tag{5.3}$$

where $\mathcal{L}_{\text{soft}}$ represents the soft supersymmetry breaking terms and $\mathcal{L}_{\text{SUSY}}$ includes the kinetic and the supersymmetry-invariant interaction terms of the fields in the chiral and gauge multiplets. The soft supersymmetry breaking terms do not reintroduce quadratic divergences in loop corrections to the Higgs mass; they generate only logarithmic UV divergences at most proportional to m^2_{soft}, where m_{soft} is the largest mass term introduced by $\mathcal{L}_{\text{soft}}$. In this way, if m_{soft} is of the order of 1 TeV, no fine tuning is necessary to obtain the correct Higgs masses. However, the insertion of $\mathcal{L}_{\text{soft}}$ is not enough to reproduce the phenomenology of the Standard Model. The most general $\mathcal{L}_{\text{MSSM}}$ allows for interaction terms that violate the baryon number B and the leptonic number L. This kind of interactions leads to proton decay and, unless their couplings are extremely suppressed, are not consistent with experimental data. The problem can be avoided imposing R-parity conservation on the $\mathcal{L}_{\text{MSSM}}$ Lagrangian, where the R-parity is defined for every field as

$$P_R = (-1)^{3(\text{B-L})+2s} \,, \tag{5.4}$$

with s equal to the spin of the field. In this way, $\mathcal{L}_{\rm MSSM}$ cannot contain renormalizable terms that violate B or L.

All the particles already present in the Standard Model and the two Higgs doublets have $P_R = +1$; their superpartners have $P_R = -1$ and are generally called sparticles. R-parity conserving interactions have important phenomenological consequences. The lightest supersymmetric particle (LSP) is stable and, if it is electrically neutral, it is a promising candidate for dark matter. Moreover, at colliders, sparticles can be produced only in even numbers and each of their possible complete decay chains ends with an odd number of LSPs. From here on in the thesis, R-parity is always implicitly assumed to be conserved.

A list of all the supersymmetric interaction terms of the MSSM is presented e.g., in [137, 138], where it is also explained how they can be derived simply requiring supersymmetry invariance. In the following subsections, we briefly address the basic phenomenological aspects of the MSSM and specify the mass spectrum emerging after supersymmetry breaking.

5.2 The mass eigenstates of the MSSM

The soft supersymmetry breaking terms in the MSSM generate differences between the mass terms of particles in the same supermultiplet and can be written as follows,

$$\begin{aligned}
\mathcal{L}_{\rm soft} \;=\; & -\frac{1}{2}\left(M_3\bar{\tilde{g}}\tilde{g} + M_2\bar{\tilde{W}}\tilde{W} + M_1\bar{\tilde{B}}\tilde{B} + \text{c.c.}\right) \\
& -\left(\tilde{u}_R^*\,\boldsymbol{a}_u\,\tilde{Q}_L H_u - \tilde{d}_R^*\,\boldsymbol{a}_d\,\tilde{Q}_L H_d - \tilde{e}_R^*\,\boldsymbol{a}_e\,\tilde{L}_L H_d + \text{c.c.}\right) \\
& -\tilde{Q}_L^*\,\boldsymbol{m}_Q^2\,\tilde{Q}_L - \tilde{L}_L^*\,\boldsymbol{m}_L^2\,\tilde{L}_L - \tilde{u}_R^*\,\boldsymbol{m}_u^2\,\tilde{u}_R - \tilde{d}_R^*\,\boldsymbol{m}_d^2\,\tilde{d}_R - \tilde{e}_R^*\,\boldsymbol{m}_e^2\,\tilde{e}_R \\
& - m_{H_u}^2 H_u^* H_u - m_{H_d}^2 H_d^* H_d - (b H_u H_d + \text{c.c.})\;, \qquad (5.5)
\end{aligned}$$

using the notation introduced in Tables 5.1 and 5.2. The first line of eq. (5.5) contains gaugino mass terms, which, in contrast to gauge vector boson mass terms, do not break gauge invariance. The second line consists of trilinear interactions of left- and right-handed sfermions with the Higgs doublets. In the third line the mass terms for the sfermions are listed; the fourth line presents mass terms for the two Higgs doublets.

In eq. (5.5) the parameters in bold are 3×3 hermitian matrices yielding non-diagonal interactions among squarks or leptons of different families. However, non-diagonal entries in these matrices induce FCNC interactions, which, e.g., lead to phenomenologically inconsistent contributions, in the case of the sleptons, to the decay $\mu \to e\gamma$ and, in the case of squarks, to the kaon mixing between K^0 and $\bar{K}^0$. This can be avoided assuming flavor-blind diagonal squared mass matrices for squarks and leptons, i.e., $\boldsymbol{m_i^2} = m_i^2\mathbb{1}$. Moreover, in order to avoid large scalar couplings for the light-flavor families, the $\boldsymbol{a_i}$ matrices can be assumed proportional to the diagonal Yukawian $\boldsymbol{y_i}$ matrices, i.e., $\boldsymbol{a_i} = A_i\boldsymbol{y_i}$.

Supersymmetry breaking parameters can be defined at some high scale Q, where supersymmetry is supposed to be broken, or, in a a more practical and phenomenological approach, directly at the TeV scale, ignoring the supersymmetry breaking mechanism that could generate them. In the first approach, the scale Q is indicated by an additional property that suggests SUSY as one of the best candidate models for BSM physics: the unification of strong, weak and electric couplings. The particle content of the MSSM is different than in the Standard Model and so also the β-functions entering the renormalization group equations (RGE) are different. In the MSSM, at $Q \sim 10^{16}$ GeV, the three couplings seem to converge to the same value [139–142]. Thus, Q can be meant as a Grand Unified Theory (GUT) scale at which the couplings unify, and, in general, parameters of the Lagrangian in eq. (5.5) might show universal properties. However, in order to perform calculations for collider physics, it is necessary to run the soft breaking parameters from the scale Q to the TeV scale. Consequently, even separately setting the m_i, a_i and M_i parameters to the same value at the GUT scale, a non degenerate mass spectrum emerges after the RGE running. In the second approach, provided that m_{soft} is not too large, the different soft breaking parameters can be set to any value that is not in conflict with the observed phenomenology.

We now examine the mass spectrum of the new particles predicted by the MSSM. First, we analyze the Higgs sector. The scalar potential responsible for EWSB in $\mathcal{L}_{\text{MSSM}}$ is

$$\begin{aligned} V \;=\; & (|\mu|^2 + m_{H_u}^2)(|H_u^0|^2 + |H_u^+|^2) + (|\mu|^2 + m_{H_d}^2)(|H_d^0|^2 + |H_d^-|^2) \\ & + [b\,(H_u^+ H_d^- - H_u^0 H_d^0) + \text{c.c.}] \\ & + \frac{1}{8}(g_W^2 + g_W'^2)(|H_u^0|^2 + |H_u^+|^2 - |H_d^0|^2 - |H_d^-|^2)^2 \\ & + \frac{1}{2} g_W^2 |H_u^+ H_d^{0*} + H_u^0 H_d^{-*}|^2 . \end{aligned} \tag{5.6}$$

The terms proportional to $|\mu|^2$ and to the electroweak couplings g_W and g'_W belong to $\mathcal{L}_{\text{SUSY}}$, the terms proportional to b, $m_{H_u}^2$ and $m_{H_d}^2$ belong to $\mathcal{L}_{\text{soft}}$. Since the quartic terms are proportional to the squared gauge couplings, in the MSSM the Higgs potential is bounded from below and the Higgs vacuum is stable. Exploiting gauge invariance, it can be proved that the VEV is determined by the conditions $\langle H_u^+ \rangle = \langle H_d^+ \rangle = 0$ and $\langle H_u^0 \rangle := v_u$ and $\langle H_d^0 \rangle := v_d$, where v_u and v_d are real values. The two VEVs are conventionally indicated by $\tan(\beta) = v_u/v_d$ and $v^2 = v_u^2 + v_d^2$, which is related to m_Z and m_W via the Standard Model relations in eq. (2.13).

In the MSSM the two complex Higgs doublets have eight degrees of freedom. EWSB yields five mass eigenstates: two CP-even neutral scalars h^0, H^0, one CP-odd neutral pseudoscalar A^0, and the charged H^+ with its conjugate H^-. The remaining three degrees of freedom are the Goldstone bosons $G^\pm, G^0$. The masses of the five physical mass eigenstates have at tree level the following values,

$$m_{A^0}^2 \;=\; 2b/\sin(2\beta) \;=\; 2|\mu|^2 + m_{H_u}^2 + m_{H_d}^2 \,, \tag{5.7}$$

$$m^2_{h^0,H^0} = \frac{1}{2}\left(m^2_{A^0} + m^2_Z \mp \sqrt{(m^2_{A^0} - m^2_Z)^2 + 4m^2_Z m^2_{A^0}\sin^2(2\beta)}\right), \tag{5.8}$$

$$m^2_{H^\pm} = m^2_{A^0} + m^2_W. \tag{5.9}$$

According to eq. (5.8) m_{h^0} is restricted to $m_{h^0} < m_Z\cos(2\beta)$, conversely the masses of H^0, A^0 and $H^\pm$ do not have an upper bound. This condition for m_{h^0} would imply that the MSSM could have already been ruled out by LEP bounds. However, relation (5.8) receives large corrections from loop effects, which substantially increase this upper bound ($m_{h^0} < 135$ GeV).[2] Thus, the Higgs discovery at the LHC is consistent with the prediction of m_{h^0} in the MSSM.

Second, the neutral fermionic superpartners of the neutral components of the two Higgs doublets, the Higgsinos $\tilde{H}^0_u$ and $\tilde{H}^0_d$, are not mass eigenstates and they mix with the neutral gauginos $\tilde{B}$ and $\tilde{W}^0$. The mass matrix $(m_\psi)_{ij}$ in the basis $\psi_i = (\tilde{B}, \tilde{W}^0, \tilde{H}^0_u, \tilde{H}^0_d)$ can be diagonalized,

$$(m_{\tilde{\chi}^0})_{ij} = N^*_{ik}(m_\psi)_{kl}N^{-1}_{lj}, \tag{5.10}$$

via an unitary matrix N_{ij}. The mass eigenstates $N_{ij}\psi_j = (\tilde{\chi}^0_1, \tilde{\chi}^0_2, \tilde{\chi}^0_3, \tilde{\chi}^0_4)$ are called neutralinos and are conventionally ordered starting from the lightest to the heaviest one. In the limit $m_Z \ll |\mu \pm M_1|, |\mu \pm M_2|$, the lightest neutralino is bino-like $\tilde{\chi}^0_1 \sim \tilde{B}$; analogously, the second lightest neutralino is wino-like $\tilde{\chi}^0_2 \sim \tilde{W}^0$ and $\tilde{\chi}^0_3$ and $\tilde{\chi}^0_4$ originate mostly from mixing of Higgsinos only.

Also the remaining charged electroweak gauginos, the winos $\tilde{W}^+$ and $\tilde{W}^-$, are not mass eigenstates. As in the neutral case, they respectively mix with the charged Higgsinos $\tilde{H}^+_u$ and $\tilde{H}^-_d$, yielding the mass eigenstates $\tilde{\chi}^\pm_1$ and $\tilde{\chi}^\pm_2$, called charginos. It is worth to note that the mixing matrices for positively (V_{ij}) and negatively (U_{ij}) charged charginos are different:

$$\begin{pmatrix}\tilde{\chi}^+_1\\ \tilde{\chi}^+_2\end{pmatrix} = \boldsymbol{V}\begin{pmatrix}\tilde{W}^+\\ \tilde{H}^+_u\end{pmatrix}, \qquad \begin{pmatrix}\tilde{\chi}^-_1\\ \tilde{\chi}^-_2\end{pmatrix} = \boldsymbol{U}\begin{pmatrix}\tilde{W}^-\\ \tilde{H}^-_d\end{pmatrix}. \tag{5.11}$$

The QCD gaugino, the gluino $\tilde{g}$, is the only colored octet fermion, hence it is a mass eigenstate and its mass is given by $m_{\tilde{g}} = M_3$

Third, assuming diagonal $\boldsymbol{m^2_i}$ and $\boldsymbol{a_i}$ matrices, sfermion mass eigenstates originate from mixings of same-flavor left- and right-handed sfermions. The tree-level mass

[2] This bound is obtained assuming large masses for the remaining Higgs fields and masses below 2 TeV for sparticles entering in loop corrections. Adding further scalars and relaxing the bounds on the masses, the upper bound for m_{h^0} can be increased to $m_{h^0} < 150$ GeV. See [137] and references therein for more details.

matrix $\boldsymbol{M}^{\boldsymbol{2}}_{\boldsymbol{u_i}}$ for the left- and right-handed squarks $(\tilde{u}_{iL}, \tilde{u}_{iR})$ of an up-type flavor u_i is

$$\boldsymbol{M}^{\boldsymbol{2}}_{\boldsymbol{u_i}} = \begin{pmatrix} m_Q^2 + m_{u_i}^2 + \Delta_{\tilde{u}_L} & v\, y_{u_i}\,(A_u^* \sin(\beta) - \mu \cos(\beta)) \\ v\, y_{u_i}\,(A_u \sin(\beta) - \mu^* \cos(\beta)) & m_{\tilde{u}_i}^2 + \Delta_{\tilde{u}_R} \end{pmatrix}, \tag{5.12}$$

whereas the tree-level mass matrix $\boldsymbol{M}^{\boldsymbol{2}}_{\boldsymbol{d_i}}$ for the left- and right-handed squark $(\tilde{d}_{iL}, \tilde{d}_{iR})$ of a down-type flavor d_i is

$$\boldsymbol{M}^{\boldsymbol{2}}_{\boldsymbol{d_i}} = \begin{pmatrix} m_Q^2 + m_{d_i}^2 + \Delta_{\tilde{d}_L} & v\, y_{d_i}\,(A_d^* \cos(\beta) - \mu \sin(\beta)) \\ v\, y_{d_i}\,(A_d \cos(\beta) - \mu^* \sin(\beta)) & m_{\tilde{d}_i}^2 + \Delta_{\tilde{d}_R} \end{pmatrix}, \tag{5.13}$$

and the mass matrices for sleptons $\boldsymbol{M}^{\boldsymbol{2}}_{\boldsymbol{l_i}}$ are defined analogously to $\boldsymbol{M}^{\boldsymbol{2}}_{\boldsymbol{d_i}}$ in eq. (5.13). In eq. (5.12) and eq. (5.13), m_{u_i} and m_{d_i} are the masses of the superpartner quarks and $m_{\tilde{u}_i}$ and $m_{\tilde{d}_i}$ are the supersymmetry breaking mass terms for right-handed squarks. The term $\Delta\phi$, defined as $\Delta\phi = (T_\phi^3 - Q_\phi s_W^2)\cos(2\beta) m_Z^2$ for every sfermion ϕ, originates, after EWSB, from interactions between sfermions and neutral Higgs scalars.

The off-diagonal terms in the sfermion mass matrices $\boldsymbol{M}^{\boldsymbol{2}}_{\boldsymbol{i}}$ are proportional to the Yukawa couplings and thus to the masses of the superpartner quarks. Consequently, the mixings in the light-flavor generations are suppressed and, typically, the left- and right-handed squarks can be considered as mass eigenstates. Conversely, in the third generation the mixing can be sizable, especially between $\tilde{t}_L$ and $\tilde{t}_R$. Thus, the mass eigenstates $(\tilde{t}_1, \tilde{t}_2)$, $(\tilde{b}_1, \tilde{b}_2)$ and $(\tilde{\tau}_1, \tilde{\tau}_2)$ are superpositions of left and right squarks.

In general, the hierarchy in the mass spectrum of the MSSM is not fixed. However, with viable supersymmetry breaking mechanisms, as, e.g., minimal supergravity or gauge mediated models, some general relations can be identified in the mass spectrum. The gluino is expected to be heavier than the lightest neutralinos and charginos, moreover the lightest neutralino[3] is typically the LSP. The gluino mass and the squark masses of the first two generations are usually of the same order; left-handed squarks are, as in the case of the sleptons, heavier than right-handed squarks.

In particular, every sfermion presents a different RGE for its mass. Squark masses, in contrast to slepton masses, are influenced by QCD effects in the running. In addition, the electroweak contribution to the RGEs is different for every sfermion. Only left-handed sfermions interact with W bosons and winos and also interactions are, e.g., different for up-type and down-type squarks. Moreover, the weak hypercharge is obviously different for every sfermion. Except for Higgs and Higgsino (negligible) corrections, proportional to the very small masses of the superpartner quarks, the RGEs for the mass of a squark in the first family and for the mass of its counterpart in the

[3]Promoting supersymmetry from a global to a local symmetry, also the graviton superpartner, the spin 3/2 gravitino $\tilde{G}$, is present and couples via gravitational interaction to another particle and its superpartner. The gravitino can be the LSP and, e.g., the lightest neutralino can decay into a photon and a gravitino.

second family are the same. Thus, even setting at the GUT scale all the masses of the scalars to the same value, 7 almost degenerate pairs of mass eigenstates are present in the first two families: $(\tilde{u}_L, \tilde{c}_L)$, $(\tilde{u}_R, \tilde{c}_R)$, $(\tilde{d}_L, \tilde{s}_L)$, $(\tilde{d}_R, \tilde{s}_R)$, $(\tilde{e}_L, \tilde{\mu}_L)$, $(\tilde{e}_R, \tilde{\mu}_R)$, $(\tilde{\nu}_e, \tilde{\nu}_\mu)$. In the third family, Higgs and Higgsino interactions are not negligible and, as said before, introduce non-diagonal mass terms for squarks with the same flavor and different chirality. Due to the mixing, the masses of the third-generation sfermions are in general different, and $\tilde{t}_1$ (or $\tilde{b}_1$) and $\tilde{\tau}_1$ are respectively expected to be the lightest squark and the lightest slepton. Last but not least, the lightest Higgs mass m_{h^0}, as previously mentioned, should be lighter than 135 GeV and can be much lighter than the other Higgs mass eigenstates.

5.3 Colored sparticles at the LHC

The search for supersymmetry at the TeV scale is one of the priorities in the current and future analyses of the ATLAS and CMS experiments, at the LHC. The luminosity and the total energy, higher than in all the previous colliders, should allow, after the 14 TeV run, to check if supersymmetry is realized in nature and broken at the TeV scale. With high luminosity, it is possible to verify if there are deviations between predictions from precise calculations for SM processes and the correspondent experimental measurements. These possible deviations can be interpreted as effects of sparticles in the intermediate state or in loop corrections. On the other hand, the compatibility of measurements with SM predictions can be used to exclude regions in the parameter space of the MSSM.

If sparticles are light enough, the high energy at the LHC allows to directly produce them. However, until now, the analyses performed on the data collected during the 7 and 8 TeV runs have only led to the exclusion of large regions of the parameter space of the MSSM.

In this section, we discuss in 5.3.1 the experimental signatures, emerging from the production of a pair of sparticles, and the procedures used in the experimental analyses to isolate a possible signal from the SM background. Here, we focus on selected illustrative cases that are relevant also for the calculations discussed in chapter 6 and the results presented in chapter 7. In 5.3.2 we address the theoretical calculations in the literature, with a particular emphasize on the production and decays of colored sparticles.

5.3.1 Signatures, exclusion limits, parameter determination

As for the SM case, cross sections for the production of colored sparticles are, unsurprisingly, larger than cross sections for the production of uncolored sparticles. Unless colored sparticles are much heavier than the uncolored sparticles, processes involving QCD interactions are favored at hadron colliders, due to the large value of the strong

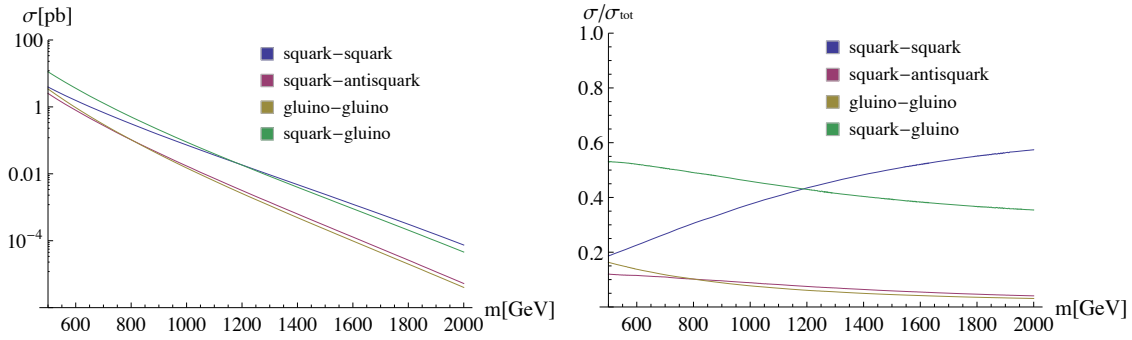

(a) (b)

Figure 5.1: Total cross sections σ (left plot) and relative contributions $\sigma/\sigma_{\rm tot}$ for the four colored production processes as function of the common mass m of squarks and gluinos ($m = m_{\tilde{q}} = m_{\tilde{g}}$), at the LHC with $\sqrt{s} = 8$. The cross sections are at NLO+NLL accuracy.

coupling. The possible processes with colored sparticle pairs in the final state are: (anti)squark–(anti)squark ($\tilde{q}\tilde{q}'$ or $\tilde{q}^*\tilde{q}^{*\prime}$), squark–antisquark ($\tilde{q}\tilde{q}'^*$), gluino–(anti)squark ($\tilde{g}\tilde{q}$ or $\tilde{g}\tilde{q}^*$) and gluino–gluino ($\tilde{g}\tilde{g}$) production.

In Figure 5.1(a) we show, for the LHC with $\sqrt{s} = 8$, the NLO+NLL production cross sections of the individual four colored production processes[4] as function of the common mass m for squark and gluino ($m = m_{\tilde{q}} = m_{\tilde{g}}$). In Figure 5.1(b) we plot the corresponding ratios of the the individual cross sections over their sum $\sigma_{\rm tot}$. These plots have been produced with the help of the numerical code *NLL-FAST* [143], using the grid obtained with the PDF set CTEQ6.6 [144].

One can see that the size of the cross sections and of the relative weights of the four processes strongly depend on the values of the masses of squarks and gluinos. The dependence of the ratios in Figure 5.1(b) on m is mainly due to the different PDFs for the possible initial states of the four processes: qq' for $\tilde{q}\tilde{q}'$ or $q^*q^{*\prime}$ for $\tilde{q}^*\tilde{q}^{*\prime}$ production, $q\bar{q}'$ for $\tilde{q}\tilde{q}'^*$ production and gg if $\tilde{q} = \tilde{q}'$, gq for $\tilde{g}\tilde{q}$ or $g\bar{q}$ for $\tilde{g}\tilde{q}^*$ production and gg or $q\bar{q}$ for $\tilde{g}\tilde{g}$ production. At small x (light sparticles), the gluon PDF has the largest values, whereas for large x (massive particles) PDFs for valence quark dominate.

The values of squark and gluino masses influence also the possible decay modes. If the gluino is heavier than squarks[5], $m_{\tilde{g}} > m_{\tilde{q}}$, the dominant gluino decay modes are into a quark q and a squark $\tilde{q}$ of the same flavor, $\tilde{g} \to q\tilde{q}$. Analogously, if squarks are heavier than the gluino, $m_{\tilde{q}} > m_{\tilde{g}}$, the dominant squark decay modes are $\tilde{q} \to q\tilde{g}$. Conversely, if $m_{\tilde{g}} > m_{\tilde{q}}$, the dominant squark decay channels are into neutralinos $\tilde{q} \to \tilde{\chi}_i^0 q$ and charginos $\tilde{q} \to \tilde{\chi}_i^{\pm} q'$. However, the branching ratios of these decay modes strongly

[4]Top squarks have not been included in the final states.

[5]Here, we assume for simplicity that all the squarks have the same masses.

depend on the particular parameter point. For instance, in the case mentioned in the previous section, where $\tilde{\chi}_1^0$ is bino-like and $\tilde{\chi}_2^0$ is wino-like, the decays of right-handed squarks into $\tilde{\chi}_2^0$ and the decays of left-handed squarks into $\tilde{\chi}_1^0$ are suppressed. Moreover, the branching ratios for heavy neutralinos and charginos are, in general, smaller due to the smaller available phase space in the decay. Finally, if $m_{\tilde{q}} > m_{\tilde{g}}$ no two-body decay is possible for the gluino. Thus, the gluino decays via an off-shell squark into a quark and a chargino or a neutralino.

Experimental signatures

Since squarks and gluinos produce quarks and gluons via their decays, jets are always present in the signatures emerging from production of colored sparticles at colliders. Also leptons, however, can appear in these signatures. A neutralino, e.g., can decay into a lepton and a slepton, $\tilde{\chi}_i^0 \to l\tilde{l}$, and the slepton can subsequently decay into a lighter neutralino and a lepton, $\tilde{l} \to \tilde{\chi}_j^0 l$, with $j < i$. But also, e.g., the neutralino can decay directly into a lighter neutralino and a Z boson or one of the Higgs bosons (h^0, H^0, A^0) subsequently decaying into a pair of leptons or quarks.

Moreover, assuming R-parity conservation, squark and gluino decays always produce an odd number of LSPs. In many viable scenarios, the LSP is the lightest neutralino, which, like neutrinos, is undetectable at colliders, since it interacts only via the weak force. However, at hadron colliders, it appears as a violation of the conservation of the total transverse momentum, when the kinematics of all the other particles in an event are taken into account.

The typical signature emerging from the production of a pair of colored sparticles thus can contain:

- missing transverse energy ($\not{E}_T$),
- jets,
- leptons.

In general, jets, leptons, and missing transverse energy represent the typical content of the signature emerging from any sparticle production process. Roughly speaking, the signatures emerging from the production of uncolored sparticles are expected to contain more leptons than jets. Conversely, colored sparticles yield always jets and possibly leptons. Additionally, also hard photons can appear in the signatures, e.g., via $\tilde{\chi}_2^0 \to \tilde{\chi}_1^0 \gamma$. In the MSSM, however, the rates and the distributions of the possible decay modes, especially for uncolored particles, strongly depend on the particular parameter point.

With $\tilde{\chi}_1^0$ as LSP, the missing transverse energy is present in any signature emerging from sparticle production processes and is exploited to separate the signal from the SM

background[6], since in the SM the missing transverse energy originates from neutrinos, which, in contrast to the lightest neutralino, are massless and are produced at hadron colliders in association with a lepton or another neutrino.

The cuts, used by ATLAS to isolate the signal of colored sparticle production from the SM background, typically require the presence of hard jets and a large missing transverse energy component that has to be not aligned to the hardest jet. In supersymmetry search analyses performed on signatures containing leptons, also additional cuts requiring the presence of hard leptons are imposed. These cuts define a signal region for cut-and-count searches, which consist in counting the number of events in the signal region and compare it with the corresponding SM prediction.

Special kinematical variables have also been introduced to define signal regions in cut-and-count searches. We show here, as illustration, a variable applied in some of the CMS analyses for signatures with jets, missing transverse energy and no lepton. It will be used also in the numerical evaluation presented in section 7.1.

At hadron colliders, the contribution from the SM to multijet production is large. In the analyses of full-hadronic signatures, CMS used the variable α_T for the definition of the signal region for production of colored sparticles [28, 145]. This variable is inspired by the analogue variable α discussed in [146], and it is defined, for a dijet system, according to [145, 147], as the ratio:

$$\alpha_T = \frac{E_T^{j_2}}{M_T}\,. \tag{5.14}$$

In eq. (5.14), $E_T^{j_2}$ is the transverse energy of the second hardest jet and M_T is the transverse mass of the two jets. The maximum possible value for α_T in a dijet system is 0.5. When the number of jets is larger than two, jets are recombined in a system of two pseudo-jets that are obtained choosing the combination of jets that minimizes the difference between the E_T of the two pseudo-jets[7]. With multijet signatures, α_T can possibly be larger than 0.5, due to missing transverse energy components arising, e.g., from experimental problems in the jet energy resolution. However, defining the signal region via $\alpha_T > 0.5$, most of the SM multijet contribution is excluded, whereas the jets from squark and gluino decays can easily pass this cut. Indeed the presence of missing transverse energy due to the lightest neutralinos allows jets to be in the $\alpha_T > 0.5$ region. Other variables, e.g. the razor [148–150] or M_{T2} [151–153], have also been used by CMS for the full-hadronic final states, but they are not used in the analyses presented in chapter 7.

[6]Signatures including leptons, quarks, and missing transverse energy can be produced via processes like, e.g., top quark pair production, single top quark production, $W+$jets, $Z+$jets and vector boson pair production (WW, WZ, ZZ).

[7]The E_T of each one of the two pseudo-jets is calculated as the scalar sum of the E_T of the jets forming the pseudo-jet.

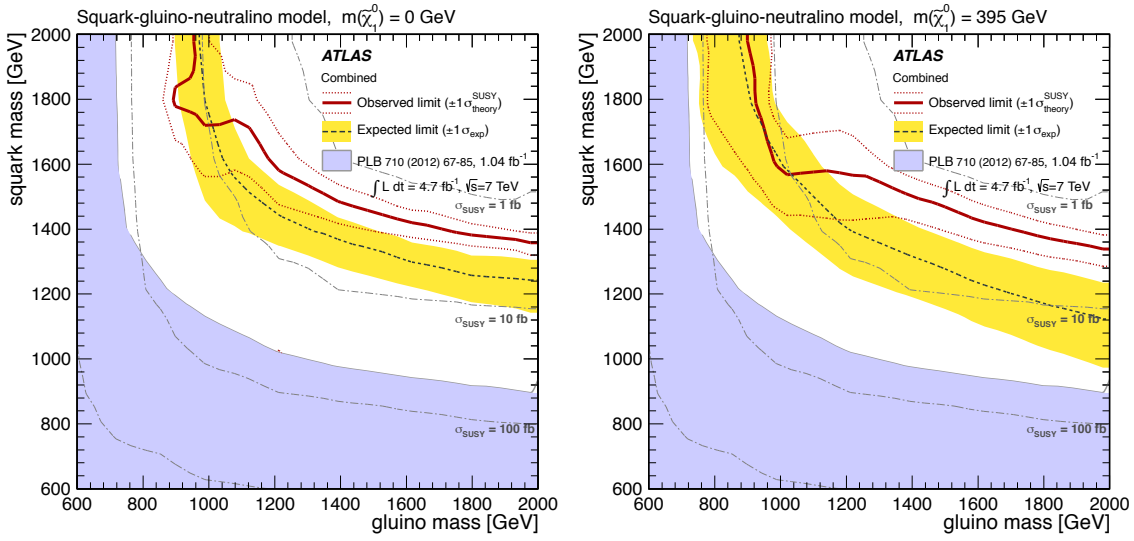

(a) (b)

Figure 5.2: Exclusion limits in the $m_{\tilde{g}} - m_{\tilde{q}}$ plane for $m_{\tilde{\chi}_1^0} = 0$ (left plot) and $m_{\tilde{\chi}_1^0} = 395$ GeV from ATLAS, at the LHC with $\sqrt{s} = 7$ TeV and an integrated luminosity of 4.7 fm^{-1}. Red lines (solid line: central value, dotted lines: $\pm 1\sigma$) indicate the observed limits, the yellow band indicates the expected limit. The violet area shows the exclusion limits from the previous analyses with an integrated luminosity of 1.04 fm^{-1}. Plots taken from [24].

Supersymmetry searches: exclusion limits

Until now no signal from supersymmetry has been detected at the LHC. Thus, analyses performed on the data collected during the 7 and 8 TeV runs have led to the exclusion of large regions of the parameter space. Often, these analyses are based on simplified models, in which two, or few more parameters, are free and the rest of the MSSM parameters are fixed. Thus, the exclusion limits always depend on the assumptions made for setting all the remaining parameters. Still, with reasonable assumptions, exclusion limits at the order of 1 TeV and even beyond have already been set for squarks and gluino masses.

For instance, a common squark mass and the gluino mass can be chosen as the only two free parameters. Also, squarks from the third generation can be decoupled and squarks of the first two generations can be assumed to decay directly into the lightest neutralino with branching ratio (BR) equal to 1. Figure 5.2(a) shows exclusion limits from ATLAS [24], based on these assumptions, in the $m_{\tilde{g}} - m_{\tilde{q}}$ plane, for $m_{\tilde{\chi}_1^0} = 0$. These analyses considered signatures containing only jets and missing transverse energy, and no hard lepton. Assuming squarks or gluinos lighter than 2 TeV, gluino masses below 860 GeV and squarks masses below 1410 GeV are excluded at 95% confidence level. However, such a simplified model might overestimate the signal and more realistic

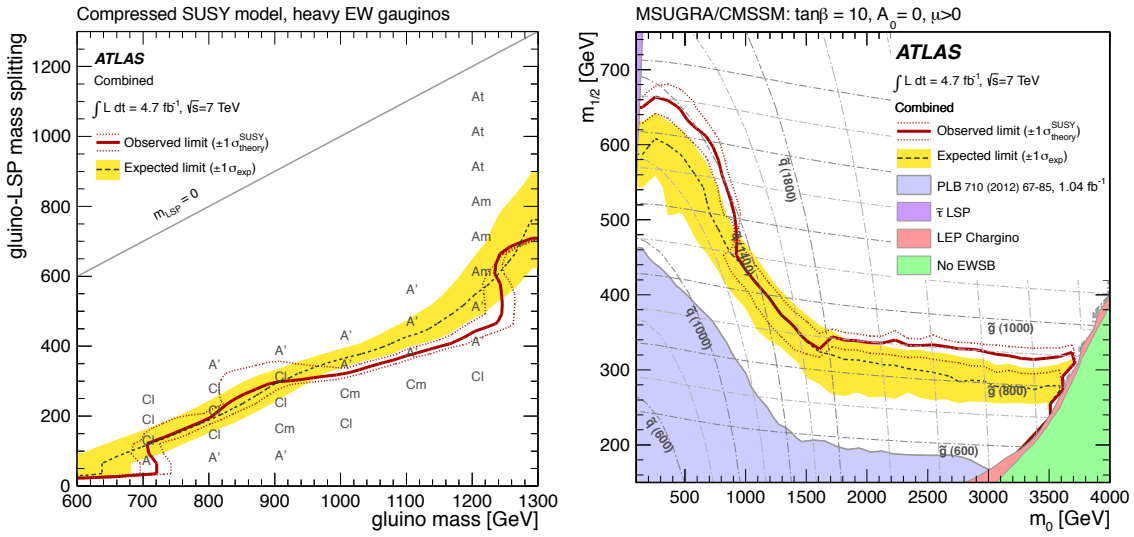

(a) (b)

Figure 5.3: Red lines (solid line: central value, dotted lines: $\pm 1\sigma$) indicate the observed limits from ATLAS at LHC with $\sqrt{s} = 7$ TeV and an integrated luminosity of 4.7 fm^{-1}, the yellow band indicates the expected limit. Left Plot: exclusion limits in the $\Delta(m_{\tilde{g}}, m_{\tilde{\chi}_1^0}) - m_{\tilde{g}}$ plane. The letters in the plot indicate the signal regions specified in [24]. Right Plot: exclusion limits in the $m_{1/2} - m_0$ plane. The violet area shows the exclusion limits from the previous analyses with an integrated luminosity of 1.04 fm^{-1}. Plots taken from [24].

bounds could be weaker. For instance, if $\tilde{\chi}_1^0$ is bino-like and $\tilde{\chi}_2^0$ is wino-like and heavier than the squarks, only a negligible fraction of left-handed squarks would decay directly into the LSP, in contrast to the assumptions of these analyses.

Figure 5.2(b) shows the same plot of Figure 5.2(a), but assuming $m_{\tilde{\chi}_1^0} = 395$ GeV. A comparison between Figure 5.2(a) and Figure 5.2(b) shows that exclusion limits depend moderately on the value of the mass of $\tilde{\chi}_1^0$. However, in both plots, the mass of $\tilde{\chi}_1^0$ is much smaller than the gluino and squark masses. In the limits $m_{\tilde{\chi}_1^0} \to m_{\tilde{g}}$ or $m_{\tilde{\chi}_1^0} \to m_{\tilde{q}}$, i.e. for the so called compressed spectra, the jets emerging from the decays $\tilde{q} \to q\tilde{\chi}_1^0$ and $\tilde{g} \to q\bar{q}\tilde{\chi}_1^0$ are soft and typically rejected by experimental cuts [154–156]. The plot in Figure 5.3(a) shows the exclusion limits in the $\Delta(m_{\tilde{g}}, m_{\tilde{\chi}_1^0}) - m_{\tilde{g}}$ plane, for the same simplified model used for the plots in Figure 5.2, but with $m_{\tilde{q}} = 0.96\, m_{\tilde{g}}$ and $m_{\tilde{\chi}_1^0}$ considered as free parameter. Exclusion limits on $m_{\tilde{g}}$ strongly depend on the mass difference $\Delta(m_{\tilde{g}}, m_{\tilde{\chi}_1^0})$ between the gluino and the $\tilde{\chi}_1^0$; they decrease for small values of $\Delta(m_{\tilde{g}}, m_{\tilde{\chi}_1^0})$ and they do not cover the region $\Delta(m_{\tilde{g}}, m_{\tilde{\chi}_1^0}) < 100$ GeV.

The results shown in Figure 5.2(a) have also been interpreted as bounds on the values of the soft supersymmetry breaking parameters of the Constrained MSSM (CMSSM). In the CMSSM all the soft supersymmetry breaking parameters depend

on five parameters defined at the GUT scale,

$$m_0\,, \qquad m_{1/2}\,, \qquad \tan(\beta)\,, \qquad A_0\,, \qquad \text{sign}(\mu)\,, \tag{5.15}$$

and the low energy MSSM spectrum is obtained via RGEs. Thus, due to the small number of independent parameters, this model has been extensively used in experimental analyses and also in theoretical and phenomenological studies.

Within the CMSSM, in eq. (5.5) the gaugino masses (M_1, M_2, M_3) are all set equal to $m_{1/2}$ and the scalar masses to m_0, i.e., $\boldsymbol{m_i^2} = m_0^2\mathbb{1}$ and $m_{H_u} = m_{H_d} = m_0$. Similarly, all the parameters A_i entering the trilinear couplings are set equal to A_0, i.e., $A_u = A_d = A_e = A_0$. The value of $|\mu|$, from the supersymmetric invariant part of the Lagrangian $\mathcal{L}_{\text{susy}}$, and b are specified by only $\tan(\beta)$ and the requirement of a correct VEV. Once the sign of μ is given, the value of μ, entering, e.g., in the neutralino diagonalizing matrix N is completely specified.

Specifically, the results showed in Figure 5.2(a) are translated in Figure 5.3(b) into the CMSSM $m_{1/2} - m_0$ plane with $\tan(\beta) = 0, A_0 = 0$ and $\mu > 0$. Similar results have also been presented by CMS in [27].

Searches for squark and gluino production have been performed also considering experimental signatures containing leptons. Furthermore, with signatures containing b-jets and/or top quarks, also exclusion limits for the third generation sfermions have been set (see [26, 157–164]). Also a possible signal from the production of sleptons or electroweak gauginos has been searched in leptonic signatures [165–171]. Again no evidence for these sparticles has been found and new bounds for their masses have been set.

Parameter determination

If a clear signal for physics beyond the Standard Model will be established, the character and parameters of the underlying model will have to be determined. Indeed, only a precise and non-ambiguous determination of TeV scale parameters allows for the identification of the underlying theory [172, 173] and, in case of SUSY, the investigation of different breaking scenarios. Moreover, different BSM models result in similar signatures at the LHC, so even the determination of the general class of models would be a major challenge [174]. In recent years various techniques tackling these challenges have been developed and many of those rely on the occurrence of cascade decay

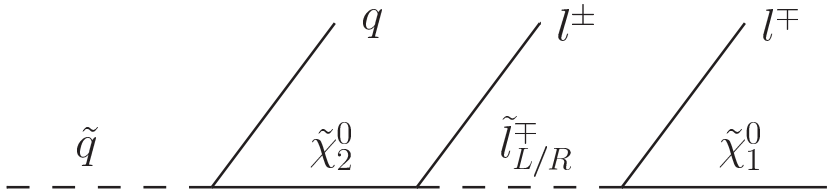

Figure 5.4: Illustration of the "golden decay chain".

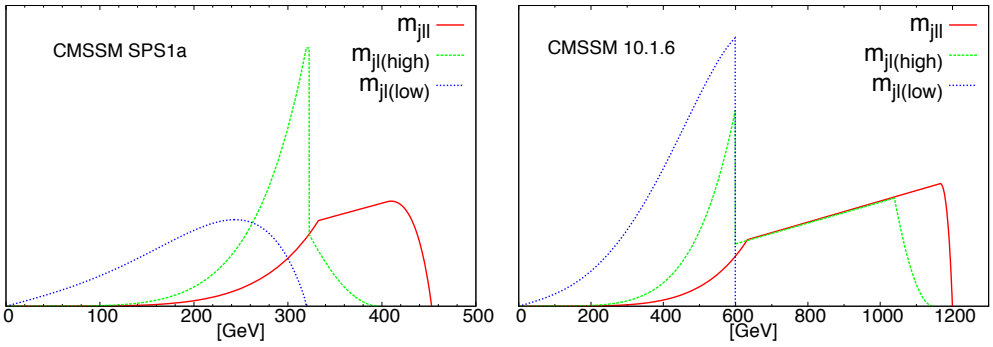

Figure 5.5: Shapes of the normalized m_{jll}, $m_{jl(\text{high})}$ and $m_{jl(\text{low})}$ distributions for SPS1a and 10.1.6 at LO.

chains. Several mass determination techniques have been proposed and are reviewed, e.g., in [175].

The "qll-chain" is one of the most interesting and promising decay chains for parameter determination and, for this reason, is also known as "golden decay chain". As shown in Figure 5.4, it corresponds to

$$\tilde{q}_L \to \quad q\ \tilde{\chi}_2^0 \quad \to q\ l^{\pm}\ \tilde{l}_{L/R}^{\mp} \to q\ l^{\pm}\ l^{\mp}\ \tilde{\chi}_1^0\,, \tag{5.16}$$

where a left-handed squark decays into a quark and a second lightest neutralino $\tilde{\chi}_2^0$, subsequently decaying, via an intermediate slepton, into a pair of opposite-sign same-flavor (OS-SF) leptons and a lightest neutralino $\tilde{\chi}_1^0$.

The "golden decay chain" (5.16) was introduced in [176, 177] and studied in many subsequent works [35, 178–194]. These analyses showed that measurements of resulting invariant-mass-distribution endpoints and shapes can be exploited to determine the masses of the intermediate SUSY particles. For instance, with the kinematic endpoints of the m_{jll}, $m_{jl(\text{high})}$ and $m_{jl(\text{low})}$ distributions[8], it is possible, in principle, to reconstruct the masses of the sparticles involved in the decay chain. However, the same kinematic endpoints can originate from very different mass values. The shapes of the distributions, calculated analytically at LO in [181], might be important to resolve these ambiguities in mass measurements from kinematic endpoints [195].

In Figure 5.5 we show invariant mass distributions in m_{jll}, $m_{jl(\text{high})}$ and $m_{jl(\text{low})}$, calculated analytically, for two CMSSM benchmark points[9]: SPS1a and CMSSM 10.1.6. As can be seen in Figure 5.5, such shapes are very sensitive to the model parameters. Mass values do not determine only the kinematic endpoints, but also the qualitative behavior of the distributions.

[8] m_{jll} is the invariant mass of the jet, i.e., at LO the quark, and the two leptons. $m_{jl(\text{high})}$ and $m_{jl(\text{low})}$ are respectively the higher and smaller invariant mass between one of the leptons and the jet.

[9] In section 7.2 these two benchmark points will be properly defined and numerical evaluations for these three distributions will be presented at NLO QCD.

Besides parameter determination, these invariant mass distributions, due to correlations between particles in the decay chain, can also be used for spin measurements of the intermediate sparticles [196]. Thus, since the $ql^+l^-\not{E}_T$ signature can emerge also in other BSM theories, these distributions can be used to determine the general model. For instance, a SUSY model can be discriminated from an Universal Extra Dimension (UED) model, see e.g., [197, 198] and [199–209].

5.3.2 Theoretical calculations: production and decay

As for SM processes, the calculation of higher-order effects is essential for obtaining reliable phenomenological predictions. In particular, for squark and gluino productions, precise theoretical calculations are necessary for the following reasons:

- correctly identifying the signal or setting accurate exclusion limits,
- refining experimental search strategies in problematic parameter regions,
- determining, in case of discovery, the parameters of the underlying model.

First LO cross section predictions, $\mathcal{O}(\alpha_s^2)$, for squark and gluino production processes were calculated many years ago [210–214] and a list of explicit formulae can be found in [126]. Also the calculation of NLO corrections in perturbative QCD has been performed quite some time ago [33, 215–217], assuming completely degenerate squark masses for the light-flavor generations. These corrections, can be very large; the ratios between LO and NLO cross sections, the so called K-factors, of the four different channels for the production of colored sparticles[10] are typically in the range between 1 and 2, i.e., NLO QCD corrections can even be as large as the LO cross section. Also, differential NLO corrections for the produced squarks and gluinos look rather flat in phase space. The calculation of [33] is implemented in the public computer code *Prospino 2* [218], which, however, can provide only total cross sections. Moreover, as already mentioned, the NLO corrections were calculated in [33] with the assumptions that squarks of all the different flavors and chiralities have the same mass. The first completely differential NLO calculation, treating independently the squarks with different flavors and chiralities, appeared for squark–squark production, as an intermediate step of the full calculation, in [32] and afterwards for all the four processes in [219].

NLO QCD corrections have to be included in any viable phenomenological study also because of the enormous scale uncertainties at LO. Including NLO corrections, the scale uncertainty on inclusive cross sections, obtained varying the factorization (μ_f) and renormalization (μ_r) scales between the half and the double of the average mass of the produced particles, is typically reduced to an order of $20\% - 30\%$. Besides

[10] From now on, we label $\tilde{q}\tilde{q}'$ and $\tilde{q}^*\tilde{q}^{*\prime}$ productions in common as "squark–squark production" and $\tilde{q}\tilde{g}$ and $\tilde{q}^*\tilde{g}$ as "squark–gluino production". The charge-conjugated process is always taken into account, if not specified otherwise.

the scale uncertainty, PDF uncertainties dominate the error of theoretical predictions for sparticle production processes. A discussion on the systematic treatment of PDFs for colored sparticle production can be found, e.g., in [220].

Recently, also results beyond NLO in QCD, based on resummation techniques, have been calculated [221–229]. These corrections increase the inclusive cross section by about $2\% - 10\%$ and further reduce the scale uncertainty. Furthermore, in [230, 231] production of sparticles was studied at the tree level matched to a parton shower simulation including additional hard jets. In these works large deviations from the LO prediction with or without showering were found particularly in the high-p^{T} tail for scenarios with the compressed spectra mentioned in the previous subsection. Very recently, the calculation of NLO QCD corrections to squark–squark production, treating independently flavor and chirality configurations, has been matched to parton shower emissions in an event generator [232], using the *POWHEG* method [233–235].

Moreover, also electroweak contributions can give sizable corrections. They were first calculated at $\mathcal{O}(\alpha^2)$ in [236,237] and at NLO, $\mathcal{O}(\alpha_s^2\alpha)$, in [238–244]. In detail, those corrections depend strongly on the model parameters and on flavors and chiralities of the squarks. Also, in contrast to NLO QCD corrections, they cannot be considered flat in phase space. For instance, corrections in p_T distributions for squark–squark production can vary from $\sim 25\%$ to $\sim -10\%$ over the p_T range up to 1.5 TeV [243]. However, sign and magnitude of the corrections change for different chirality and flavor configurations of the squarks.

Several calculations have also been performed to investigate the impact of higher-order corrections on integrated decay widths and branching ratios of colored sparticles. NLO QCD corrections to the decay of light-flavor squarks into neutralinos and charginos were first calculated in [34, 245] and to heavy-flavor squarks also in [34] and in [246]. Corrections to the total decay width of light squarks are in general moderate (below 10 %) and can change sign, depending on the involved mass ratios.

As an illustration, Figure 5.6 shows the percentage NLO QCD corrections to the decay width[11] for $\tilde{q} \to q\tilde{\chi}_i^0$ as function of $\kappa = m^2_{\tilde{\chi}_i^0}/m^2_{\tilde{q}}$. The three lines correspond to three different values of the ratio $\gamma = m^2_{\tilde{g}}/m^2_{\tilde{q}}$. Corrections, as said, are moderate, but, for very small mass splittings between the decaying squark and the neutralinos ($\kappa \sim 1$), these corrections increase significantly. In contrast, higher-order corrections to the decay of top-squarks are in general sizable [34]. Moreover, they depend strongly on the mixing in the heavy squark sector. Related to this mixing also decays into weak gauge bosons or Higgs bosons can become relevant [247, 248], receiving large higher-order corrections [249–251]. Decays of a gluino into a light squark and a quark at NLO QCD together with the decay of a light squark into a gluino and a quark have been calculated in [252]. Corresponding decays involving top squarks were presented

[11] The calculation of this quantity is performed in section 6.7.2 and, as explained there, it applies also to the decay of a squark into a chargino and a quark with different flavor.

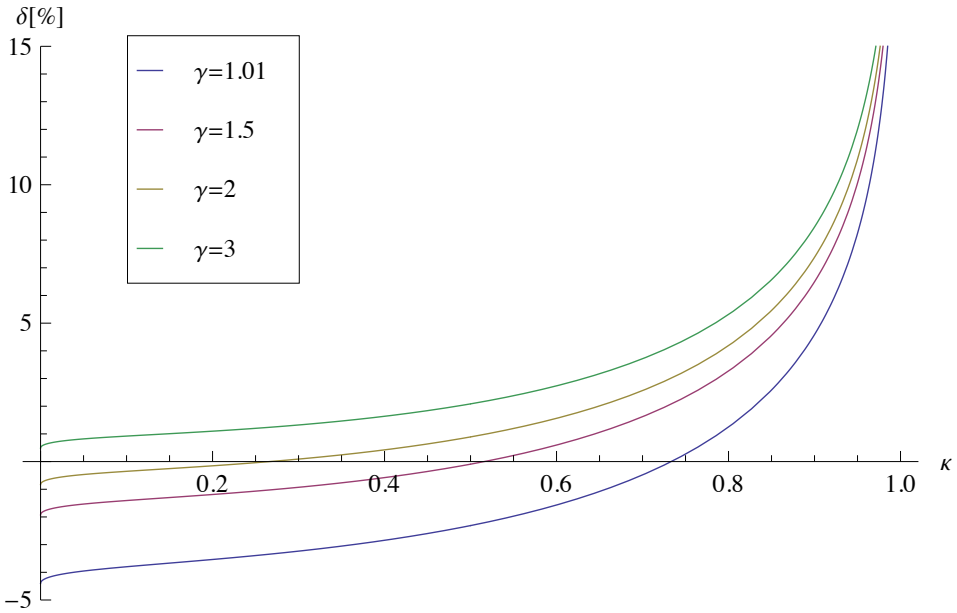

Figure 5.6: Percentage NLO QCD corrections to the decay width for $\tilde{q} \to q\tilde{\chi}_i^0$ as function of $\kappa = m^2_{\tilde{\chi}_i^0}/m^2_{\tilde{q}}$ for different values of $\gamma = m^2_{\tilde{g}}/m^2_{\tilde{q}}$.

in [253]. All these decays including their NLO QCD corrections have been implemented in the public code *SDECAY* [254] linked in the program package *SUSY-HIT* [255], which calculates the particle spectrum and the decay widths and branching ratios of supersymmetric particles and Higgs bosons.

Besides NLO QCD, also NLO electroweak corrections to squark decays into neutralinos and charginos have been investigated in the literature [256, 257] and can give sizable contributions. These corrections often compensate those from QCD, however, they depend strongly on the model parameters. Corresponding NLO electroweak corrections for third generation squark decays have been studied in [258–261]. Few studies were also performed investigating invariant mass distributions of SM particles emitted from cascade chains including various higher-order corrections [35, 262]. In [35] the "golden decay chain" was investigated at NLO QCD in the squark rest frame. There, real gluon radiation contributions are given in a fully analytical form and leading soft- and collinear gluon contributions are resummed. Furthermore, a study of predictions for the LHC, using LO production cross sections is presented. In their numerical analyses, the authors of [35] concentrate on the effect on distributions sensitive to spin correlations, as the ones mentioned in the previous subsection. Similar results are presented in section 7.2, where we (re)performed and extended the calculation of [35] to a more general case, as explained in chapter 6.

Chapter 6

Squark–squark production and decay: calculation

6.1 Motivations for the calculations

Most of the studies of higher-order calculations, mentioned in section 5.3.2, focussed on inclusive observables (total cross sections and total decay widths). Some of them analyzed differential distributions for the production processes, however, these distributions are in terms of sparticles, i.e., unstable particles that cannot be directly detected. Although these quantities are of fundamental interest, they are in practice not directly observable in high-energy collider experiments. On the one hand, with total cross sections or even cross sections differential with respect to sparticle momenta, it is not possible to take into account phase-space cuts that, in any experimental analysis, are applied to signatures emerging from sparticle decays. Thus, the identification of a signal or the extraction of exclusion limits based on these quantities could in principle miss important effects due to the dependence of higher-order corrections on experimental cuts. On the other hand, higher-order corrections could distort shapes and thus affect the accuracy of, e.g., endpoint determination techniques as those mentioned in 5.3.1 for the case of the "golden decay chain". Precise knowledge of distributions of the decay products could be necessary to determine the fundamental parameters of the model. Moreover, higher-order corrections could be important for the determination of the spin of the new particles, which helps to discriminate SUSY models from possible other extensions of the SM with similar signatures [174, 263].

Typically, in the experimental analyses of a certain signature, the simulation of the signal is performed according to the following general steps. Firstly, specific MSSM models for the interpretation of the possible signal are chosen, and the sparticle production processes contributing to the signature are selected. Secondly, these processes are simulated producing events via a LO parton shower event generator, as e.g. *Herwig* [264, 265] or *Pythia* [266, 267], that takes into account the radiation of partons at

LL accuracy and includes the decays of the produced sparticles. Thirdly, after simulating the hadronization of partons and the effects from the detector, a jet clustering algorithm is applied on the generated events. Finally, the experimental cuts that define the signal region are applied and the weights of the events are rescaled by a flat NLO (or NLO+NLL) QCD K-factor for the corresponding production processes, not including the decays.

This procedure is, at the moment, the best way to simulate the signal from colored sparticles, using public codes and including detector simulation. However, some of the steps of this procedure correspond to using approximations that might be, in general, not valid. We can summarize them in the following list,

- **NLO QCD corrections to the decays are neglected**:
  NLO corrections to the decays are not taken into account. However, for some parameter points or some phase-space regions, they can be non-negligible.

- **K-factors are considered flat in phase space**:
  Event weights are rescaled by K-factors, calculated for total cross sections of the production of sparticles without including decays. Although these K-factors are in general rather flat in the sparticle phase space, they cannot correctly take into account the possible effects from experimental cuts on particles emerging from sparticle decays.

- **The dependence of K-factors on squark flavors and chiralities is neglected**:
  Typically, the K-factors are calculated including all the possible chirality and flavor configurations of the squarks. However, different chirality and flavor configurations can have different K-factors. Moreover, they contribute in a very different way to a given signature, since the branching ratios of the different squark decay modes strongly depend on flavors and chiralities.

- **Sparticle decay products do not interact with partons in the initial state and with particles emerging from another sparticle decay**:
  Even including both NLO corrections to the production and to the decays, not all the possible NLO corrections to the full processes (production combined with decays) are considered. Additional corrections arise, e.g, from interactions between partons emerging from a sparticle decay and partons in the initial state or from another sparticle decay.

- **Effects from off-shell sparticles are neglected**:
  Although the ratio Γ/m is in general small for colored sparticles, there are parameter points with larger widths, yielding off-shell contributions that might be non-negligible.

It is also important to note that, multiplying weights of events from parton shower generators by NLO QCD K-factors is generally a procedure not completely consistent from

a theoretical point of view.[1] Furthermore, besides QCD corrections, also electroweak corrections can in principle add non-negligible contributions, especially applying cuts.

Ideally, given a final-state signature, precise and theoretically well defined predictions would be provided by a parton shower event generator, that includes all the contributing MSSM processes, at full NLO QCD accuracy properly matched to the parton shower with possibly also off-shell effects and electroweak corrections.

Also without the inclusion of electroweak corrections, the realization of such an ideal event generator is well beyond the status of the art and would involve several technical difficulties. Anyway, in order to investigate the size of the differences between the procedure used in the experimental analyses and the results that would be obtained using this ideal generator, different intermediate steps can be performed.

Here, we start the investigation of the size of these differences for one of the four processes yielding the production of colored sparticles, analyzing the contribution of squark–squark production to two different experimental signatures, obtained via two different configurations for the squarks decays. The choice of squark–squark production is also of practical importance. From recent searches at the LHC, mass bounds for squarks and gluinos are generically shifted to higher values and, for heavy squarks and gluinos, squark–squark production is, as can be seen in Figure 5.1, the dominant channel (see also [268]). Specifically we study:

- the contribution from $pp \to \tilde{q}\tilde{q}' \to q\tilde{\chi}_1^0 q'\tilde{\chi}_1^0$ to the experimental signature containing two jets and missing transverse energy: $2j + \not{E}_T(+X)$,
- the contribution from $pp \to \tilde{q}_L\tilde{q}'_R \to q\tilde{\chi}_1^0 q' l^\pm l^\mp \tilde{\chi}_1^0$ to the experimental signature containing two jets, two OS-SF leptons and missing transverse energy: $2j + l^+l^-(\text{OS-SF}) + \not{E}_T(+X)$.

The first case corresponds to squark–squark production with both the squarks decaying into the lightest neutralino, $\tilde{q} \to q\tilde{\chi}_1^0$. With this process we investigate observable differential distributions and the impact on cut-and-count searches performed at the LHC.

The second case corresponds to the production of a left-handed squark and a right-handed squark, where the right-handed squark decays as in the first case into the lightest neutralino, $\tilde{q} \to q\tilde{\chi}_1^0$, and the left-handed squark decays via the "golden decay chain", $\tilde{q}_L \to q\ \tilde{\chi}_2^0 \to q\ l^\pm\ \tilde{l}_{L/R}^\mp \to q\ l^\pm\ l^\mp\ \tilde{\chi}_1^0$. Combining the production of squark pairs and their subsequent decays in a consistent way at the NLO level, we present an analysis of higher-order corrections for the "golden decay chain". Thus, in this case,

[1] Parton showers take into account and resum corrections of order $\alpha_s^n L^n$, where L indicates the typical leading logarithms that involve the different scales of the process. The first of these logarithms, $\alpha_s L$, is already included in the NLO QCD corrections. Thus, multiplying the event weights by NLO QCD K-factors, a double-counting of the order $\alpha_s L$ contribution is introduced. NLO and LL corrections must be matched in order to achieve a theoretically well defined prediction.

besides analyzing inclusive event rates involved in the cut-and-count searches as those in e.g. [269, 270], we focus on effects, from NLO corrections and from the combination with the production process, on relevant distributions for mass determination.

In both cases the calculation is performed including, at fully differential level, the factorizable NLO QCD corrections to the full process (production combined with decays) and treating independently flavor and chirality configurations of the intermediate squarks. Thereby, the Narrow-Width Approximation (NWA) for the intermediate squarks is applied. These approximations are motivated and explained in sections 6.2, 6.3 and in appendix A. Recently, a very similar calculation was performed for the production of a pair of scalar BSM top quark partners, like e.g. the top squark, which produce with their decays a pair of top quarks and particles appearing as missing transverse energy [271].

In principle, our calculation does not depend on mass relations among the squarks and the gluino. However, in our numerical evaluation we only consider benchmark points where the mass $m_{\tilde{q}}$ of all light-flavor squarks is smaller than the gluino mass ($m_{\tilde{g}} > m_{\tilde{q}}$); otherwise the decay of a squark into a gluino and a quark would be dominant, leading to a different final-state signature.

We want to anticipate that, with our calculation, it will be possible to give a quantitative estimate of effects due to the approximations indicated by the first three points of the list on page 76. The possible effects due to the approximation indicated by the fourth and fifth point will not be analyzed quantitatively, however, theoretical problems connected to a well defined treatment of off-shell effects and effects from interactions between initial and final-state partons will be discussed in sections 6.2.2 and 6.4.3 and in appendix A.

6.2 Theoretical framework

In this section we introduce and explain the approximation used for the calculation of production and decays of squark–squark pairs. In the discussion we refer to the case in which squarks decay directly into the lightest neutralino, $pp \to \tilde{q}\tilde{q}' \to q\tilde{\chi}_1^0 q'\tilde{\chi}_1^0$.

Since we want to select the particles in the intermediate state, i.e., the resonating squarks, the complete NLO QCD corrections to the full process $pp \to \tilde{q}\tilde{q}' \to q\tilde{\chi}_1^0 q'\tilde{\chi}_1^0$, illustrated in Figure 6.1, can lead to to some ambiguities. Indeed $\mathcal{O}(\alpha_s)$ corrections involve also diagrams as the one in Figure 6.2. This diagram exhibit squarks that can be resonant, but it can be more naturally categorized as part of LO squark–gluino production, where the gluino decays into a quark and a squark subsequently decaying into a quark and a neutralino. Already without including the decays of the squarks, the calculation of NLO corrections to squark–squark production carries problems of double counting. Parts of NLO corrections to squark–squark production can be identified as LO of squark–gluino production, where the decay of the gluino is already included. This

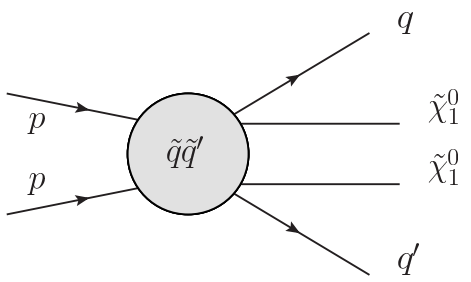

Figure 6.1: Structure of the complete NLO corrections to $pp \to \tilde{q}\tilde{q}' \to \tilde{\chi}_1^0 q \tilde{\chi}_1^0 q'$.

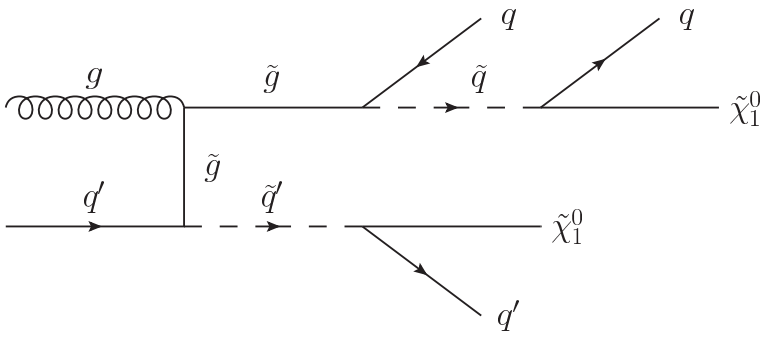

Figure 6.2: Real quark radiation diagram contributing to NLO QCD corrections.

problem is well known in the literature, but the standard solution [33], used to avoid this double counting problem, cannot be straightforwardly extended to the calculation including squark decays, especially with off-shell configurations of squarks.

Also, besides the double counting problem, the calculation of the complete NLO QCD corrections to a $2 \to 4$ process is in general technically highly involved. In view of the required level of accuracy of a few percent, it is sufficient to use an approximation that neglects $\mathcal{O}(\Gamma_{\tilde{q}}/m_{\tilde{q}})$ corrections from off-shell effects and contains the bulk of the NLO effects. Thus, as a first step towards the calculation of the complete NLO QCD corrections, we choose to consider the contributions from on-shell squarks only, neglecting $\mathcal{O}(\Gamma_{\tilde{q}}/m_{\tilde{q}})$ corrections from off-shell effects.

6.2.1 LO in Narrow-Width Approximation

At LO, the only partonic subprocess that contributes to a given intermediate configuration $\tilde{q}\tilde{q}'$ arises from a quark pair qq', where these quarks have the same flavors of the squarks. The corresponding diagram is depicted in Figure 6.3.[2] The on-shell configuration of the squarks can be obtained at LO applying the Narrow-Width Approximation (NWA): $\Gamma_{\tilde{q}}/m_{\tilde{q}} \to 0$. In this limit, the resonating contributions of the squarks in the

[2]If $\tilde{q}$ and $\tilde{q}'$ have the same flavor, also a u-channel diagram for $qq \to \tilde{q}\tilde{q}$ is possible. Moreover the quarks q can emerge from the first or second squark $\tilde{q}$.

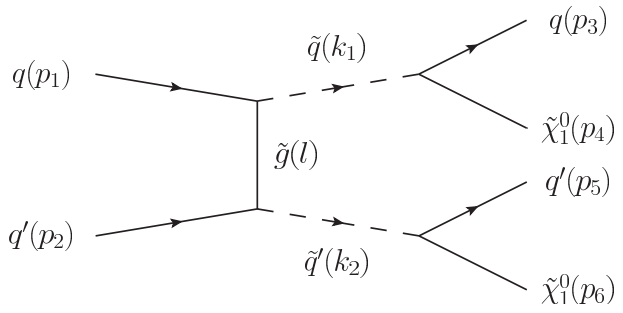

Figure 6.3: Born diagram for the process $qq' \to \tilde{q}\tilde{q}' \to q\tilde{\chi}_1^0 q'\tilde{\chi}_1^0$. The momenta of the particles are in brackets.

squared amplitude can be approximated via the replacement

$$\frac{1}{(p^2 - m_{\tilde{q}}^2)^2 + m_{\tilde{q}}^2 \Gamma_{\tilde{q}}^2} \;\to\; \frac{\pi}{m_{\tilde{q}} \Gamma_{\tilde{q}}} \delta(p^2 - m_{\tilde{q}}^2)\,, \tag{6.1}$$

for each squark with momentum p.

In NWA, the phase-space integration of the squared amplitude for the total cross section of the $2 \to 4$ processes factorizes into a production and a decay part. At the partonic level, since squarks are scalar particles, the LO cross section gets the following form,

$$\hat{\sigma}^{(0)}_{\text{NWA}}(qq' \to \tilde{q}\tilde{q}' \to q\tilde{\chi}_1^0 q'\tilde{\chi}_1^0) \;=\; \hat{\sigma}^{(0)}_{qq' \to \tilde{q}\tilde{q}'} \cdot \text{BR}^{(0)}_{\tilde{q} \to q\tilde{\chi}_1^0} \cdot \text{BR}^{(0)}_{\tilde{q}' \to q'\tilde{\chi}_1^0}\,, \tag{6.2}$$

with the LO partonic production cross section $\hat{\sigma}^{(0)}_{qq' \to \tilde{q}\tilde{q}'}$ and the LO branching ratios $\text{BR}^{(0)}$ for the squark decays into the lightest neutralino.

A direct generalization of eq. (6.2) yields the cross section in a fully differential form, which can be written at the hadronic level as follows,

$$d\sigma^{(0)}_{\text{NWA}}(pp \to \tilde{q}\tilde{q}' \to q\tilde{\chi}_1^0 q'\tilde{\chi}_1^0) \;=\; d\sigma^{(0)}_{pp \to \tilde{q}\tilde{q}'} \, \frac{1}{\Gamma^{(0)}_{\tilde{q}}} \, d\Gamma^{(0)}_{\tilde{q} \to q\tilde{\chi}_1^0} \, \frac{1}{\Gamma^{(0)}_{\tilde{q}'}} \, d\Gamma^{(0)}_{\tilde{q}' \to q'\tilde{\chi}_1^0}\,. \tag{6.3}$$

Therein, $\Gamma^{(0)}_{\tilde{q}}$ and $\Gamma^{(0)}_{\tilde{q}'}$ denote the LO total widths of the two squarks; $d\Gamma^{(0)}_{\tilde{q} \to q\tilde{\chi}_1^0}$ and $d\Gamma^{(0)}_{\tilde{q}' \to q'\tilde{\chi}_1^0}$ are the respective differential decay distributions boosted to the moving frames of $\tilde{q}$ and $\tilde{q}'$. The other basic ingredient, $d\sigma^{(0)}_{pp \to \tilde{q}\tilde{q}'}$, is the hadronic differential production cross section, expressed in terms of the partonic cross section $d\hat{\sigma}^{(0)}_{qq' \to \tilde{q}\tilde{q}'}$ as a convolution

$$d\sigma^{(0)}_{pp \to \tilde{q}\tilde{q}'} \;=\; \int_{\tau_0}^{1} d\tau \, \mathcal{L}_{qq'}(\tau) \, d\hat{\sigma}^{(0)}_{qq' \to \tilde{q}\tilde{q}'}(\tau)\,, \tag{6.4}$$

with the parton luminosity

$$\mathcal{L}_{qq'}(\tau) = \frac{1}{1+\delta_{qq'}} \int_\tau^1 \frac{dx}{x} \left[f_q(x,\mu_F)\, f_{q'}\Big(\frac{\tau}{x},\mu_F\Big) + (q \leftrightarrow q') \right] , \tag{6.5}$$

where $f_i(x,\mu_F)$ is the PDF, at the scale μ_F, of the quark i with momentum fraction x inside the proton. τ denotes the ratio between the squared center-of-mass energies of the partonic and hadronic processes, $\tau = s/S$, and the kinematical production threshold corresponds to $\tau_0 = (m_{\tilde{q}} + m_{\tilde{q}'})^2/S$.

6.2.2 NLO in Narrow-Width Approximation: Problems

One may expect to extend this treatment to the full set of NLO corrections. Unfortunately this is in general not possible. Even in a pole expansion, considering only diagrams with squarks that can be resonant, the NWA cannot always be applied.

The necessary condition for applying the NWA is the presence of Breit-Wigner distributions, which allow the replacement indicated in (6.1). The interference, e.g., of the two resonating diagrams in Figure 6.4 does not contain a Breit-Wigner distribution for the squark from which the quark with momentum p_3 and the $\tilde{\chi}_1^0$ with momentum p_4 emerge.[3]

Also, unless the momentum q of the gluon is equal to zero, this squark cannot be on-shell. For given external momenta, a squark on-shell in Figure 6.4(a) is off-shell in Figure 6.4(b) and vice versa. The same arguments also apply to the interference of the loop diagram in Figure 6.5 with the Born diagram of Figure 6.3.

Both the separately squared diagrams of Figure 6.4, however, contain a Breit-Wigner distribution for each of the two resonating squarks. Thus, in this case, the two squarks can be consistently set on-shell via (6.1), independently of the value of the momentum q of the gluon. In general, the on-shell condition can be set in all the real and loop corrections that can be illustrated as in Figure 6.6, i.e., as corrections to just the production or the decays. This kind of corrections, called factorizable corrections, contain Breit-Wigner distributions and can be calculated in NWA. The contributions where squarks cannot be set on-shell, as the interference of the diagrams in Figure 6.4 or of the loop diagrams in Figure 6.5 and the tree-level diagram in Figure 6.3, are called non-factorizable corrections and cannot be evaluated in NWA.

From the previous considerations, we expect that the leading contributions to the differential cross section for production of squark–squark pairs and subsequent decays

[3]The momentum k_1 of the squark in the upper part of the first diagram is equal to the sum of the momentum p_3 of the quark and the momentum p_4 of the $\tilde{\chi}_1^0$, emerging from its decay. Conversely, the momentum of the squark in the upper part of the second diagram is equal to $k_1 + q$, i.e., it includes also the momentum q of the gluon. Thus, since the momentum of this squark is different in the two diagrams, their interference cannot produce a Breit-Wigner distribution.

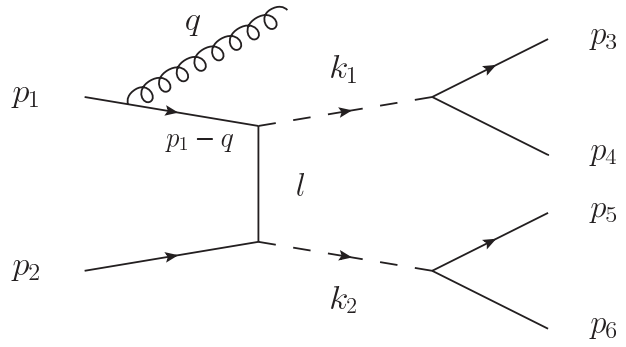

(a) Initial-state radiation.

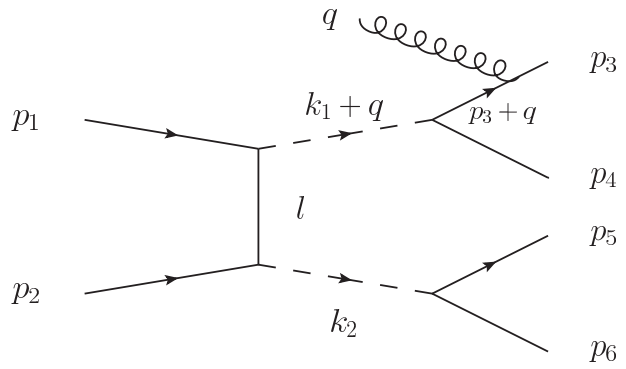

(b) Final-state radiation.

Figure 6.4: Initial- and final-state real gluon radiation (illustrative diagrams).

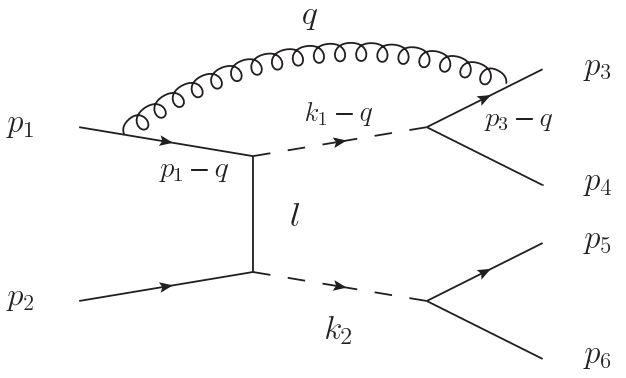

Figure 6.5: Loop diagram connecting quarks in the initial and final state.

can be written in the following form,

$$
\begin{aligned}
d\sigma^{(0+1)}(pp \to \tilde{q}\tilde{q}' \to q\tilde{\chi}_1^0 q'\tilde{\chi}_1^0(+X)) \;=\; & \frac{1}{\Gamma_{\tilde{q}}^{(0+1)}\,\Gamma_{\tilde{q}'}^{(0+1)}} \Big[d\sigma^{(0)}_{pp\to\tilde{q}\tilde{q}'}\, d\Gamma^{(0)}_{\tilde{q}\to q\tilde{\chi}_1^0}\, d\Gamma^{(0)}_{\tilde{q}'\to q'\tilde{\chi}_1^0} \\
& + d\sigma^{(0)}_{pp\to\tilde{q}\tilde{q}'}\, d\Gamma^{(1)}_{\tilde{q}\to q\tilde{\chi}_1^0}\, d\Gamma^{(0)}_{\tilde{q}'\to q'\tilde{\chi}_1^0} \;+\; d\sigma^{(0)}_{pp\to\tilde{q}\tilde{q}'}\, d\Gamma^{(0)}_{\tilde{q}\to q\tilde{\chi}_1^0}\, d\Gamma^{(1)}_{\tilde{q}'\to q'\tilde{\chi}_1^0} \\
& + d\sigma^{(1)}_{pp\to\tilde{q}\tilde{q}'(X)}\, d\Gamma^{(0)}_{\tilde{q}\to q\tilde{\chi}_1^0}\, d\Gamma^{(0)}_{\tilde{q}'\to q'\tilde{\chi}_1^0} \Big] + NF\,, \qquad (6.6)
\end{aligned}
$$

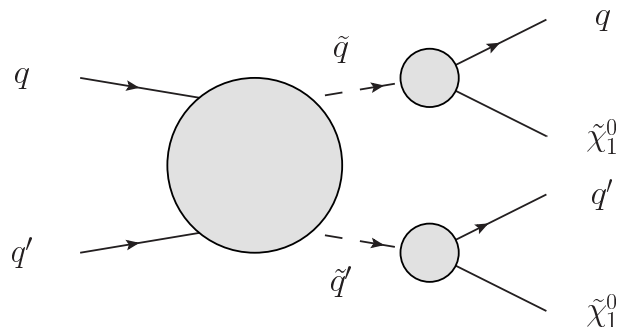

Figure 6.6: General structure of factorizable corrections.

where the term NF represents the non-factorizable corrections. All the other terms in eq. (6.6) consist in the factorizable corrections in NWA, which, as their name suggests, can be factorized into corrections to the production and corrections to the decay. The first line of eq. (6.6) is the LO contribution, already expressed in eq. (6.3), but with the NLO corrections to the total decay widths included in $\Gamma_{\tilde{q}}^{(0+1)}$ and $\Gamma_{\tilde{q}'}^{(0+1)}$. The second and third line involve the NLO corrections to the decay distributions $d\Gamma^{(1)}$ and the production cross section $d\sigma^{(1)}$, respectively.

In the explicit calculations and numerical results presented in this thesis, the contribution from NF has not been considered. This contribution is expected to be smaller than the contribution from factorizable corrections, since the non-factorizable corrections result from squarks that are in general off-shell. However, also in non-factorizable corrections squarks can go on shell in the soft gluon limit. The resulting contributions are $\mathcal{O}(\alpha_s)$ corrections to eq. (6.3), which do not vanish also in the limit $\Gamma_{\tilde{q}}/m_{\tilde{q}} \to 0$. However, they are substantially smaller than the factorizable corrections in NWA, since large cancellations between different classes of diagrams occur.

More details about the definition and the classification of factorizable and non-factorizable contributions can be found in appendix A. There, we also show that these two classes of contributions are independently gauge invariant. This allows us to omit non-factorizable corrections and include them later in a second step using an approximation different from the NWA. We have already evaluated non-factorizable corrections for particular mass configurations, $m_{\tilde{\chi}_1^0} \sim 0$, using the theoretical framework and the calculation techniques discussed in appendix A. With $m_{\tilde{\chi}_1^0} \sim 0$, non-factorizable corrections are, even at differential level, smaller than 1% of the LO cross section and thus negligible.

6.3 Calculation method

6.3.1 Process classes $pp \to \tilde{q}\tilde{q}' \to q\tilde{\chi}_1^0 q'\tilde{\chi}_1^0$

Since we are interested in the experimental signature $2j + \not{E}_T(+X)$, we include all contributions from light-flavor squarks. The squarks of the third generations are not included, because, via their decays, they produce bottom and top quarks, which can be distinguished from jets generated by the other colored particles. Hence, the cross section is given by the sum over all flavor and chirality configurations,

$$d\sigma = \sum_{\tilde{q}_{ia}\tilde{q}_{jb}} \Big[d\sigma(pp \to \tilde{q}_{ia}\tilde{q}_{jb} \to q_i\tilde{\chi}_1^0 q_j\tilde{\chi}_1^0(+X)) + d\sigma(pp \to \tilde{q}_{ia}^*\tilde{q}_{jb}^* \to \bar{q}_i\tilde{\chi}_1^0\bar{q}_j\tilde{\chi}_1^0(+X)) \Big], \tag{6.7}$$

which, as we said, we treat independently in the calculation. Indices i, j denote the flavors of the (s)quarks of the first two generations and a, b their chiralities.

At LO, as already said in section 6.2.1, the only partonic subprocess that contributes to a given intermediate configuration $\tilde{q}_{ia}\tilde{q}_{jb}$ (or $\tilde{q}_{ia}^*\tilde{q}_{jb}^*$) arises from quark and anti-quark pairs with the same flavor configurations of the squarks, i.e, $q_iq_j \to \tilde{q}_{ia}\tilde{q}_{jb} \to q_i\tilde{\chi}_1^0 q_j\tilde{\chi}_1^0$ (or $\bar{q}_i\bar{q}_j \to \tilde{q}_{ia}^*\tilde{q}_{jb}^* \to \bar{q}_i\tilde{\chi}_1^0\bar{q}_j\tilde{\chi}_1^0$). For simplifying the notation, we will write $qq' \to \tilde{q}\tilde{q}' \to q\tilde{\chi}_1^0 q'\tilde{\chi}_1^0$ whenever the specification of flavor and chiralities is not required[4]. Moreover, we will perform the discussion without the charge-conjugate subprocesses; they are, however, included in the final results. The differential cross sections entering eq. (6.7) correspond, at LO, to eq. (6.3).

At NLO, we include the factorizable corrections in NWA, so the differential cross sections entering eq. (6.7) can be written as,

$$\begin{aligned} d\sigma^{(0+1)}_{\text{NWA}}(pp \to \tilde{q}\tilde{q}' \to & q\tilde{\chi}_1^0 q'\tilde{\chi}_1^0(+X)) = \\ &= \frac{1}{\Gamma^{(0)}_{\tilde{q}}\,\Gamma^{(0)}_{\tilde{q}'}} \Big[d\sigma^{(0)}_{pp\to\tilde{q}\tilde{q}'}\, d\Gamma^{(0)}_{\tilde{q}\to q\tilde{\chi}_1^0}\, d\Gamma^{(0)}_{\tilde{q}'\to q'\tilde{\chi}_1^0} \left(1 - \frac{\Gamma^{(1)}_{\tilde{q}}}{\Gamma^{(0)}_{\tilde{q}}} - \frac{\Gamma^{(1)}_{\tilde{q}'}}{\Gamma^{(0)}_{\tilde{q}'}}\right) \\ &+ d\sigma^{(0)}_{pp\to\tilde{q}\tilde{q}'}\, d\Gamma^{(1)}_{\tilde{q}\to q\tilde{\chi}_1^0}\, d\Gamma^{(0)}_{\tilde{q}'\to q'\tilde{\chi}_1^0} + d\sigma^{(0)}_{pp\to\tilde{q}\tilde{q}'}\, d\Gamma^{(0)}_{\tilde{q}\to q\tilde{\chi}_1^0}\, d\Gamma^{(1)}_{\tilde{q}'\to q'\tilde{\chi}_1^0} \\ &+ d\sigma^{(1)}_{pp\to\tilde{q}\tilde{q}'(X)}\, d\Gamma^{(0)}_{\tilde{q}\to q\tilde{\chi}_1^0}\, d\Gamma^{(0)}_{\tilde{q}'\to q'\tilde{\chi}_1^0} \Big], \end{aligned} \tag{6.8}$$

which corresponds to the factorizable contributions of eq. (6.6), formally expanded in α_s.[5]

[4] In this notation $\tilde{q} = \tilde{q}'$ implies $q = q'$, but not vice versa.

[5] An analogous treatment has been used, e.g., for the calculation of NLO corrections of top pair production and decay [87, 88].

In order to evaluate the terms contained in eq. (6.8), we produce, for all different combinations of light flavors and chiralities, weighted events for squark–squark production and squark decays. Production events for $pp \to \tilde{q}\tilde{q}'(X)$ are generated in the laboratory frame. Decay events for $\tilde{q} \to q\tilde{\chi}_1^0(g)$ and $\tilde{q}' \to q'\tilde{\chi}_1^0(g)$ are generated in the respective squark rest frame. Finally, $pp \to qq'\tilde{\chi}_1^0\tilde{\chi}_1^0(+X)$ events are obtained by boosting the decay events from the squark rest frames, defined by the production events, into the laboratory frame. The weights of the $pp \to qq'\tilde{\chi}_1^0\tilde{\chi}_1^0(+X)$ events are obtained combining the different LO and NLO weights of production and decays according to eq. (6.8).

The calculations of the weights for production and decays, i.e., the LO and NLO calculation of production cross section ($d\sigma^{(0)}_{pp\to\tilde{q}\tilde{q}'}$, $d\sigma^{(1)}_{pp\to\tilde{q}\tilde{q}'}$), decay distributions ($d\Gamma^{(0)}_{\tilde{q}\to q\tilde{\chi}_0^0}$, $d\Gamma^{(0)}_{\tilde{q}\to q\tilde{\chi}_1^0}$) and total decay widths ($\Gamma^{(0)}_{\tilde{q}}, \Gamma^{(1)}_{\tilde{q}}$), entering eq. (6.8), are respectively discussed in sections 6.4, 6.5 and 6.7. After the description of these intermediate calculations, it will be clear that NLO corrections to the production or to the decay cannot be simulated with only one set of events. Real radiation and virtual corrections, e.g, have different final states and belong to different phase spaces. Thus, the boosting and combining procedure described before is technically more involved. Each of the subsets of events yielding the NLO corrections to the production or to the decays is respectively combined with events for the decays or for the production at LO.

6.3.2 Process classes $\mathbf{pp \to \tilde{q}_L\tilde{q}'_R \to q'\tilde{\chi}_1^0 q l^{\pm} l^{\mp}\tilde{\chi}_1^0}$

In our analysis we assume $\tilde{\chi}_1^0$ and $\tilde{\chi}_2^0$ to be mainly bino- and wino-like, as they appear in large parameter regions of models with unified gaugino masses at the GUT scale. In such scenarios the decays, $\tilde{q}_L \to \tilde{\chi}_1^0 q$ and $\tilde{q}_R \to \tilde{\chi}_2^0 q$, as said in section 5.3.1, are highly suppressed for squarks of the first and second generation. For this reason, we consider only intermediate chirality configurations $\tilde{q}_L\tilde{q}'_R$ ($\tilde{q}^*_L\tilde{q}'^*_R$), where the right-handed squark directly decays into the lightest neutralino $\tilde{\chi}_1^0$ and the left-handed one into a $\tilde{\chi}_2^0$ and subsequently into $l^+l^-\tilde{\chi}_1^0$ via an intermediate left- or right-handed slepton $\tilde{l}^{\pm}_{L/R}$.

At LO, the only partonic subprocess that contributes to a given intermediate $\tilde{q}_L\tilde{q}'_R$ ($\tilde{q}^*_L\tilde{q}'^*_R$) configuration arises, also in this case, from a quark (anti-quark) pair qq' ($\bar{q}\bar{q}'$) with the same flavor configuration of the squark pair. Since we are interested in the contribution to the experimental signature 2 jets + 2 leptons + missing transverse energy with the two leptons of opposite sign and same flavor, $2j + l^+l^-$(OS-SF) + $\not{E}_T(+X)$, we include all flavor configurations with (s)quarks of the first two generations. Also with this process, we will perform in general the discussion without referring to the charge-conjugate subprocesses ($\tilde{q}^*_L\tilde{q}'^*_R$); in the final results, however, they are included.

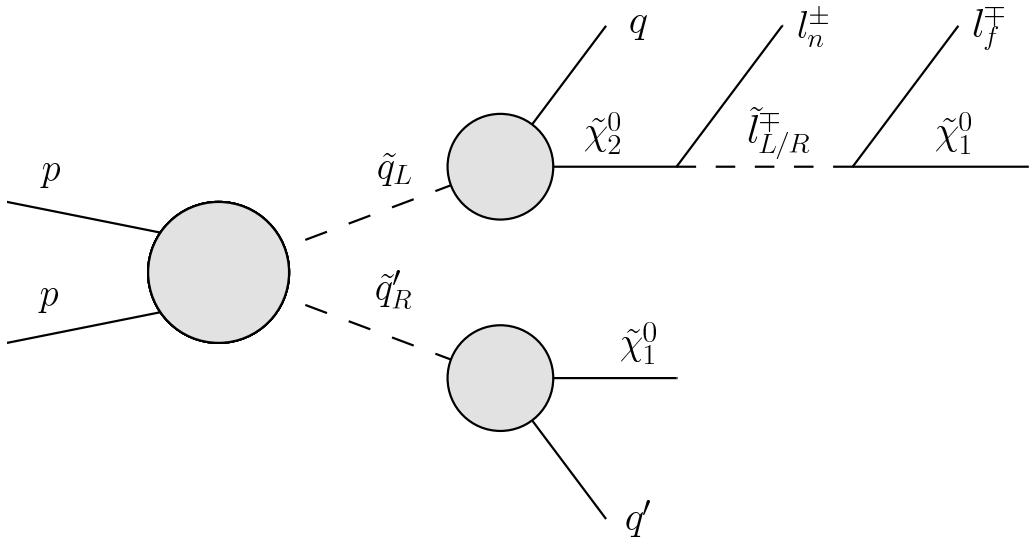

Figure 6.7: General structure of factorizable NLO QCD corrections to $pp \to \tilde{q}_L \tilde{q}'_R \to q' \tilde{\chi}_1^0 q l^{\pm} l^{\mp} \tilde{\chi}_1^0$.

Hence the cross section is given by

$$d\sigma = \sum_{i,j} \Big[d\sigma(pp \to \tilde{q}_{iL} \tilde{q}_{jR} \to q_j \tilde{\chi}_1^0 q_i l^{\pm} l^{\mp} \tilde{\chi}_1^0 (+X)) + d\sigma(pp \to \tilde{q}_{iL}^* \tilde{q}_{jR}^* \to \bar{q}_j \tilde{\chi}_1^0 \bar{q}_i l^{\pm} l^{\mp} \tilde{\chi}_1^0 (+X)) \Big] . \tag{6.9}$$

At LO, in NWA, the differential cross sections entering eq. (6.9) can be calculated, in analogy to eq. (6.3), as

$$d\sigma^{(0)}_{\text{NWA}}(pp \to \tilde{q}_L \tilde{q}'_R \to q \tilde{\chi}_1^0 q' l^+ l^- \tilde{\chi}_1^0 (+X)) = d\sigma^{(0)}_{pp \to \tilde{q}_L \tilde{q}'_R} \, \frac{1}{\Gamma^{(0)}_{\tilde{q}_L}} \, d\Gamma^{(0)}_{\tilde{q}_L \to q \tilde{\chi}_1^0 l^+ l^-} \, \frac{1}{\Gamma^{(0)}_{\tilde{q}'_R}} \, d\Gamma^{(0)}_{\tilde{q}' \to q' \tilde{\chi}_1^0} \, . \tag{6.10}$$

The quantity $d\Gamma^{(0)}_{\tilde{q}_L \to q \tilde{\chi}_1^0 l^+ l^-}$ indicates the LO decay distribution, at fully differential level, for the "golden decay chain". The remaining quantities have already been explained in the discussion for the $pp \to \tilde{q}\tilde{q}' \to q \tilde{\chi}_1^0 q' \tilde{\chi}_1^0$ process. Again, when it is not important to specify the flavor structure, we will indicate the squark pair as $q_L q'_R$.

Also at NLO, we use the same approximation adopted for the calculation of squark–squark production and direct decays into lightest neutralinos, i.e., we include the NLO factorizable corrections in NWA, illustrated for this process in Figure 6.7.

For any flavor configuration, the systematic expansion of the differential cross sec-

tion in the strong coupling α_s yields

$$
\begin{aligned}
&d\sigma^{(0+1)}_{\mathrm{NWA}}(pp \to \tilde{q}_L \tilde{q}'_R \to q\tilde{\chi}^0_1 q' l^+ l^- \tilde{\chi}^0_1 (+X)) = \frac{1}{\Gamma^{(0)}_{\tilde{q}_L}\,\Gamma^{(0)}_{\tilde{q}'_R}} \times \\
&\Bigg[d\sigma^{(0)}_{pp\to\tilde{q}_L\tilde{q}'_R}\, d\Gamma^{(0)}_{\tilde{q}_L\to q\tilde{\chi}^0_1 l^+ l^-}\, d\Gamma^{(0)}_{\tilde{q}'_R\to q'\tilde{\chi}^0_1} \left(1 - \frac{\Gamma^{(1)}_{\tilde{q}_L}}{\Gamma^{(0)}_{\tilde{q}_L}} - \frac{\Gamma^{(1)}_{\tilde{q}'_R}}{\Gamma^{(0)}_{\tilde{q}'_R}}\right) \\
&+ d\sigma^{(0)}_{pp\to\tilde{q}_L\tilde{q}'_R}\, d\Gamma^{(1)}_{\tilde{q}_L\to q\tilde{\chi}^0_1 l^+ l^-}\, d\Gamma^{(0)}_{\tilde{q}'_R\to q'\tilde{\chi}^0_1} + d\sigma^{(0)}_{pp\to\tilde{q}_L\tilde{q}'_R}\, d\Gamma^{(0)}_{\tilde{q}_L\to q\tilde{\chi}^0_1 l^+ l^-}\, d\Gamma^{(1)}_{\tilde{q}'_R\to q'\tilde{\chi}^0_1} \\
&+ d\sigma^{(1)}_{pp\to\tilde{q}_L\tilde{q}'_R}\, d\Gamma^{(0)}_{\tilde{q}_L\to q\tilde{\chi}^0_1 l^+ l^-}\, d\Gamma^{(0)}_{\tilde{q}'_R\to q'\tilde{\chi}^0_1} \Bigg] .
\end{aligned}
\tag{6.11}
$$

In order to evaluate the factorizable corrections we combine squark–squark production events and squark decay events. Moreover, due to chirality-dependent interactions, we treat the decay chain of an antisquark independently from the corresponding one from the squark decay. The quantities entering eq. (6.11) are the same as those in eq. (6.8), with the exception of $d\Gamma^{(0)}_{\tilde{q}_L\to q\tilde{\chi}^0_1 l^+ l^-}$ and $d\Gamma^{(1)}_{\tilde{q}_L\to q\tilde{\chi}^0_1 l^+ l^-}$, i.e., the LO decay distribution for the "golden decay chain" and the corresponding NLO corrections. The calculations of these two quantities are described in section 6.6.

6.4 Squark–squark production

6.4.1 Squark–squark production at LO

The structure of the hadronic differential cross section at LO has already been shown in eq. (6.4), so we need to specify only the expression of the possible partonic cross sections ($d\hat{\sigma}^{(0)}_{qq'\to\tilde{q}\tilde{q}'}$). In the calculation of the partonic cross sections, we treat the quarks as massless. On the one hand this choice is motivated by theoretical consistency in the convolution with PDFs. DGLAP equations and, in general, all the formalism used in the extraction of PDFs from experimental data, are based on the assumption of massless partons. On the other hand, in our calculation we consider only squarks of the first two generations, thus the corresponding quarks have masses that are negligible at the typical energy scale of these processes.

Amplitudes and cross sections for squark production depend on the flavors (indices i, j) and on the chiralities (indices a, b) of the squarks. If the two produced squarks are of the same flavor, the contributing Feynman diagrams correspond to t- and u-channel gluino exchange (Figure 6.8). For squarks of the same chirality, the partonic cross section reads as follows,

$$
\frac{d\hat{\sigma}^{(0)}_{q_i q_i\to\tilde{q}_{ia}\tilde{q}_{ia}}}{dt} = \frac{\pi\alpha_s^2}{9s^2}\, m_{\tilde{g}}^2 s \left(\frac{1}{(t-m_{\tilde{g}}^2)^2} + \frac{1}{(u-m_{\tilde{g}}^2)^2} + \frac{2/3}{(u-m_{\tilde{g}}^2)(t-m_{\tilde{g}}^2)}\right) , \tag{6.12}
$$

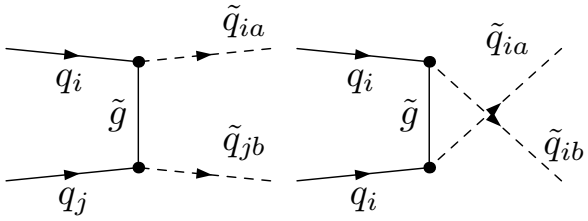

Figure 6.8: Tree-level Feynman diagrams for squark–squark production.

where s, t and u are the usual Mandelstam variables for $2 \to 2$ processes. For different chiralities, $m_q = 0$ implies vanishing interference between the t- and u-channel diagrams, yielding

$$\frac{d\hat{\sigma}^{(0)}_{q_i q_i \to \tilde{q}_{ia}\tilde{q}_{ib}}}{dt} = \frac{2\pi\alpha_s^2}{9s^2}\left(\frac{-st-(t-m^2_{\tilde{q}_{ia}})(t-m^2_{\tilde{q}_{ib}})}{(t-m^2_{\tilde{g}})^2} + \frac{-su-(u-m^2_{\tilde{q}_{ia}})(u-m^2_{\tilde{q}_{ib}})}{(u-m^2_{\tilde{g}})^2}\right). \tag{6.13}$$

If the two squarks are of different flavors, there is no u-channel exchange diagram; the partonic cross section for equal chiralities is hence given by

$$\frac{d\hat{\sigma}^{(0)}_{q_i q_j \to \tilde{q}_{ia}\tilde{q}_{ja}}}{dt} = \frac{2\pi\alpha_s^2}{9s^2}\,\frac{m^2_{\tilde{g}}s}{(t-m^2_{\tilde{g}})^2}\,, \tag{6.14}$$

and for different chiralities by

$$\frac{d\hat{\sigma}^{(0)}_{q_i q_j \to \tilde{q}_{ia}\tilde{q}_{jb}}}{dt} = \frac{2\pi\alpha_s^2}{9s^2}\,\frac{(-t+m^2_{\tilde{q}_{ia}})(t-m^2_{\tilde{q}_{ib}})-st}{(t-m^2_{\tilde{g}})^2}\,. \tag{6.15}$$

Besides the dominating QCD contributions, there are also tree-level electroweak production channels [236, 243] with chargino and neutralino exchange, which can contribute to the cross section at $\mathcal{O}(\alpha^2)$ and, interfering with the QCD amplitude, at $\mathcal{O}(\alpha\alpha_s)$. In principle these terms can be numerically of similar importance as the NLO QCD, $\mathcal{O}(\alpha_s^3)$, corrections we are investigating. For the present study, the electroweak contributions are neglected.

6.4.2 Squark–squark production at NLO

The NLO QCD corrections to squark–squark production, as mentioned in section 5.3.2, have been known for many years [33] and an efficient public code (*Prospino 2*) is available for the calculation of total cross sections at NLO. However, in order to study systematically the $2j + \not{E}_T(+X)$ signature emerging from production of squark–squark pairs and subsequent decays into the lightest neutralino, we need the fully differential cross section. To this purpose, we perform an independent (re)calculation of the NLO QCD corrections. Moreover, we treat the masses of $\tilde{q}_L$, $\tilde{q}_R$ and all chirality and flavor

configurations independently. In this way, we can investigate the quality of the approximation indicated by the third point of the list on page 76.

Besides UV divergences, which are eliminated via the renormalization of the bare quantities, NLO corrections involve infrared/soft and collinear divergences in the intermediate steps of the calculation. In QCD corrections, infrared divergences arise when gluons, in real emissions from external particles or in loop corrections, are soft. Collinear divergences arise when gluons, in real emission from external particles or in loop corrections, are collinear to the massless particle from which they originate.

First of all, in order to perform a calculation, divergences must be regularized. For example, for the regularization of soft divergences a fictitious gluon mass λ can be introduced. The purpose of the fictitious gluon mass can be understood analyzing the specific terms containing this kind of divergences. If $p = (E_p, \vec{p})$ is the four-momentum of an external particle, interacting with a gluon with momentum $k = (E_k, \vec{k})$, a propagator

$$\frac{1}{(p-k)^2 - m_p^2} = \frac{1}{\lambda^2 - 2pk} = \frac{1}{\lambda^2 - 2E_k E_p[1 - \beta_p \beta_k \cos(\theta_{pk})]} \tag{6.16}$$

appears in the amplitude, and, if $\lambda = 0$, it is divergent for $E_k \to 0$; a non vanishing value of λ regularizes this divergence. In eq. (6.16), θ_{pk} is the angle between $\vec{p}$ and $\vec{k}$, $\beta_p = \sqrt{1 - m_p^2/E_p^2}$ and $\beta_k = \sqrt{1 - \lambda^2/E_k^2}$.

Typically, in QCD calculations, soft divergences are regulated, as in the case of UV divergences, via dimensional regularization. Indeed, a mass term for a non-abelian gauge boson, in general, violates gauge invariance. However, our calculation does not involve any soft divergence due to non-Abelian vertices. Thus, these singularities can be safely regularized by a gluon mass (λ), as usually done in QED corrections, where infrared divergences from soft photons are regularized by a small λ photon mass.

The term in eq. (6.16) contains also collinear singularities. With $\lambda = 0$, if the particle with momentum p is massless, the propagator in eq. (6.16) diverges for $\theta_{pk} \to 0$, i.e., in the collinear configuration. This divergence does not appear if $m_p \neq 0$, so it can be regularized by a fictitious mass m_p, which is kept at zero everywhere else in the calculation. In our calculation these massless particles are the quarks in the initial states, and collinear divergences are regularized by the non-physical parameter m_q.

Soft and collinear divergences appear both in real gluon emissions and in loop corrections. The cancellation of these two kinds of singularities is obtained by summing the virtual loop contributions and the real gluon bremsstrahlung part and removing the remaining initial-state collinear divergences via mass factorization and the corresponding PDF subtraction terms.

Here, we use the phase-space slicing method for the evaluation of real gluon emission, as done in chapter 4. The phase space for the real emission of gluons is sliced into four regions via the phase-space parameters ΔE and $\Delta\theta$, which are assumed to be

much smaller than the other scales involved in the process. Given an external particle and naming θ the angle between it and the radiated gluon with energy E_g, the four regions correspond to:

- hard non-collinear gluons: $(E_g > \Delta E)$, $(\theta > \Delta\theta)$
- hard collinear gluons: $(E_g > \Delta E)$, $(\theta < \Delta\theta)$
- soft non-collinear gluons: $(E_g < \Delta E)$, $(\theta > \Delta\theta)$
- soft and collinear gluons: $(E_g < \Delta E)$, $(\theta < \Delta\theta)$

From now on in the text, if it is not explicitly specified, with the term hard gluons we will refer to the first region, with the term collinear gluons to the second region and with the term soft gluons to the third and fourth region combined. Only the emission of hard gluons is evaluated via numerical integration, the soft and collinear emission of gluons are calculated analytically. Indeed, the analytic integration is easier for soft and collinear gluon radiation, since the structure of the amplitudes simplifies in these regions, while the real radiation can be numerically integrated in the hard region without encountering instabilities. Moreover, producing events during the numerical integration of hard gluon emission, we can achieve a fully differential calculations. Gluons, soft or collinear to the proton–proton axis, are anyway experimentally undetectable, thus with analytic integration we do not loose predictive power.

The only drawback in this procedure is the introduction of two new unphysical parameters, in addition to the infrared and collinear regulators λ and m_q, i.e., the slicing parameters ΔE and $\Delta\theta$. The complete NLO corrections to the differential cross section can be written symbolically in the following way,

$$\begin{aligned} d\sigma^{(1)}_{pp\to\tilde{q}\tilde{q}'(X)} &= d\sigma^{\text{virtual+soft}}_{pp\to\tilde{q}\tilde{q}'(g)}(m_q,\Delta E) + d\sigma^{\text{coll}}_{pp\to\tilde{q}\tilde{q}'(g)}(m_q,\Delta E,\Delta\theta) + d\sigma^{\text{hard}}_{pp\to\tilde{q}\tilde{q}'g}(\Delta E,\Delta\theta) \\ &\quad + d\sigma^{\text{real-quark}}_{pp\to\tilde{q}\tilde{q}'\bar{q}^{(\prime)}} \,. \end{aligned} \tag{6.17}$$

With $d\sigma^{\text{virtual+soft}}_{pp\to\tilde{q}\tilde{q}'(g)}$ we denote the summed contributions from the renormalized virtual corrections and soft gluon emission; $d\sigma^{\text{coll}}_{pp\to\tilde{q}\tilde{q}'(g)}$ corresponds to the initial-state collinear gluon radiation including the proper subtraction term for the collinear divergences; $d\sigma^{\text{hard}}_{pp\to\tilde{q}\tilde{q}'g}$ denotes the remaining hard gluon emission outside the soft and collinear phase-space regions. Any term shows, in brackets, the slicing and regulator parameters on which it depends.

The term $d\sigma^{\text{real-quark}}_{pp\to\tilde{q}\tilde{q}'\bar{q}^{(\prime)}}$ is the contribution from real quark emission from additional quark–gluon initial states, contributing at NLO. It includes also the proper subtraction term for the collinear divergences. Indeed, as it will be explained in section 6.4.3, also an emission of a massless quark gives rise to collinear divergences that are absorbed in the PDFs. Thus, the intermediate steps of the calculation of $d\sigma^{\text{real-quark}}_{pp\to\tilde{q}\tilde{q}'\bar{q}^{(\prime)}}$ depend on unphysical parameters. However the entire term $d\sigma^{\text{real-quark}}_{pp\to\tilde{q}\tilde{q}'\bar{q}^{(\prime)}}$ in eq. (6.17) does not depend

on unphysical parameters and can be calculated independently from the remaining terms of eq. (6.17).

The calculation of $d\sigma^{\text{real-quark}}_{pp\to\tilde{q}\tilde{q}'\bar{q}^{(\prime)}}$ is explained in the separate section 6.4.3, because it involves contributions from squark–gluino production that have to be subtracted. There, we discuss different approaches to perform the subtraction, showing problems in defining, at NLO, the different channels of production and decays of colored sparticles.

Technically, the calculation of the loop corrections and real radiation contributions of eq. (6.17) is performed with the help of *FeynArts* [122] and *FormCalc* [123, 272]. Loop integrals are numerically evaluated with the library *LoopTools* [123]. Thereby, every flavor and chirality combination, $q_i q_j \to \tilde{q}_{ia}\tilde{q}_{jb}$, is independently evaluated.

Virtual corrections and real soft gluon radiation

In the term $d\sigma^{\text{virtual+soft}}_{pp\to\tilde{q}\tilde{q}'(g)}$ the virtual and soft contributions are summed at the parton level, according to

$$\begin{aligned} d\sigma^{\text{virtual+soft}}_{pp\to\tilde{q}\tilde{q}'(g)} &= \int_{\tau_0}^{1} d\tau\, \mathcal{L}_{qq'}(\tau)\, d\hat{\sigma}^{\text{virtual+soft}}_{qq'\to\tilde{q}\tilde{q}'(g)}(\tau)\,, \\ d\hat{\sigma}^{\text{virtual+soft}}_{qq'\to\tilde{q}\tilde{q}'(g)}(\tau) &= d\hat{\sigma}^{\text{virtual}}_{qq'\to\tilde{q}\tilde{q}'}(m_q,\lambda) + d\hat{\sigma}^{\text{soft}}_{qq'\to\tilde{q}\tilde{q}'(g)}(m_q,\lambda,\Delta E)\,, \end{aligned} \tag{6.18}$$

where $\mathcal{L}_{qq'}(\tau)$ has been defined in eq. (6.5). Both the virtual, $d\hat{\sigma}^{\text{virtual}}_{qq'\to\tilde{q}\tilde{q}'}$, and soft, $d\hat{\sigma}^{\text{soft}}_{qq'\to\tilde{q}\tilde{q}'(g)}$, contributions are infrared divergent and thus depend on λ. In their sum, $d\hat{\sigma}^{\text{virtual+soft}}_{qq'\to\tilde{q}\tilde{q}'(g)}$, the dependence on λ is analytically canceled.

The virtual contribution originates from the interference of tree-level diagrams of Figure 6.8 and loop and counterterm diagrams shown in appendix B. Here, we used for the calculation of the counterterms the results presented in [239]. In the following we discuss only the renormalization of the strong coupling, which deserves a particular attention. All the other mass and field renormalization constants are determined according to the on-shell scheme and are discussed in appendix C.

Since partonic cross sections are convoluted with PDFs, the renormalization of the QCD coupling constant has to be done in accordance with the scheme for α_s in the PDFs, i.e., the $\overline{\text{MS}}$ scheme with five flavors. As shown in [33], this corresponds to defining the g_s coupling renormalization constant δZ_{g_s} (see eq. (C.2)) as

$$\delta Z_{g_s} = -\frac{\alpha_s}{4\pi}\Big[\Delta\frac{\beta_0}{2} + \frac{1}{3}\log\frac{m_t^2}{\mu_R^2} + \log\frac{m_{\tilde{g}}^2}{\mu_R^2} + \frac{1}{12}\sum_{\tilde{q}}\log\frac{m_{\tilde{q}}^2}{\mu_R^2}\Big]\,, \tag{6.19}$$

where the UV divergences are included in $\Delta = 2/\epsilon - \gamma_E + \log(4\pi)$ and μ_R is the renormalization scale. The quantity $\beta_0 = 3$ is the leading term of the β function for

the QCD coupling in the MSSM, whereas the other terms in the r.h.s. of eq. (6.19) are added in order to remove from the running of $\alpha_s(\mu_R) = g_s^2(\mu_R)/(4\pi)$ the effects induced by the top quark, the squarks and the gluino.

Typically, the regularization of UV divergences in NLO corrections for MSSM processes are performed via dimensional reduction, which preserves supersymmetry also in d dimensions with $d \neq 4$. However, the $\overline{\text{MS}}$ scheme is based on the intermediate regularization of UV divergences in dimensional regularization, which, in contrast to dimensional reduction, violates supersymmetry in $d \neq 4$ dimension. Thus, it also breaks the supersymmetric Slavnov-Taylor identity that relates the qqg vertex function and the $q\tilde{q}\tilde{g}$ vertex function at one-loop order. This identity can be restored (see [33, 273]) by an extra finite shift of the $\hat{g}_s$ coupling in the $q\tilde{q}\tilde{g}$ vertex with respect to g_s in the qqg vertex,

$$\hat{g}_s = g_s(1 + \delta Z_{\hat{g}_s}), \qquad \delta Z_{\hat{g}_s} = \delta Z_{g_s} + \frac{\alpha_s}{3\pi}. \tag{6.20}$$

Thus, in our calculations we regularize UV divergences with dimensional regularization and we perform the shift indicated in eq. (6.20).

The second term $d\hat{\sigma}^{\text{soft}}_{qq'\to\tilde{q}\tilde{q}'(g)}$ in eq. (6.18) contains the contributions from real gluon emission integrated over the soft-gluon phase space with $E_g < \Delta E$. It is similar to the case of soft-photon emission [124, 274], yielding a multiplicative correction factor to the LO cross section. In the case of gluons, however, the color structures are different for emission from t and u channel diagrams and hence the various bremsstrahlung integrals enter the cross section with different weights. Accordingly, we decompose the partonic LO cross section for $qq' \to \tilde{q}\tilde{q}'$, in obvious notation, in the following way,

$$d\hat{\sigma}^{(0)}_{qq'\to\tilde{q}\tilde{q}'} = d\hat{\sigma}^{(tt)}_{\tilde{q}\tilde{q}'} + d\hat{\sigma}^{(ut)}_{\tilde{q}\tilde{q}'} + d\hat{\sigma}^{(uu)}_{\tilde{q}\tilde{q}'} = \left[C^{(tt)}_{\tilde{q}\tilde{q}'} + C^{(ut)}_{\tilde{q}\tilde{q}'} + C^{(uu)}_{\tilde{q}\tilde{q}'}\right] d\hat{\sigma}^{(0)}_{qq'\to\tilde{q}\tilde{q}'}, \tag{6.21}$$

where the coefficients $C^{(tt)}_{\tilde{q}\tilde{q}'}$, $C^{(ut)}_{\tilde{q}\tilde{q}'}$ and $C^{(uu)}_{\tilde{q}\tilde{q}'}$ for the individual channels can be easily read off from the LO cross sections in eqs. (6.12)–(6.15). Defining $\epsilon_i = 1$ for incoming and $\epsilon_i = -1$ for outgoing particles, the soft-gluon contribution at the partonic level can be written as follows, using the label assignment $\{q, q', \tilde{q}, \tilde{q}'\} \leftrightarrow \{1, 2, 3, 4\}$,

$$d\hat{\sigma}^{\text{soft}}_{qq'\to\tilde{q}\tilde{q}'(g)} = -\frac{\alpha_s}{2\pi}\Bigg\{\sum_{i,j=1;i\leq j}^{4} \epsilon_i\epsilon_j\, \mathcal{I}_{ij}\Bigg\} d\hat{\sigma}^{(0)}_{qq'\to\tilde{q}\tilde{q}'}. \tag{6.22}$$

The $\mathcal{I}_{ij}$ terms involve the bremsstrahlung integrals and the weight factors $C^{(tt)}_{\tilde{q}\tilde{q}'}$, $C^{(ut)}_{\tilde{q}\tilde{q}'}$ and $C^{(uu)}_{\tilde{q}\tilde{q}'}$ from (6.21) and phase-space integrals [124, 243]. Keeping a finite quark mass m_q only in the mass-singular terms, the following expressions $\mathcal{I}_{ij}$ for the production

process $qq' \to \tilde{q}\tilde{q}'$ are obtained:

for $i = \{1,2\}$: (6.23)

$$\mathcal{I}_{ii} = \frac{4}{3}\left[\ln\left(\frac{4(\Delta E)^2}{\lambda^2}\right) + \ln\left(\frac{m_i^2}{s_{12}}\right)\right],$$

for $i = \{3,4\}$: (6.24)

$$\mathcal{I}_{ii} = \frac{4}{3}\left[\ln\left(\frac{4(\Delta E)^2}{\lambda^2}\right) + \frac{1}{\beta_i}\ln\left(\frac{1-\beta_i}{1+\beta_i}\right)\right],$$

for $i = 1$ and $j = 2$: (6.25)

$$\mathcal{I}_{12} = \left(-\frac{1}{3}C^{(tt)}_{\tilde{q}\tilde{q}'} - \frac{1}{3}C^{(uu)}_{\tilde{q}\tilde{q}'} - \frac{5}{3}C^{(ut)}_{\tilde{q}\tilde{q}'}\right)\sum_{i=1,2}\left[\ln\left(\frac{s_{12}}{m_i^2}\right)\ln\left(\frac{4(\Delta E)^2}{\lambda^2}\right) - \frac{1}{2}\ln^2\left(\frac{s_{12}}{m_i^2}\right) - \frac{\pi^2}{3}\right],$$

for $i = 3$ and $j = 4$: (6.26)

$$\mathcal{I}_{34} = \left(-\frac{1}{3}C^{(tt)}_{\tilde{q}\tilde{q}'} - \frac{1}{3}C^{(uu)}_{\tilde{q}\tilde{q}'} - \frac{5}{3}C^{(ut)}_{\tilde{q}\tilde{q}'}\right)\frac{1}{v_{34}}\sum_{i=3,4}\Big[\ln\left(\frac{1+\beta_i}{1-\beta_i}\right)\ln\left(\frac{4(\Delta E)^2}{\lambda^2}\right) - 2\mathrm{Li}_2\left(\frac{2\beta_i}{1+\beta_i}\right) - \frac{1}{2}\ln^2\left(\frac{1-\beta_i}{1+\beta_i}\right)\Big],$$

for $i + j = 5$: (6.27)

$$\mathcal{I}_{ij} = \left(\frac{7}{6}C^{(tt)}_{\tilde{q}\tilde{q}'} - \frac{1}{6}C^{(uu)}_{\tilde{q}\tilde{q}'} - \frac{1}{6}C^{(ut)}_{\tilde{q}\tilde{q}'}\right)\Big[\ln\left(\frac{s_{ij}^2}{m_i^2 m_j^2}\right)\ln\left(\frac{4(\Delta E)^2}{\lambda^2}\right) - \frac{1}{2}\ln^2\left(\frac{s_{12}}{m_i^2}\right) - \frac{1}{2}\ln^2\left(\frac{1-\beta_j}{1+\beta_j}\right) - \frac{\pi^2}{3} - 2\mathrm{Li}_2\left(1 - \frac{2p_i^0 p_j^0}{s_{ij}}(1+\beta_j)\right) - 2\mathrm{Li}_2\left(1 - \frac{2p_i^0 p_j^0}{s_{ij}}(1-\beta_j)\right)\Big],$$

for $i + j = 4$ or $i + j = 6$: (6.28)

$$\mathcal{I}_{ij} = \left(-\frac{1}{6}C^{(tt)}_{\tilde{q}\tilde{q}'} + \frac{7}{6}C^{(uu)}_{\tilde{q}\tilde{q}'} - \frac{1}{6}C^{(ut)}_{\tilde{q}\tilde{q}'}\right)\Big[\ln\left(\frac{s_{ij}^2}{m_i^2 m_j^2}\right)\ln\left(\frac{4(\Delta E)^2}{\lambda^2}\right) - \frac{1}{2}\ln^2\left(\frac{s_{12}}{m_i^2}\right) - \frac{1}{2}\ln^2\left(\frac{1-\beta_j}{1+\beta_j}\right) - \frac{\pi^2}{3} - 2\mathrm{Li}_2\left(1 - \frac{2p_i^0 p_j^0}{s_{ij}}(1+\beta_j)\right) - 2\mathrm{Li}_2\left(1 - \frac{2p_i^0 p_j^0}{s_{ij}}(1-\beta_j)\right)\Big].$$

In these equations the notation $s_{ij} = 2\,p_i{\cdot}p_j$, $\beta_i = |\vec{p}_i|/p_i^0$ and $v_{ij} = \sqrt{1 - 4m_i^2 m_j^2/s_{ij}^2}$ has been used.

Initial-state collinear real gluon radiation and PDFs subtraction terms

$d\sigma^{\text{virtual+soft}}_{pp\to\tilde{q}\tilde{q}'(g)}$ still depends on the quark mass (m_q) owing to the initial-state collinear singularities. This dependence cancels by adding the term $d\sigma^{\text{coll}}_{pp\to\tilde{q}\tilde{q}'(g)}$ which includes the contribution from gluon emission into the hard collinear region and the subtraction term for initial state divergences, already absorbed in the definition of the PDFs,

$$d\sigma^{\text{coll}}_{pp\to\tilde{q}\tilde{q}'(g)} = d\sigma^{\text{coll-cone}}_{pp\to\tilde{q}\tilde{q}'(g)} + d\sigma^{\text{sub-pdf}}_{pp\to\tilde{q}\tilde{q}'}\,. \tag{6.29}$$

The collinear gluon emission into a narrow cone around the emitting particle ($\theta < \Delta\theta$) and energy larger than ΔE is given by

$$d\sigma^{\text{coll-cone}}_{pp\to\tilde{q}\tilde{q}'(g)} = \int_{\tau_0}^{1} d\tau \int_{\tau}^{1} \frac{dx}{x} \int_{x}^{1-\delta_s} \frac{dz}{z}\, \mathcal{L}^{\text{coll}}_{qq'}(\tau,x,z)\; d\hat{\sigma}^{\text{coll-cone}}_{qq'\to\tilde{q}\tilde{q}'(g)}(\tau,z)\,, \tag{6.30}$$

where $\delta_s = 2\Delta E/\sqrt{s}$ and the parton luminosity $\mathcal{L}^{\text{coll}}_{qq'}$ is defined as

$$\mathcal{L}^{\text{coll}}_{qq'}(\tau,x,z) = \frac{1}{1+\delta_{qq'}} \left[f_q\Big(\frac{x}{z},\mu_F\Big)\; f_{q'}\Big(\frac{\tau}{x},\mu_F\Big) + f_q(\frac{\tau}{x},\mu_F)\, f_{q'}\Big(\frac{x}{z},\mu_F\Big)\right]. \tag{6.31}$$

The partonic cross section $d\sigma^{\text{coll-cone}}_{pp\to\tilde{q}\tilde{q}'(g)}$ for the collinear emission of a gluon into the cones with opening angle $\Delta\theta$ around the two quarks in the initial state can be written as

$$d\hat{\sigma}^{\text{coll-cone}}_{qq'\to\tilde{q}\tilde{q}'(g)}(\tau,z) = d\hat{\sigma}^{(0)}_{qq'\to\tilde{q}\tilde{q}'}(\tau)\; \frac{4}{3\pi}\alpha_s \left[\frac{1+z^2}{1-z}\log\left(\frac{s\,\delta_\theta}{2m_q^2 z}\right) - \frac{2z}{1-z}\right], \tag{6.32}$$

where $\delta_\theta = 1-\cos(\Delta\theta) \simeq \Delta\theta^2/2$ and the variable z is the ratio between the momenta of the emitter parton after and before the emission. Eq. (6.32) corresponds to the results of [275] with the replacement $\alpha Q_q^2 \to (4/3)\alpha_s$.

The subtraction term, in the $\overline{\text{MS}}$ scheme, can be written for the phase-space slicing in the following way,

$$\begin{aligned} d\sigma^{\text{sub-pdf}}_{pp\to\tilde{q}\tilde{q}'} = &-2\int_{\tau_0}^{1} d\tau \int_{\tau}^{1} \frac{dx}{x} \int_{x}^{1-\delta_s} \frac{dz}{z}\, \mathcal{L}^{\text{coll}}_{qq'}(\tau,x,z)\; d\hat{\sigma}^{\text{sub1}}_{qq'\to\tilde{q}\tilde{q}'}(\tau,z) \\ &-2\int_{\tau_0}^{1} d\tau\; \mathcal{L}_{qq'}(\tau)\; d\hat{\sigma}^{\text{sub2}}_{qq'\to\tilde{q}\tilde{q}'}(\tau)\,, \end{aligned} \tag{6.33}$$

The z-dependent part $d\hat{\sigma}^{\text{sub1}}_{qq'\to\tilde{q}\tilde{q}'}(\tau,z)$ of the subtraction term for one quark PDF is given by

$$d\hat{\sigma}^{\text{sub1}}_{qq'\to\tilde{q}\tilde{q}'}(\tau,z) = d\hat{\sigma}^{(0)}_{qq'\to\tilde{q}\tilde{q}'}(\tau)\; \frac{2}{3\pi}\alpha_s \left[\frac{1+z^2}{1-z}\log\left(\frac{\mu_F^2}{(1-z)^2 m_q^2}\right) - \frac{1+z^2}{1-z}\right], \tag{6.34}$$

where μ_F is the factorization scale. $d\hat{\sigma}^{\text{sub1}}_{qq'\to\tilde{q}\tilde{q}'}(\tau,z)$ enters eq. (6.33) via the convolution with $\mathcal{L}^{\text{coll}}_{qq'}(\tau,x,z)$ of eq. (6.31).

The term $d\hat{\sigma}^{\text{sub2}}_{qq'\to\tilde{q}\tilde{q}'}(\tau)$ is given by

$$d\hat{\sigma}^{\text{sub2}}_{qq'\to\tilde{q}\tilde{q}'}(\tau) = d\hat{\sigma}^{(0)}_{qq'\to\tilde{q}\tilde{q}'}(\tau)\; \frac{4}{3\pi}\alpha_s \left[1-\log(\delta_s)-\log^2(\delta_s)+\left(\log(\delta_s)+\frac{3}{4}\right)\log\left(\frac{\mu_F^2}{m_q^2}\right)\right] \tag{6.35}$$

and corresponds to the z-independent part of the subtraction term for one quark PDF. $d\hat{\sigma}^{\text{sub2}}_{qq'\to\tilde{q}\tilde{q}'}(\tau)$ depends also on the soft-gluon phase space cut via $\delta_s = 2\Delta E/\sqrt{s}$.

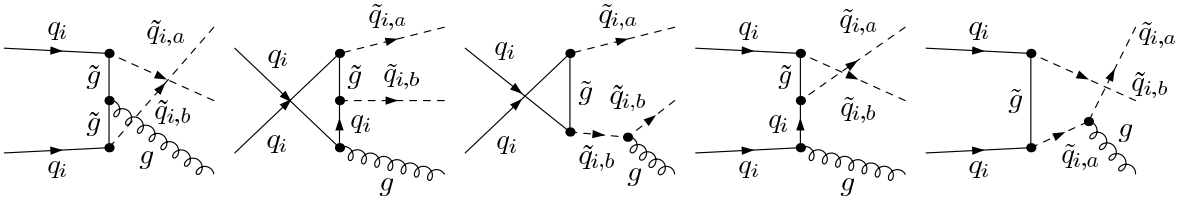

Figure 6.9: Real gluon radiation diagrams contributing only for equal flavor squarks.

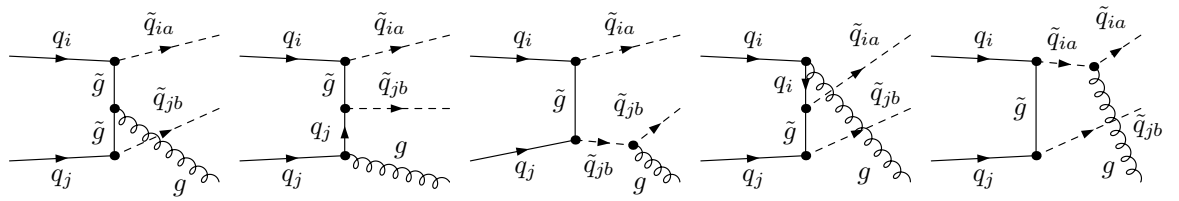

Figure 6.10: Real gluon radiation diagrams contributing to all flavor and chirality configurations.

Often, in the literature, these formulae used for the calculation of the collinear contribution are parametrized in a different, but equivalent, way. In this alternative parametrization, the partonic formulae in eq. (6.32) and eq. (6.34) include the LO cross section $d\hat{\sigma}^{(0)}_{qq'\to\tilde{q}\tilde{q}'}(\tau)$, where $s = \tau S$ is equal to the squared sum of the momenta of the final-state particles excluding the gluon, i.e., for our process, the squark–squark pair. Instead, in our calculation, s is the usual squared sum of the momenta of the parton in the initial state, i.e., the squared total energy in the partonic center-of-mass frame. Obviously, with a different definition of s, the z-dependence changes in eq. (6.32), eq. (6.34) and also in the partonic luminosity eq. (6.31).

With this alternative parametrization, a special treatment would be necessary for the generation of the events. Partonic events generated via $d\hat{\sigma}^{(0)}_{qq'\to\tilde{q}\tilde{q}'}(\tau)$ in eq. (6.32) could not be boosted to the laboratory frame as the events for all the other contributions (LO, virtual+soft, hard); it would be necessary to include the value of z in the definition of the boost. Conversely, in the formulae of this section, the LO cross section in eq. (6.32) and eq. (6.34) is expressed in term of the total energy in the center-of-mass frame of the partonic process. Thus, events generated via $d\hat{\sigma}^{(0)}_{qq'\to\tilde{q}\tilde{q}'}(\tau)$ can be boosted as in the other cases.

Hard real gluon radiation

The sum $d\sigma^{\text{virtual+soft}}_{pp\to\tilde{q}\tilde{q}'(g)}(m_q, \Delta E) + d\sigma^{\text{coll}}_{pp\to\tilde{q}\tilde{q}'(g)}(m_q, \Delta E, \Delta\theta)$ does not depend on the regulator parameters λ and m_q. The remaining dependence on the slicing parameters $\Delta\theta$ and ΔE is canceled adding $d\sigma^{\text{hard}}_{pp\to\tilde{q}\tilde{q}'(g)}$. This contribution is calculated numerically, integrating the squared matrix elements obtained from diagrams shown in Figure 6.9 and Figure 6.10.

6.4.3 Real quark radiation

The $\mathcal{O}(\alpha_s)$ corrections to $pp \to \tilde{q}_{ia}\tilde{q}_{jb}(X)$ get also a contribution from the gluon-initiated subprocesses $q_i g \to \tilde{q}_{ia}\tilde{q}_{jb}\bar{q}_j$ and $q_j g \to \tilde{q}_{ia}\tilde{q}_{jb}\bar{q}_i$, which also have to be included for a consistent treatment of NLO PDFs. Diagrams for these two subprocesses can be divided into resonant (Figure 6.11(a) and 6.12(a)) and non-resonant (Figure 6.11(b) and 6.12(b)) diagrams, where in the resonant diagrams the intermediate gluino can be on-shell. This resonant production channel, when gluinos are on-shell, corresponds basically to LO production of a squark–gluino pair (with subsequent gluino decay). Such contributions are generally classified as squark–gluino production and have to be removed in order to avoid double-counting.[6] Our NLO calculation of the production of squark–squark pairs, however, is meant as a necessary ingredient of eq. (6.8) and eq. (6.11) for NLO factorizable corrections to squark–squark production and decays. Thus, our primary goal is the consistency of the calculation at NLO of the full process with decays included and not only of the production of squarks.

In a general context, combining production and decays for all colored SUSY particles ($\tilde{q}, \tilde{q}^*$ and $\tilde{g}$), also off-shell configurations from resonant diagrams appear. For the case of quark radiation, they correspond to the contribution from diagrams where gluinos, but also squarks, can be in principle off-shell, e.g., Figure 6.2. Thus, combining production and decays, the off-shell contributions from resonant diagrams in Figure 6.11(a) and 6.12(a) can, in the same way, be classified as part of the contribution from the production and decays of squark–gluino pairs with the squark on-shell and the gluino off-shell. Conversely, in the context of a calculation of production of all colored SUSY particles ($\tilde{q}, \tilde{q}^*$ and $\tilde{g}$) without decays, as e.g. in [33, 219], such configuration cannot be present, since final-state colored sparticles are treated on-shell.

The most important difference in calculations with and without including decays is, indeed, the role of the colored supersymmetric particles. In one case they belong to the final state, in the other one they are intermediate states. Thus, due to the quark radiation at NLO, a separation of squark–gluino and squark–squark channel contributions to $pp \to 2j + \not{E}_T(+X)$ or to $pp \to 2j + l^+l^-(\text{OS-SF}) + \not{E}_T(+X)$ is only an intermediate organizational instrument.

In the following, we address the structure of the various terms contributing to the real quark radiation and describe three different approaches to perform the subtraction of the contributions corresponding to squark–gluino production (with subsequent gluino decay). Afterwards, we describe the technical steps involved in the calculation with the phase-space slicing method, as discussed so far.

[6] The same type of problem is present in the calculation of NLO corrections to Wt production channel for single top quark production [276], where quark radiation creates configurations corresponding to top quark pair production with one on-shell top quark that decays.

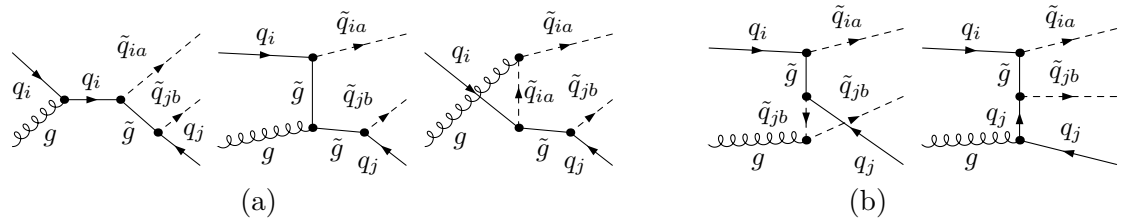

Figure 6.11: Resonant (a) and non-resonant (b) diagrams contributing to $q_i g \to \tilde{q}_{ia}\tilde{q}_{jb}\bar{q}_j$.

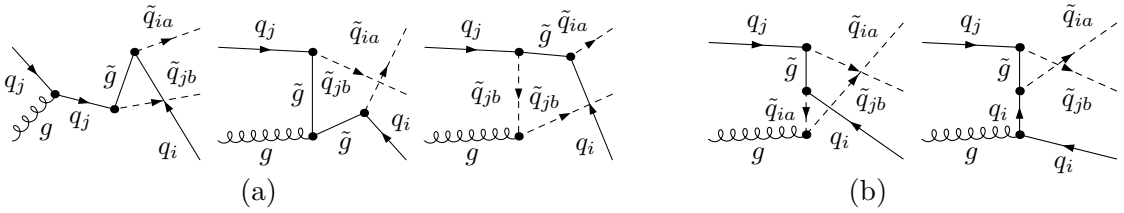

Figure 6.12: Resonant (a) and non-resonant (b) diagrams contributing to $q_j g \to \tilde{q}_{ia}\tilde{q}_{jb}\bar{q}_i$.

Resonant and non-resonant contributions

In the case of different flavors $i \neq j$, there are two parton processes which provide NLO differential cross sections for real quark emission, given by

$$d\hat{\sigma}_{q_i g\to\tilde{q}_{ia}\tilde{q}_{jb}\bar{q}_j} \sim d\Pi_{(2\to3)} \left[\overline{\left|\mathcal{M}_{\text{nonres},i}\right|^2} + 2\text{Re}\overline{\left(\mathcal{M}_{\text{nonres},i}\mathcal{M}^*_{\text{res},i}\right)} + \overline{\left|\mathcal{M}_{\text{res},i}\right|^2} \right] , \tag{6.36}$$

$$d\hat{\sigma}_{q_j g\to\tilde{q}_{ia}\tilde{q}_{jb}\bar{q}_i} \sim d\Pi_{(2\to3)} \left[\overline{\left|\mathcal{M}_{\text{nonres},j}\right|^2} + 2\text{Re}\overline{\left(\mathcal{M}_{\text{nonres},j}\mathcal{M}^*_{\text{res},j}\right)} + \overline{\left|\mathcal{M}_{\text{res},j}\right|^2} \right] ,$$

where *overline* represents the usual summing and averaging of external helicities and colors and $d\Pi_{(2\to3)}$ is the usual phase-space element for three particles in the final state. $\mathcal{M}_{\text{res},i}$ and $\mathcal{M}_{\text{nonres},i}$ correspond to the diagrams of Figure 6.11(a) and Figure 6.11(b), respectively, and $\mathcal{M}_{\text{res},j}$ and $\mathcal{M}_{\text{nonres},j}$ to those of Figure 6.12(a) and Figure 6.12(b).

For the case of equal flavors $i = j$, we have

$$d\hat{\sigma}_{q_i g\to\tilde{q}_{ia}\tilde{q}_{ib}\bar{q}_i} \sim d\Pi_{(2\to3)} \left[\overline{\left|\mathcal{M}_{\text{nonres}}\right|^2} + 2\text{Re}\overline{\left(\mathcal{M}_{\text{nonres}}\mathcal{M}^*_{\text{res}}\right)} + \overline{\left|\mathcal{M}_{\text{res}}\right|^2} \right] , \tag{6.37}$$

with $\mathcal{M}_{\text{res}}$ from the diagrams of Figure 6.11(a) and Figure 6.12(a), which we will call in this case $\mathcal{M}_{\text{res},1}$ and $\mathcal{M}_{\text{res},2}$; $\mathcal{M}_{\text{nonres}}$ is the part from the diagrams of Figure 6.11(b) and Figure 6.12(b). The term $2\text{Re}\overline{\left(\mathcal{M}_{\text{res},1}\mathcal{M}^*_{\text{res},2}\right)}$ appears only for equal chiralities ($a = b$) and flavors ($i = j$) of the squarks.

We describe, only for the case with equal flavor, how the terms contained also in the calculation of the squark–gluino channel are subtracted; analogous arguments apply to the different-flavor case. We refer to three different strategies,

- DS: Diagram Subtraction,
- CR: Channel Removal,
- DR: Diagram Removal,

where the DR and DS schemes defined here are almost equal to the approaches extensively studied in [276]. The few differences are described in the following and, for the DS case, also in appendix D in more detail.

DS scheme

In the DS scheme the contribution from the LO on-shell production of a squark–gluino pair with the gluino decaying into a squark is removed:

$$\begin{aligned} d\hat{\sigma}^{DS}_{q_i g \to \tilde{q}_{ia} \bar{q}_{ib} \bar{q}_i} \;\sim\; & \left[\overline{|\mathcal{M}_{\text{nonres}}|^2} + 2\text{Re}\overline{(\mathcal{M}_{\text{nonres}} \mathcal{M}^*_{\text{res}})} + \overline{|\mathcal{M}_{\text{res}}|^2} \right] \, d\Pi_{(2\to3)} \\ & - \left[\overline{\left|\mathcal{M}_{\text{res},1}\right|^2} + \overline{\left|\mathcal{M}_{\text{res},2}\right|^2} \right] \, d\Pi_{(2\to2)\times(1\to2)} \; . \end{aligned} \tag{6.38}$$

In eq. (6.38), $d\Pi_{(2\to2)\times(1\to2)}$ is the phase space with three particles in the final state applying consistently the on-shell condition $(p_{\tilde{q}} + p_q)^2 = m^2_{\tilde{g}}$ for the two different resonant cases. Eq. (6.38) is conceptually equal to the DS scheme explained in [276] and the "Prospino scheme" in [33, 277]; in practice there is a difference with respect to our approach. We subtract at global level exactly what we would obtain from LO on-shell production of a squark–gluino pair with the gluino decaying into a squark. This is done by producing two different sets of events corresponding to the two lines of eq. (6.38), respectively. In [33,276,277] a local subtraction of the on-shell contribution involving a mapping or reshuffling of momenta from the general $d\Pi_{2\to3}$ phase space into an equivalent on-shell configuration is performed. These two implementations of the DS scheme give slightly different results even in the limit $\Gamma_{\tilde{g}} \to 0$. The threshold conditions $p^2_{\tilde{g}} > m^2_{\tilde{q}}$ and $\sqrt{s} > \left(\sqrt{p^2_{\tilde{g}}} + m_{\tilde{q}}\right)$ in the local subtraction, together with the convolution of the PDFs and the precise on-shell mapping, produce small differences from numerical results of the global subtraction. More details can be found in appendix D, where the origin of these differences are explained.

The DS scheme, both in the local approach discussed in [276] and in the global approach, defined in eq. (6.38), is gauge invariant in the limit $\Gamma_{\tilde{g}} \to 0$. The decay width of the gluino is used thereby as a numerical regulator and not as a physical parameter.

CR scheme

In an extreme approach, the quark radiation calculation could even be completely excluded from the NLO corrections in the squark–squark channel. Then, all diagrams, resonant and non-resonant, constituting a gauge-invariant subset, have to be included

in the squark–gluino production and decay channel. This is possible because, due to the quark radiation at NLO, a separation of squark–gluino and squark–squark channel contributions to $pp \to q\tilde{\chi}_1^0 q'\tilde{\chi}_1^0$ is only an intermediate organizational instrument. Moving all the quark radiation contribution in the squark–gluino channel calculation, we just alter the organizational separation of squark/gluino channels.

Since the term $\overline{|\mathcal{M}_{\text{nonres}}|^2}$ contains initial-state collinear singularities, also the subtraction term of the PDFs has to be excluded and computed within the squark–gluino channel. However, quark NLO PDFs include in their DGLAP evolution equation contribution from quark radiation. Thus, in the CR scheme, every single channel is not independently consistent with PDF evolutions. Only when all the different squark/gluino channels are taken into account, the consistency with PDF evolutions is achieved.

DR scheme

The DR scheme represents, in a certain sense, an intermediate step between the DS and CR schemes. Here, one removes, from a diagrammatic perspective, the minimal set of contributions in the squared amplitude that contain a resonant gluino. In our calculation this results in

$$d\hat{\sigma}^{DR}_{q_i g \to \tilde{q}_{ia}\bar{q}_{ib}\bar{q}_i} \sim \quad d\Pi_{(2\to3)} \left[\overline{|\mathcal{M}_{\text{nonres}}|^2} + 2\text{Re}\overline{(\mathcal{M}_{\text{nonres}}\mathcal{M}^*_{\text{res}})} + \delta_{ab}\ 2\text{Re}\overline{\left(\mathcal{M}_{\text{res},1}\mathcal{M}^*_{\text{res},2}\right)} \right]. \tag{6.39}$$

In the different-flavor cases the third term in eq. (6.39) does not appear. Comparing eq. (6.39) with eq. (6.37), it is clear that the removed terms are $\overline{|\mathcal{M}_{\text{res},1}|^2}$ and $\overline{|\mathcal{M}_{\text{res},2}|^2}$. In the definition of DR given in [276] also the interference term $2\text{Re}(\mathcal{M}_{\text{nonres}}\mathcal{M}^*_{\text{res}})$ is removed (with a study of the impact of the inclusion of this contribution), whereas we keep this interference term. In both definitions, the DR scheme is not gauge invariant. Indeed, $\mathcal{M}_{\text{res}}$ and $\mathcal{M}_{\text{nonres}}$ are separately gauge invariant only when the gluino is on-shell, as in the subtraction term in the DS scheme.

Although the DR scheme formally violates gauge invariance, a consistent description is achieved when the procedure presented here is combined with the squark–gluino channel contributions that include $\overline{|\mathcal{M}_{\text{res},1}|^2}$ and $\overline{|\mathcal{M}_{\text{res},2}|^2}$ terms, with gluinos also off-shell. Again, we just altered with this scheme the organizational separation of squark/gluino channels.

Comparison among different schemes

The narrow-width approximation, in the DR, CR and DS scheme, is not an exact description; as an approximation it has a natural uncertainty arising from missing off-shell contributions and non-factorizable NLO corrections. Numerical differences among different schemes do not represent the dominant uncertainty, e.g., as shown in section 7.1.4, the dependence of cross sections on the scale variation is larger.

In our numerical results we basically employ the DR scheme, however, we compare it with results in the DS scheme, both for inclusive K-factors and for differential distributions.

The three schemes seem to be equally acceptable; however, from a pure theoretical point of view, they all present some flaws. In the calculation of just production of colored sparticle, the DS scheme, especially in the global approach[7], seems to be preferable. Including decays of the squarks in NWA, the choice of the DS scheme does not represent the best option anymore. If we include in all production and decay channels only on-shell configurations for the resonant intermediate supersymmetric particles (as performed here for the squark–squark channel), quark radiation in the NLO corrections introduces unavoidably off-shell contributions. The DS scheme includes, in the squark–squark channel, off-shell gluino effects from squark–gluino production, thus we are not strictly in NWA for all the different intermediate particles. The NWA can be obtained removing in the individual channels also the off-shell effects. This procedure corresponds to the DR scheme. In this way, one obtains the NWA, but the single channels separately violate gauge invariance. Reorganizing the contributions from the different channels as in the CR scheme, yields gauge invariant contributions from each channel. However, single channels are not consistent with PDFs at NLO. In conclusion, in all the three schemes, the NLO QCD calculation of the production of colored sparticles, including their decays, does not satisfy at the same time the following three conditions:

- NWA is consistently applied to all the intermediate colored sparticles,
- Every squark/gluino channel contribution is gauge-invariant,
- Every squark/gluino channel contribution is consistent with PDFs evolution.

Calculation with the phase-space slicing method

Finally, for the practical calculation of the real quark radiation contributions, in all the three schemes one has to perform the phase-space integration over the final-state quark. The squared non-resonant terms lead, as mentioned before, to initial-state collinear singularities. Again, these singular terms have to be subtracted since they are factorized and absorbed into the PDFs. The formulae shown in the following are, again, obtained from [275] and [278] with the replacement $\alpha Q_q^2 \to (4/3)\alpha_s$. As in the case of the gluon radiation, we divide the emission of a quark into a collinear and a non-collinear region (since no IR singularities occur, a separation into soft and hard

[7] In the local approach some spurious terms, indicated in eq. (D.6) of appendix D, are also included. These terms, however, do not belong to squark–gluino production combined with gluino decay in NWA. Thus, the contribution from $\tilde{g} \to \tilde{q}q$, implicitly included in LO squark–gluino production, is not exactly subtracted from quark radiation correction to squark–squark production.

quark emission is not required),

$$d\sigma^{\text{real-quark}}_{pp\to\tilde{q}_{ia}\tilde{q}_{jb}\bar{q}^{(\prime)}} = \sum_{k=i,j} \frac{1}{1+\delta_{i,j}} \left[d\sigma^{\text{coll-quark}}_{pp\to\tilde{q}_{ia}\tilde{q}_{jb}\bar{q}_k}(\Delta\theta) + d\sigma^{\text{noncoll-quark}}_{pp\to\tilde{q}_{ia}\tilde{q}_{jb}\bar{q}_k}(\Delta\theta) \right] . \tag{6.40}$$

The non-collinear contribution

$$d\sigma^{\text{noncoll-quark}}_{pp\to\tilde{q}_{ia}\tilde{q}_{jb}\bar{q}_{j/i}} = \int_{\tau_0}^{1} d\tau\, \mathcal{L}^{\text{noncoll-quark}}_{i/j}(\tau)\; d\hat{\sigma}_{q_{i/j}g\to\tilde{q}_{ia}\tilde{q}_{jb}\bar{q}_{j/i}}(\tau)\,, \tag{6.41}$$

contains $\mathcal{L}_i^{\text{noncoll}-\text{quark}}(\tau)$ as given by

$$\mathcal{L}_i(\tau)^{\text{noncoll-quark}} = 2\int_{\tau}^{1} \frac{dx}{x}\; g(x,\mu_F) f_i\Big(\frac{\tau}{x},\mu_F\Big)\;, \tag{6.42}$$

where $g(x,\mu_F)$ indicates the PDF of the gluon.

The collinear emission, expressed in this case together with the subtraction terms for the PDFs, instead can be written as follows,

$$d\sigma^{\text{coll-quark}}_{pp\to\tilde{q}_{ia}\tilde{q}_{jb}\bar{q}_{j/i}} = \int_{\tau_0}^{1} d\tau \int_{\tau}^{1} \frac{dx}{x} \int_{x}^{1} \frac{dz}{z}\, \mathcal{L}^{\text{coll-quark}}_{i/j}(\tau,x,z)\; d\hat{\sigma}^{\text{coll-quark}}_{q_{i/j}g\to\tilde{q}_{ia}\tilde{q}_{jb}\bar{q}_{j/i}}(\tau,z)\,, \tag{6.43}$$

with $\mathcal{L}_i^{\text{coll-quark}}(\tau,x,z)$ given by

$$\mathcal{L}_i(\tau,x,z)^{\text{coll-quark}} = \; 2\; g\left(\frac{x}{z},\mu_F\right) f_i\Big(\frac{\tau}{x},\mu_F\Big)\;. \tag{6.44}$$

The partonic cross section entering eq. (6.43) is given by

$$\begin{aligned} d\hat{\sigma}^{\text{coll-quark}}_{q_{i/j}g\to\tilde{q}_{ia}\tilde{q}_{jb}\bar{q}_{j/i}}(\tau,z) = {} & d\hat{\sigma}^{(0)}_{q_iq_j\to\tilde{q}_{ia}\tilde{q}_{jb}} \cdot \\ & \cdot\; \frac{\alpha_s}{2\pi}\, P_{qg}(z) \left[\log\left(\frac{s(1-z)^2\,\delta_\theta}{2m_q^2 z}\right) + 2z(1-z) - \log\left(\frac{\mu_F^2}{m_q^2}\right)\right]. \end{aligned} \tag{6.45}$$

The last term in the brackets of eq. (6.45) is the PDF subtraction term; the remaining terms originate from the collinear emission of a quark into a cone of angle $\Delta\theta$ related to δ_θ via $\delta_\theta = 1-\cos(\Delta\theta) \simeq \Delta\theta^2/2$. It is easy to see in eq. (6.45) the analytical cancellation of m_q from the collinear emission of a quark and the subtraction term for the PDFs. The remaining dependence on $\Delta\theta$ cancels at the hadronic level in eq. (6.40), adding the contribution from non-collinear radiation.

6.5 Distributions for the squark decay $\tilde{\mathrm{q}} \to \mathrm{q}\tilde{\chi}^0_\mathrm{j}$

6.5.1 Distributions at LO

The LO partial decay width for a squark decaying into a neutralino and a quark, $\tilde{q}_{ia} \to q_i \tilde{\chi}^0_j$, depends on the flavor and chirality of the squark. Also here, consistently with the calculation of the production of squark–squark pairs, we set $m_q = 0$. With this assumption, the width can be written as follows,

$$\Gamma^{(0)}_{\tilde{q}_{ia}\to q_i\tilde{\chi}^0_j} = \frac{\alpha}{4} m_{\tilde{q}_{ia}} \left(1 - \frac{m^2_{\tilde{\chi}^0_j}}{m^2_{\tilde{q}_{ia}}}\right) f_a^2 \,, \tag{6.46}$$

where $m_{\tilde{\chi}^0_j}$ indicates the neutralino mass. The coupling constants f_a can be expressed in terms of the isospin $T^3_{q_i}$ and the charge Q_{q_i} of the quark, and the neutralino mixing matrix N_{jk}, defined in eq. (5.10). Denoting the electroweak mixing angle by $s_W = \sin(\theta_W)$ and $c_W = \cos(\theta_W)$, one has

$$f_L = \sqrt{2}\Big[Q_{q_i} N'_{j1} + (T^3_{q_i} - Q_{q_i} s^2_W) \frac{1}{c_W s_W} N'_{j2}\Big] \,, \tag{6.47}$$

$$f_R = -\sqrt{2}\Big[Q_{q_i} N'_{j1} - Q_{q_i} \frac{s_W}{c_W} N'_{j2}\Big] \,, \tag{6.48}$$

$$N'_{j1} = c_W N_{j1} + s_W N_{j2}, \qquad N'_{j2} = -s_W N_{j1} + c_W N_{j2} \,. \tag{6.49}$$

For a scalar particle decaying in its rest frame there is no preferred direction, and hence the differential decay distribution is isotropic. Consequently, for squark decays into neutralino and quark, the decay distribution is simply given by

$$d\Gamma^{(0)}_{\tilde{q}\to q\tilde{\chi}^0_j} = \frac{1}{4\pi} \Gamma^{(0)}_{\tilde{q}\to q\tilde{\chi}^0_j} \, d\cos\theta \, d\phi \,, \tag{6.50}$$

with polar angle θ and azimuth ϕ referring to the quark momentum.

6.5.2 Distributions at NLO

The differential decay width for $\tilde{q} \to q\tilde{\chi}^0_j$ at NLO is obtained in analogy to the steps in section 6.4.2. We regulate also here infrared divergences with the gluon mass λ and collinear singularities with the fictitious quark mass m_q. The evaluation of the real radiation is performed, again, with the phase-space slicing method. Thus, the differential decay can be written as follows,

$$\begin{aligned} d\Gamma^{(1)}_{\tilde{q}\to q\tilde{\chi}^0_j} = {} & d\Gamma^{\text{virtual}}_{\tilde{q}\to q\tilde{\chi}^0_j}(m_q, \lambda) + d\Gamma^{\text{soft}}_{\tilde{q}\to q\tilde{\chi}^0_j(g)}(m_q, \lambda, \Delta E) + d\Gamma^{\text{coll}}_{\tilde{q}\to q\tilde{\chi}^0_j(g)}(m_q, \Delta E, \Delta\theta) \\ & + d\Gamma^{\text{hard}}_{\tilde{q}\to q\tilde{\chi}^0_j g}(\Delta E, \Delta\theta) \,. \end{aligned} \tag{6.51}$$

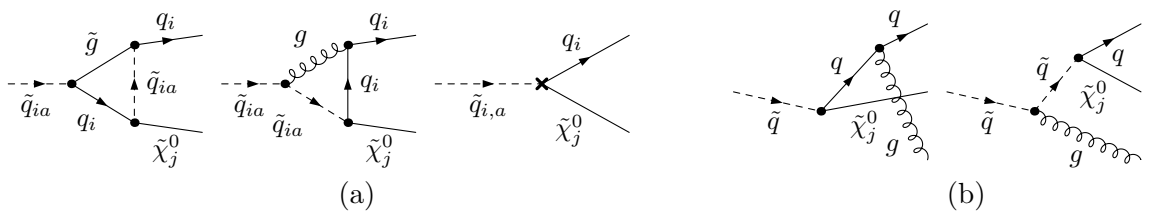

Figure 6.13: Loop and counterterm diagrams (a) and gluon radiation diagrams (b) for squark decays.

As in the discussion for the calculation of NLO corrections to squark–squark production, in eq. (6.51) we explicitly show for each term the dependence on regulating and slicing parameters. Summing $d\Gamma^{\text{virtual}}_{\tilde{q}\to q\tilde{\chi}_j^0}(m_q,\lambda)$ and $d\Gamma^{\text{soft}}_{\tilde{q}\to q\tilde{\chi}_j^0(g)}(m_q,\lambda,\Delta E)$, the dependence on λ analytically cancels, adding also $d\Gamma^{\text{coll}}_{\tilde{q}\to q\tilde{\chi}_j^0(g)}(m_q,\Delta E,\Delta\theta)$ the dependence on m_q is eliminated, again, analytically. The remaining dependence on the slicing parameters ΔE and $\Delta\theta$ is removed adding the term $d\Gamma^{\text{hard}}_{\tilde{q}\to q\tilde{\chi}_j^0 g}(\Delta E,\Delta\theta)$.

Virtual corrections

The virtual corrections $d\Gamma^{\text{virtual}}_{\tilde{q}\to q\tilde{\chi}_j^0}$, for $m_q = 0$, correspond to the interference of the tree-level diagram (the $\tilde{q} \to q\tilde{\chi}_j^0$ vertex) with the two vertex-loop diagrams in Figure 6.13(a) and the vertex counterterm (indicated by the cross in Figure 6.13(a)), which consists of the wave-function renormalization constants of the external quark and squark line. We do not need loop diagrams with self-energy corrections on external lines, because, as for the production amplitudes, the renormalization constants are determined in the on-shell renormalization scheme and are discussed in appendix C. Here, in contrast to the calculation for squark–squark production, we do not need to renormalize α_s, so we regularize UV divergences via dimensional reduction, directly preserving supersymmetry and the related Slavnov-Taylor identities. Details on the vertex counterterm can be found in [239], and the analytical expression is also explicitly given afterwards in eq. (6.63).

Real soft gluon radiation

The term $d\Gamma^{\text{soft}}_{\tilde{q}\to q\tilde{\chi}_j^0(g)}$ can be calculated in analogy to $d\hat{\sigma}^{\text{soft}}_{qq'\to\tilde{q}\tilde{q}'(g)}$ in the production case, yielding

$$d\Gamma^{\text{soft}}_{\tilde{q}\to q\tilde{\chi}_j^0(g)} \;=\; -\frac{2\alpha_s}{3\pi}\left\{\sum_{i,k=1;i<k}^{2}\epsilon_i\epsilon_k\,\mathcal{I}_{ik}\right\} d\Gamma^{(0)}_{\tilde{q}\to q\tilde{\chi}_j^0}\,. \tag{6.52}$$

The color factor, in contrast to the case of $d\hat{\sigma}^{\text{soft}}_{qq'\to\tilde{q}\tilde{q}'(g)}$, is the same for the different contributions. Thus, it is included directly in eq. (6.52).

Here, the corresponding expressions for $\mathcal{I}_{ij}$, with the label assignment $\tilde{q} \to 1$, $q \to 2$ (and $\tilde{\chi}_j^0 \to 3$), read as follows,

$$\begin{aligned}
\mathcal{I}_{11} &= \ln\left(\frac{4(\Delta E)^2}{\lambda^2}\right) - 2\,, \\
\mathcal{I}_{12} &= \ln\left(\frac{4(p_2^0)^2}{m_q^2}\right)\ln\left(\frac{4(\Delta E)^2}{\lambda^2}\right) - \frac{1}{2}\ln^2\left(\frac{4(p_2^0)^2}{m_q^2}\right) - \frac{\pi^2}{3}\,, \\
\mathcal{I}_{22} &= \ln\left(\frac{4(\Delta E)^2}{\lambda^2}\right) + \ln\left(\frac{m_q^2}{4(p_2^0)^2}\right)\,.
\end{aligned} \tag{6.53}$$

Final-state collinear real gluon radiation

Here, collinear divergences are of different nature respect to the calculation of the production case. They emerge from the final state, whereas in the production they originate from the initial state. In the production case, the collinear remnants are absorbed into PDF definitions. Here they cancel at parton level, summing real and virtual contributions.

Making again use of the results of [275], the collinear emission of gluons with energy larger than ΔE into a cone with opening angle $\Delta\theta$ yields the contribution

$$\begin{aligned}
d\Gamma^{\text{coll}}_{\tilde{q}\to q\tilde{\chi}_j^0(g)} \;&=\; d\Gamma^{(0)}_{\tilde{q}\to q\tilde{\chi}_j^0} \\
&\cdot\; \frac{2\alpha_s}{3\pi}\left[\frac{9}{2} - \frac{2}{3}\pi^2 - \frac{3}{2}\,\log\left(\frac{2E_{q,\max}^2\,\delta_\theta}{m_q^2}\right) + 2\log(\delta_s)\left(1 - \log\left(\frac{2E_{q,\max}^2\,\delta_\theta}{m_q^2}\right)\right)\right]\,,
\end{aligned} \tag{6.54}$$

where $\delta_s = 2\Delta E/m_{\tilde{q}}$, $\delta_\theta = 1 - \cos(\Delta\theta) \simeq \Delta\theta^2/2$, and $E_{q,\max} = \frac{m_{\tilde{q}}^2 - m_{\tilde{\chi}_j^0}^2}{2m_{\tilde{\chi}_j^0}}$, the maximum energy available for the quark in the squark rest frame. In this way, gluons with $\theta < \Delta\theta$ are recombined with the emitter quark into a quark with momentum $p_{\text{recomb}} = p_q + p_g$. Thus, before recombining partons into jets, differential distributions in the quark momenta depend on the slicing parameter $\Delta\theta$. However, this dependence disappears when a jet clustering algorithm is applied to obtain predictions that are collinear and infrared safe. Indeed, in any experimental analysis, parameters of jet clustering algorithms are much more inclusive than the values of the regulator $\Delta\theta$ used in our numerical evaluation.

Hard real gluon radiation

The contribution $d\Gamma^{\text{hard}}_{\tilde{q}\to q\tilde{\chi}_j^0}$ from real emission of hard gluons is evaluated by numerical integration of the squared matrix elements, obtained from the diagrams in Figure 6.13(b), in the phase-space region $E_g > \Delta E$ and $\theta > \Delta\theta$.

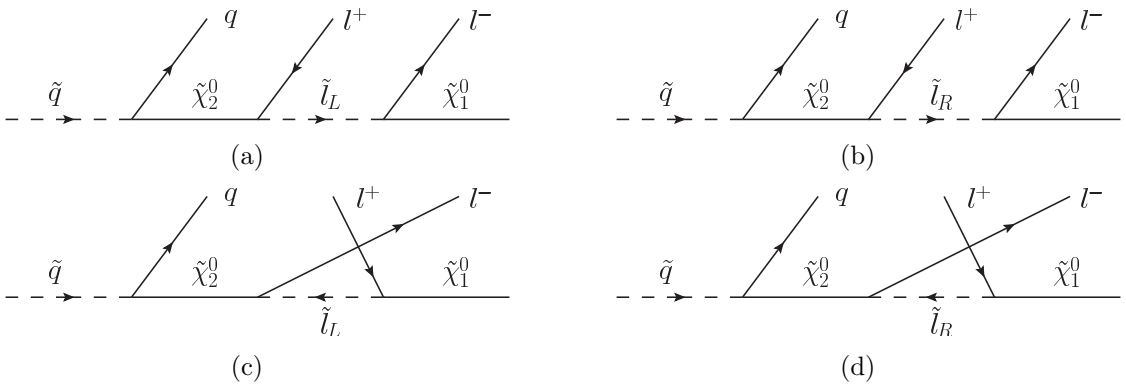

Figure 6.14: The four Feynman diagrams contributing to the tree-level amplitude for the "golden decay chain".

6.6 Distributions for the squark decay chain

6.6.1 Distributions at LO

The structure of the "golden decay chain" has already been discussed in section 5.3.1 and illustrated in Figure 5.4. Here, in Figure 6.14 we show explicitly the four Feynman diagrams contributing to the tree-level amplitude for this process. According to Figure 6.14, either of the leptons can emerge from the $\tilde{\chi}_2^0$ decay or from the decay of the slepton $\tilde{l}_L$ and the slepton $\tilde{l}_R$. Thus, for calculation purposes, it is useful to introduce the concept of *near lepton* and *far lepton*.

With *near lepton* we indicate the lepton $l_n^\pm$ emerging from the $\tilde{\chi}_2^0$ decay, whereas with *far lepton* we indicate the lepton $l_f^\mp$ emerging from the slepton decay. However, the near and far lepton cannot be distinguished experimentally.

For non-degenerate left- and right-handed sleptons, as in the scenarios investigated in section 7.2, in NWA the structure of the squared amplitude of this decay chain becomes much simpler. Indeed, the dependence of the momenta of the slepton and the $\tilde{\chi}_2^0$ on the external momenta is different in each of the four diagrams; consequentially, after fixing external momenta, only one diagram can have both the intermediate slepton and $\tilde{\chi}_2^0$ on-shell. Thus, at LO, in the limit $\frac{\Gamma}{m} \to 0$ for the sleptons and for $\tilde{\chi}_2^0$, the contribution from interferences between different diagrams vanishes. Naming $\mathcal{M}$ the tree-level amplitude for this process, at LO, the squared amplitude for this process corresponds to

$$|\mathcal{M}|^2 = |\mathcal{M}_a + \mathcal{M}_b + \mathcal{M}_c + \mathcal{M}_d|^2 \xrightarrow{\Gamma/m \to 0} |\mathcal{M}_a|^2 + |\mathcal{M}_b|^2 + |\mathcal{M}_c|^2 + |\mathcal{M}_d|^2 \,, \quad (6.55)$$

where the various $\mathcal{M}_i$ terms are the individual contributions from the four different Feynman diagrams in Figure 6.14. As usual for NWA, the intermediate particles can be treated on-shell and thus they induce different invariant-mass conditions on external particles for each $|\mathcal{M}_i|^2$ term.

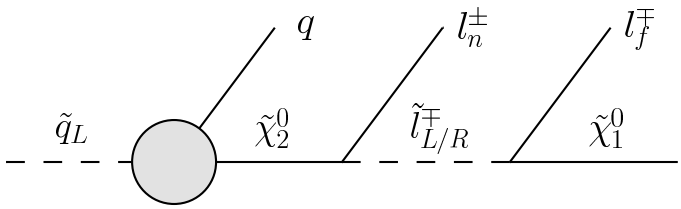

Figure 6.15: Structure of the decay chain. NLO QCD corrections involve only the first step $\tilde{q}_L \to q\tilde{\chi}_2^0$.

6.6.2 Distributions at NLO

The NLO corrections include virtual corrections, originating from the interference of tree-level and one-loop amplitudes, and real-gluon-emission corrections, originating from the squared real-gluon-emission amplitude.

The one-loop amplitudes can be illustrated as in Figure 6.15. This figure is not a Feynman diagram, however, it represents, in a compact notation, the NLO corrections to the four Feynman diagrams contributing to the tree-level amplitude for the decay, i.e., $\tilde{q}_L \to q l_n^+ l_f^- \tilde{\chi}_1^0$ and $\tilde{q}_L \to q l_n^- l_f^+ \tilde{\chi}_1^0$ with a left- or right-handed intermediate (anti)slepton. The NLO corrections do not involve the electroweak decay chain of the $\tilde{\chi}_2^0$. Thus, the NWA can also be applied in this case, leading to similar consequences to the ones indicated in eq. (6.55). Specifically, one obtains for the virtual part

$$\begin{aligned} 2Re(\mathcal{M}^*\mathcal{M}^{\text{loop}}) \xrightarrow{\Gamma/m\to 0} & 2Re(\mathcal{M}_a^*\mathcal{M}_a^{\text{loop}}) + 2Re(\mathcal{M}_b^*\mathcal{M}_b^{\text{loop}}) + \\ & 2Re(\mathcal{M}_c^*\mathcal{M}_c^{\text{loop}}) + 2Re(\mathcal{M}_d^*\mathcal{M}_d^{\text{loop}}) \,, \end{aligned} \tag{6.56}$$

where $\mathcal{M}^{\text{loop}}$ indicates the one-loop amplitude and $\mathcal{M}_i^{\text{loop}}$ are the one-loop corrections to $\mathcal{M}_i$ in Figure 6.14.

Also the real-emission corrections affect only the squark and the quark, so all the discussion for the LO and virtual contributions applies also in this case. Thus, the calculation of the decay distribution for the "golden decay chain", at LO or NLO QCD with intermediate on-shell particles, can be technically divided into two steps: the calculation at LO or NLO QCD of $\tilde{q}_L \to q\tilde{\chi}_2^0$, and the tree-level electroweak decay chain of $\tilde{\chi}_2^0$. In this way LO and NLO contributions can be written as follows,

$$d\Gamma^{(0,1)}_{\tilde{q}_L \to q l^+ l^- \tilde{\chi}_1^0} = \sum_{\sigma=\pm 1/2} \frac{d\Gamma^{(0,1)}_{\tilde{q}_L \to q\tilde{\chi}^0_{2,\sigma}}}{\Gamma_{\tilde{\chi}_2^0}} \left[d\Gamma_{\tilde{\chi}^0_{2,\sigma} \to l_n^+ l_f^- \tilde{\chi}_1^0} + d\Gamma_{\tilde{\chi}^0_{2,\sigma} \to l_n^- l_f^+ \tilde{\chi}_1^0} \right], \tag{6.57}$$

where the index σ represents the helicity of $\tilde{\chi}_2^0$, on which the terms entering eq. (6.57) depend. The two terms contained in the square brackets of eq. (6.57) correspond to the

two different charge configurations for near and far leptons in the decay of $\tilde{\chi}_2^0$, where both configurations get contributions from the left- and the right-handed slepton.

Technically, we use, both at LO and at NLO, the matrix elements for the entire chain and set consistently the different on-shell conditions according to the intermediate states for the various contributions. In this way, the sum over the helicity states is automatically performed and off-shell effects can be straightforwardly switched on for a further possible study. The calculation method discussed in section 6.5 can be applied also for this decay process, since it does not depend on the specification of the helicity of $\tilde{\chi}_2^0$ and on its subsequent decay.

For the concrete evaluation in specific cases, we concentrate on scenarios where the $\tilde{\chi}_2^0$ is dominantly wino-like. Thus, in the considered decay chain the coupling to a right-handed slepton, $\tilde{l}_R$, is heavily suppressed compared to the corresponding decay chain via a left-handed $\tilde{l}_L$. Only if the decay into a left-handed slepton is kinematically forbidden, $m_{\tilde{l}_L} > m_{\tilde{\chi}_2^0} > m_{\tilde{l}_R}$, the decay via a $\tilde{l}_R$ can substantially contribute. Moreover, the l^+ and l^- distributions are in general different in the decay chain from anti-squarks $\tilde{q}_L^*$, thus we generate separate events for squarks and anti-squarks "golden decay chains".

Basically, also the decay of the $\tilde{\chi}_2^0$ into a OS-SF lepton pair via a Z boson contributes when kinematically allowed; these effects are, however, numerically not significant for the benchmark points considered in section 7.2.

6.7 Squark total decay widths

6.7.1 Decay widths at LO

The total squark decay width $\Gamma_{\tilde{q}}^{(0)}$ at LO, assuming $m_{\tilde{g}} > m_{\tilde{q}}$, is obtained by summing the partial decay widths of the six different possible decay channels into neutralinos (four channels) and charginos (two channels). The partial decay widths into neutralinos are directly given by eq. (6.46). For charginos, the partial decay widths $\Gamma^{(0)}_{\tilde{q}\to q'\tilde{\chi}_j^\pm}$ are also described by the formula (6.46), with the specification $f_R = 0$ and

$$f_L = \frac{V_{j1}}{s_W} \quad \text{for} \quad \tilde{q} = \tilde{u}, \tilde{c}, \qquad f_L = \frac{U_{j1}}{s_W} \quad \text{for} \quad \tilde{q} = \tilde{d}, \tilde{s}, \tag{6.58}$$

for the coupling constants. Here, U and V are the mixing matrices in the chargino sector defined in eq. (5.11).

6.7.2 Decay widths at NLO

For the total decay width at NLO, one has to calculate the NLO QCD corrections for each of the six channels. We can calculate analytically both the contributions from loop

corrections and real gluon radiation. The second contribution is obtained performing the full phase-space integration over the three-particle final state.

The calculation can be done once for all the six partial decay widths contributing to $\Gamma_{\tilde{q}}^{(0+1)}$. At NLO, each partial width can be expressed in terms of their respective LO result and a NLO form factor F^{QCD},

$$\Gamma^{(0+1)}_{\tilde{q}\to q\tilde{\chi}_j^0/q'\tilde{\chi}_j^\pm} = \Gamma^{(0)}_{\tilde{q}\to q\tilde{\chi}_j^0/q'\tilde{\chi}_j^\pm}\left[1+\frac{4}{3}\frac{\alpha_s}{\pi}F^{QCD}\left(\frac{m_{\tilde{\chi}_j^0/\tilde{\chi}_j^\pm}}{m_{\tilde{q}}},\frac{m_{\tilde{q}}}{m_{\tilde{g}}}\right)\right]. \tag{6.59}$$

The factor F^{QCD} depends only on two independent ratios involving the masses of the neutralino/chargino, the squark and the gluino, e.g.,

$$\kappa = \left(\frac{m_{\tilde{\chi}_j^0/\tilde{\chi}_j^\pm}}{m_{\tilde{q}}}\right)^2, \qquad \gamma = \left(\frac{m_{\tilde{g}}}{m_{\tilde{q}}}\right)^2. \tag{6.60}$$

Here, we perform the derivation of the form factor F^{QCD}, following the steps of the former calculation [34], but keeping explicitly the dependence on the masses m_q for the collinear singularities and λ for the IR singularities. The form factor F^{QCD} receives four contributions,

$$F^{\mathrm{QCD}} = F_g + F_{\tilde{g}} + F_{ct} + F_r\,, \tag{6.61}$$

namely loop corrections involving gluons (F_g) and gluinos ($F_{\tilde{g}}$), the counterterm contribution (F_{ct}), and the contribution from real gluon emission (F_r) .

Keeping m_q and λ as independent mass parameters for the singular terms, in dimensional reduction F_g and F_{ct} can be written as follows,

$$\begin{aligned} F_g =& \frac{\Delta}{2} - \frac{1}{2}\log\left(\frac{m_{\tilde{q}}^2}{\mu^2}\right) + 1 - \log\left(\frac{m_q^2}{m_{\tilde{q}}^2}\right) + \frac{1}{4}\log^2\left(\frac{m_q^2}{m_{\tilde{q}}^2}\right) - \frac{1}{2}\log\left(\frac{\lambda^2}{m_{\tilde{q}}^2}\right)\log\left(\frac{m_q^2}{m_{\tilde{q}}^2}\right) \\ &+ \log\left(\frac{\lambda^2}{m_{\tilde{q}}^2}\right)\log(1-\kappa) - \log^2(1-\kappa) + \log(1-\kappa) - \mathrm{Li}_2(\kappa)\,, \end{aligned} \tag{6.62}$$

$$\begin{aligned} F_{\mathrm{ct}} =& -\frac{\Delta}{2} + \frac{1}{2}\log\left(\frac{m_{\tilde{q}}^2}{\mu^2}\right) - \log\left(\frac{\lambda^2}{m_{\tilde{q}}^2}\right) + \frac{3}{4}\log\left(\frac{m_q^2}{m_{\tilde{q}}^2}\right) + \frac{\gamma}{4\,(1-\gamma)} - \frac{\gamma}{2} - \frac{15}{8} \\ &- \frac{1}{2}(\gamma^2-1)\log\left(\frac{\gamma-1}{\gamma}\right) + \frac{1}{4}\left[\frac{2\,\gamma-1}{(1-\gamma)^2}+3\right]\log(\gamma)\,, \end{aligned} \tag{6.63}$$

where Δ denotes the UV divergence, cf. eq. (6.19), and κ and γ are defined in eq. (6.60).

$F_{\tilde{g}}$ is free of soft, collinear, and UV singularities, hence it is not affected by the choice of regulators,

$$F_{\tilde{g}} = \sqrt{\kappa\gamma}\left[\frac{1}{\kappa}\ln(1-\kappa) + \frac{1}{1-\kappa}\left[\gamma\ln\gamma - (\gamma-1)\ln(\gamma-1)\right] + \frac{\kappa+\gamma-2}{(1-\kappa)^2}\,I_{\tilde{g}}\right]. \tag{6.64}$$

The function $I_{\tilde{g}}$ is given, for $\kappa\gamma < 1$, by

$$I_{\tilde{g}} = \mathrm{Li}_2\left(\frac{\gamma-1}{\gamma\kappa-1}\right) - \mathrm{Li}_2\left(\kappa\frac{\gamma-1}{\gamma\kappa-1}\right) - \mathrm{Li}_2\left(\frac{\gamma+\kappa-2}{\gamma\kappa-1}\right) + \mathrm{Li}_2\left(\kappa\frac{\gamma+\kappa-2}{\gamma\kappa-1}\right),$$

and for $\kappa\gamma > 1$ by

$$\begin{aligned} I_{\tilde{g}} \;=\; & -\mathrm{Li}_2\left(\frac{\gamma\kappa-1}{\gamma-1}\right) + \mathrm{Li}_2\left(\frac{\gamma\kappa-1}{\gamma+\kappa-2}\right) + \mathrm{Li}_2\left(\frac{\gamma\kappa-1}{\kappa(\gamma-1)}\right) - \mathrm{Li}_2\left(\frac{\gamma\kappa-1}{\kappa(\gamma+\kappa-2)}\right) \\ & - \log(\kappa)\,\log\frac{\gamma+\kappa-2}{\gamma-1}\,. \end{aligned}$$

The part from real gluon emission, integrated over the full phase space, can be expressed with the help of the bremsstrahlung integrals given in [124], evaluated in the limit $m_q = 0$ except for the mass-singular terms. The fully integrated decay width for $\tilde{q} \to (q\tilde{\chi}_j^0/q'\tilde{\chi}_j^\pm)g$ can be written as follows,

$$\Gamma_{\tilde{q}\to(q\tilde{\chi}_j^0/q'\tilde{\chi}_j^\pm)g} = \Gamma^{(0)}_{\tilde{q}\to q\tilde{\chi}_j^0/q'\tilde{\chi}_j^\pm} \cdot \frac{4}{3}\frac{\alpha_s}{\pi}\,F_r\,, \tag{6.65}$$

$$F_r = \frac{2}{m_{\tilde{q}}^2 - m_{\tilde{\chi}}^2}\left[2(m_{\tilde{\chi}}^2 - m_{\tilde{q}}^2)\,(m_{\tilde{q}}^2\,I_{00} + m_q^2\,I_{11} + I_0 + I_1) - 2(m_{\tilde{\chi}}^2 - m_{\tilde{q}}^2)^2\,I_{01} - I - I_1^0\right]$$

with $\Gamma^{(0)}_{\tilde{q}\to q\tilde{\chi}_j^0/q'\tilde{\chi}_j^\pm}$ from eq. (6.46) and (6.58). The phase-space integrals $I \equiv I(m_{\tilde{q}}, m_q, m_{\tilde{\chi}})$ are given by

$$\begin{aligned} I_{00} =& \frac{1}{4\,m_{\tilde{q}}^4}\left[m_{\tilde{\chi}}^2 - m_{\tilde{q}}^2 + m_{\tilde{q}}^2\log\left[\frac{m_{\tilde{q}}^2 - m_{\tilde{\chi}}^2}{\lambda m_{\tilde{q}}}\right] + m_{\tilde{\chi}}^2\log\left[\frac{\lambda m_{\tilde{\chi}}^2}{m_{\tilde{q}}^3 - m_{\tilde{q}}m_{\tilde{\chi}}^2}\right]\right], \\ I_{11} =& \frac{1}{4\,m_q^2\,m_{\tilde{q}}^2}\,(m_{\tilde{q}}^2 - m_{\tilde{\chi}}^2)\left[\log\left(\frac{m_q}{\lambda}\right) - 1\right], \\ I_{01} =& \frac{1}{4\,m_{\tilde{q}}^2}\left[\frac{\pi^2}{2} + \log^2\left(\frac{m_q}{\lambda}\right) - \log^2\left(\frac{m_{\tilde{q}}^2 - m_{\tilde{\chi}}^2}{\lambda m_{\tilde{q}}}\right) - \mathrm{Li}_2\left(1 - \frac{m_{\tilde{\chi}}^2}{m_{\tilde{q}}^2}\right)\right], \\ I =& \frac{1}{8\,m_{\tilde{q}}^2}\left[m_{\tilde{q}}^4 - m_{\tilde{\chi}}^4 + 4m_{\tilde{\chi}}^2 m_{\tilde{q}}^2\log\left(\frac{m_{\tilde{\chi}}}{m_{\tilde{q}}}\right)\right], \end{aligned}$$

$$\begin{aligned} I_0 =& \frac{1}{4\,m_{\tilde{q}}^2}\left[m_{\tilde{\chi}}^2 - m_{\tilde{q}}^2 - 2m_{\tilde{\chi}}^2\,\log\left(\frac{m_{\tilde{\chi}}}{m_{\tilde{q}}}\right)\right], \\ I_1 =& \frac{1}{4\,m_{\tilde{q}}^2}\left[m_{\tilde{\chi}}^2 - m_{\tilde{q}}^2 + 2m_{\tilde{\chi}}^2\,\log\left(\frac{m_q m_{\tilde{\chi}}}{m_{\tilde{q}}^2 - m_{\tilde{\chi}}^2}\right) - 2m_{\tilde{q}}^2\,\log\left(\frac{m_q m_{\tilde{q}}}{m_{\tilde{q}}^2 - m_{\tilde{\chi}_j^0}^2}\right)\right], \\ I_1^0 =& \frac{1}{16\,m_{\tilde{q}}^2}\left[5m_{\tilde{\chi}}^4 - 8m_{\tilde{\chi}}^2 m_{\tilde{q}}^2 + 3m_{\tilde{q}}^4 + 4(m_{\tilde{\chi}}^4 - 2m_{\tilde{\chi}}^2 m_{\tilde{q}}^2)\,\log\left(\frac{m_q m_{\tilde{\chi}}}{m_{\tilde{q}}^2 - m_{\tilde{\chi}}^2}\right)\right. \\ & \left. +\; 4m_{\tilde{q}}^4\,\log\left(\frac{m_q m_{\tilde{q}}}{m_{\tilde{q}}^2 - m_{\tilde{\chi}}^2}\right)\right]. \end{aligned} \tag{6.66}$$

With these expressions, eq. (6.65) yields F_r for the real-gluon part of F^{QCD} in eq. (6.61),

$$\begin{aligned} F_r = \quad & \frac{-5+8\kappa-3\kappa^2-8\kappa\log(\kappa)+6\kappa^2\log(\kappa)}{8(1-\kappa)^2} \\ & +4-\frac{\pi^2}{2}-\frac{5}{2}\log(1-\kappa)+\log(1-\kappa)^2-\log^2\left(\frac{m_q}{\lambda}\right)+2\log\left(\frac{m_{\tilde{q}}}{\lambda}\right) \\ & +\frac{1}{2}\log\left(\frac{m_q}{m_{\tilde{q}}}\right)+2\log(1-\kappa)\log\left(\frac{m_{\tilde{q}}}{\lambda}\right)+\log^2\left(\frac{m_{\tilde{q}}}{\lambda}\right)+\mathrm{Li}_2\left(1-\kappa\right) . \end{aligned} \tag{6.67}$$

Combining all four contributions in eq. (6.61) we obtain a compact analytical expression for the form factor F^{QCD}, which agrees with the result in [34],

$$\begin{aligned} & F^{\mathrm{QCD}} = F_{\mathrm{g}}+F_{\tilde{\mathrm{g}}}+F_{\mathrm{ct}}+F_{\mathrm{r}} = \\ & -\frac{1}{8}\left(\frac{4\,\gamma^2-27\,\gamma+25}{\gamma-1}+\frac{3\,\kappa-5}{\kappa-1}\right)-\frac{\pi^2}{3}-2\,\mathrm{Li}_2(\kappa)-\frac{1}{2}\left(\gamma^2-1\right)\,\log\left(\frac{\gamma-1}{\gamma}\right) \\ & +\frac{3\,\gamma^2-4\,\gamma+2}{4\,(1-\gamma)^2}\,\log\left(\gamma\right)-\frac{3}{2}\,\log(1-\kappa)+\frac{1}{4}\cdot\frac{3\,\kappa^2-4\,\kappa}{(\kappa-1)^2}\,\log\left(\kappa\right)-\log\left(\kappa\right)\,\log(1-\kappa) \\ & +\sqrt{\kappa\gamma}\left[\frac{1}{\kappa}\log(1-\kappa)+\frac{1}{1-\kappa}\left[\gamma\log(\gamma)-(\gamma-1)\log(\gamma-1)\right]+\frac{\kappa+\gamma-2}{(1-\kappa)^2}\,I_{\tilde{g}}\right] , \end{aligned} \tag{6.68}$$

In the threshold limit $m_{\tilde{\chi}_j^0/\tilde{\chi}_j^\pm} \to m_{\tilde{q}}$ the correction in eq. (6.68) becomes very large, as already shown in Figure 5.6, and the fixed-order calculation is not reliable (relative corrections remain finite only after proper resummation, see for example [35]). However, for all parameter points considered in the numerical evaluation in chapter 7 the corrections are still sufficiently small and threshold problems are negligible.

Chapter 7

Squark–squark production and decay: numerical results

In this chapter we show, in section 7.1, numerical results for the $pp \to \tilde{q}\tilde{q}' \to q\tilde{\chi}_1^0 q'\tilde{\chi}_1^0$ contribution to the experimental signature $2j + \not{E}_T(+X)$ and, in section 7.2, numerical results for the $pp \to \tilde{q}_L\tilde{q}'_R \to q\tilde{\chi}_1^0 q' l^{\pm} l^{\mp}\tilde{\chi}_1^0$ contribution to the experimental signature $2j + l^+l^-(\text{OS-SF}) + \not{E}_T(+X)$.

7.1 The signature $\mathbf{2j + \not{E}_T(+X)}$

In this section, we first specify in 7.1.1 the input parameters and benchmark scenarios considered in our numerical evaluation and we introduce in 7.1.2 all considered distributions and observables. Then, we present our numerical results focusing on three different kinds of quantities:

- inclusive cross sections,
- differential distributions,
- event rates in cut-and-count searches.

Firstly, in 7.1.3, we compare our results for inclusive production of squark–squark pairs with results of *Prospino 2*, which, as already said, is used in most of the experimental analyses for calculating inclusive K-factors, and we investigate how these inclusive K-factors vary for different chirality and flavor configurations. Secondly, in 7.1.4, we present several differential distributions for various benchmark scenarios and center-of-mass energies, comparing our results in our approximation and at LO rescaled by a flat K-factor. Thirdly, using again these two different approximations, in 7.1.5 we investigate the impact of higher-order corrections on total event rates and thus on cut-and-count searches for supersymmetry at the LHC.

7.1.1 Input parameters

Standard Model input parameters are chosen according to [126],

$$M_Z = 91.1876 \text{ GeV}, \quad M_W = 80.399 \text{ GeV}, \quad G_F = 1.16637 \cdot 10^{-5} \text{ GeV},$$
$$m_b^{\overline{\text{MS}}}(m_b) = 4.2 \text{ GeV}, \quad m_t = 173.3 \text{ GeV}, \quad m_\tau = 1.777 \text{ GeV}. \tag{7.1}$$

We use the PDF sets CTEQ6.6 [144] via the Les Houches Accord PDF Interface (LHAPDF) package [279] both for LO and NLO contributions. The strong coupling constant $\alpha_s^{\overline{\text{MS}}}(\mu_R)$ is also taken from this set of PDFs. Factorization scale μ_F and renormalization scale μ_R are, if not stated otherwise, set to a common value, $\mu = \mu_F = \mu_R = \overline{m_{\tilde{q}}}$, with $\overline{m_{\tilde{q}}}$ corresponding to the average mass of all light-flavor squarks of a given benchmark point. The same α_s value has been used in the numerical evaluation of corrections to the decays and of LO and NLO production, as it would be naturally done in the complete NLO corrections to the full process.

For SUSY parameters, we refer to three different benchmark scenarios. First, we investigate the well studied Constrained MSSM (CMSSM) parameter point SPS1a [280]. Although it is excluded by recent searches at the LHC [281–283], this point still serves as a valuable benchmark for comparisons with numerous numerical results available in the literature. Second, we study the benchmark point CMSSM10.1.5 introduced in [284]. Due to its larger $m_{1/2}$ parameter, compared to SPS1a, squark and gluino masses are considerably larger, resulting in a generally reduced production cross section at the LHC. The overall spectrum is very similar to the one of SPS1a, but shifted to larger masses. Third, we consider a phenomenological benchmark point defined at the scale $Q = 1$ TeV. We follow the definitions of [284], where such a point sits on a line called p19MSSM1, which can be parametrized by essentially one parameter, the gaugino mass parameter M_1. On this line, a unified parameter for the gluino and the light-generations sfermion soft masses $M_3 = m_{\tilde{f}_{L/R}^{\text{1st/2nd gen}}}$ is fixed to $M_3 = m_{\tilde{f}_{L/R}^{\text{1st/2nd gen}}} = 1.2\ M_1$. For our benchmark scenario p19MSSM1A we choose $M_1 = 300$ GeV. All other masses and parameters as well as the soft masses for right-handed sleptons of the first two generations are at a higher scale and irrelevant for our analysis. This scenario belongs to the class of the compressed spectra discussed in section 5.3.1. It has been chosen to study a particular parameter region with rather light squarks, which is difficult to exclude experimentally, since the mass difference between squarks and the lightest neutralino $\Delta(m_{\tilde{q}}, m_{\tilde{\chi}_1^0})$ is small and thus resulting jets tend to be very soft, escaping the experimental analyses. Particularly in such parameter regions precise theoretical predictions of the resulting SUSY signal including higher orders on the level of distributions seem to be necessary for a conclusive study.

Parameters of the CMSSM benchmark scenarios are defined universally at the GUT scale and are shown in Table 7.1. They act as boundary conditions for the renormalization group running of the soft-breaking parameters down to the scale m_{soft}. This

benchmarkpoint	m_0	$m_{1/2}$	A_0	tan	sign(μ)
SPS1a	100 GeV	250 GeV	−100 GeV	10	+
10.1.5	175 GeV	700 GeV	0	10	+

Table 7.1: High-energy input parameters for the two considered CMSSM scenarios.

benchmarkpoint	M_1	M_2	M_3	A_i	tan	sign(μ)
p19MSSM1A	300 GeV	2500 GeV	360 GeV	0	10	+

Table 7.2: Low-energy input parameters for the p19MSSM1A scenario. The first two generation sfermion soft-masses (apart from the right handed sleptons) equal the gluino mass $m_{\tilde{f}^{\text{1st/2nd gen}}_{L/R}} = M_3$. All other parameters are at a higher scale $m_{\tilde{f}^{\text{3rd gen}}_{L/R}} = m_{\tilde{e}_R,\tilde{\mu}_R} = \mu = M_A = M_2$.

benchmarkpoint	$\tilde{u}_L$	$\tilde{u}_R$	$\tilde{d}_L$	$\tilde{d}_R$	$\tilde{g}$	$\tilde{\chi}^0_1$
SPS1a	563.6	546.7	569.0	546.6	608.5	97.0
10.1.5	1437.7	1382.3	1439.7	1376.9	1568.6	291.3
p19MSSM1A	339.6	394.8	348.3	392.7	414.7	299.1

Table 7.3: On-shell masses of the squarks, the gluino, and the lightest neutralino within the different SUSY scenarios considered. All masses are given in GeV.

running has been evaluated with the program *SOFTSUSY* [285], which also calculates physical on-shell parameters for all SUSY mass eigenstates to be used directly as inputs for our calculation. Low-scale soft input parameters for the p19MSSM1A benchmark scenario are given in Table 7.2. The physical spectrum is equivalently calculated with *SOFTSUSY*. For all considered benchmark scenarios we summarize relevant low energy physical masses in Table 7.3. Due to non-vanishing Yukawa corrections implemented in *SOFTSUSY*, the physical on-shell masses for second-generation squarks are slightly different from their first-generation counterparts. To simplify our numerical evaluation we set all second-generation squark masses to their first-generation counterparts. However, the general setup of our calculation is independent of this choice. We checked that in the results this adjustment is numerically negligible.

For all considered benchmark scenarios the gluino is heavier than all light-flavor squarks, $m_{\tilde{g}} > m_{\tilde{q}}$. Thus, squarks decay only into electroweak gauginos and quarks. For SPS1a and 10.1.5, right-handed squarks dominantly decay directly into the lightest neutralino $\tilde{\chi}^0_1$ (due to its bino nature). On the contrary, left-handed squarks decay dominantly into heavier (wino-like) neutralinos and charginos. Consequently, left-handed squarks suppress the contribution to the experimental signature investigated in this section. However, for point p19MSSM1A, all neutralinos and charginos, but the lightest one, are heavier than any light-flavor squark. Thus, only the direct decay is

benchmarkpoint		$\tilde{u}_L$	$\tilde{u}_R$	$\tilde{d}_L$	$\tilde{d}_R$	$\tilde{g}$
SPS1a	$\Gamma^{(0)}$	5.361	1.148	5.253	0.287	6.849
	$\Gamma^{(0+1)}$	5.357	1.131	5.255	0.283	
10.1.5	$\Gamma^{(0)}$	12.47	2.854	12.46	0.710	10.04
	$\Gamma^{(0+1)}$	12.31	2.821	12.30	0.702	
p19MSSM1A	$\Gamma^{(0)}$	$2.414 \cdot 10^{-3}$	0.1625	$3.411 \cdot 10^{-3}$	$3.917 \cdot 10^{-2}$	3.441
	$\Gamma^{(0+1)}$	$2.497 \cdot 10^{-3}$	0.1621	$3.503 \cdot 10^{-3}$	$3.912 \cdot 10^{-2}$	

Table 7.4: Leading order $\Gamma^{(0)}$ and next-to-leading order $\Gamma^{(0+1)}$ total widths of light squarks and gluinos for the considered SUSY scenarios. All widths are given in GeV.

allowed and all channels equally contribute to the signature under consideration.

In Table 7.4 we list, at LO and NLO, all the total decay widths of the squarks, calculated as explained in section 6.5 and entering eq. (6.8) for the different flavor and chirality configurations. NLO corrections in the total decay widths are of the order of a few percent for all three benchmark scenarios. In the numerical evaluation of these corrections we observed a disagreement with the partial decay widths at NLO for p19MSSM1A obtained from *SDECAY*, which includes as NLO contributions exactly the analytical results calculated in [34] and in section 6.7.2. After corresponding with the authors, this problem was solved by correcting a typo in *SDECAY*.

In Table 7.4 we list also the total decay width of the gluino, calculated with *SDECAY* at LO. In the calculation presented here this width is not used explicitly. Instead, we numerically employ the limit $\Gamma_{\tilde{g}} \to 0$. However, we checked that, using the physical widths, all the results showed in the following present negligible differences.

Besides physical quantities, in our calculation phase-space-slicing and regulator parameters enter as inputs in the calculation of virtual and real NLO contributions, as explained in sections 6.4 and 6.5. In the results of this section, we set $\delta_s = 2\Delta E/\sqrt{s} = 2 \cdot 10^{-4}$, $\delta_\theta = \Delta\theta^2/2 = 10^{-4}$ and $m_q = 10^{-1.5}$ GeV, both for production and decay. Numerically we checked carefully that varying their values our results remain unchanged on the level of individual distributions once jets are recombined using a clustering algorithm, as explained below. We made sure that this holds for all terms of eq. (6.8) individually.

As illustration, we show in Figure 7.1 the dependence on the slicing parameters of the contributions to the NLO QCD corrections to the inclusive $\sigma_{pp\to\tilde{u}_1\tilde{u}_1}$ (top plots) and $\Gamma_{\tilde{u}_2\to u\tilde{\chi}_1^0}$ (bottom plots). In the plots on the left we show the dependence on $\Delta\theta$, via δ_θ, for a fixed value of δ_s. In the plots on the right we show the dependence on ΔE, via δ_s, for a fixed value of δ_θ. All the plots are for SPS1a at the LHC with $\sqrt{S} = 14$ TeV.

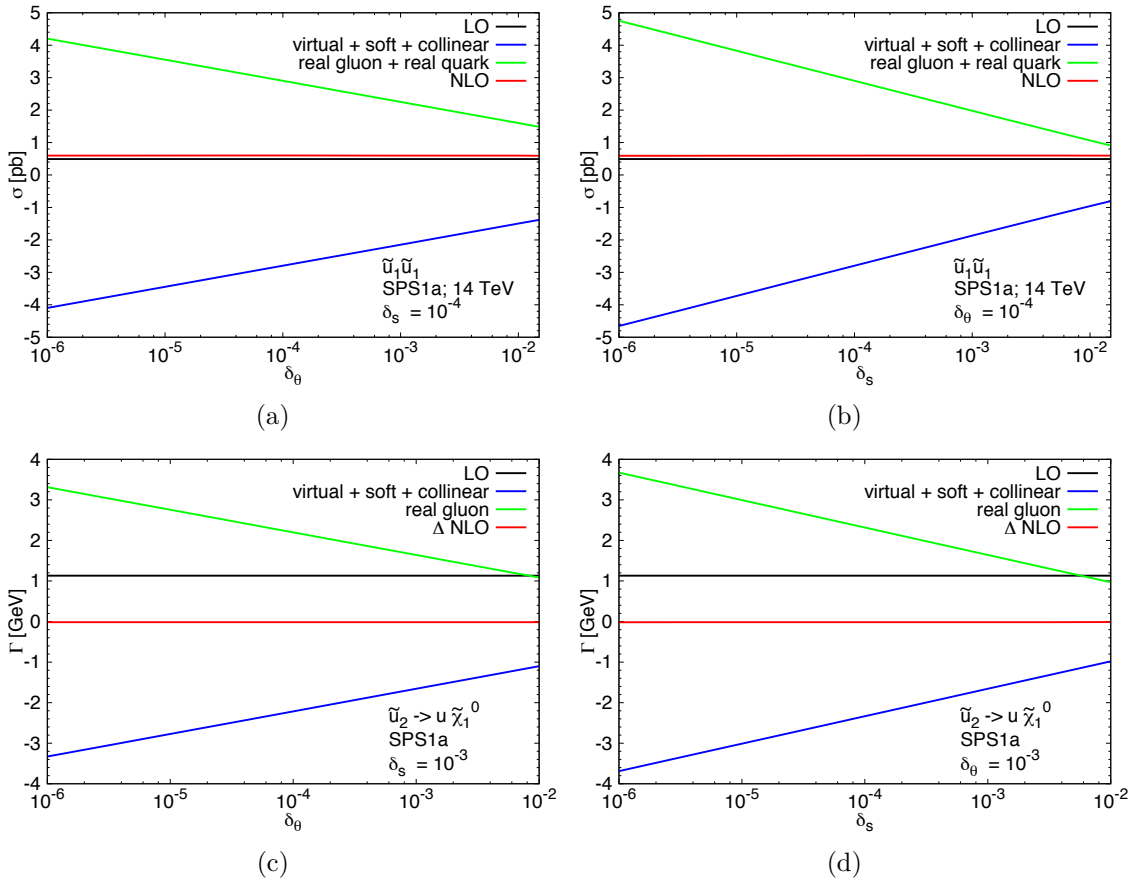

Figure 7.1: Dependence of contributions to NLO corrections on slicing parameters. Top plots: $\tilde{u}_1\tilde{u}_1$ production channel, dependence on $\Delta\theta$ (left) and dependence on ΔE (right). Bottom plots: $\tilde{u}_2$ decay, dependence on $\Delta\theta$ (left) and dependence on ΔE (right).

7.1.2 Observables and kinematical cuts

In order to arrive at an experimentally well defined two-jet-signature we always employ the anti-k_T jet clustering algorithm [286] implemented in *FastJet 3.0.2* [287]. Thus, we provide a realistic prediction on the level of partonic jets, i.e., jet clustering algorithm is applied to events produced from our calculation, but no QCD showering or hadronization is included in the simulation.

In general we use a jet radius[1] of $R = 0.4$, as in the SUSY searches performed by the ATLAS collaboration [282]. CMS instead uses a radius of $R = 0.5$ [281]. We employ $R = 0.5$ in the distributions and signal regions used by CMS (i.e. particularly the α_T

[1]In the anti-k_T jet clustering algorithm, the definition of the measure of the distance between two jets involves the parameter $R = \sqrt{(\eta_1 - \eta_2)^2 + (\phi_1 - \phi_2)^2}$, where $\eta_1(\eta_2)$ and $\phi_1(\phi_2)$ are respectively the pseudorapidity and the azimuthal angle of the first(second) jet.

distribution as described below). Our results seem to be independent of the choice between $R = 0.4$ and $R = 0.5$, however, we did not perform a systematic study. After performing the jet clustering we sort the partonic jets by their transverse momentum p^{T} and we keep only jets with

$$p^{\mathrm{T}}_{j_{1/2}} > 20 \text{ GeV}, \quad |\eta_j| < 2.8, \tag{7.2}$$

$$p^{\mathrm{T}}_{j_i} > 50 \text{ GeV}, \quad |\eta_j| < 3.0 \text{ (for CMS observables)}\,. \tag{7.3}$$

Cuts of eq. (7.2) are used for all the differential distributions, but in the observables used specifically by CMS (α_T and H_T), where we apply cuts of eq. (7.3).

In section 7.1.4 we investigate the effect of NLO corrections, for the different benchmark points, on the differential distributions listed in the following:

- the transverse momentum of the two hardest jets p^{T}_1 and p^{T}_2,
- the pseudorapidity of the two hardest jets η_1 and η_2,
- the missing transverse energy $\not{E}_T$,
- the effective mass $m_{\text{eff}} = \sum_{i=1,2} p^{\mathrm{T}}_i + \not{E}_T$,
- the scalar sum of the p^{T} of all jets (visible after cuts of eq. (7.3)), $H_T = \sum_{i=1,2(,3)} p^{\mathrm{T}}_i$,
- the invariant mass of the two hardest jets $m_{\text{inv}}(jj)$,
- the cosine of the angle between the two hardest jets $\cos\Theta_{jj}$, which depends on the spin of the produced particles and therefore might help to distinguish SUSY from other BSM models [263],
- $\cos\hat{\Theta} = \tanh\left(\frac{\Delta\eta_{jj}}{2}\right)$, $\Delta\eta_{jj} = \eta_1 - \eta_2$, introduced in [288] as a possible observable for early spin determination at the LHC,
- the α_T variable described in section 5.3.1. In all α_T distributions we require $H_T > 350$ GeV as in [145].

Searches for sparticle production performed by ATLAS are based on p^{T}, $\not{E}_T$ and m_{eff} cuts; CMS instead uses α_T to reduce SM backgrounds. In section 7.1.5 we examine NLO corrections in the resulting event rates after cuts. Explicitly we employ the following cuts used by ATLAS,

$$\begin{gathered} p^{\mathrm{T}}_{j_1} > 130 \text{ GeV},\ p^{\mathrm{T}}_{j_2} > 40 \text{ GeV},\ |\eta_{j_{1/2}}| < 2.8,\ \Delta\phi(j_{1/2}, \vec{\not{E}}_T) > 0.4, \\ m_{\text{eff}} > 1 \text{ TeV},\ \not{E}_T/m_{\text{eff}} > 0.3, \end{gathered} \tag{7.4}$$

in their two-jet analysis [282]. Here, $\Delta\phi(j_{1/2}, \vec{\not\!\!E}_T)$ denotes, for the two hardest jets, the angular separation with the direction of the missing transverse energy. Instead, the CMS signal region [145] is defined as

$$\begin{aligned} p_{j_{1/2}}^{\mathrm{T}} > 100 \text{ GeV},\ |\eta_{j_1}| < 2.5,\ |\eta_{j_2}| < 3.0, \\ H_T > 350 \text{ GeV},\ \not\!\!H_T/\not\!\!E_T < 1.25,\ \alpha_T > 0.55, \end{aligned} \tag{7.5}$$

where $\not\!\!H_T$ is calculated from the vectorial sum $\vec{H}_T$ of the p^{T} of the jets.

7.1.3 Inclusive cross sections

In Table 7.5 we list inclusive LO cross sections and corresponding NLO K-factors for the three benchmark scenarios SPS1a, 10.1.5, p19MSSM1A, varying the LHC center-of-mass energy $\sqrt{S} = 7, 8, 14$ TeV. K-factors, here and in the following, are always defined as ratios between NLO and LO predictions, where both are calculated using the same NLO PDFs and associated α_s. On the one hand, we list inclusive cross sections, $\sigma^{(0)}_{pp\to\tilde{q}\tilde{q}'}$, and K-factors for just the production of squark–squark pairs summed over all flavor and chirality configuration. These K-factors are calculated in the DR scheme defined in section 6.4.3, which is always used in this chapter, if not stated otherwise. On the other hand, we list cross section predictions for combined production and decay at LO $\sigma^{(0)}_{2j+\not\!\!E_T(+X)}$ and the corresponding NLO K-factors $K_{2j+\not\!\!E_T(+X)}$ calculated using eq. (6.8), summed over all flavor and chirality configurations. Here, cuts defined in eq. (7.2) are also applied and cross sections are strongly decreased due to the branching ratios for the lightest neutralino. In this way we investigate at the same time the approximations indicated in the first and second point of the list on page 76.

All K-factors of the combined process are bigger than the corresponding K-factors of inclusive production. For point 10.1.5 (and thus rather heavy squarks) these increments are less than 0.05. For the other two benchmark points (and thus smaller squark masses) increments in the K-factors can be of the order of 0.1 and increase with higher center-of-mass energies. In general, however, K-factors decrease with higher center-of-mass energies and increase with higher masses, both for inclusive production and for combined production and decay.

In Table 7.6 we compare the inclusive production with the combined production and decay for benchmark point 10.1.5 at a center-of-mass energy of $\sqrt{S} = 14$ TeV. Here, we list results for individual flavor and chirality configurations. In general, our calculation is set up to treat all $36 + c.c$ possible flavor and chirality combinations independently. However, for simplicity and to save computing time, we always sum combinations with identical masses and matrix elements, obtaining 16 channels for the production and thus for the combination. This categorization depends on the four possible LO cross sections discussed in section 6.4.1. For example, the channel $\tilde{u}_L\tilde{u}_L$ also includes $\tilde{c}_L\tilde{c}_L$ (and as everywhere else in this study, the charge-conjugate processes).

benchmark	$\sqrt{S}$ [TeV]	$\sigma^{(0)}_{pp\to\tilde{q}\tilde{q}'}$	$K^{DR}_{pp\to\tilde{q}\tilde{q}'}$	$\sigma^{(0)}_{2j+\not{E}_T(+X)}$	$K_{2j+\not{E}_T(+X)}$
SPS1a	7	1.02 pb	1.37	0.37 pb	1.41
	8	1.49 pb	1.35	0.53 pb	1.40
	14	5.31 pb	1.28	1.74 pb	1.36
10.1.5	7	0.90 fb	1.57	0.45 fb	1.61
	8	2.62 fb	1.52	1.24 fb	1.56
	14	50.04 fb	1.40	20.41 fb	1.44
p19MSSM1A	7	7.90 pb	1.40	6.31 pb	1.50
	8	10.48 pb	1.39	8.35 pb	1.50
	14	29.01 pb	1.34	22.60 pb	1.47

Table 7.5: LO cross sections $\sigma^{(0)}_{pp\to\tilde{q}\tilde{q}'}$ and NLO K-factors for inclusive squark–squark production, $K^{DR}_{pp\to\tilde{q}\tilde{q}'}$, LO cross sections of inclusive combined squark–squark production and decay $\sigma^{(0)}_{2j+\not{E}_T(+X)}$ and corresponding K-factor $K_{2j+\not{E}_T(+X)}$, for the three benchmark scenarios SPS1a, 10.1.5, p19MSSM1A and center-of-mass energies $\sqrt{S} = 7, 8, 14$ TeV. In the combined predictions cuts of eq. (7.2) are applied.

Similarly, the channel $\tilde{u}_L\tilde{d}_L$ also includes $\tilde{c}_L\tilde{s}_L$, $\tilde{u}_L\tilde{s}_L$ and $\tilde{c}_L\tilde{d}_L$; and the channel $\tilde{u}_L\tilde{c}_R$ also includes $\tilde{u}_R\tilde{c}_L$. K-factors, both, in just the production and in the combined result, vary by up to 0.15 between different channels[2]. Moreover, already at LO, the contributions to $\sigma^{(0)}_{pp\to\tilde{q}\tilde{q}'}$ and $\sigma^{(0)}_{2j+\not{E}_T(+X)}$ are very different for every channel. At the level of just squark–squark production, $\sigma^{(0)}_{pp\to\tilde{q}\tilde{q}'}$, besides a dependence on the chirality configuration, the main differences originate from the flavor configurations, i.e., from the contribution from PDFs in the initial states. At the level of experimental signature, $\sigma^{(0)}_{2j+\not{E}_T(+X)}$, the main differences are due to the chirality configurations. This can easily be seen from the very different order of magnitude of the various values of $\sigma^{(0)}_{2j+\not{E}_T(+X)}$ in Table 7.6. For a given flavor configuration in Table 7.6, the contribution to $\sigma_{2j+\not{E}_T(+X)}$ from the right–right configuration is typically 2 orders of magnitude larger than the one from the left–right configuration and 4 orders of magnitudes larger than the one from the left–left configuration. The suppression from left-handed squarks depends on the branching ratio of the $\tilde{q}_L \to q\tilde{\chi}^0_1$ decay, which is very small for CMSSM 10.1.5. This is different, e.g., for the point p19MSSM1A, where $\tilde{q} \to \tilde{\chi}^0_1 q$ is the only decay kinematically allowed and thus its branching ratio is equal to one, independently from the chirality of the squark. Thus, an independent treatment of any flavor and chirality configuration is, in general, preferable and consequently results from experimental analyses might be altered without using the approximation indicated in the third point

[2]In the very recent paper [232], the authors state that they have found very good agreement with our values of $\sigma^{(0)}_{pp\to\tilde{q}\tilde{q}'}$ and $\sigma^{(0+1)}_{pp\to\tilde{q}\tilde{q}'}$ for the individual channels in Table 7.6.

channel	$\sigma^{(0)}_{pp\to\tilde{q}\tilde{q}'}$ [fb]	$\sigma^{(0+1)}_{pp\to\tilde{q}\tilde{q}'}$ [fb]	$K^{DR}_{pp\to\tilde{q}\tilde{q}'}$	$\sigma^{(0)}_{2j+\not{E}_T(+X)}$ [fb]	$\sigma^{(0+1)}_{2j+\not{E}_T(+X)}$ [fb]	$K_{2j+\not{E}_T(+X)}$
$\tilde{u}_L\tilde{u}_L$	7.08	9.44	1.33	$1.22\cdot10^{-3}$	$1.68\cdot10^{-3}$	1.38
$\tilde{u}_R\tilde{u}_R$	8.64	11.5	1.33	8.25	11.36	1.38
$\tilde{d}_L\tilde{d}_L$	1.07	1.44	1.36	$2.82\cdot10^{-4}$	$3.96\cdot10^{-4}$	1.40
$\tilde{d}_R\tilde{d}_R$	1.39	1.88	1.35	1.33	1.84	1.39
$\tilde{u}_L\tilde{u}_R$	6.00	8.49	1.42	$7.78\cdot10^{-2}$	$11.33\cdot10^{-2}$	1.45
$\tilde{d}_L\tilde{d}_R$	$8.20\cdot10^{-1}$	1.19	1.45	$1.32\cdot10^{-2}$	$1.96\cdot10^{-5}$	1.49
$\tilde{u}_L\tilde{d}_L$	8.25	11.9	1.44	$1.76\cdot10^{-3}$	$2.62\cdot10^{-3}$	1.49
$\tilde{u}_R\tilde{d}_R$	10.5	15.1	1.44	10.00	14.92	1.49
$\tilde{u}_L\tilde{c}_L$	$3.28\cdot10^{-1}$	$4.33\cdot10^{-1}$	1.32	$5.65\cdot10^{-5}$	$7.73\cdot10^{-5}$	1.37
$\tilde{u}_R\tilde{c}_R$	$4.29\cdot10^{-1}$	$5.74\cdot10^{-1}$	1.34	$4.09\cdot10^{-1}$	$5.68\cdot10^{-1}$	1.39
$\tilde{d}_L\tilde{s}_L$	$1.95\cdot10^{-1}$	$2.75\cdot10^{-1}$	1.41	$5.16\cdot10^{-5}$	$7.5097\cdot10^{-5}$	1.46
$\tilde{d}_R\tilde{s}_R$	$2.71\cdot10^{-1}$	$3.87\cdot10^{-1}$	1.42	$2.59\cdot10^{-1}$	3.82	1.48
$\tilde{u}_L\tilde{d}_R$	2.44	3.50	1.44	$3.16\cdot10^{-2}$	$4.67\cdot10^{-2}$	1.48
$\tilde{u}_R\tilde{d}_L$	2.40	3.46	1.44	$3.87\cdot10^{-2}$	$5.70\cdot10^{-2}$	1.48
$\tilde{u}_L\tilde{c}_R$	$1.69\cdot10^{-1}$	$2.39\cdot10^{-1}$	1.41	$2.19\cdot10^{-3}$	$3.18\cdot10^{-3}$	1.46
$\tilde{d}_L\tilde{s}_R$	$9.51\cdot10^{-2}$	$1.39\cdot10^{-1}$	1.46	$1.52\cdot10^{-3}$	$2.29\cdot10^{-3}$	1.50
sum	50.04	69.86	1.40	20.41	29.32	1.44

Table 7.6: For the benchmark point 10.1.5 at a center-of-mass energy of $\sqrt{S} = 14$ TeV inclusive production cross sections at LO $\sigma^{(0)}_{pp\to\tilde{q}\tilde{q}'}$ and NLO $\sigma^{(0+1)}_{pp\to\tilde{q}\tilde{q}'}$ together with the corresponding K-factors $K_{pp\to\tilde{q}\tilde{q}'}$ are listed for all different flavor and chirality channels (as explained in the text). Also listed for all channels are LO $\sigma^{(0)}_{2j+\not{E}_T(+X)}$ and NLO $\sigma^{(0+1)}_{2j+\not{E}_T(+X)}$ predictions of combined production and decay and the corresponding K-factor $K_{2j+\not{E}_T(+X)}$, where the cuts of eq. (7.2) are applied. All cross sections are given in fb.

of the list on page 76. Furthermore, as already seen in Table 7.5, K-factors increase from inclusive production to the combined result (where the cuts given in eq. (7.2) are applied).

In Table 7.7 we compare the results from the different subtraction schemes defined in section 6.4.3. In order to also consistently compare them with the results from *Prospino 2*, we set, just here, the mass of all squarks to the average mass $\overline{m_{\tilde{q}}}$ for all benchmark points. In Table 7.7 we show LO cross sections and NLO K-factors from our calculation in the DR scheme, $K^{DR}_{pp\to\tilde{q}\tilde{q}'}$, and in the DS scheme in the global approach as described by eq. (6.38), $K^{DS}_{pp\to\tilde{q}\tilde{q}'}$. We also list K-factors obtained from *Prospino 2*, $K^{\text{Prospino}}_{pp\to\tilde{q}\tilde{q}'}$, where we adjusted *Prospino 2*, employing the DS scheme in the local approach, to use the same set of PDFs and the same definition of the strong coupling $\alpha_s(\mu_R)$ as in our calculation. The use of a common average mass results in a small

benchmark	$\sqrt{S}$ [TeV]	$\sigma^{(0)}_{pp\to\tilde{q}\tilde{q}'}$	$K^{DR}_{pp\to\tilde{q}\tilde{q}'}$	$K^{DS}_{pp\to\tilde{q}\tilde{q}'}$	$K^{\text{Prospino}}_{pp\to\tilde{q}\tilde{q}'}$
SPS1a	7	1.01 pb	1.37	1.39	1.41
	8	1.48 pb	1.35	1.38	1.40
	14	5.31 pb	1.28	1.34	1.38
10.1.5	7	0.89 fb	1.58	1.58	1.59
	8	2.59 fb	1.53	1.53	1.54
	14	49.87 fb	1.39	1.40	1.41
p19MSSM1A	7	7.65 pb	1.39	1.41	1.37
	8	10.17 pb	1.37	1.41	1.37
	14	28.34 pb	1.31	1.39	1.38

Table 7.7: LO cross sections $\sigma^{(0)}_{pp\to\tilde{q}\tilde{q}'}$ and NLO K-factors for inclusive squark–squark production from our computation in the DR scheme, $K^{DR}_{pp\to\tilde{q}\tilde{q}'}$, in the DS scheme $K^{DS}_{pp\to\tilde{q}\tilde{q}'}$ and also from *Prospino 2*, $K^{\text{Prospino}}_{pp\to\tilde{q}\tilde{q}'}$. All squark masses taken to the average squark mass $\overline{m_{\tilde{q}}}$.

shift in the LO cross section and also in the NLO K-factor $K^{DR}_{pp\to\tilde{q}\tilde{q}'}$ between Table 7.5 and Table 7.7. Numerical differences between K-factors in the DR scheme and the DS scheme are of the order of a few percent for SPS1a and p19MSSM1A and negligible for 10.1.5, since, for a heavier spectrum the contribution from the gluon PDF in eq. (6.42) and eq. (6.44) is suppressed. Differences between $K^{DS}_{pp\to\tilde{q}\tilde{q}'}$ and $K^{\text{Prospino}}_{pp\to\tilde{q}\tilde{q}'}$ originate from the different approaches, global in our calculation and local in *Prospino 2*, for the DS scheme. We checked numerically, excluding real quark radiation, i.e. using the CR scheme, that inclusive NLO corrections from our calculation and results[3] from *Prospino 2* are in perfect agreement. The differences appearing with the inclusion of quark radiation are of the order expected from eq. (D.6), as discussed in appendix D.

7.1.4 Differential distributions

Now we turn to the investigation of differential distributions in various observables. First, we compare the differential scale dependence between our LO and NLO prediction. We do this by varying at the same time renormalization and factorization scale between $\mu/2$ and 2μ, with $\mu = \overline{m_{\tilde{q}}}$. For SPS1a and an energy of $\sqrt{S} = 14$ TeV, the resulting LO and NLO bands are shown in blue and red in Figure 7.2 for differential distributions in $p_1^{\text{T}}, p_2^{\text{T}}, \eta_1, \eta_2, \not{E}_T$ and H_T. As can be seen in Figure 7.2, in all considered distributions the scale dependence and thus the theoretical uncertainty is sizably

[3]The CR scheme can be very easily adapted in *Prospino 2* for squark–squark production. It is sufficient to set the gluon PDF equal to zero.

reduced by our NLO calculation. At the same time, one finds that large parts of the NLO bands are outside the LO bands. Still, for example in the p^{T} distributions, in the high-p^{T} tail the NLO bands move entirely inside the LO bands.

Second, in Figure 7.3 we illustrate the difference between the subtraction schemes introduced in section 6.4.3 for the benchmark point SPS1a at a center-of-mass energy $\sqrt{S} = 14$ TeV. In Figure 7.3 we show distributions in $\not{E}_T$ and H_T, where we observe the largest deviations between the DS and DR schemes. The upper part of these plots show the same bands as already displayed at the bottom of 7.2, however in a logarithmic scale. In the lower part we show, for the DR scheme, the band between the NLO results at $\mu = 2\overline{m_{\tilde{q}}}$ and $\mu = \overline{m_{\tilde{q}}}/2$ divided by the LO result at $\mu = \overline{m_{\tilde{q}}}$. We also display the ratio between the NLO result in the DS scheme and the LO result, both at the central scale $\mu = \overline{m_{\tilde{q}}}$. In these two distributions the difference between the two schemes increases in the tail of the distributions. However the DS scheme remains within the theoretical uncertainty of the DR scheme. The distributions for $\not{E}_T$ and H_T show the largest differences; in general, the differences between the schemes are smaller.

Third, we investigate the change in the shape of distributions relevant for searches for supersymmetry at the LHC induced by NLO corrections. Here, we present distributions for a center-of-mass energy $\sqrt{S} = 14$ TeV. Lower center-of-mass energies show qualitatively the same behavior. For benchmark point SPS1a plots are shown in Figure 7.4, for 10.1.5 in Figure 7.5, and for p19MSSM1A in Figure 7.6. We present distributions in p_1^{T}, p_2^{T}, m_{eff}, $\not{E}_T$ (all in fb/GeV), where the ATLAS jet choice $R = 0.4$ and cuts of eq. (7.2) are applied. Also distributions in H_T (in fb/GeV) and in α_T (in pb) are displayed, where the CMS jet choice $R = 0.5$ and corresponding cuts of eq. (7.2) are applied. In the α_T distribution, events are reclustered into two pseudo-jets, as explained in section 5.3.1, and a cut of $H_T > 350$ GeV is applied. In the upper part of any plot we show each distribution at LO in black, NLO in red, and in blue the LO prediction rescaled by the ratio, K^{NLO}, between the integrated NLO and LO result. In the lower part of any plot we show the NLO divided by the rescaled LO $\cdot\, K^{\mathrm{NLO}}$ distribution. In this way we present corrections purely in the shape and not in the normalization of the distributions. For SPS1a and 10.1.5 corrections are qualitatively very similar and rather flat for p_1^{T}, p_2^{T} and $\not{E}_T$, as expected from [33]. Corrections in the H_T distribution grow for larger H_T and can be sizable. This can be explained from the high-p^{T} behavior of the contribution from hard real gluon radiation to this observable. H_T is the scalar sum of the p^{T} of the jets and clearly this variable strongly depends on kinematic effects from gluon radiation. Thus, as verified by our calculation, differential corrections in H_T are expected to be not flat. Corrections to the shape of the α_T observable change sign at $\alpha_T = 0.5$ and fall off continuously in the signal region $\alpha_T > 0.55$. As explained in section 5.3.1, the value $\alpha_T = 0.5$ is a physical boundary, since the SM multijet signature belongs to the region $\alpha_T < 0.5$.

Looking at the distributions of p19MSSM1A in Figure 7.6 a completely different

behavior of the NLO corrections cannot be missed. The tail of the p_1^{T}, p_2^{T}, m_{eff} and $\not{E}_T$ distributions completely departs from the LO predictions. This can be understood from the following considerations. Due to the small mass difference between squarks and the $\tilde{\chi}_1^0$ for benchmark point p19MSSM1A, jets from squark decays tend to be soft. Now, the p^{T} of an additional jet (which cannot be distinguished from the decay jets) from hard gluon radiation in the production can easily be of the same order as the ones from squark decays and result in the given distortions. Such a behavior for compressed spectra was already partly discussed in [231], where sparticle production and decay including additional hard jets matched to a parton shower was investigated. We verified our findings by comparing LO predictions plus real hard gluon radiation in the production stage with a corresponding calculation performed with *MadGraph 5* [289]. The tail of the considered distributions can adequately be described only by additional gluon radiation, which should thus be seen, from the numerical impact and not the order of expansion in α_s, as the LO prediction for these phase-space regions. Turning to the α_T distribution, the shapes of LO and NLO predictions are clearly different and, here, we refrain from showing explicitly corrections in the shape or a rescaled LO prediction.

Next to the distributions shown in Figures 7.4, 7.5 and 7.6, we also investigated pseudorapidity distributions of the two hardest jets $\eta_{1/2}$. Here, in the relevant region $|\eta_{1/2}| < 3.0$, corrections in the shapes are always smaller than about 5% for all benchmark scenarios and energies.

In Figure 7.7 we present plots for angular distributions between the two hardest jets. On the left, we show distributions in the invariant mass of the two hardest jets $m_{\mathrm{inv}}(jj)$, on the right distributions in the cosine of the angle between the two hardest jets $\cos\Theta_{jj}$. Again, results are given for all three benchmark points and a center-of-mass energy $\sqrt{S} = 14$ TeV. Corrections in these distributions can be quite large. In general, in the NLO results one observes larger corrections for small angles between the two hardest jets (up to 20% in the $\cos\Theta_{jj}$ distributions). In the high-invariant-mass tail for SPS1a and 10.1.5 corrections are negative and grow to 40% in the considered invariant mass range. Such corrections could potentially be absorbed into a dynamical renormalization/factorization scale definition as, e.g., $\mu = H_T$. In the invariant mass distribution of p19MSSM1A we observe the same deviation of the NLO result from the LO shape as already discussed above.

Finally, in Figure 7.8 we investigate NLO corrections to the $\cos\hat{\Theta}$ distribution for the benchmark points SPS1a (top left), 10.1.5 (top right) and p19MSSM1A (bottom) at a center-of-mass energy of $\sqrt{S} = 14$ TeV. Corrections can reach the value of 15%; still, the general shapes and thus the potential for extraction of spin information about the intermediate squarks seem to be robust under higher-order corrections.

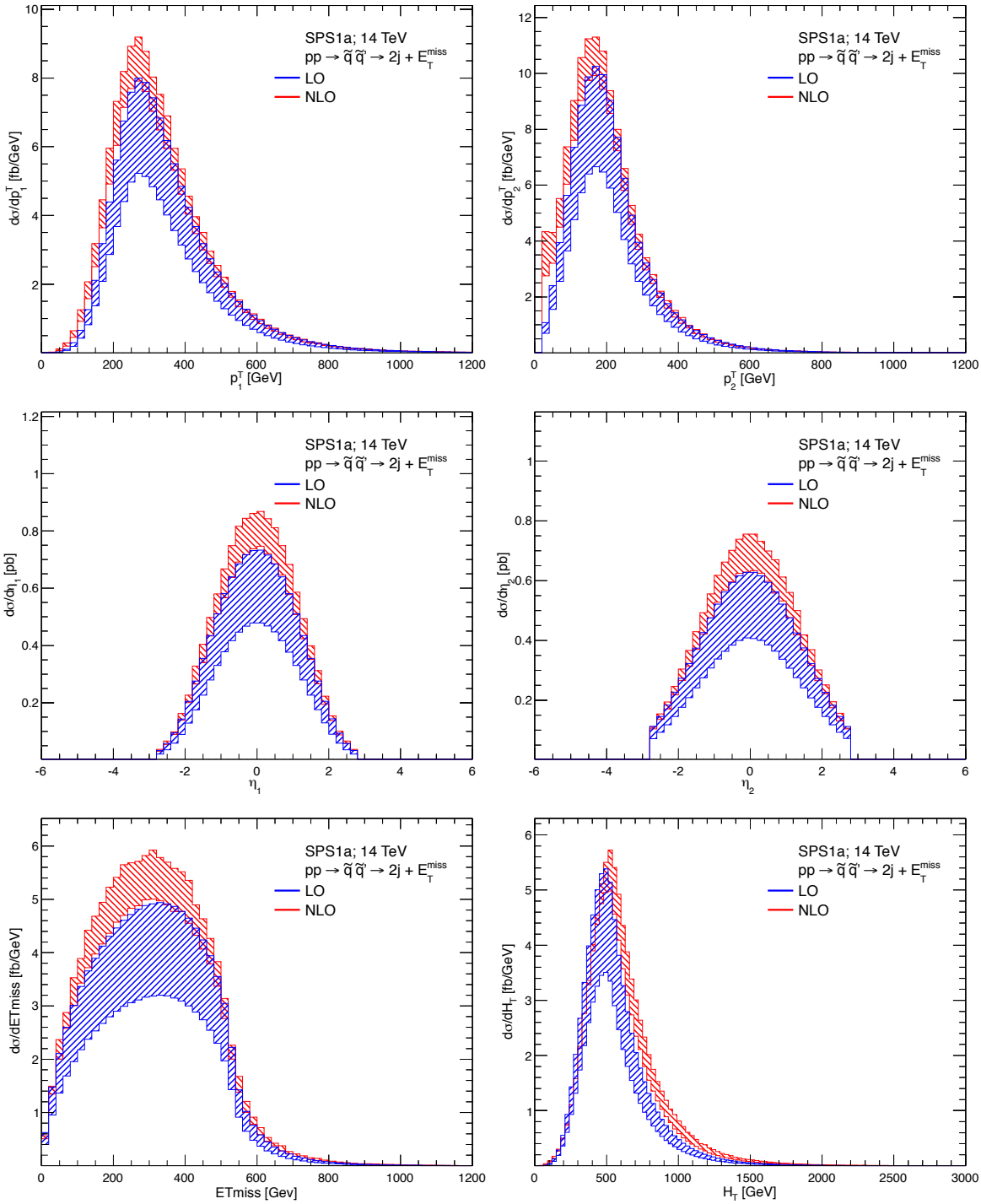

Figure 7.2: Differential distributions in $p_1^{\mathrm{T}}, p_2^{\mathrm{T}}$ (in fb/GeV), η_1, η_2 (in pb/GeV), $\not{E}_T$ and H_T (in fb/GeV) for SPS1a and $\sqrt{S} = 14$ TeV, where for, both, LO (blue) and NLO (red) the common renormalization and factorization scale is varied between $\mu/2$ and 2μ, with $\mu = \overline{m_{\tilde{q}}}$.

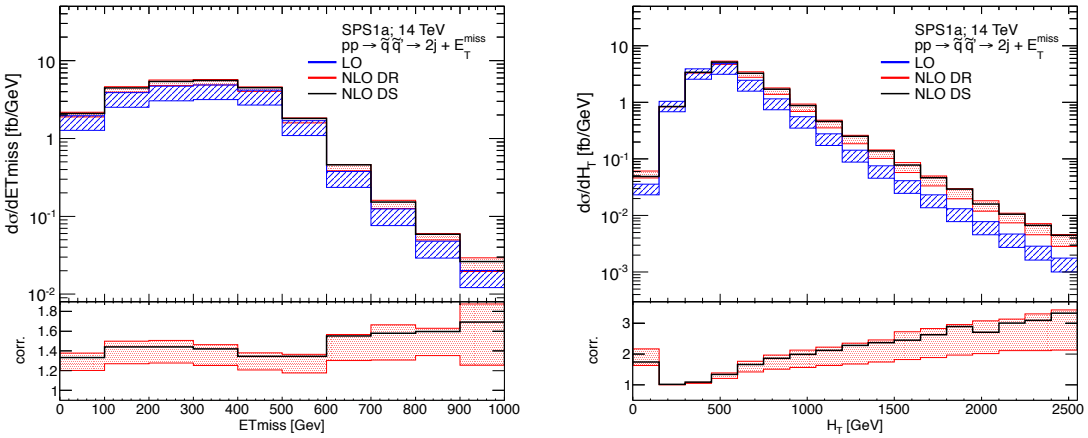

Figure 7.3: Differential distributions in $\not{E}_T$ and H_T (in fb/GeV) for SPS1a and $\sqrt{S} =$ 14 TeV. In the upper part the common renormalization and factorization scale is varied between $\mu/2$ and 2μ, with $\mu = \overline{m_{\tilde{q}}}$ for LO (blue) and NLO^{DR} (red). In the lower part we show in red the ratio of the NLO^{DR} uncertainty band and the LO result (at scale $\mu = \overline{m_{\tilde{q}}}$). We also show in black the ratio of the NLO result in the DS scheme and the central LO result.

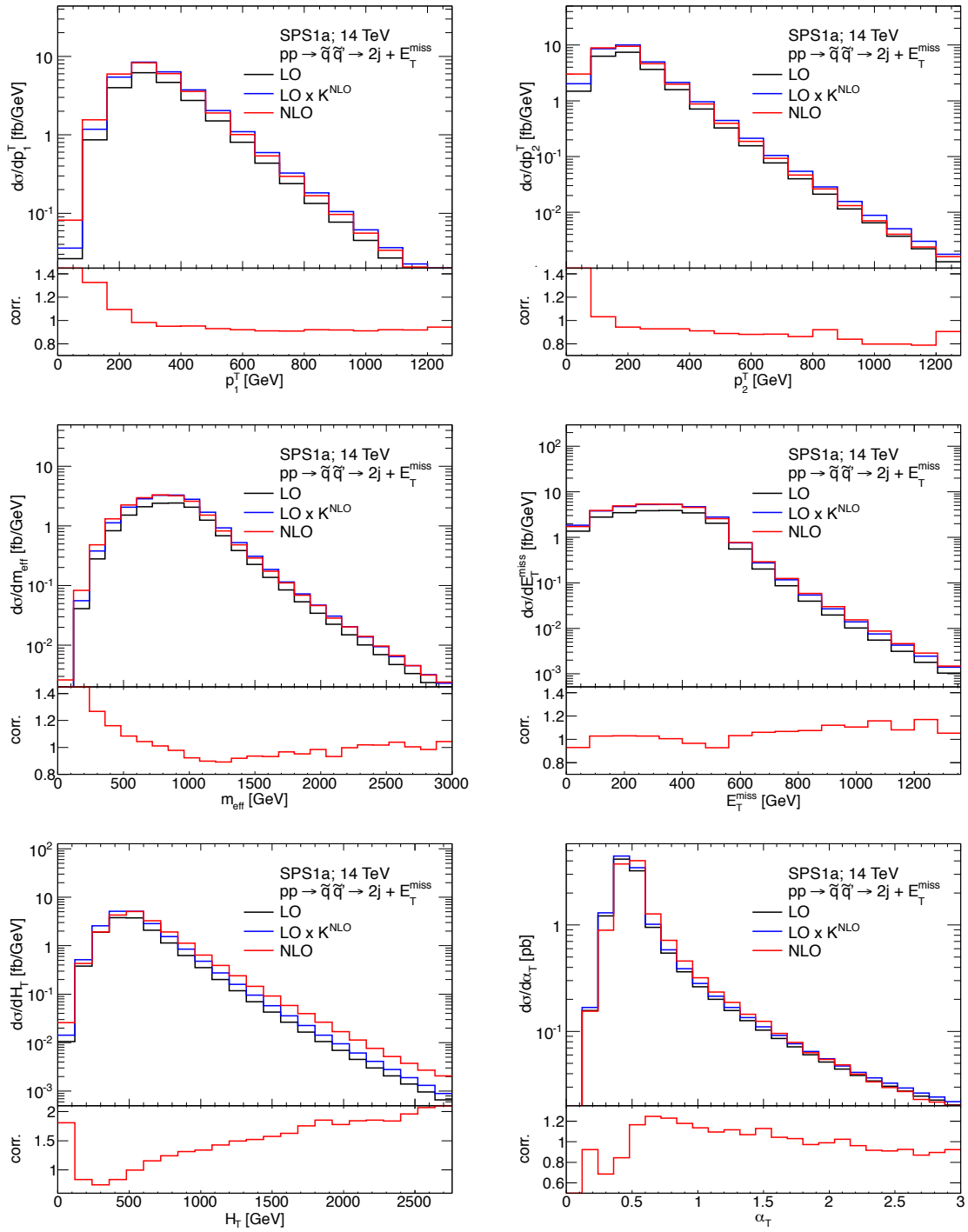

Figure 7.4: Differential distributions of benchmark point SPS1a at a center-of-mass energy $\sqrt{S} = 14$. In the upper part of the plots we show in black LO, in red NLO and in blue LO distributions rescaled by the ratio K^{NLO} between the integrated NLO and LO results. In the lower part of the plots NLO corrections in the shapes are shown, defined as the full NLO divided by the rescaled LO $\cdot\, K^{\mathrm{NLO}}$ distribution. From top left to bottom right we show differential distributions in p_1^{T}, p_2^{T}, m_{eff}, $\not{E}_T$, H_T (all in fb/GeV) and in α_T (in pb).

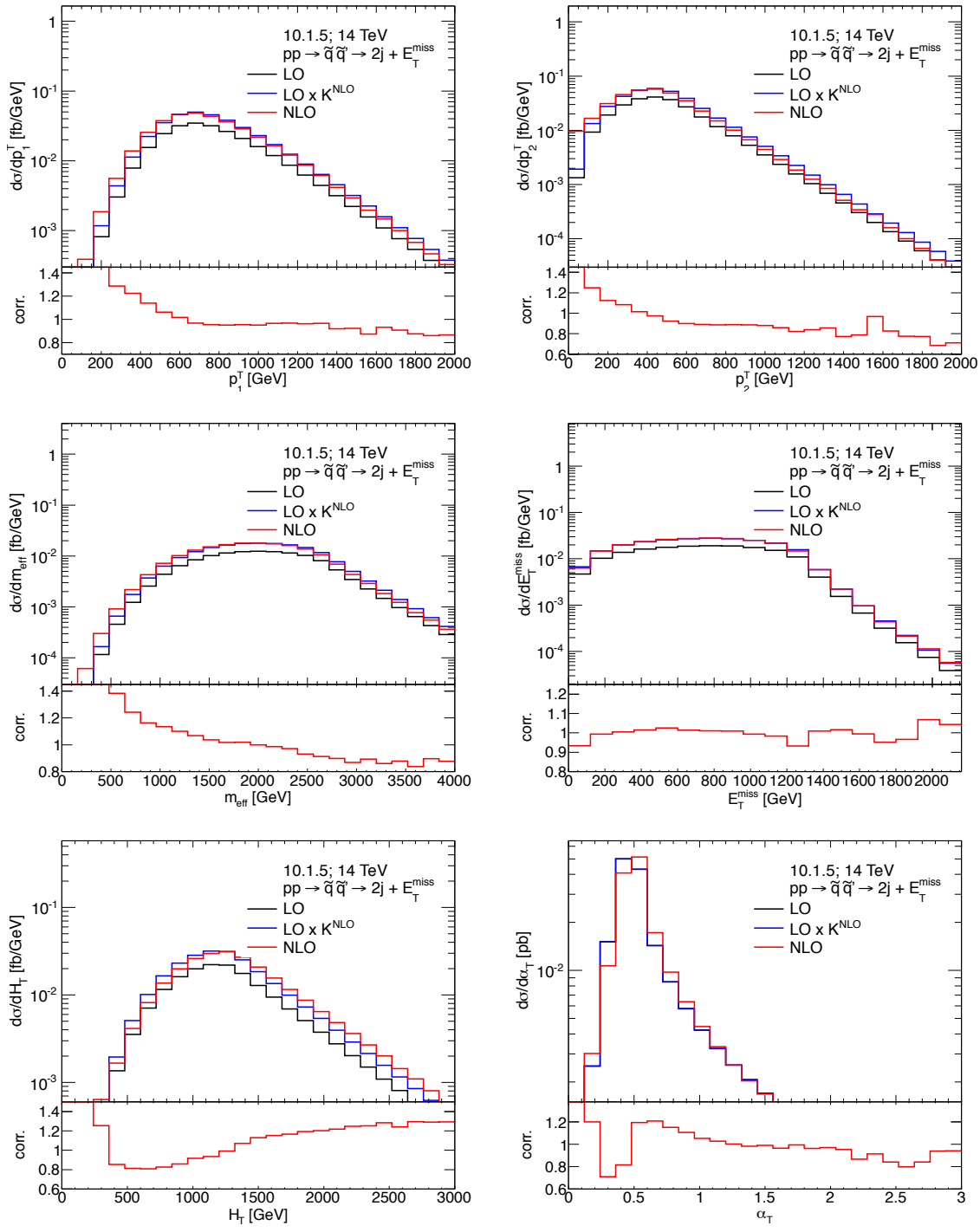

Figure 7.5: Differential distributions of benchmark point 10.1.5 at a center-of-mass energy $\sqrt{S} = 14$. In the upper part of the plots we show in black LO, in red NLO and in blue LO distributions rescaled by the ratio K^{NLO} between the integrated NLO and LO results. In the lower part of the plots NLO corrections in the shapes are shown, defined as the full NLO divided by the rescaled LO $\cdot\, K^{\mathrm{NLO}}$ distribution. From top left to bottom right we show differential distributions in p_1^{T}, p_2^{T}, m_{eff}, $\not{E}_T$, H_T (all in fb/GeV) and in α_T (in pb).

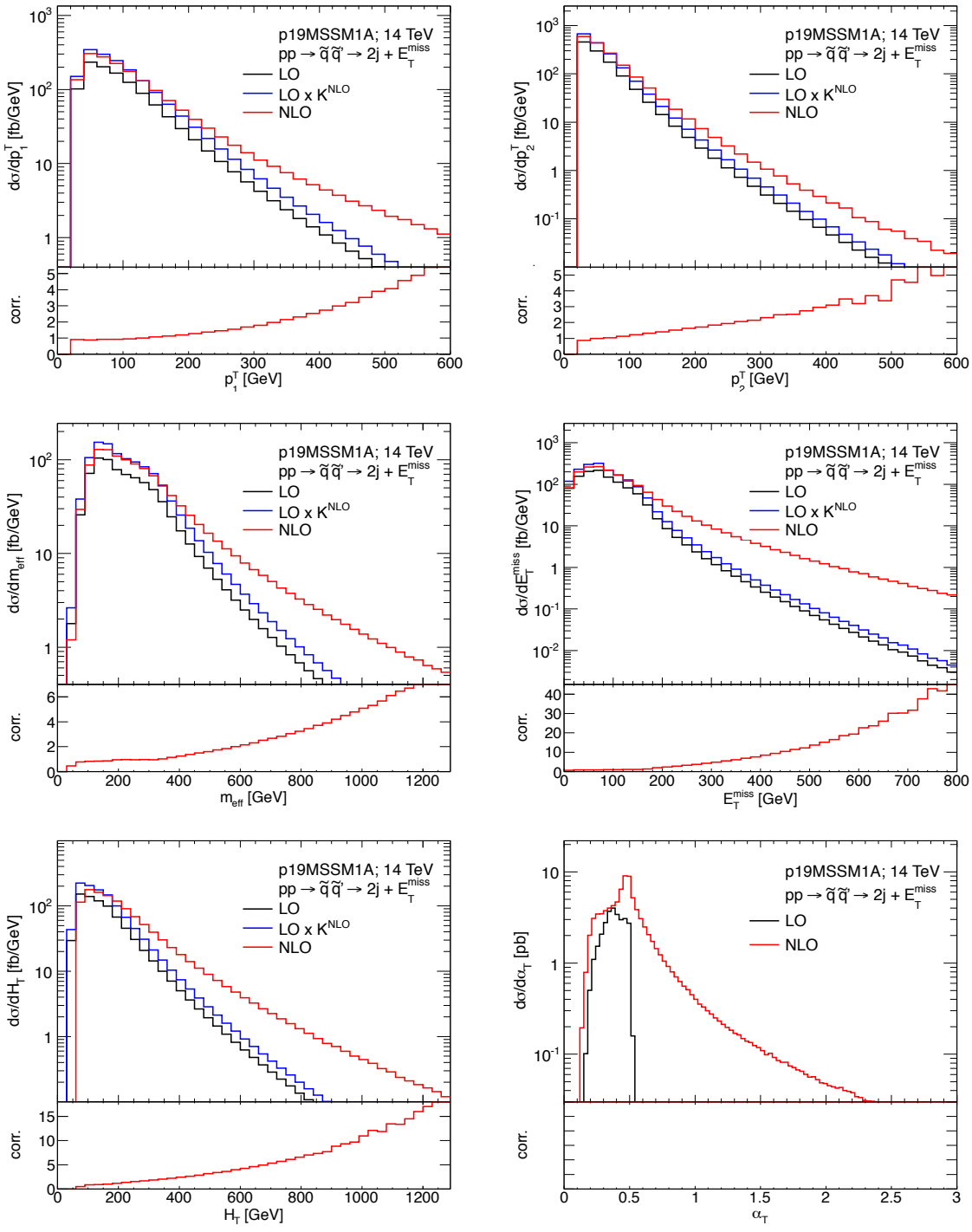

Figure 7.6: Differential distributions of benchmark point p19MSSM1A at a center-of-mass energy $\sqrt{S} = 14$. In the upper part of the plots we show in black LO, in red NLO and in blue LO distributions rescaled by the ratio K^{NLO} between the integrated NLO and LO results. In the lower part of the plots NLO corrections in the shapes are shown, defined as the full NLO divided by the rescaled LO $\cdot\, K^{\mathrm{NLO}}$ distribution. From top left to bottom right we show differential distributions in p_1^{T}, p_2^{T}, m_{eff}, $\not{E}_T$, H_T (all in fb/GeV) and in α_T (in pb).

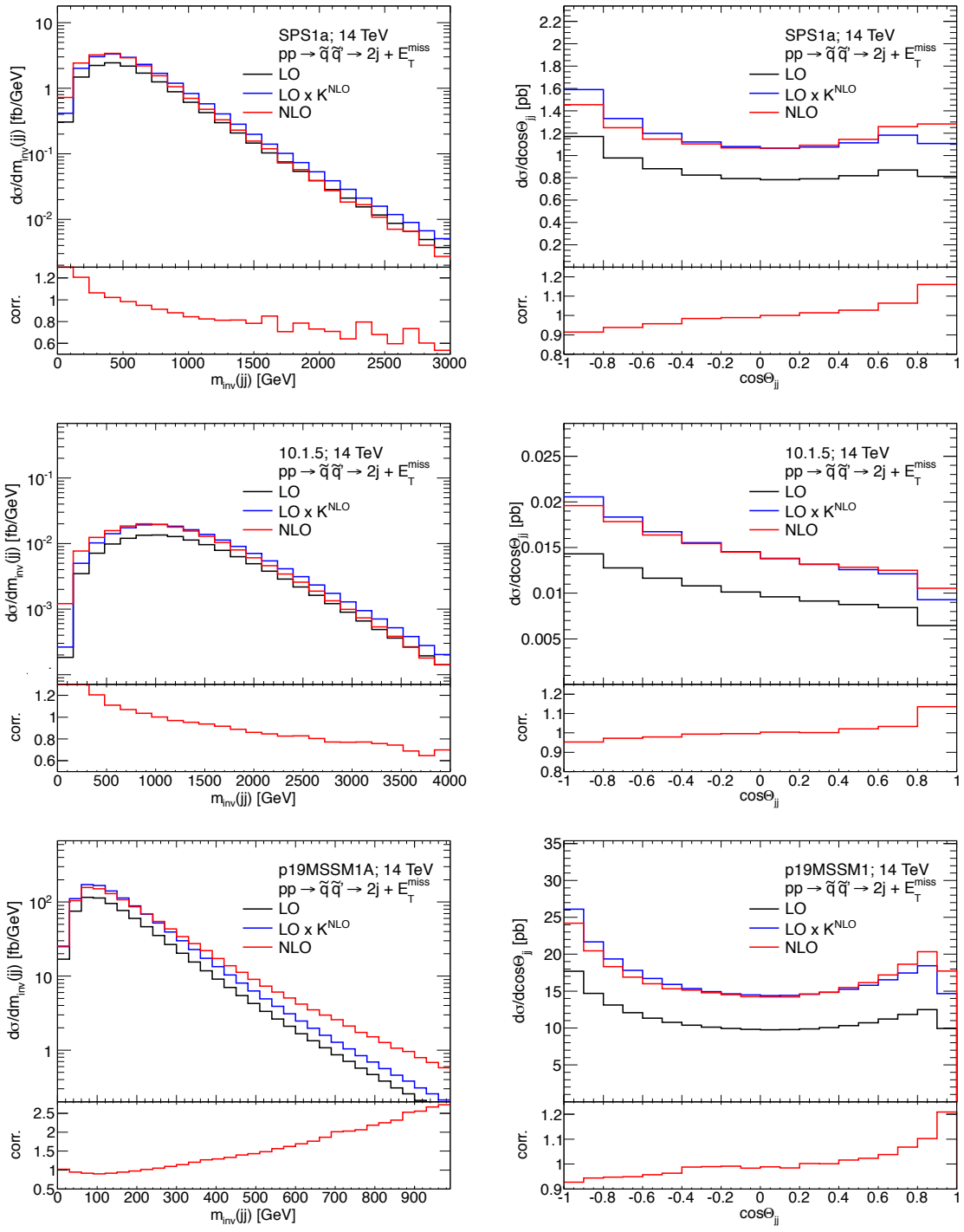

Figure 7.7: Distributions in the invariant mass $m_{\rm inv}(jj)$ (in fb/GeV) and the cosine of the angle between the two hardest jets $\cos\Theta_{jj}$ (in pb) for the benchmark points SPS1a (top), 10.1.5 (middle), p19MSSM1A (bottom) at a center-of-mass energy $\sqrt{S} = 14$ TeV. In the upper part of the plots we show in black LO, in red NLO and in blue LO distributions rescaled by the ratio $K^{\rm NLO}$ between the integrated NLO and LO results. In the lower part of the plots NLO corrections in the shapes are shown, defined as the full NLO divided by the rescaled LO $\cdot\, K^{\rm NLO}$ distribution.

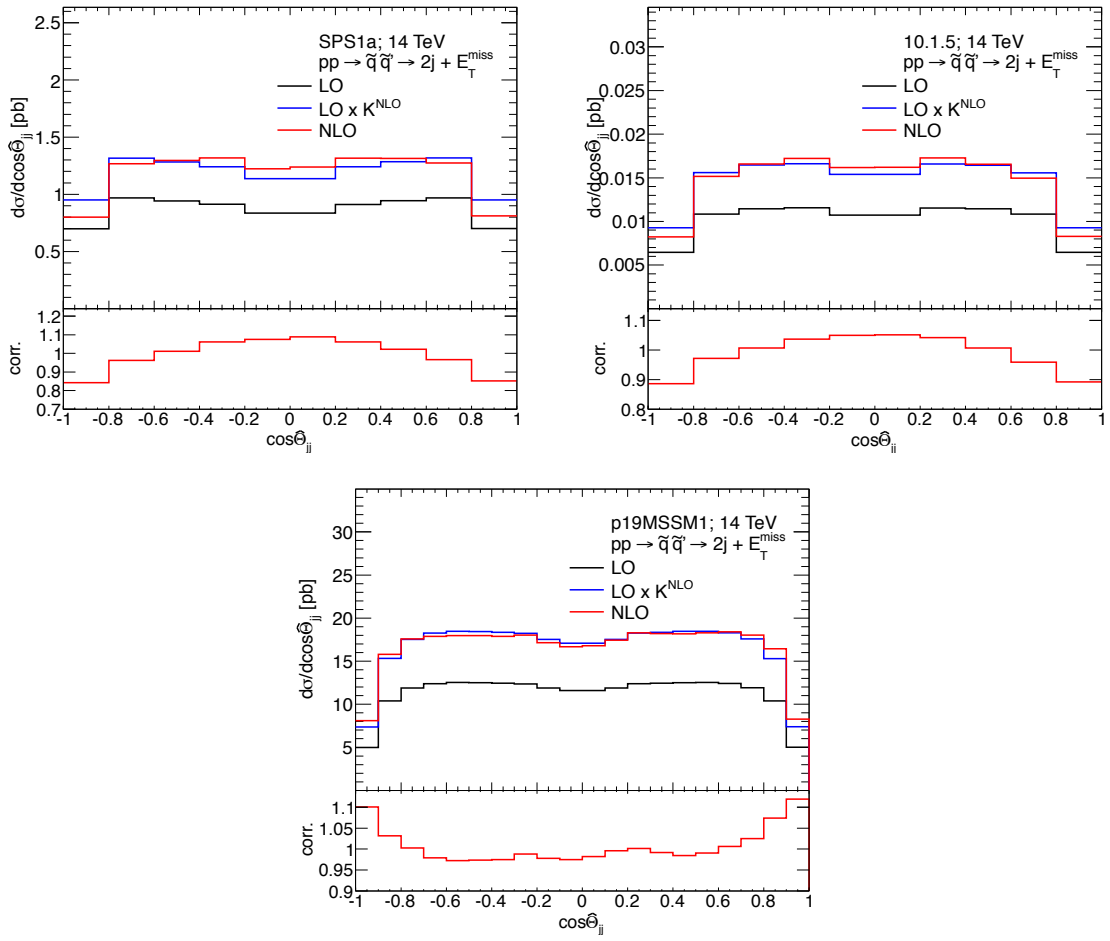

Figure 7.8: Distributions in $\cos\hat{\Theta}$ (in pb) for the benchmark points SPS1a (upper left), 10.1.5 (upper right) p19MSSM1A (bottom) at a center-of-mass energy of $\sqrt{S} = 14$ TeV. In the upper part of the plots we show in black LO, in red NLO and in blue LO distributions rescaled by the ratio K^{NLO} between the integrated NLO and LO results. In the lower part of the plots NLO corrections in the shapes are shown, defined as the full NLO divided by the rescaled LO $\cdot\, K^{\mathrm{NLO}}$ distribution.

7.1.5 Event rates

After the investigation of inclusive cross sections and differential distributions, we analyze here event rates, i.e., cross sections integrated on signal regions defined to reduce background contributions. In this way we quantify a possible impact of our calculation on current searches for supersymmetry and future measurements of event rates at the LHC. Specifically, we check the effects, in the cut-and-count searches, due to the approximations in the first three points of the list on page 76.

In table 7.8 we list cross sections after applying cuts of eq. (7.4), and in table 7.9 cross sections after applying cuts of eq. (7.5). We show LO and NLO cross sections for all three benchmark points and all three energies together with resulting K-factors. For comparison we again list inclusive K-factors of just production, already shown in table 7.5. From these results, a fully differential description of all squark and gluino channels including NLO effects in production and decay seems inevitable for a conclusive interpretation of SUSY searches (or signals) at the LHC. The numbers in table 7.8 and table 7.9 again show that, for compressed spectra like p19MSSM1A, a pure LO approximation is unreliable for a realistic phenomenological description of the experimental signatures considered here. Furthermore, as already suggested in [290] and expected from the differential distributions shown in section 7.1.4, interpretations based on α_T, as in Table 7.9, seem to be highly affected by the accuracy of higher-order corrections. The sign of corrections, in α_T distributions, changes around $\alpha_T = 0.5$ and cuts from eq. (7.5) include the requirement $\alpha_T > 0.55$. Thus, flat K-factors underestimate the impact of NLO contributions.

benchmarkpoint	**Energy [TeV]**	$\boldsymbol{N^{(0)}_{\text{ATLAS}}}$	$\boldsymbol{N^{(0+1)}_{\text{ATLAS}}}$	$\boldsymbol{K_{N_{\text{ATLAS}}}}$	$\boldsymbol{K_{pp\to\tilde{q}\tilde{q}'}}$
SPS1a	7	0.066 pb	0.083 pb	1.26	1.37
	8	0.097 pb	0.121 pb	1.25	1.35
	14	0.347 pb	0.424 pb	1.22	1.28
10.1.5	7	0.313 fb	0.503 fb	1.61	1.57
	8	0.861 fb	1.344 fb	1.56	1.52
	14	13.82 fb	19.77 fb	1.43	1.40
p19MSSM1A	7	0.140 fb	20.76 fb	~ 150	1.40
	8	0.339 fb	37.96 fb	~ 110	1.39
	14	0.0044 pb	0.264 pb	~ 60	1.34

Table 7.8: LO $N^{(0)}_{\text{ATLAS}}$ and NLO $N^{(0+1)}_{\text{ATLAS}}$ cross section predictions and K-factors $K_{N_{\text{ATLAS}}}$ for the three benchmark scenarios SPS1a, 10.1.5, p19MSSM1A and center-of-mass energies $\sqrt{S} = 7, 8, 14$ TeV where the cuts of eq. (7.4) are applied. For comparison we also list is the inclusive NLO production K-factor $K_{pp\to\tilde{q}\tilde{q}'}$ already shown in Table 7.5.

benchmarkpoint	Energy [TeV]	$N^{(0)}_{\mathrm{CMS}}$	$N^{(0+1)}_{\mathrm{CMS}}$	$K_{N_{\mathrm{CMS}}}$	$K_{pp\to\tilde{q}\tilde{q}'}$
SPS1a	7	0.112 pb	0.141 pb	1.26	1.37
	8	0.157 pb	0.197 pb	1.25	1.35
	14	0.488 pb	0.614 pb	1.26	1.28
10.1.5	7	0.201 pb	0.261 pb	1.30	1.57
	8	0.542 fb	0.674 fb	1.24	1.52
	14	8.129 fb	8.884 fb	1.09	1.40
p19MSSM1A	7	10^{-6} pb	0.095 pb	$\mathcal{O}(10^4)$	1.40
	8	10^{-6} pb	0.151 pb	$\mathcal{O}(10^4)$	1.39
	14	$2 \cdot 10^{-5}$ pb	0.687 pb	$\mathcal{O}(10^4)$	1.34

Table 7.9: LO $N^{(0)}_{\mathrm{CMS}}$ and NLO $N^{(0+1)}_{\mathrm{CMS}}$ cross section predictions and K-factors $K_{N_{\mathrm{CMS}}}$ for the three benchmark scenarios SPS1a, 10.1.5, p19MSSM1A and center-of-mass energies $\sqrt{S} = 7, 8, 14$ TeV where the cuts of eq. (7.5) are applied. For comparison we also list the inclusive NLO production K-factor $K_{pp\to\tilde{q}\tilde{q}'}$ already shown in Table 7.5.

7.2 The signature $\mathbf{2j + l^+l^-(OS\text{-}SF) + \not{E}_T(+X)}$

This section is structured similarly to the previous section 7.1. We firstly specify in 7.2.1 input parameters and experimental cuts and, afterwards, we present numerical results. In 7.2.2 we investigate, in the squark rest frame, NLO corrections to the single decay chain not combined with the production. These results can be interpreted as a cross check with the study presented in [35] and as a reference for the interpretation of results for the $2j + l^+l^-(\text{OS-SF}) + \not{E}_T(+X)$ signature. Finally we consider the decay chain combined with $\tilde{q}_L\tilde{q}'_R$: differential distributions in 7.2.3 and event rates in 7.2.4.

7.2.1 Parameters and observables

Standard Model input parameters are chosen as in section 7.2 according to [126]. Also, the same set of PDFs, CTEQ6.6 [144], with the associated $\alpha_s^{\overline{\mathrm{MS}}}(\mu_R)$ at NLO is used. Renormalization scale μ_R and factorization scale μ_F are, again, both set to the average mass of all light-flavor squarks, $\mu = \mu_F = \mu_R = \overline{m_{\tilde{q}}}$.

Numerical results in this section are presented for the LHC with a center-of-mass energy of $\sqrt{S} = 14$ TeV using two CMSSM representative benchmark scenarios: SPS1a, already employed in section 7.1 and 10.1.6 defined in [280, 284]. The value of the CMMSM parameters at the GUT scale for the point 10.1.6 are similar those of the point 10.1.5, defined in Table 7.1. The values of m_0 and $m_{1/2}$ for the point 10.1.6 are slightly larger, namely $m_0 = 750$ GeV and $m_{1/2} = 187.5$ GeV. As already said, the scenario SPS1a has been excluded by searches at LHC, but it still serves as a valuable

mass [GeV]	$\tilde{u}_L$	$\tilde{u}_R$	$\tilde{d}_L$	$\tilde{d}_R$	$\tilde{g}$	$\tilde{l}_L$	$\tilde{l}_R$	$\tilde{\chi}_2^0$	$\tilde{\chi}_1^0$
SPS1a	563.6	546.7	569.0	546.6	608.5	202.4	144.1	180.2	97.0
10.1.6	1531.7	1472.2	1533.6	1466.1	1672.1	536.6	340.6	592.4	313.3

Table 7.10: On-shell masses of the first-generation squarks and sleptons, the gluino, and the lightest and second-lightest neutralino within the SUSY scenarios considered. All masses are given in GeV.

BR [%]	$\tilde{q}_R \to \tilde{\chi}_1^0$	$\tilde{q}_R \to \tilde{\chi}_2^0$	$\tilde{q}_L \to \tilde{\chi}_1^0$	$\tilde{q}_L \to \tilde{\chi}_2^0$	$\tilde{\chi}_2^0 \to \tilde{l}_L^\pm$	$\tilde{\chi}_2^0 \to \tilde{l}_R^\pm$	$\tilde{\chi}_2^0 \to Z$
SPS1a	98.5	1.0	1.5	31.2	–	13.1	–
10.1.6	99.8	0.03	1.5	32.1	28.4	0.2	0.2

Table 7.11: Branching ratios for the decay of squarks into $\tilde{\chi}_1^0$ and $\tilde{\chi}_2^0$ and for the decay of $\tilde{\chi}_2^0$ into right- and left-handed sleptons. Squarks and sleptons of the first two families are considered, where branching ratios into second- and first- generation sleptons and their charge-conjugate contributions are summed. The branching ratios of squarks are at NLO accuracy; differences with values at LO accuracy are lower than per mill level.

benchmark point for comparisons with numerous numerical results available in the literature. Sparticle on-shell masses relevant for our analysis are obtained again with *SOFTSUSY* [285] and listed in Table 7.10 for both the scenarios SPS1a and 10.1.6.

Also here, we set all second-generation masses equal to their first-generation counterparts, since, for these two scenarios, the phenomenological effects originating from the small mass differences are negligible in this study.

As already mentioned, our calculation is phenomenologically sensible for scenarios with the gluino heavier than all light flavor squarks, where all these squarks decay exclusively into charginos and neutralinos. As can be seen in Table 7.10, the scenarios SPS1a and 10.1.6 satisfy this condition.

In Table 7.11 we list the branching ratios, calculated with *SDECAY* [254], of two-body decays relevant for this study. We show only the average value of the branching ratios for up- and down-type squarks, since they differ at most by $\sim 1\%$. Differences between branching ratios at LO and NLO for squark decays are even smaller (less than per mill) for the considered scenarios and so we do not show them. Again, Table 7.11 shows that the right-handed squarks decay dominantly directly into the bino-like $\tilde{\chi}_1^0$, and the left-handed squarks into $\tilde{\chi}_2^0$ and the lighter chargino, $\tilde{\chi}_1^\pm$.

In Table 7.11 we also list branching ratios for the second-lightest neutralino into light-flavor sleptons. Branching ratios into first- and second-generation sleptons are identical, and in Table 7.11 we sum those contributions. For benchmark point SPS1a only the right-handed $\tilde{l}_R$ is lighter than the $\tilde{\chi}_2^0$, yielding together with the decay into a τ-slepton the only available two-body decays. In our numerical analysis of SPS1a, both for the decay chain alone and combined with the production, only the decay via a right-handed slepton is considered. In contrast, for the CMMSM point 10.1.6

both sleptons are lighter than the $\tilde{\chi}_2^0$. However, due to its wino-like nature the $\tilde{\chi}_2^0$ here decays dominantly into the left-handed $\tilde{l}_L$ despite the smaller mass of the $\tilde{l}_R$. For simplification, in our numerical analysis of the CMMSM point 10.1.6 only the decay via a left-handed slepton is considered. As can be seen from Table 7.11, the contribution from the decay into a $\tilde{l}_R$ can be safely neglected. Table 7.11 shows also the branching ratio of the $\tilde{\chi}_2^0 \to \tilde{\chi}_1^0 Z$ decay, entering the decay chain $\tilde{q} \to q\tilde{\chi}_2^0 \to qZ\tilde{\chi}_1^0 \to ql^+l^-\tilde{\chi}_1^0$, which gives the same signature of the "golden decay chain". This decay chain via the Z boson is kinematically forbidden with SPS1a, for on-shell Z and $\tilde{\chi}_2^0$, and negligible for the CMMSM point 10.16. Thus, it can be safely neglected in our analysis for these two scenarios.

In all numerical results presented in the following we employ the anti-k_T jet clustering algorithm with a jet radius of $R = 0.4$ implemented in *FastJet 3.0.2* [287]. Furthermore, in order to obtain an experimentally well defined result, jets that do not pass the cut conditions

$$p_{j_i}^T \geq 20 \text{ GeV}\,, \qquad |\eta_{j_i}| \leq 2.8\,, \tag{7.6}$$

are discarded. In the analyses of sections 7.2.3 and 7.2.4, where decays are combined with squark–squark production, the following realistic experimental cuts are applied:

$$\begin{aligned} p_{j_1}^T &\geq 150 \text{ GeV}\,, \quad p_{j_2}^T \geq 100 \text{ GeV}\,, \\ |\eta_{j,l}| &\leq 2.5\,, \qquad p_{l_{1,2}}^T \geq 20 \text{ GeV (OS-SF)}\,, \\ \not{E}_T &\geq 100 \text{ GeV}\,, \end{aligned} \tag{7.7}$$

where we implicitly require the two leptons to have opposite charge and same flavor (OS-SF). Such cuts efficiently reduce SM backgrounds [179, 269, 270]. Furthermore, we assume that contributions from leptonic decays of τ-leptons (from the corresponding signal decay chain with intermediate tau sleptons) are removed in the standard way by subtracting events with opposite-sign different-flavor lepton pairs (OS-DF), see e.g. [175, 176, 178–180]. For this reason we do not include contributions from $\tilde{l} = \tilde{\tau}$ in our numerical evaluation.

7.2.2 Squark decay chain

Here we investigate the NLO corrections to the isolated "golden decay chain" evaluated in the squark rest frame. In Figure 7.9 we show various invariant mass distributions at LO and NLO in the final-state leptons and jet(s) for the benchmark scenario SPS1a. As explained in section 5.3.1, shapes of such distributions are important for the determination of masses and spins of sparticles. In order to highlight NLO corrections purely in the shapes, here and also afterward in section 7.2.3, we show all distributions, both at LO and at NLO, normalized to unity.

Two kinds of combinatorial problems arise for invariant mass distributions involving the final-state leptons and jet(s). First, as already mentioned in section 6.6, from an

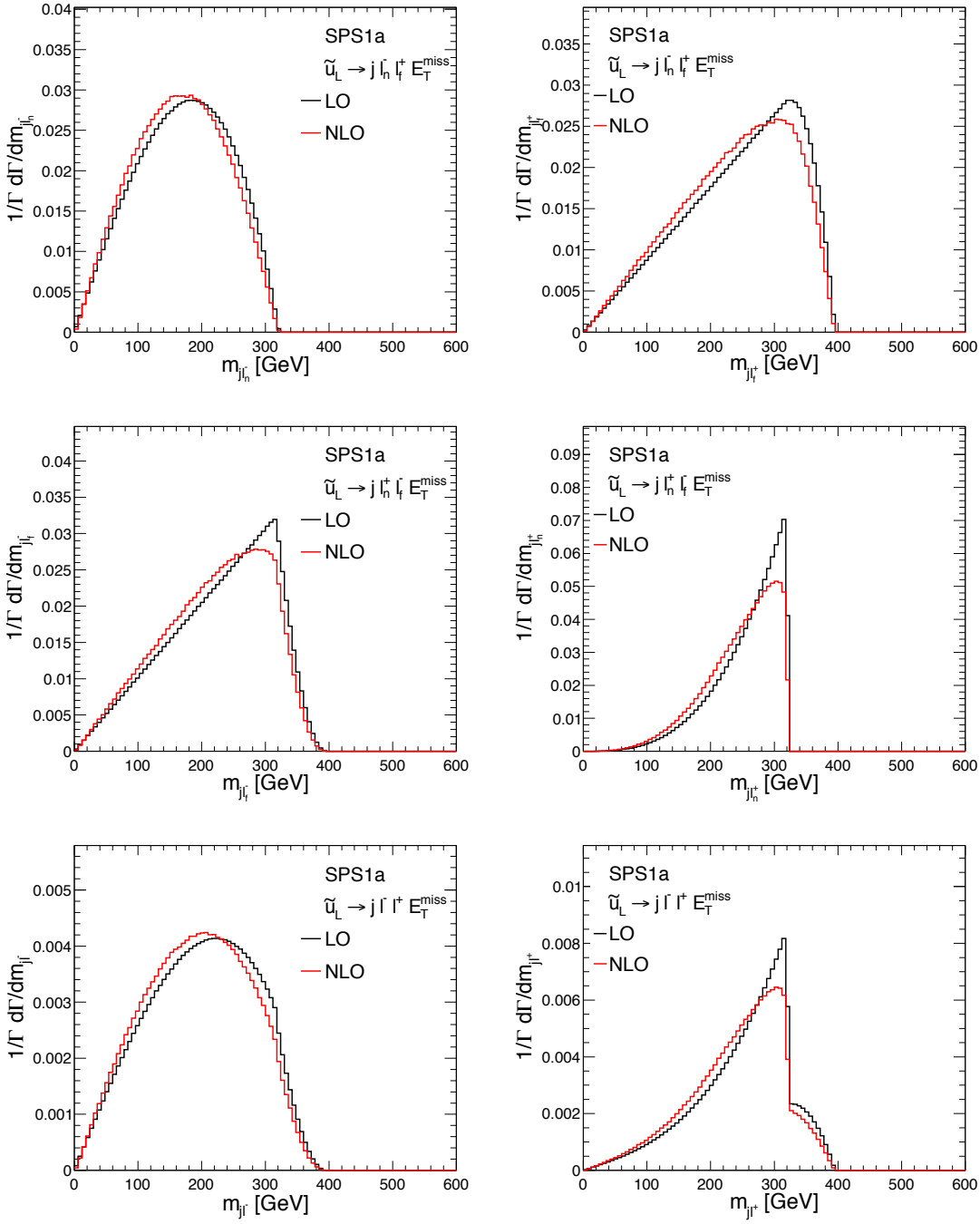

Figure 7.9: Normalized differential distributions for SPS1a in m_{jl_f}, m_{jl_n} for the two unobservable decays $\tilde{u}_L \to j l_n^- l_f^+ \tilde{\chi}_1^0$ (upper two) and $\tilde{u}_L \to j l_n^+ l_f^- \tilde{\chi}_1^0$ (central two) and in m_{jl^+} and m_{jl^-} (lower two) where contributions from the two decays are summed.

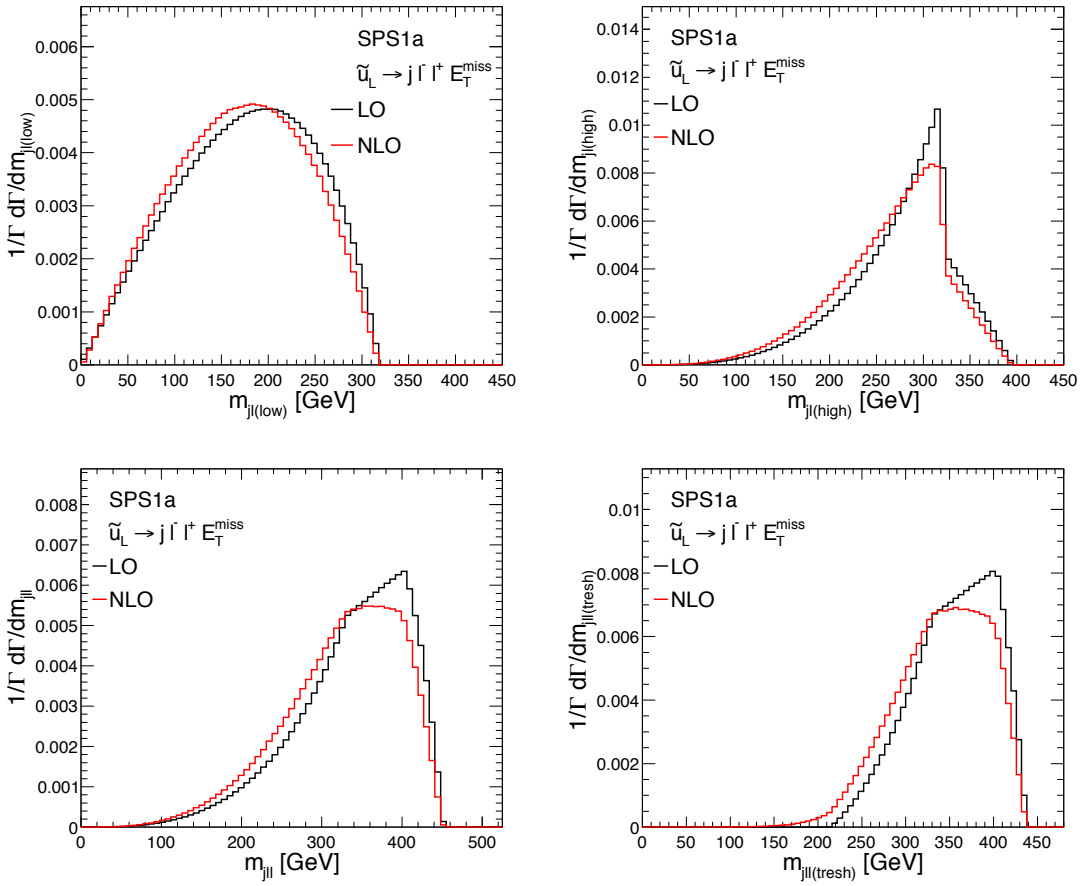

Figure 7.10: LO and NLO normalized differential distributions for SPS1a in $m_{jl(\text{low})}$, $m_{jl(\text{high})}$, m_{jll} and $m_{jll(\text{thresh})}$ (from top left to bottom right) for the decay chain $\tilde{q}_L \to q\ \tilde{\chi}_2^0 \to q\ l^{\pm}\ \tilde{l}_R^{\mp} \to q\ l^{\pm}\ l^{\mp}\ \tilde{\chi}_1^0$.

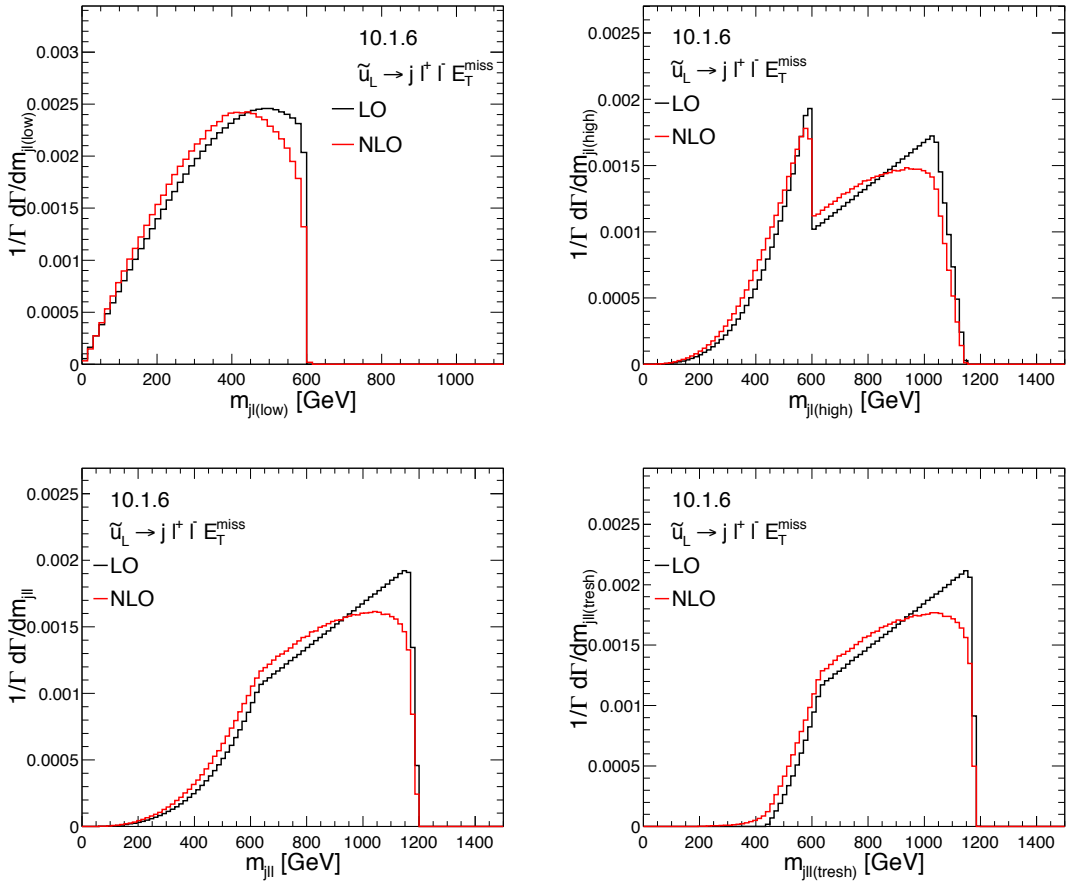

Figure 7.11: LO and NLO normalized differential distributions for 10.1.6 in $m_{jl(\mathrm{low})}$, $m_{jl(\mathrm{high})}$, m_{jll} and $m_{jll(\mathrm{thresh})}$ (from top left to bottom right) for the decay chain $\tilde{q}_L \to q\ \tilde{\chi}_2^0 \to q\ l^\pm\ \tilde{l}_L^\mp \to q\ l^\pm\ l^\mp\ \tilde{\chi}_1^0$.

experimental point of view we cannot distinguish between the near and the far lepton on an event-by-event basis. This is a well known problem and many solutions have been suggested in the literature, see e.g. [175]. Second, it is not obvious which jet has to be chosen to build the desired invariant mass distributions. Considering only the isolated decay chain, at LO the jet from the squark decay is the only one in the final state. But at higher orders, due to real gluon radiation, further jets can appear. Here we always choose the hardest available jet to build the invariant mass distributions, as done in [35].

In the upper left/right part of Figure 7.9 we show (unobservable) distributions in the invariant mass of the hardest jet and the negatively/positively charged near/far lepton from the decay chain $\tilde{u}_L \to j l_n^- l_f^+ \tilde{\chi}_1^0$. Here and in the remainder of this section we do not apply any cut but the jet definition cuts in eq. (7.6). In the center left/right part, on the other hand, we show (again unobservable) distributions in the invariant

mass of the hardest jet and the negatively/positively charged far/near lepton from the decay chain with the opposite charges for far and near leptons, $\tilde{u}_L \to j l_n^+ l_f^- \tilde{\chi}_1^0$. Finally, in the lower part of Figure 7.9 we show, in some sense[4], the sums of the two previous contributions. These distributions are in principle experimentally observable (after combination with the corresponding production process). The lower left/right panel shows the invariant mass of the hardest jet and the negatively/positively charged lepton summed over near and far contributions (m_{jl^-} and m_{jl^+}).

In the case of the decay of a left-handed anti-squark, all the distributions introduced so far are equal to the charge-conjugate ones of the corresponding squark, e.g, the $m_{jl_n^+}$ distribution from an $\tilde{u}_L^*$ decay chain is equal to the $m_{jl_n^-}$ distribution from an $\tilde{u}_L$ decay chain. Hence, the analogue of Figure 7.9 for $\tilde{q}_L^*$ would present the shapes of the distributions of the left column exchanged with the ones of the right column. Differences between squarks and anti-squarks obviously do not appear for quantities that are inclusive in the different charges of the leptons[5].

In all of the plots in Figure 7.9 NLO corrections tend to shift the distributions to smaller invariant masses, however, locations of endpoints are unaffected. Indeed, in general, the gluon radiation reduces the energy of the remaining particles, but with soft gluons, $E_g = 0$, the position of the endpoints are not changed. Kinematical edges in the NLO predictions are rounded off compared to LO; still, overall shapes of the considered contributions seem to be unaltered. Results and distributions of the same type have also been calculated in [35]. In their numerical evaluation the slightly different parameter point SPS1a' was investigated resulting in LO shapes somewhat different to those presented here. Qualitatively the NLO corrections shown in [35] for SPS1a' and ours for SPS1a agree. Moreover, we also investigated distributions and corrections for SPS1a' and found a qualitative agreement with [35]. However, in reference [35] a different jet algorithm was used. Results for SPS1a' presented there for $y_c = 0.002$ (see [35] for the definition) agree best with our results obtained using the anti-k_T jet clustering algorithm.

In Figure 7.10 we look, again for SPS1a, at the invariant mass distributions introduced in section 5.3.1: $m_{jl(\text{low})}$, $m_{jl(\text{high})}$ and m_{jll} plus $m_{jll(\text{thresh})}$, defined in the following. For $m_{jl(\text{low})}$ and $m_{jl(\text{high})}$ we select on an event-by-event basis the smaller and higher invariant mass between one of the leptons and the hardest jet. m_{jll} is the invariant mass between the hardest jet and the two leptons, and $m_{jll(\text{thresh})}$ is the same distribution where an additional constraint on the invariant mass of the two leptons, $\frac{m_{ll}^{\max}}{\sqrt{2}} < m_{ll}$, is applied. Here, $m_{ll}^{\max}$ is the well measurable endpoint of the dilepton invariant mass distribution. In our numerical analysis we use the theoretical endpoints,

[4]Since all plots are individually normalized to one, the plots in the last row of Figure 7.9 are not exactly the sums of the plots of the first and second rows.

[5]All the observable distributions discussed in this section but the one respect to A, satisfy this condition.

from LO analytical relations[6], $m_{ll}^{\max} = 80.0$ GeV for SPS1a and $m_{ll}^{\max} = 203.8$ GeV for the parameter point 10.1.6.

All these invariant mass distributions are in principle experimentally measurable and have been extensively discussed in the literature [175,176,179,180] (and references therein). From a measurement of their upper (and in case of $m_{jll(\text{thresh})}$ the lower) endpoints one might be able to extract relations for the masses of the intermediate sparticles. As mentioned in section 5.3.1, these relations often show ambiguities and, in particular, measurements of the threshold of $m_{jll(\text{thresh})}$ might help to resolve them. Also, shapes of the presented invariant mass distributions might help to overcome these difficulties.

Let us now look at the NLO corrections to these invariant mass distributions. Overall, again, distributions are shifted to smaller invariant masses. Also, upper kinks of m_{jll} and $m_{jll(\text{thresh})}$ are rounded off. These shifts might result in a slightly lowered accuracy in the measurement of the upper endpoints. Furthermore, the threshold of the $m_{jll(\text{thresh})}$, given by $m_{jll(\text{thresh})}^{\min} = 215.4$ for SPS1a and $m_{jll(\text{thresh})}^{\min} = 437.1$ for 10.1.6 [178], is diluted due to NLO corrections. In contrast to upper endpoints, the position of lower endpoints different from zero can be affected from real radiation. Also, due to this dilution, a precise measurement of this observable seems to be questionable.

The same set of invariant mass distributions, $m_{jl(\text{low})}$, $m_{jl(\text{high})}$, m_{jll} and $m_{jll(\text{thresh})}$, is shown in Figure 7.11 for the parameter point 10.1.6 and the corresponding decay chain involving a $\tilde{l}_L$. For the main part, again, NLO corrections shift the differential distributions to smaller invariant masses and round off the upper kinks. Particularly for $m_{jl(\text{low})}$ this might result in a smaller possible experimental accuracy for determining the upper endpoint. Apart from the rounding off of the kinks, general shapes of the distributions are mostly unaltered by NLO corrections. Also, a possible dilution of the lower endpoint of $m_{jll(\text{thresh})}$ due to NLO corrections seems to be less severe for the parameter point 10.1.6 compared to SPS1a.

7.2.3 Combined production and decay: distributions

Now we want to investigate the combined process, where cuts defined in eq. (7.7) have been applied. Here, we first examine the impact on various differential distributions important for parameter determination. Afterwards, in section 7.2.4 we investigate the impact of NLO QCD corrections on inclusive OS-SF dilepton observables and thus on searches currently performed at the LHC.

In the combination of production and decay, already at LO a combinatorial problem arises looking at invariant mass distributions. As already mentioned in section 7.2.2 it is not clear which jet to choose for building the different invariant masses. Just choosing the hardest jet as was done in section 7.2.2 does not seem to be sensible,

[6]The analytic relations for $m_{ll}^{\max}$, as the ones used afterwards in the text to calculate $m_{jll(\text{thresh})}^{\min}$ and $m_{jll}^{\max}$, are given in [187].

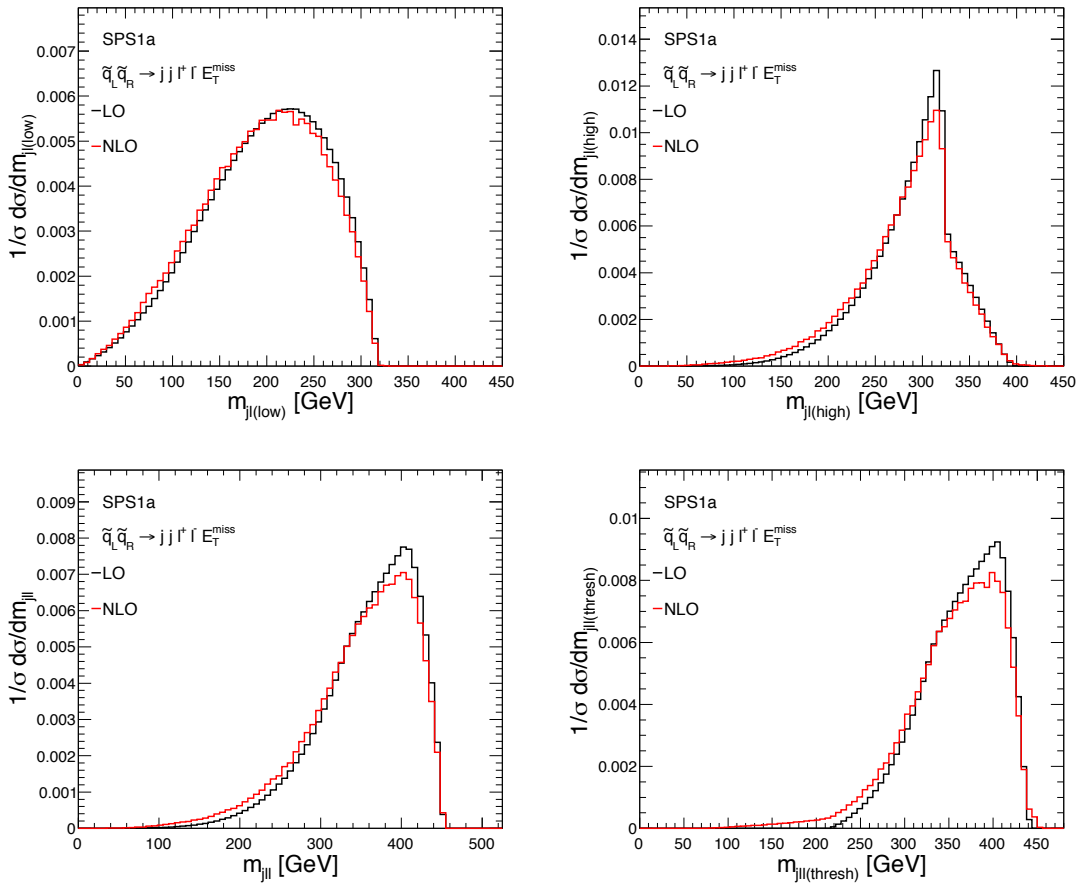

Figure 7.12: LO and NLO normalized differential distributions for SPS1a in $m_{jl(\text{low})}$, $m_{jl(\text{high})}$, m_{jll} and $m_{jll(\text{thresh})}$ (from top left to bottom right) for combined production and decay.

since the jet from the second decay, present already at LO, is often the hardest one. This is a well known problem in the application of the endpoint methods for mass determination and various methods have been developed to reduce this ambiguity. The easiest method is to always use the jet which gives e.g. the smaller m_{jll} value. In this way one improves the measurements of the upper endpoints without losing statistics; however, shapes are heavily distorted already at LO. In principle there are advanced techniques to solve this problem, amongst others, full kinematic event reconstruction [291] or hemisphere techniques [292–294]. However, these techniques are quite involved, parameter point dependent, and not generally applicable. Here, we apply consistency cuts, also discussed in [180], to reduce the impact of the jet combinatorics ambiguity. Applying such consistency cuts means that we accept only events where one jet j_i out of the two hardest jets j_i, j_k gives an invariant mass smaller than $m_{jll}^{\max}$ and the other jet j_k an invariant mass larger than $m_{jll}^{\max}$,

$$m_{j_i ll} < m_{jll}^{\max} < m_{j_k ll} \ . \tag{7.8}$$

Now j_i will be used in the following to build the invariant mass distributions. In this way we restrict to the case in which for sure we do not include, for building the invariant masses, one of the two jets not corresponding to the quark in the decay chain, i.e., either the jet from real correction or the jet from $\tilde{q}'_R \to q\tilde{\chi}_1^0$ decay.

This technique is very efficient in reducing the jet combinatorics ambiguity, however, event rates are also reduced (see section 7.2.4 and particularly Table 7.12). From an experimental point of view the endpoint $m_{jll}^{\max}$ is assumed to be measured in a first step where for example always the jet is chosen yielding the smaller m_{jll}. Here, we use the theoretical endpoints $m_{jll}^{\max} = 450.6$ GeV for SPS1a and $m_{jll}^{\max} = 1147.7$ GeV for 10.1.6.

In Figure 7.12 we show for SPS1a the same invariant mass distributions as already shown in Figure 7.10. Here, production and decays are combined at NLO, cuts of eq. (7.7) and further consistency cuts of eq. (7.8) are applied. Due to the NLO corrections, distributions are in general shifted to smaller invariant masses. Comparing just LO predictions in Figure 7.12 and Figure 7.10, particularly m_{jll} and $m_{jll(\text{thresh})}$ show a slightly different behavior introduced by the consistency cuts: the plateau is less prominent in Figure 7.12. Here, again we observe a dilution of the threshold in the $m_{jll(\text{thresh})}$ distribution at NLO. Similar observations can be made looking at Figure 7.13 (and comparing with Figure 7.11) for the combined results of parameter point 10.1.6. Overall, changes to the shapes are moderate and, concerning the measurements of the upper endpoints, only for $m_{jl(\text{low})}$ might be experimentally detectable. The consistency cuts, eq. (7.8), are based only on m_{jll} and this is why we observe, already at LO, contributions also beyond the theoretical upper endpoint of the other distributions; moreover, this effect is enhanced at NLO. Jets from real radiation in production and from $\tilde{q}'_R \to q'\tilde{\chi}_1^0$ decay can yield, if selected, invariant masses higher than the theoretical endpoints expected from the isolated decay chain.

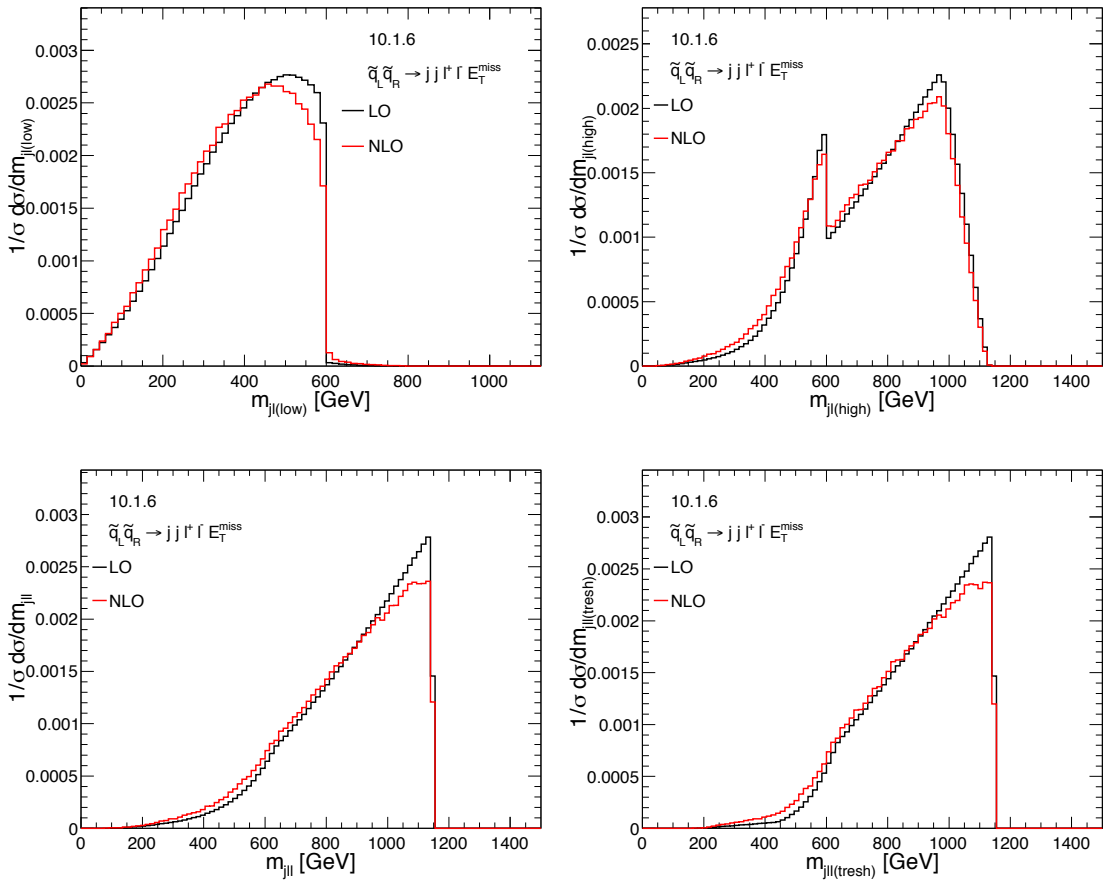

Figure 7.13: LO and NLO normalized differential distributions for 10.1.6 in $m_{jl(\text{low})}$, $m_{jl(\text{high})}$, m_{jll} and $m_{jll(\text{thresh})}$ (from top left to bottom right) for combined production and decay.

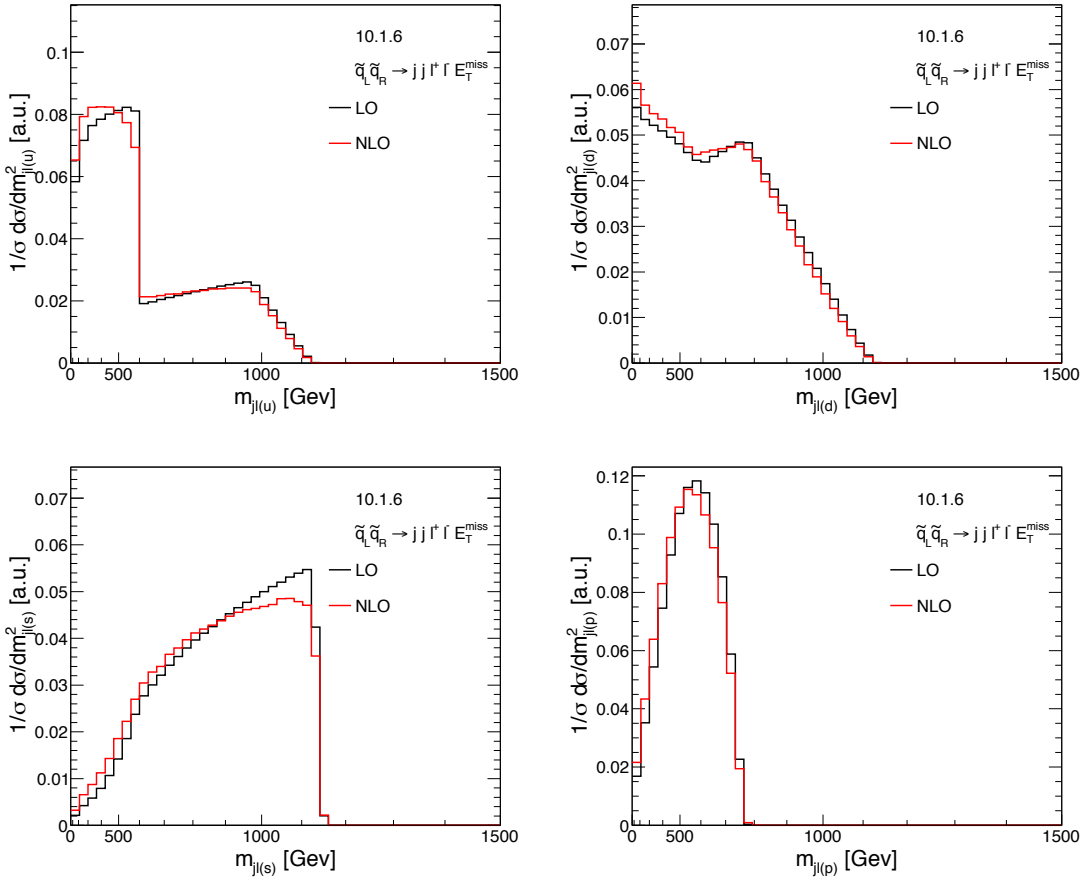

Figure 7.14: LO and NLO normalized differential distributions for 10.1.6 in $m_{jl(\mathrm{u})}$, $m_{jl(\mathrm{d})}$, $m_{jl(\mathrm{s})}$ and $m_{jl(\mathrm{p})}$ (from top left to bottom right) for combined production and decay shown with a quadratic scale.

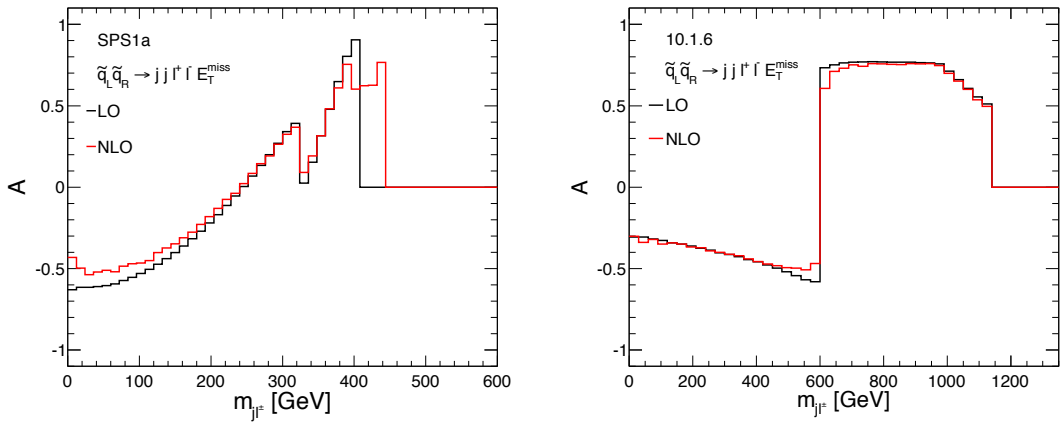

Figure 7.15: LO and NLO normalized differential distributions for SPS1a (left) and 10.1.6 (right) in the asymmetry A for combined production and decay.

From the discussion above, the usefulness of the threshold of $m_{jll(\text{thresh})}$ seems questionable. Additionally, a measurement of a lower endpoint is always subject to large experimental backgrounds [182, 187]. Since this threshold was introduced to solve ambiguities in the mass determination due to the near–far indistinguishability, new techniques for this purpose have been invented. In [187] the authors argue that all invariant mass distributions used for mass determination from the given decay chain should be built symmetrically under the interchange $l^{\text{near}} \leftrightarrow l^{\text{far}}$. In this spirit they introduce a new set of invariant mass distributions, $m^2_{jl(u)} \equiv m^2_{jl_n} \cup m^2_{jl_f}$, $m^2_{jl(d)} \equiv |m^2_{jl_n} - m^2_{jl_f}|$, $m^2_{jl(s)} \equiv m^2_{jl_n} + m^2_{jl_f}$ and $m^2_{jl(p)} \equiv m_{jl_n} \cdot m_{jl_f}$. The variable $m^2_{jl(u)} \equiv m^2_{jl_n} \cup m^2_{jl_f}$ denotes the distribution obtained making the union of $m^2_{jl_n}$ and $m^2_{jl_f}$ distributions. Here we study the impact of the NLO QCD corrections on this class of distributions. In Figure 7.14 we show the normalized LO and NLO distributions in $m^2_{jl(u)}, m^2_{jl(d)}, m^2_{jl(s)}$ and $m^2_{jl(p)}$ against a quadratic scale. Shapes of these distributions are slightly changed due to NLO corrections; however, the possibility of measuring their upper endpoints (both endpoints in the case of $m_{jl(\text{u})}$) seems to be unaffected.

Besides for mass determination, the given decay chain can also be used for spin determination or, more precisely, for spin distinction. As pointed out in [196] and many subsequent works, the asymmetry between the m_{jl^+} and m_{jl^-} distributions defined as

$$A = \frac{d\sigma/dm_{jl^+} - d\sigma/dm_{jl^-}}{d\sigma/dm_{jl^+} + d\sigma/dm_{jl^-}} \tag{7.9}$$

can help to discriminate between a SUSY model and other models like Universal Extra Dimensions (UED) in which a similar decay chain is possible, but the intermediate particles have different spins [197]. In Figure 7.15 we show LO and NLO predictions

for this asymmetry for SPS1a (left) and 10.1.6 (right). Again, cuts of eq. (7.7) and consistency cuts of eq. (7.8) have been applied. It seems that the NLO QCD corrections do not spoil the possibility of using these observables for spin determination and/or model discrimination. For SPS1a, at NLO, there is a contribution beyond the upper endpoint not present for this observable at LO. Indeed, this NLO contribution originates from events that pass the consistency cuts, based on the endpoint of the m_{jll} distribution. However, the expected rate for events, in this region of the asymmetry distribution, are experimentally negligible.

7.2.4 Combined production and decay: inclusive observables

The signature with two jets, two OS-SF leptons and missing transverse energy can also be used for searches for supersymmetry. At the LHC, using this signature, cut-and-count searches have been performed in the analyses of the 7 and 8 TeV runs [269, 270] and will be performed also at 14 TeV. Consequently, precise calculations of inclusive cross sections for the specific signal regions used in the cut-and-count searches are necessary. Moreover, also inclusive rates can be used, in principle, for parameter determination within a global fit [295].

Here, we discuss the differences between predictions in our calculation and rescaling LO with a flat K-factor from NLO corrections to squark-squark production without including decays and cuts. Also, we analyze the impact of the additional consistency cuts defined in eq. (7.8).

In Table 7.12 various integrated quantities at 14 TeV for the parameter points SPS1a and 10.1.6 are listed. Starting from the first column on the left we display: the total cross section $N^{(0)}_{2j+2l+\not{E}_T}$ at LO in the signal region defined by the cuts of eq. (7.7) and $N^{(0),\text{cons. cuts}}_{2j+2l+\not{E}_T}$ applying also the consistency cuts, together with the corresponding K-factors for these two quantities, $K_{N_{2j+2l+\not{E}_T}}$ and $K^{\text{cons. cuts}}_{N_{2j+2l+\not{E}_T}}$. Furthermore, we list the K-factors for just the production, including only the $\tilde{q}_L\tilde{q}'_R$ channels, $K_{pp\to\tilde{q}_L\tilde{q}'_R}$, and the K-factors including all chirality configurations, $K_{pp\to\tilde{q}\tilde{q}'}$.

The difference between the K-factors including the cuts defining the signal region, $K_{N_{2j+2l+\not{E}_T}}$, and the K-factors for production of $\tilde{q}_L\tilde{q}_R$ pairs, $K_{pp\to\tilde{q}_L\tilde{q}_R}$, is small, namely

	$N^{(0)}_{2j+2l+\not{E}_T}$	$N^{(0),\text{cons. cuts}}_{2j+2l+\not{E}_T}$	$K_{N_{2j+2l+\not{E}_T}}$	$K^{\text{cons. cuts}}_{N_{2j+2l+\not{E}_T}}$	$K_{pp\to\tilde{q}_L\tilde{q}'_R}$	$K_{pp\to\tilde{q}\tilde{q}'}$
SPS1a	38.2 fb	23.0 fb	1.36	1.23	1.34	1.28
10.1.6	0.628 fb	0.243 fb	1.46	1.39	1.44	1.41

Table 7.12: LO $N^{(0)}$ and NLO $N^{(0+1)}$ cross section predictions and K-factors K_N for the two benchmark scenarios SPS1a, 10.1.6 at a center-of-mass energy $\sqrt{S} = 14$ TeV where the cuts of eq. (7.7) are applied. For comparison we also list the inclusive NLO production K-factor $K_{pp\to\tilde{q}\tilde{q}'}$ and $K_{pp\to\tilde{q}_L\tilde{q}'_R}$.

0.02. This difference increases to 0.08 for SPS1a and 0.05 for the parameter point 10.1.6, if the K-factor for just the production includes all the chirality configurations. Thus, for the scenarios analyzed here, NLO corrections can be safely approximated by rescaling LO predictions with the K-factor obtained for the production part, provided that only the contributing chirality configurations are included in the calculation of the K-factor. It seems that, in this case, the effects due to the approximation indicated by the third point of the list on page 76 are dominant compared to the approximation indicated in the first two points. This feature, however, cannot easily be generalized; for example, as can be seen from Table 7.12, applying consistency cuts the differences between NLO and rescaled LO predictions increase also using $K_{pp\to\tilde{q}_L\tilde{q}'_R}$ as K-factor.

Consistency cuts are designed for the study of distributions relevant for parameter determination, as the ones discussed in the previous section. However, they decrease the cross sections, as can be seen comparing $N^{(0)}_{2j+2l+\not{E}_T}$ and $N^{(0),\text{cons. cuts}}_{2j+2l+\not{E}_T}$, without adding any obvious benefit in the context of searches. On the other hand, so far, we did not discuss the different normalization of the LO and NLO distributions shown in the previous sections. The values of $K^{\text{cons. cuts}}_{N_{2j+2l+\not{E}_T}}$ are exactly the ratios between the normalization of the LO and NLO results. These values are smaller than the K-factors obtained without consistency cuts. As discussed, such cuts are designed to solve the jet combinatorial problems arising from the combination with the production process and from NLO corrections. However, NLO corrections introduce combinatorial problems only via real radiation, but not via loop corrections. Neglecting the combinatorial problem due to the combination with production, consistency cuts reject only events for the real radiation contribution, but not events taking into account loop corrections. In this way, consistency cuts also reduce the positive contributions from real radiation of a gluon or a quark and consequently reduce the resulting K-factors. Thereby, in contrast to the case without consistency cuts applied, fully differential factorizable corrections have to be taken into account for a precise estimation of NLO effects.

Chapter 8

Conclusions

In this thesis we have discussed the calculation and the phenomenological impact of higher-order corrections for two different types of processes involving the production of massive particles at hadron colliders. We considered a SM process, top quark pair production, and a class of MSSM processes, squark–squark production and decays. In particular, we studied

- the electroweak contribution to the top quark forward-backward asymmetry at the Tevatron,
- the contribution of the factorizable NLO QCD corrections in NWA to the production of squark–squark pairs combined with subsequent squark decays, at fully differential level.

In both the studies the phenomenological impact of the considered higher-order corrections turned out to be relevant.

In the first study, our detailed analysis of the electroweak contributions to the forward-backward asymmetry in top quark pair production showed that $\mathcal{O}(\alpha_s^2\alpha)$ and $\mathcal{O}(\alpha^2)$ terms of the cross section provide a non-negligible addition, with the same overall sign, to the QCD-induced asymmetry. In this way, they enlarge the Standard Model prediction for the asymmetry at the Tevatron by a factor ~ 1.2, diminishing the deviation from experimental measurements. The precise value of the factor depends on the different definitions of the asymmetry and on applied cuts. However, the QED part of the contribution from the $\mathcal{O}(\alpha_s^2\alpha)$ term, which gives the largest part of the electroweak corrections, can be calculated multiplying the QCD-induced contribution from $\mathcal{O}(\alpha_s^3)$ cross section with a factor that does not depend on the definition of the asymmetry and the possible applied cuts.

Taking into account these corrections, in recent analyses with a larger data set, the 3.5σ deviation from SM prediction previously observed by CDF collaboration for high invariant masses of the top quark pair decreased to 2.5σ. Still, the dependence of the

asymmetry on the invariant mass remains and is not in agreement with SM predictions. This dependence of the forward-backward asymmetry could be an indication for the presence of new physics below the TeV scale. However, the BSM models that are designed to explain these deviations, must not considerably alter the SM predictions for top quark pair cross section and the charge asymmetry at the LHC. Indeed, in contrast to the case of the forward-backward asymmetry at the Tevatron, for these two observables SM predictions are in good agreement with experimental measurements. On the other hand, additional SM contributions to the prediction of the asymmetry might arise from the $\mathcal{O}(\alpha_s^4)$ differential cross section, which has not been calculated yet.

In the second study we considered the production of squark–squark pairs combined with two different decay configurations, which lead to two different experimental signatures. Firstly, we studied squark–squark production with both the squarks decaying directly into the lightest neutralino, which leads to the signature corresponding to 2 jets + missing transverse energy. Secondly, we studied the production of a left-handed squark and a right-handed squark combined with two different decays: the right-handed squark decaying directly into the lightest neutralino and the left-handed squark decaying via the "golden decay chain". In this way the emerging signature corresponds to 2 jets+ 2 leptons + missing transverse energy with the two leptons of opposite sign and same flavor. In both cases we used the same theoretical framework, calculating NLO QCD corrections in NWA and treating independently each flavor and chirality configuration of the squarks, at the fully differential level.

In the first case, we studied inclusive cross sections, differential distributions for jet observables, and experimental signatures with appropriate cuts. The NLO corrections are important and generally not flat in phase space. Thus, precise limits on the sparticle masses and model parameters cannot be in general obtained by rescaling LO predictions with a global K-factor. Moreover, this rescaling leads to unrealistic results in the case of compressed spectra. Also, in our calculation, the theoretical uncertainty at the level of differential distributions is reduced.

In the second case, we focused on the impact of NLO corrections on invariant-mass distributions that can be used, in case of discovery of supersymmetric particles, for parameter determination. We observed that general shapes, besides smoothing of edges and kinks and a shift towards smaller invariant masses, are not strongly altered. This seems to be an universal behavior despite the strong dependence of shapes on the parameter region. We also analyzed the impact of NLO corrections including decays on the predictions for cut-and-count strategies used in discovery searches. The predictions depend on the cuts applied and in general can be different from the results obtained rescaling LO predictions with flat K-factors obtained from the cross section of just production without decays and cuts included. However, in particular cases, results obtained in this approximation can be in very good agreement with those from our calculation, provided that only the contributing chirality configurations are included in the calculation of the flat K-factor.

Appendix A

Separation of factorizable and non-factorizable contributions

In this appendix, expanding the discussion in section 6.2.2, we explain in more detail the structure of factorizable and non-factorizable contributions and show that these two classes of contributions are independently gauge invariant. We also motivate and briefly describe the general features of the techniques for the evaluation of non-factorizable contributions. For completeness, and an easier reading of this appendix, we repeat here Figure 6.4 and Figure 6.5 shown in chapter 6.

As said in section 6.2.2, part of the NLO corrections to the combined production and decays of squark–squark pairs cannot be factorized into separate contributions to the production and to the decays. Indeed, loop diagrams as, e.g., the one shown in Figure A.1 involve interactions between quarks in the initial state and quarks emerging from squark decays. Analogously, for real gluon radiation, contributions as the one from the interference of the diagrams in Figure A.2 cannot be expressed as a correction for either production or decays separately. However, considering the same two

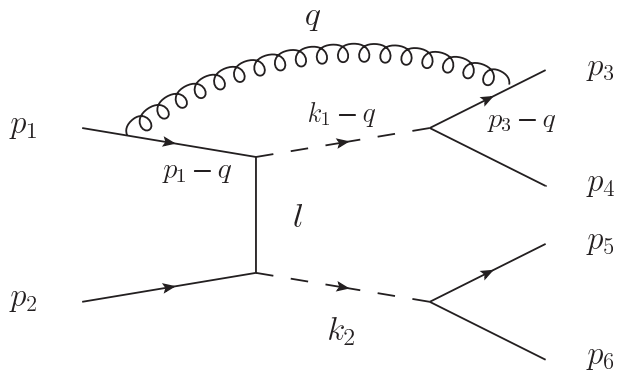

Figure A.1: Loop connecting quarks in the initial and final state.

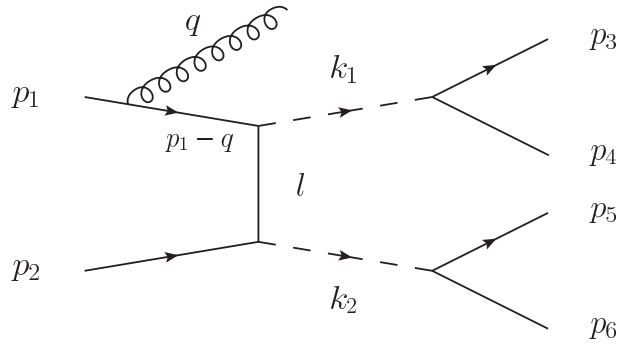

(a) Initial-state radiation.

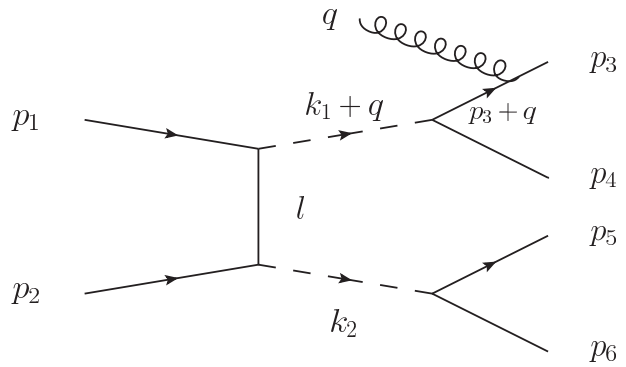

(b) Final-state radiation.

Figure A.2: Initial- and final-state real gluon radiation. Illustrative examples.

diagrams, the contributions from the separate squared diagrams of Figure A.2(a) and Figure A.2(b) can be factorized into contributions to the production and to the decays. Thus, the classification of factorizable and non-factorizable contributions has to be done at the level of squared amplitudes. Moreover, considering diagrams with real radiation of gluons from squarks, as e.g. the one shown in Figure A.3, or loop diagrams in which a gluon is connected to a squark propagator, the classification becomes more involved. The interference between this kind of diagrams and another diagram gives rise to both factorizable corrections to the production and the decays and to non-factorizable corrections. Thus, the division of factorizable and non-factorizable contributions cannot be based on a pure diagrammatical classification.

In general, the interference of real radiation diagrams and the interference of Born and loop diagrams can be classified according to:

- factorizable terms,
- manifestly non-factorizable terms,
- non-manifestly non-factorizable terms.

The first group gives rise only to factorizable contributions and includes terms as, e.g.,

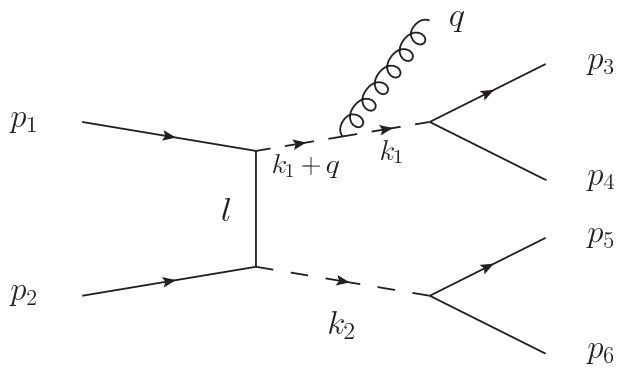

Figure A.3: Real emission of a gluon from a squark.

the two separate squared diagrams in Figure A.2. The second group gives rise only to non-factorizable corrections and contains terms as, e.g., the interference of the two diagrams in Figure A.2. The third group includes terms that produce both factorizable and non-factorizable contributions, as, e.g, the interferences of the diagram in Figure A.3 with the diagrams in Figure A.2. Since the Born diagram have no ambiguities, for virtual corrections this classification can be directly applied at the level of loop diagrams.

Factorizable and non-factorizable contributions are separately gauge-invariant. This can be shown in two different ways, according to [296, 297] or [298–300], where the same problem has been studied for the case of the electroweak NLO corrections to WW production, with W bosons decaying into fermions. The first approach, based on [296, 297] appears more practical for performing calculations and obtaining phenomenological predictions. The second approach, based on [298–300], provides a more general classification of factorizable and non-factorizable terms and does not require to specify every single contribution. Both approaches lead to well defined quantities, and the final results differ only by terms beyond the intrinsic order of accuracy, i.e., $\mathcal{O}(\alpha_s)$ corrections to the LO in NWA, eq. (6.3), including only the leading terms in the expansion in $\Gamma_{\tilde{q}}/m_{\tilde{q}}$.

In the first approach, non-factorizable corrections are identified, inside the complete set of NLO corrections to production and decay of squarks in Double-Pole-Approximation (DPA)[1], as part of the set complementary to the subset of factorizable corrections evaluated in NWA.

NLO corrections to just the production of squarks are gauge invariant. Thus, attaching tree-level diagrams for the decays to the diagrams for the squark–squark production at NLO, a gauge-invariant subset of the complete set of NLO corrections

[1]In DPA, only contributions arising form diagrams with at least two squark propagators that can potentially be on shell are taken into account.

is generated. Analogously, NLO corrections to just the decay of a squark are gauge invariant. Thus, attaching the corresponding diagrams to the tree-level diagram for squark–squark production, another gauge-invariant subset of the complete set of NLO corrections is generated. These two sets of corrections correspond to the terms explicitly shown in eq. (6.6) dropping NF, and form the gauge-invariant set of factorizable corrections in NWA.

Since the complete set of NLO corrections to the entire process is gauge invariant, the remaining contribution, complementary to factorizable corrections in NWA, is also gauge invariant. This complement contains non-factorizable corrections, which in the soft gluon limit, by allowing squarks to be on-shell, contribute to $\mathcal{O}(\alpha_s)$ corrections to the LO cross section in NWA, eq. (6.3). In addition, this complement also contains terms that contribute only to $\mathcal{O}(\alpha_s \frac{\Gamma_{\tilde{q}}}{m_{\tilde{q}}})$ corrections to the LO cross section in NWA, but not to $\mathcal{O}(\alpha_s)$ corrections. Thus, non-factorizable corrections can be correctly taken into account keeping in the complement only the contributions from non-manifestly and manifestly non-factorizable terms and discarding the remaining contributions from factorizable terms originating from off-shell configurations of the squarks and yielding only $\mathcal{O}(\alpha_s \frac{\Gamma_{\tilde{q}}}{m_{\tilde{q}}})$ corrections.

The evaluation of the non-factorizable corrections can be performed keeping the dependence on the gluon momentum only in infrared and collinear divergent terms (soft-gluon approximation) and in the squark propagators[2], and integrating the gluon momentum in the full phase space. In this way, the $\mathcal{O}(\alpha_s)$ corrections to the LO in NWA from non-factorizable contributions are correctly taken into account and their practical evaluation is technically easier.

In this approximation, it is possible to express loop diagrams as tree-level diagrams multiplied by a factor and a scalar loop integral. We illustrate the method for the diagram in Figure A.1, yielding:

$$\begin{aligned}
&\int \frac{d^4q}{(2\pi)^4} \bar{u}(p_3)(-i)g_s t^A \gamma^\mu (-i) \frac{\not{p}_3 - \not{q}}{(p_3-q)^2 - m_q^2} V^{\tilde{q}q\tilde{\chi}_1^0} \frac{-i}{(k_1-q)^2 - m_{\tilde{q}}^2 + i m_{\tilde{q}}\Gamma_{\tilde{q}}} V^{\tilde{g}q\tilde{q}} \mathcal{M}^{\text{out}} \\
&\times (-i) \frac{\not{p}_1 - \not{q}}{(p_1-q)^2 - m_q^2} (-i) g_s t^A \gamma_\mu \frac{-i}{q^2 - \lambda^2} u(p_1) \longrightarrow \\
&\bar{u}(p_3) V^{q\tilde{q}\tilde{\chi}_1^0} \frac{-i}{k_1^2 - m_{\tilde{q}}^2 + i m_{\tilde{q}}\Gamma_{\tilde{q}}} V^{q\tilde{q}\tilde{g}} \mathcal{M}^{\text{out}} u(p_1) \times [(k_1^2 - m_{\tilde{q}}^2 + i m_{\tilde{q}}\Gamma_{\tilde{q}})\, 4 p_3 \cdot p_1\, F_{\text{color}}] \\
&\times i \int \frac{d^4q}{(2\pi)^4} \frac{1}{q^2-\lambda^2} \frac{1}{2p_3 q - q^2} \frac{1}{2p_1 q - q^2} \frac{1}{(k_1-q)^2 - m_{\tilde{q}}^2 + i m_{\tilde{q}}\Gamma_{\tilde{q}}} \,. \qquad \text{(A.1)}
\end{aligned}$$

In eq. (A.1), $V^{\tilde{q}q\tilde{\chi}_1^0}$ and $V^{\tilde{g}q\tilde{q}}$ are the $\tilde{q}q\tilde{\chi}_1^0$ and $\tilde{g}q\tilde{q}$ vertices, F_{color} is a color factor[3] and $\mathcal{M}^{\text{out}}$ is the part of the amplitude not involved in the loop. The third line presents

[2] In [296], the analogous approximation for the photon momentum in electroweak corrections is called Extended-Soft-Photon-Approximation (ESPA). The only difference with the standard SPA is the presence of the photon momentum in the resonating intermediate propagators.

[3] If $\tilde{q} = \tilde{q}'$, two diagrams are present at tree level and F_{color} can vary in the different interferences.

the tree-level amplitude multiplied by a factor, and the fourth line is a scalar loop integral as another factor. Thus, the contribution to the cross section originating from this diagram can be written as the LO cross section with a multiplicative correction including a scalar loop integral. Similar arguments apply to the other loop diagrams.

This approximation can be used also to evaluate the real radiation. The contribution from the interference of two diagrams can be again written as the LO cross section with a multiplicative correction including a scalar integral. In this case, the scalar integrals contain integrands with the same structure as in the loop case, but the integration is performed on $\frac{d^3\vec{q}}{(2\pi)^3 2E_q}$. When loop and real radiation integrals are combined, the dependence on m_q and on λ, regulating collinear and infrared divergences, analytically cancels.

The second strategy consists in splitting the amplitudes into gauge-invariant terms and using them to classify factorizable and non-factorizable contributions in the squared matrix elements. For simplicity we start the discussion considering the real gluon radiation contribution, virtual corrections are discussed afterward.

As previously said, the classification of factorizable and non-factorizable contributions is at the level of squared amplitudes and is obtained in a non-diagrammatic way. Thus, also the gauge-invariant subsets in the real gluon emission amplitude cannot follow a diagrammatic classification. In order to divide the amplitude into gauge-invariant terms, we start applying the DPA. In this approximation also the contributions from diagrams with gluon emission from a squark, as in Figure A.3, are included. The emissions of a gluon from squarks are the problematic part, since we cannot define them as a correction to the initial or final state. They can, however, be decomposed into two parts and combined with initial- or final-state emission. In this way the real gluon radiation amplitude is divided into three gauge-invariant terms.

The key point is splitting the product of the squark propagators attached to the gluon, as e.g. in Figure A.3, into a sum of two propagators, as was already discussed in [301]. Ignoring, for a moment, couplings and color factors, this product of the two propagators and the $\tilde{q}\tilde{q}g$ vertex can be written as

$$\begin{aligned}&\frac{2k_1^\mu + q^\mu}{[k_1^2 - m_{\tilde{q}}^2 + im_{\tilde{q}}\Gamma_{\tilde{q}}][(k_1+q)^2 - m_{\tilde{q}}^2 + im_{\tilde{q}}\Gamma_{\tilde{q}}]} = \\ &= \frac{2k_1^\mu + q^\mu}{2k_1 q}\Big(\frac{1}{[k_1^2 - m_{\tilde{q}}^2 + im_{\tilde{q}}\Gamma_{\tilde{q}}]} - \frac{1}{[(k_1+q)^2 - m_{\tilde{q}}^2 + im_{\tilde{q}}\Gamma_{\tilde{q}}]}\Big)\,, \qquad \text{(A.2)}\end{aligned}$$

where k_1 is the sum of the momenta of the neutralino and the quark from the decay of the squark and q is the momentum of the emitted gluon. The two terms in the second line of eq. (A.2) are respectively similar to the corresponding contributions from a gluon emitted from initial- or final-state quarks. Indeed, in an emission of a gluon from the initial state, as e.g. in Figure A.2(a), the quark propagator introduces in the Born amplitude a term $(\not{p}_1 - \not{q})\gamma^\mu/(-2p_1 q)$, where p_1 is the momentum of the initial-state quark. Including also the first squark propagator, the change in the amplitude

corresponds to the term

$$\frac{(\not{p}_1 - \not{q})\gamma^\mu}{(-2p_1q)[k_1^2 - m_{\tilde{q}}^2 + im_{\tilde{q}}\Gamma_{\tilde{q}}]}\,. \tag{A.3}$$

Analogously, with an emission of a gluon from the final state, as e.g. in Figure A.2(b), the quark propagator introduces in the Born amplitude a term $(\not{p}_3+\not{q})\gamma^\mu/(2p_3q)$, where p_3 is the momentum of the final-state quark. In addition, the momentum of the squark is shifted to k_1+q, leading to a change in the amplitude

$$\frac{\gamma^\mu(\not{p}_3 + \not{q})}{(2p_3q)[(k_1+q)^2 - m_{\tilde{q}}^2 + im_{\tilde{q}}\Gamma_{\tilde{q}}]}\,. \tag{A.4}$$

A term in the amplitude for the $qq' \to \tilde{q}\tilde{q}'g$ process is gauge invariant if it vanishes for longitudinally polarized gluons. When the index μ is contracted with q_μ, the sum of the term in (A.3) and the first term in the r.h.s of eq. (A.2) and the sum of the second term of the r.h.s of eq. (A.2) and the term in (A.4) separately vanish between external spinors,

$$\begin{aligned}
&\Big\{\frac{(\not{p}_1 - \not{q})\gamma^\mu}{(-2p_1q)[k_1^2 - m_{\tilde{q}}^2 + im_{\tilde{q}}\Gamma_{\tilde{q}}]} \;+\; \frac{2k_1^\mu + q^\mu}{2k_1q}\frac{1}{[k_1^2 - m_{\tilde{q}}^2 + im_{\tilde{q}}\Gamma_{\tilde{q}}]}\Big\}q_\mu \to \\
&\to \frac{-1+1}{[(k_1+q)^2 - m_{\tilde{q}}^2 + im_{\tilde{q}}\Gamma_{\tilde{q}}]} \;=\; 0\,, \\
&\Big\{-\frac{2k_1^\mu + q^\mu}{2k_1q}\frac{1}{[(k_1+q)^2 - m_{\tilde{q}}^2 + im_{\tilde{q}}\Gamma_{\tilde{q}}]} \;+\; \frac{\gamma^\mu(\not{p}_3 + \not{q})}{(2p_3q)[(k_1+q)^2 - m_{\tilde{q}}^2 + im_{\tilde{q}}\Gamma_{\tilde{q}}]}\Big\}q_\mu \to \\
&\to \frac{-1+1}{[k_1^2 - m_{\tilde{q}}^2 + im_{\tilde{q}}\Gamma_{\tilde{q}}]} \;=\; 0\,.
\end{aligned} \tag{A.5}$$

Thus, the amplitude $\mathcal{M}_{\rm real}$ for $qq' \to \tilde{q}\tilde{q}'g$ can be written as,

$$\mathcal{M}_{\rm real} = \mathcal{M}_{\rm real,prod} + \mathcal{M}_{\rm real,decay1} + \mathcal{M}_{\rm real,decay2}\,. \tag{A.6}$$

In $\mathcal{M}_{\rm real,prod}$ we include all the contributions from initial-state emission and contributions from the intermediate emission, as the first term in the second line of eq. (A.2). In $\mathcal{M}_{\rm real,decay1}$ we include the contribution of the emission from the quark of the decay in the upper part of the diagram and contributions from the intermediate emission from the squark in the upper part of the diagram, as the second term in the second line of eq. (A.2). In the same way, in $\mathcal{M}_{\rm real,decay2}$ we include the emission from the quark of the decay in the lower part of the diagram and contributions as the second term of eq. (A.2) for the emission from the squark in the lower part of the diagram. The analogue formulae for this case can be obtained with the replacements $p_1 \to p_2$,

$p_3 \to p_5$, $k_1 \to k_2$ in formulae (A.2)-(A.4). Thus, according to eq. (A.5), the three terms $\mathcal{M}_{\rm real,prod}$, $\mathcal{M}_{\rm real,decay1}$ and $\mathcal{M}_{\rm real,decay2}$ are gauge invariant.

Squaring $\mathcal{M}_{\rm real}$, we get

$$|\mathcal{M}_{\rm real}|^2 = |\mathcal{M}_{\rm real,prod}|^2 + |\mathcal{M}_{\rm real,decay1}|^2 + |\mathcal{M}_{\rm real,decay2}|^2 + 2Re(\mathcal{M}_{\rm real,prod}, \mathcal{M}^*_{\rm real,decay1}) + 2Re(\mathcal{M}_{\rm real,prod}, \mathcal{M}^*_{\rm real,decay2}) + 2Re(\mathcal{M}_{\rm real,decay1}, \mathcal{M}^*_{\rm real,decay2}) \,. \quad \text{(A.7)}$$

The factorizable contributions originate from the first three squared terms of eq. (A.7). Each one of the terms $\mathcal{M}_{\rm real,prod}$, $\mathcal{M}_{\rm real,decay1}$ and $\mathcal{M}_{\rm real,decay2}$ is the sum of contributions that contain the same two resonating squark propagators. Thus, factorizable corrections contain two Breit-Wigner distributions for the squark momenta and can be calculated in NWA, setting squarks on-shell. The non-factorizable corrections originate from the remaining interference terms of eq. (A.7). In contrast to non-factorizable corrections, they do not contain two Breit-Wigner distributions for squark momenta and thus cannot be calculated in NWA.

For simplicity, we skipped in the previous discussion the effect of color matrices. Including them, we would not get zero in the second equation in (A.5). The color structure of gluon radiation from a squark is equal to the case of gluon radiation from the quark emerging from its decay, but not to the case of the radiation from a quark in the initial state. Moreover, for fixed external momenta, the momentum of the gluino is different when a gluon is radiated from the upper part of the diagram, as in Figure A.2 and Figure A.3, or from the lower part. However, this mismatch of the gluino momentum and the different color structures are compensated by including gluon emission from the gluino in $\mathcal{M}_{\rm real,prod}$.

The evaluation of the non-factorizable contributions from real gluon radiation can be performed, as in the first strategy, in the soft-gluon approximation and keeping the dependence on the gluon momentum in the propagators of the intermediate resonating squarks. Every contribution from the different diagrams can be expressed as the Born amplitude, with an additional $SU(3)_C$ color matrix from the emission vertex, multiplied by an eikonal soft factor. This factor has to include the possible modification induced by the gluon momenta in the squark propagator. For illustration, we explicitly show how the contributions of diagrams in Figure A.2, named respectively $\mathcal{M}^{\mu,A}_{\rm ini}$ and $\mathcal{M}^{\mu,A}_{\rm fin}$, are expressed in this approximation,

$$\begin{aligned} \mathcal{M}^{\mu,A}_{\rm ini} &= -ig_s \mathcal{M}^A_{\rm Born} \frac{2p_1^\mu}{2qp_1} \,, \\ \mathcal{M}^{\mu,A}_{\rm fin} &= -ig_s \mathcal{M}'^A_{\rm Born} \frac{2p_3^\mu}{2qp_3} \frac{k_1^2 - m^2_{\tilde q} + im_{\tilde q}\Gamma_{\tilde q}}{(k_1+q)^2 - m^2_{\tilde q} + im_{\tilde q}\Gamma_{\tilde q}} \,. \end{aligned} \quad \text{(A.8)}$$

In eq. (A.8) A is the color index of the radiated gluon and $\mathcal{M}^A_{\rm Born}$ is the Born amplitude with a matrix t^A inserted before the upper $q\tilde q\tilde g$ vertex; in the case of final-state radiation

the matrix is inserted after the vertex, yielding $\mathcal{M}'^{A}_{\rm Born}$. The two contributions arising in eq. (A.2) from the splitting of gluon emission from squarks can be written in an analogue way. Squaring the amplitudes, the non-factorizable contribution from real radiation can be again expressed as the LO cross section multiplied by a factor. This factor consists in the integration in $\frac{d^3\vec{q}}{(2\pi)^3 E_q}$ of the interferences of all the q-dependent terms in this approximation, as, e.g., the ones explicitly shown in eq. (A.8). For example, the structure of the integrand generated by $\mathcal{M}^{\mu,A}_{\rm ini}(\mathcal{M}^{B}_{{\rm fin},\mu})^*$ yields a multiplicative factor that, besides some signs, is equal to the one explicitly shown in eq. (A.1).

In the case of virtual corrections, the loop amplitude can be divided into two gauge-invariant terms, yielding respectively the factorizable and non-factorizable contributions. As mentioned before, loop diagrams can be divided into: factorizable (loops not involving squark propagators), non-manifestly non-factorizable, and manifestly non-factorizable. This division is not gauge invariant, but every non-manifestly non-factorizable diagram, involving interactions of squarks and gluons, can be split into a factorizable contribution and a non-factorizable contribution. This splitting can be obtained using the equivalent of relation eq. (A.2) for loop diagrams, in which in general $q^2 \neq 0$,

$$\begin{aligned}&\frac{2k_1^\mu + q^\mu}{[k_1^2 - m_{\tilde{q}}^2 + im_{\tilde{q}}\Gamma_{\tilde{q}}][(k_1+q)^2 - m_{\tilde{q}}^2 + im_{\tilde{q}}\Gamma_{\tilde{q}}]} = \\ &= \frac{2k_1^\mu + q^\mu}{2k_1 q + q^2}\Big(\frac{1}{[(k_1+q)^2 - m_{\tilde{q}}^2 + im_{\tilde{q}}\Gamma_{\tilde{q}}]} - \frac{1}{[k_1^2 - m_{\tilde{q}}^2 + im_{\tilde{q}}\Gamma_{\tilde{q}}]}\Big)\end{aligned} \tag{A.9}$$

and a similar relation for the second squark. Contracting q^μ with the gluon propagator in the loop, the terms proportional to $1/(k_1^2 - m_{\tilde{q}}^2 + im_{\tilde{q}}\Gamma_{\tilde{q}}) \times 1/(k_2^2 - m_{\tilde{q}'}^2 + im_{\tilde{q}'}\Gamma_{\tilde{q}'})$, produce factorizable corrections. Indeed, these terms with, outside the loop, the same propagators as the Born amplitude produce Breit-Wigner distributions in their contribution to the virtual corrections. The remaining terms produce non-factorizable contributions. Once non-manifestly non-factorizable diagrams are split into factorizable and non-factorizable contributions, all the factorizable and non-factorizable contributions in the loop amplitude can be arranged to yield two gauge-invariant classes.

The integrand in the loop amplitude can also be expressed in the soft-gluon approximation, keeping the dependence of squark propagators on the gluon momentum. Integrating over the full gluon momentum, the loop amplitude can be written as the Born amplitude multiplied by a factor containing a scalar loop integral, as shown in eq. (A.1).

In general, the integrands present the same structures of those entering the soft factor integral in the real-radiation contribution. However, in this case the integration is performed, as usual, in $\frac{d^4q}{(2\pi)^4}$.

Appendix B

Diagrams of NLO corrections

Here, we display all relevant loop diagrams involved in our NLO calculation of squark–squark production.

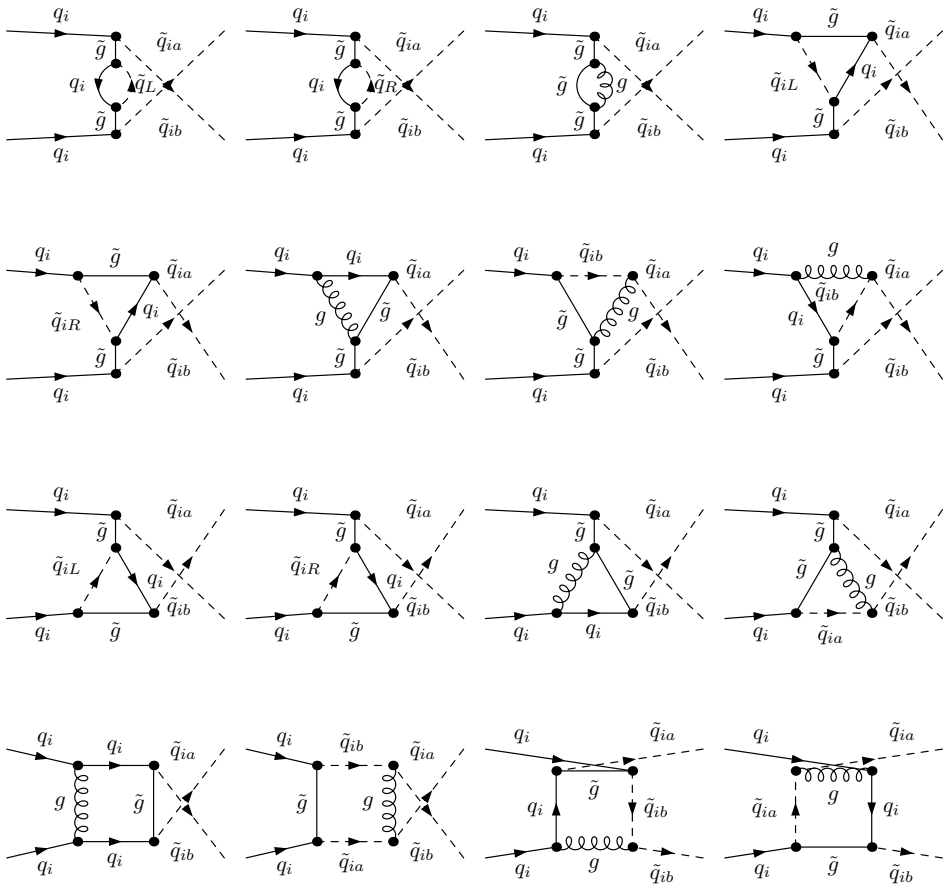

Figure B.1: Loop diagrams contributing only for squarks with equal flavor.

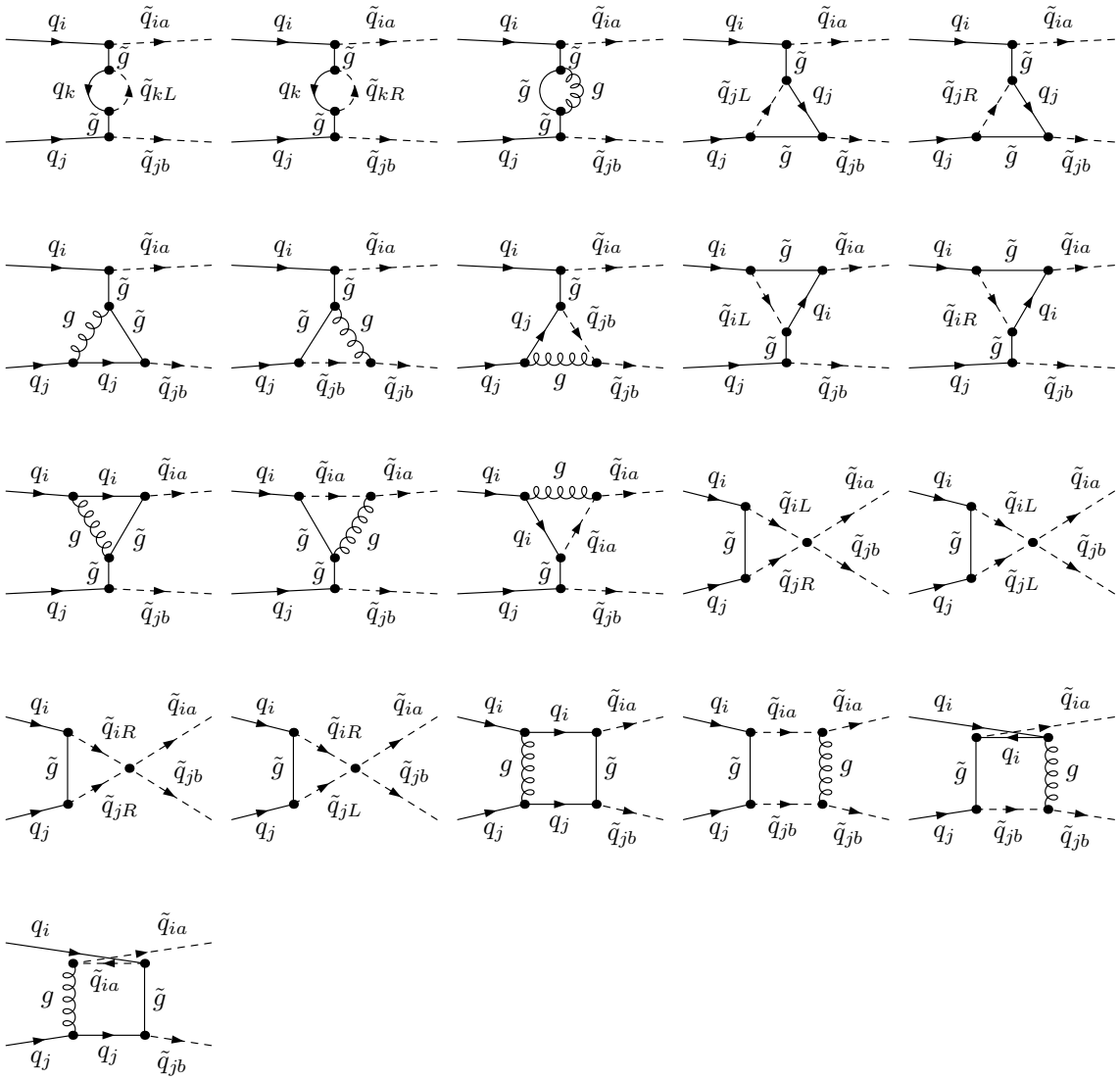

Figure B.2: Loop diagrams contributing to all flavor and chirality structures of squark–squark production.

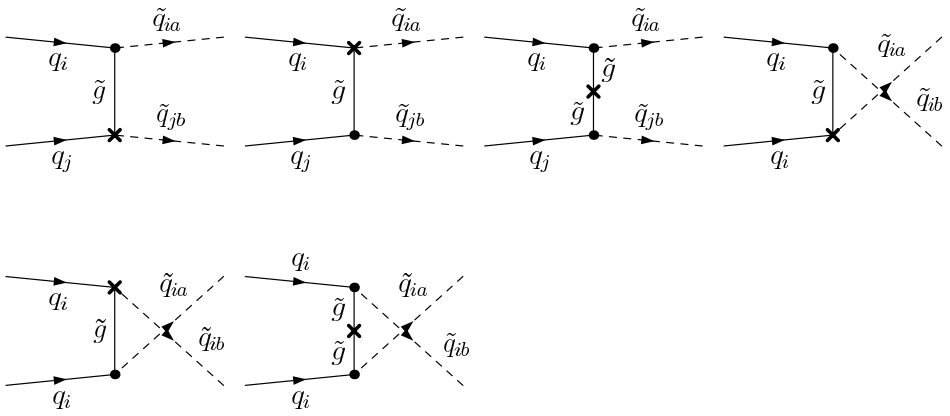

Figure B.3: Counterterms diagrams. The first three diagrams are always present, the remaining diagrams appear only for squarks with the same flavor.

Appendix C

Counterterms and renormalization constants

In this appendix we specify the renormalization counterterms used to eliminate the UV divergences stemming from the calculations of the virtual contributions discussed in chapter 6. As said, for squarks of the first two generations, assuming massless quarks, left–right mixing can be neglected and thus squark gauge eigenstates are also mass eigenstates. We denote, as usual, the chirality of a squark with an index $a = L, R$, which, in this appendix, is used also to specify the chirality of quarks.

The Feynman rules for the counterterms entering our calculations can be expressed via the field renormalization constants of quarks, squarks, gluons, and gluinos,

$$\begin{aligned} q_{ia}^{\text{bare}} &= q_{ia}^{\text{ren}} \left(1 + \frac{1}{2}\delta Z_{q_{ia}}\right), & \tilde{q}_{ia}^{\text{bare}} &= \tilde{q}_{ia}^{\text{ren}} \left(1 + \frac{1}{2}\delta Z_{\tilde{q}_{ia}}\right), \\ G_\mu^{\text{bare}} &= G_\mu^{\text{ren}} \left(1 + \frac{1}{2}\delta Z_G\right), & \tilde{g}^{\text{bare}} &= \tilde{g}^{\text{ren}} \left(1 + \frac{1}{2}\delta Z_{\tilde{g}}\right), \end{aligned} \tag{C.1}$$

and via the renormalization constants for the strong coupling g_s, for the strong Yukawa coupling $\hat{g}_s$, and for the squark and gluino masses,

$$\begin{aligned} g_s^{\text{bare}} &= g_s^{\text{ren}}(1 + \delta Z_{g_s}), & \hat{g}_s^{\text{bare}} &= \hat{g}_s^{\text{ren}}(1 + \delta Z_{\hat{g}_s}), \\ m^{2\,\text{bare}}_{\tilde{q}_{ia}} &= m^{2\,\text{ren}}_{\tilde{q}_{ia}} + \delta m^2_{\tilde{q}_{ia}}, & m_{\tilde{g}}^{\text{bare}} &= m_{\tilde{g}}^{\text{ren}} + \delta m_{\tilde{g}}. \end{aligned} \tag{C.2}$$

Since there is no gluon in the tree-level amplitudes, δZ_G and δZ_{g_s} are not explicitly involved in our calculations. However, Slavnov-Taylor identities relates δZ_{g_s} and $\delta Z_{\hat{g}_s}$ via eq. (6.20) and also δZ_G and δZ_{g_s} via the relation

$$\delta Z_G = 2\delta Z_{g_s}. \tag{C.3}$$

As said in section 6.4.2, eq. (6.20) is due to supersymmetry and it is valid at NLO QCD in the $\overline{\text{MS}}$ scheme, whereas eq. (C.3) is due to the $SU(3)_C$ gauge symmetry.

The expressions of the counterterms, that are relevant for our calculation of NLO QCD corrections to squark–squark production and $\tilde{q}_{ia} \to q_i \tilde{\chi}_j^0$ squark decays, are given in the following,

- Gluino self energy counterterm:

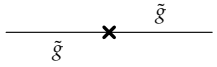

$$= \quad i[(\not{p} - m_{\tilde{g}})\delta Z_{\tilde{g}} - \delta m_{\tilde{g}}]$$

- Vertex counterterms:

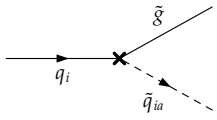

$$= \quad -i\tfrac{g_s}{\sqrt{2}}[\ (\ \delta Z_{\tilde{q}_{ia}} + 2\delta Z_{\hat{g}_s} + \delta Z_{\tilde{g}} + \delta Z_{q_{iL}}\ )\ \delta_{aL}\ P_L - (\ \delta Z_{\tilde{q}_{ia}} + 2\delta Z_{\hat{g}_s} + \delta Z_{\tilde{g}} + \delta Z_{q_{iR}}\ )\ \delta_{aR}\ P_R\ ]\ t^C$$

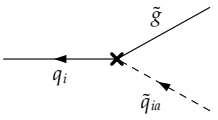

$$= \quad i\tfrac{g_s}{\sqrt{2}}[\ (\ \delta Z_{\tilde{q}_{ia}} + 2\delta Z_{\hat{g}_s} + \delta Z_{\tilde{g}} + \delta Z_{q_{iR}}\ )\ \delta_{aR}\ P_L - (\ \delta Z_{\tilde{q}_{ia}} + 2\delta Z_{\hat{g}_s} + \delta Z_{\tilde{g}} + \delta Z_{q_{iL}}\ )\ \delta_{aL}\ P_R\ ]\ t^C$$

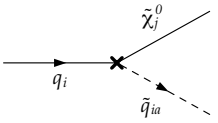

$$= \quad ie[A_-^j(q_i)\ (\delta Z_{\tilde{q}_{ia}} + \delta Z_{q_{iL}})\delta_{aL}\ P_L + A_+^j(q_i)\ (\delta Z_{\tilde{q}_{ia}} + \delta Z_{q_{iR}})\delta_{aR}\ P_R]$$

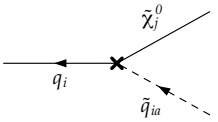

$$= \quad ie[A_+^{j*}(q_i)\ (\delta Z_{\tilde{q}_{ia}} + \delta Z_{q_{iR}})\delta_{aR}\ P_L + A_-^{j*}(q_i)\ (\delta Z_{\tilde{q}_{ia}} + \delta Z_{q_{iL}})\delta_{aL}\ P_R]$$

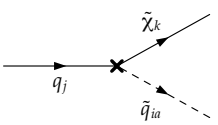

$$= \quad -ie\tfrac{B^k(q_j)}{2s_W}(\delta Z_{\tilde{q}_{ia}} + \delta Z_{q_{jL}})\delta_{aL}\ P_L$$

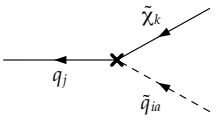

$$= \quad -ie\tfrac{B^{k*}(q_j)}{2s_W}(\delta Z_{\tilde{q}_{ia}} + \delta Z_{q_{jL}})\delta_{aL}\ P_R$$

The vertices involving neutralinos are defined via the quantities

$$A_+^j(q_i) = \frac{1}{\sqrt{2}}\frac{Q_{q_i}N_{j1}}{c_W}, \qquad A_-^j(q_i) = -\frac{1}{\sqrt{2}}\left(\frac{1}{6}\frac{N_{j1}^*}{c_W} + T_{q_i}^3\frac{N_{j2}^*}{s_W}\right), \tag{C.4}$$

where N_{ij} is the mixing matrix of the neutralinos introduced in eq. (5.10) and, again, s_W and c_W denote respectively the sine and the cosine of the electroweak mixing angle θ_W. The terms P_L and P_R respectively indicate the left-handed projector $(1-\gamma^5)/2$

and the right handed projector $(1+\gamma^5)/2$. The vertices involving charginos are defined via the quantities $B^k(q_j)$, which can be expressed in terms of the mixing matrices U and V (see eq. (5.11)) of the chargino sector: $B^k(q_j) = U^*_{k1}$ for up-type quarks and $B^k(q_j) = V^*_{k1}$ for down-type quarks. In the calculation of Feynman rules involving Majorana particles, the prescription of Ref. [302] has been used; the arrows in the quark lines indicate the fermion flow.

The renormalization constants of the squark sector are fixed by on-shell conditions (see also Ref. [303, 304]),

$$\begin{aligned}
\delta Z_{\tilde{q}_{ia}} &= -Re\left\{\frac{\partial \Sigma_{\tilde{q}_{ia}}(p^2)}{\partial p^2}\right\}_{\Big|p^2=m^2_{\tilde{q}_{ia}}}, & \delta m^2_{\tilde{q}_{ia}} &= Re\left\{\Sigma_{\tilde{q}_{ia}}(m^2_{\tilde{q}_{ia}})\right\}, \\
\delta Z_{\tilde{q}_{ja}} &= -Re\left\{\frac{\partial \Sigma_{\tilde{q}_{ja}}(p^2)}{\partial p^2}\right\}_{\Big|p^2=m^2_{\tilde{q}_{ia}}}, & \delta m^2_{\tilde{q}_{jR}} &= Re\left\{\Sigma_{\tilde{q}_{jR}}(m^2_{\tilde{q}_{jR}})\right\}, \qquad \text{(C.5)}
\end{aligned}$$

where in eq. (C.5) the pair of indices (i, j) are from a $SU(2)_L$ doublets and $\Sigma_{\tilde{q}_{ia}}$ is the self energy of the squark $\tilde{q}_{ia}$. Due to $SU(2)_L$ invariance, the mass counterterm of the left-handed down-type squark is a dependent quantity,

$$\delta m^2_{\tilde{q}_{jL}} = \delta m^2_{\tilde{q}_{iL}} \qquad \text{(C.6)}$$

The field renormalization constants of the quarks are obtained in on-shell scheme as follows [124],

$$\delta Z_{q_{ia}} = -Re\left\{\Sigma^a_{q_i}(m^2_q)\right\} - m^2_q Re\left\{\frac{\partial}{\partial p^2}\left(\Sigma^L_{q_i}(p^2) + \Sigma^R_{q_i}(p^2) + 2\Sigma^S_{q_i}(p^2)\right)\right\}_{\Big|p^2=m^2_q} \qquad \text{(C.7)}$$

via the scalar coefficients in the Lorentz decomposition of the self energy,

$$\Sigma(p^2) = \not{p} P_L \Sigma^L(p^2) + \not{p} P_R \Sigma^R(p^2) + m_q \Sigma^S(p^2). \qquad \text{(C.8)}$$

In our calculation we considered massless quark, however, in eq. (C.7) we assumed the mass of the quark equal to the regulator parameter m_q, in order to regulate collinear singularities. Analogously, the infrared singularities are regularized via the fictitious gluon mass λ.

Finally, also in the gluino sector the renormalization constants are determined by on-shell conditions,

$$\begin{aligned}
\delta m_{\tilde{g}} &= \frac{1}{2} Re\left\{m_{\tilde{g}}\left(\Sigma^L_{\tilde{g}}(m^2_{\tilde{g}}) + \Sigma^R_{\tilde{g}}(m^2_{\tilde{g}}) + 2\Sigma^S_{\tilde{g}}(m^2_{\tilde{g}})\right)\right\}, \qquad \text{(C.9)} \\
\delta Z_{\tilde{g}} &= -Re\left\{\Sigma^L_{\tilde{g}}(m^2_{\tilde{g}})\right\} - m^2_{\tilde{g}} Re\left\{\frac{\partial}{\partial p^2}\left(\Sigma^L_{\tilde{g}}(p^2) + \Sigma^R_{\tilde{g}}(p^2) + 2\Sigma^S_{\tilde{g}}(p^2)\right)\right\}_{\Big|p^2=m^2_{\tilde{g}}}.
\end{aligned}$$

Appendix D

Comparison between local and global DS schemes

In this appendix, expanding the discussion in section 6.4.3, we analyze in more detail the differences between the implementations of the DS scheme in the global approach, as indicated in eq. (6.38), and in the local approach, as used e.g. in [33,276,277]. In the following, we consider the contribution from the resonant diagrams of Figure 6.12(a), however, the same arguments apply also to the other contributions from resonant diagrams.

In a notation similar to the one of appendix B.1 of [33], where the DS scheme in the local approach was introduced, the contribution to the partonic cross section emerging from these diagrams of Figure 6.12(a) can be written as

$$\hat{\sigma} = \int_{m^2_{\tilde{q}_{ia}}}^{q^2_{\max}} dq^2 \frac{f(q^2)}{(q^2 - m^2_{\tilde{g}})^2 + m^2_{\tilde{g}}\Gamma^2_{\tilde{g}}}\,, \tag{D.1}$$

where $f(q^2)$ is the differential cross section in q^2 (the squared invariant mass of $\tilde{q}_{ia}$ and q_i) without the squared gluino propagator. Given the squared total energy s in the partonic center-of-mass frame, the maximum allowed value for q^2 is $q^2_{\max} = (\sqrt{s} - m_{\tilde{q}_{jb}})^2$.

In the global approach the contribution from on-shell $\tilde{q}_{jb}\tilde{g}$ production is subtracted by substituting $\hat{\sigma}$ with

$$\Delta\hat{\sigma}_{\text{Global}} = \hat{\sigma} - \hat{\sigma}_{\tilde{q}_{jb}\tilde{g}} \frac{\Gamma_{\tilde{g}\to\tilde{q}_{ia}}}{\Gamma_{\tilde{g}}}\,, \tag{D.2}$$

i.e. subtracting exactly the total cross section for on-shell production of $\tilde{q}_{jb}\tilde{g}$ multiplied by the branching ratio of $\tilde{g} \to \tilde{q}_{ia}q_i$.

In the local approach, before phase-space integration, $f(q^2)$ evaluated in the on-shell gluino configuration

$$f(m^2_{\tilde{g}}) = \hat{\sigma}_{\tilde{q}_{jb}\tilde{g}} \frac{m_{\tilde{g}}\Gamma_{\tilde{g}}}{\pi} \frac{\Gamma_{\tilde{g}\to\tilde{q}_{ia}}}{\Gamma_{\tilde{g}}} \tag{D.3}$$

is subtracted in the numerator of the integrand of eq. (D.1),

$$\Delta\hat{\sigma}_{\rm Local} = \int_{m^2_{\tilde{q}_{ia}}}^{q^2_{\rm max}} dq^2 \frac{f(q^2)-f(m^2_{\tilde{g}})}{(q^2-m^2_{\tilde{g}})^2+m^2_{\tilde{g}}\Gamma^2_{\tilde{g}}} := \hat{\sigma} - I\,, \quad \text{with} \quad I = \int_{m^2_{\tilde{q}_{ia}}}^{q^2_{\rm max}} dq^2 \frac{f(m^2_{\tilde{g}})}{(q^2-m^2_{\tilde{g}})^2+m^2_{\tilde{g}}\Gamma^2_{\tilde{g}}}\,. \tag{D.4}$$

In this parton level example the integral I can be analytically calculated. For $m_{\tilde{g}} > m_{\tilde{q}_{ia}}$ and $\sqrt{s} > m_{\tilde{g}} + m_{\tilde{q}_{jb}}$, i.e. in the region where the subtraction is required, it yields

$$\begin{aligned} I &= \frac{f(m^2_{\tilde{g}})}{\Gamma_{\tilde{g}} m_{\tilde{g}}}\left[\arctan\left(\frac{q^2_{\rm max}-m^2_{\tilde{g}}}{\Gamma_{\tilde{g}} m_{\tilde{g}}}\right) - \arctan\left(\frac{m^2_{\tilde{q}_{ia}}-m^2_{\tilde{g}}}{\Gamma_{\tilde{g}} m_{\tilde{g}}}\right)\right] \\ &= \hat{\sigma}_{\tilde{q}_{jb}\tilde{g}} \frac{\Gamma_{\tilde{g}\to\tilde{q}_{ia}}}{\Gamma_{\tilde{g}}}\left[1 - \frac{\Gamma_{\tilde{g}} m_{\tilde{g}}}{\pi}\left(\frac{q^2_{\rm max}-m^2_{\tilde{q}_{ia}}}{(q^2_{\rm max}-m^2_{\tilde{g}})(m^2_{\tilde{g}}-m^2_{\tilde{q}_{ia}})}\right)\right] + \mathcal{O}(\Gamma_{\tilde{g}})\,. \end{aligned} \tag{D.5}$$

Comparing in this way the global and local approach for the DS subtraction we find

$$\Delta\hat{\sigma}_{\rm Global} - \Delta\hat{\sigma}_{\rm Local} = -\hat{\sigma}_{\tilde{q}_{jb}\tilde{g}}\Gamma_{\tilde{g}\to\tilde{q}_{ia}} \frac{m_{\tilde{g}}}{\pi}\left(\frac{q^2_{\rm max}-m^2_{\tilde{q}_{ia}}}{(q^2_{\rm max}-m^2_{\tilde{g}})(m^2_{\tilde{g}}-m^2_{\tilde{q}_{ia}})}\right) + \mathcal{O}(\Gamma_{\tilde{g}})\,, \tag{D.6}$$

where the leading term is $\mathcal{O}(1)$ in the expansion in $\Gamma_{\tilde{g}}$. Hence, even in the limit $\Gamma_{\tilde{g}} \to 0$, the two approaches differ by a finite term depending on the physical phase-space boundaries, see also [305]. This can be understood from the fact that the approximation of the Breit-Wigner distribution $m_{\tilde{g}}\Gamma_{\tilde{g}}/[(q^2-m^2_{\tilde{g}})^2+m^2_{\tilde{g}}\Gamma^2_{\tilde{g}}] \to \pi\delta(q^2-m^2_{\tilde{g}})$, i.e. eq. (6.1), in the integrand of I is strictly valid only for an integration over the entire real axis, where

$$\int_{-\infty}^{\infty} dq^2 \frac{m_{\tilde{g}}\Gamma_{\tilde{g}}}{(q^2-m^2_{\tilde{q}})^2+m^2_{\tilde{q}}\,\Gamma^2_{\tilde{q}}} = \pi\,. \tag{D.7}$$

However, if the decay products of $\tilde{q}$ are not massless, the integration cannot be performed over the entire real axes. Moreover, the result in eq. (D.6) can be altered if the mapping $q^2 \to m^2_{\tilde{g}}$ in the local subtraction is performed before the integration of the other phase-space variables. This mapping is not uniquely defined and can lead to further differences. Indeed, the set of Lorentz invariant variables used, in addition to q^2, to write the cross section is not unique. Practically, the mapping consists in setting q^2 equal to $m^2_{\tilde{g}}$ and keeping fixed the remaining Lorentz-invariant variables. However, as said, a different set of variable can also be used and thus, in general, different results can be obtained.

At the hadronic level the numerical differences between the two approaches can be of the order of a few per mill of the on-shell $\tilde{q}_{jb}\tilde{g}$ production. Thus, depending on the parameter region, few per-cent differences can appear for the $\tilde{q}_{ia}\tilde{q}_{jb}$ NLO relative corrections. For example, for SPS1a and $\sqrt{S} = 14$ TeV, corrections for the $\tilde{d}_R\tilde{d}_R$ cross section arising from eq. (D.6) amount to 0.08% of $\sigma^{(0)}_{\tilde{d}_R\tilde{g}}$ and to 1.9% of $\sigma^{(0)}_{\tilde{d}_R\tilde{d}_R}$, since $\sigma^{(0)}_{\tilde{d}_R\tilde{g}}/\sigma^{(0)}_{\tilde{d}_R\tilde{d}_R} \approx 23$.

For different flavor and chirality configurations these corrections vary. Typically, the relative difference between global and local DS schemes are enhanced for processes with non-valence quarks in the LO partonic subprocess $q_i q_j \to \tilde{q}_i \tilde{q}_j$. However, the contribution from these processes are smaller than in the case with valence quark in the initial state.

Finally, we want to note that both the local and the global approach can be extended to a fully differential level.

Bibliography

[1] S. Glashow, *Partial Symmetries of Weak Interactions*, *Nucl.Phys.* **22** (1961) 579–588.

[2] S. Weinberg, *A Model of Leptons*, *Phys.Rev.Lett.* **19** (1967) 1264–1266.

[3] A. Salam, *Weak and Electromagnetic Interactions*, *Conf.Proc.* **C680519** (1968) 367–377.

[4] G. 't Hooft and M. Veltman, *Regularization and Renormalization of Gauge Fields*, *Nucl.Phys.* **B44** (1972) 189–213.

[5] D. Gross and F. Wilczek, *Ultraviolet Behavior of Nonabelian Gauge Theories*, *Phys.Rev.Lett.* **30** (1973) 1343–1346.

[6] H. D. Politzer, *Reliable Perturbative Results for Strong Interactions?*, *Phys.Rev.Lett.* **30** (1973) 1346–1349.

[7] H. Fritzsch, M. Gell-Mann, and H. Leutwyler, *Advantages of the Color Octet Gluon Picture*, *Phys.Lett.* **B47** (1973) 365–368.

[8] **ATLAS Collaboration**, G. Aad *et. al.*, *Observation of a new particle in the search for the Standard Model Higgs boson with the ATLAS detector at the LHC*, *Phys.Lett.* **B716** (2012) 1–29, [arXiv:1207.7214].

[9] **CMS Collaboration**, S. Chatrchyan *et. al.*, *Observation of a new boson at a mass of 125 GeV with the CMS experiment at the LHC*, *Phys.Lett.* **B716** (2012) 30–61, [arXiv:1207.7235].

[10] F. Englert and R. Brout, *Broken Symmetry and the Mass of Gauge Vector Mesons*, *Phys.Rev.Lett.* **13** (1964) 321–323.

[11] P. W. Higgs, *Broken symmetries, massless particles and gauge fields*, *Phys.Lett.* **12** (1964) 132–133.

[12] P. W. Higgs, *Broken Symmetries and the Masses of Gauge Bosons*, *Phys.Rev.Lett.* **13** (1964) 508–509.

[13] G. Guralnik, C. Hagen, and T. Kibble, *Global Conservation Laws and Massless Particles*, *Phys.Rev.Lett.* **13** (1964) 585–587.

[14] P. W. Higgs, *Spontaneous Symmetry Breakdown without Massless Bosons*, *Phys.Rev.* **145** (1966) 1156–1163.

[15] T. Kibble, *Symmetry breaking in nonAbelian gauge theories*, *Phys.Rev.* **155** (1967) 1554–1561.

[16] **CDF Collaboration**, F. Abe *et. al.*, *Observation of top quark production in $\bar{p}p$ collisions*, *Phys.Rev.Lett.* **74** (1995) 2626–2631, [hep-ex/9503002].

[17] **D0 Collaboration**, S. Abachi *et. al.*, *Observation of the top quark*, *Phys.Rev.Lett.* **74** (1995) 2632–2637, [hep-ex/9503003].

[18] **Muon G-2 Collaboration**, G. Bennett *et. al.*, *Final Report of the Muon E821 Anomalous Magnetic Moment Measurement at BNL*, *Phys.Rev.* **D73** (2006) 072003, [hep-ex/0602035].

[19] **ALEPH Collaboration, DELPHI Collaboration, L3 Collaboration, OPAL Collaboration, SLD Collaboration, LEP Electroweak Working Group, SLD Electroweak Group, SLD Heavy Flavour Group**, S. Schael *et. al.*, *Precision electroweak measurements on the Z resonance*, *Phys.Rept.* **427** (2006) 257–454, [hep-ex/0509008].

[20] **CDF Collaboration**, T. Aaltonen *et. al.*, *Evidence for a Mass Dependent Forward-Backward Asymmetry in Top Quark Pair Production*, *Phys.Rev.* **D83** (2011) 112003, [arXiv:1101.0034].

[21] J. Wess and B. Zumino, *Supergauge Transformations in Four-Dimensions*, *Nucl. Phys.* **B70** (1974) 39–50.

[22] H. P. Nilles, *Supersymmetry, Supergravity and Particle Physics*, *Phys.Rept.* **110** (1984) 1–162.

[23] H. E. Haber and G. L. Kane, *The Search for Supersymmetry: Probing Physics Beyond the Standard Model*, *Phys.Rept.* **117** (1985) 75–263.

[24] **ATLAS Collaboration**, G. Aad *et. al.*, *Search for squarks and gluinos with the ATLAS detector in final states with jets and missing transverse momentum using* $4.7 fb^{-1}$ *of* $\sqrt{s} = 7$ *TeV proton-proton collision data*, *Phys.Rev.* **D87** (2013) 012008, [arXiv:1208.0949].

[25] **ATLAS Collaboration**, G. Aad *et. al.*, *Hunt for new phenomena using large jet multiplicities and missing transverse momentum with ATLAS in 4.7* fb^{-1} *of* $\sqrt{s} = 7$ *TeV proton-proton collisions*, *JHEP* **1207** (2012) 167, [arXiv:1206.1760].

[26] **ATLAS Collaboration**, G. Aad *et. al.*, *Search for top and bottom squarks from gluino pair production in final states with missing transverse energy and at least three b-jets with the ATLAS detector*, *Eur.Phys.J.* **C72** (2012) 2174, [arXiv:1207.4686].

[27] **CMS Collaboration**, S. Chatrchyan *et. al.*, *Search for new physics in the multijet and missing transverse momentum final state in proton-proton collisions at* $\sqrt{s} = 7$ *TeV*, *Phys.Rev.Lett.* **109** (2012) 171803, [arXiv:1207.1898].

[28] **CMS Collaboration**, S. Chatrchyan *et. al.*, *Search for supersymmetry in final states with missing transverse energy and 0, 1, 2, or at least 3 b-quark jets in 7 TeV pp collisions using the variable alphaT*, *JHEP* **1301** (2013) 077, [arXiv:1210.8115].

[29] W. Hollik and D. Pagani, *The electroweak contribution to the top quark forward-backward asymmetry at the Tevatron*, *Phys.Rev.* **D84** (2011) 093003, [arXiv:1107.2606].

[30] J. H. Kuhn and G. Rodrigo, *Charge asymmetry of heavy quarks at hadron colliders*, *Phys.Rev.* **D59** (1999) 054017, [hep-ph/9807420].

[31] **CDF Collaboration**, T. Aaltonen *et. al.*, *Measurement of the top quark forward-backward production asymmetry and its dependence on event kinematic properties*, *Phys.Rev.* **D87** (2013) 092002, [arXiv:1211.1003].

[32] W. Hollik, J. M. Lindert, and D. Pagani, *NLO corrections to squark-squark production and decay at the LHC*, *JHEP* **1303** (2013) 139, [arXiv:1207.1071].

[33] W. Beenakker, R. Hopker, M. Spira, and P. M. Zerwas, *Squark and gluino production at hadron colliders*, *Nucl. Phys.* **B492** (1997) 51–103, [hep-ph/9610490].

[34] A. Djouadi, W. Hollik, and C. Junger, *QCD corrections to scalar quark decays*, *Phys. Rev.* **D55** (1997) 6975–6985, [hep-ph/9609419].

[35] R. Horsky, M. Kramer, A. Muck, and P. M. Zerwas, *Squark Cascade Decays to Charginos/Neutralinos: Gluon Radiation*, *Phys. Rev.* **D78** (2008) 035004, [arXiv:0803.2603].

[36] W. Hollik, J. M. Lindert, and D. Pagani, *On cascade decays of squarks at the LHC in NLO QCD*, *Eur.Phys.J.* **C73** (2013) 2410, [arXiv:1303.0186].

[37] **Planck Collaboration**, P. Ade *et. al.*, *Planck 2013 results. XVI. Cosmological parameters*, arXiv:1303.5076.

[38] M. L. Perl, G. Abrams, A. Boyarski, M. Breidenbach, D. Briggs, *et. al.*, *Evidence for Anomalous Lepton Production in e+ - e- Annihilation*, *Phys.Rev.Lett.* **35** (1975) 1489–1492.

[39] S. Herb, D. Hom, L. Lederman, J. Sens, H. Snyder, *et. al.*, *Observation of a Dimuon Resonance at 9.5-GeV in 400-GeV Proton-Nucleus Collisions*, *Phys.Rev.Lett.* **39** (1977) 252–255.

[40] **ARGUS COLLABORATION**, H. Albrecht *et. al.*, *Observation of B0 - anti-B0 Mixing*, *Phys.Lett.* **B192** (1987) 245.

[41] **JADE Collaboration**, W. Bartel *et. al.*, *A Measurement of the Electroweak Induced Charge Asymmetry in e+ e- $\to$ B anti-B*, *Phys.Lett.* **B146** (1984) 437.

[42] **Particle Data Group**, J. Beringer *et. al.*, *Review of Particle Physics (RPP)*, *Phys.Rev.* **D86** (2012) 010001.

[43] T. Han, *The 'Top Priority' at the LHC*, *Int.J.Mod.Phys.* **A23** (2008) 4107–4124, [arXiv:0804.3178].

[44] W. Bernreuther, *Top quark physics at the LHC*, *J.Phys.* **G35** (2008) 083001, [arXiv:0805.1333].

[45] E. Laenen, *Top quark in theory*, *Pramana* **79** (2012) 629–641, [arXiv:0809.3158].

[46] D. Wackeroth, *Top quark theory review for the Tevatron, LHC, and ILC*, arXiv:0810.4176.

[47] F.-P. Schilling, *Top Quark Physics at the LHC: A Review of the First Two Years*, *Int.J.Mod.Phys.* **A27** (2012) 1230016, [arXiv:1206.4484].

[48] K. Lannon, F. Margaroli, and C. Neu, *Measurements of the Production, Decay and Properties of the Top Quark: A Review*, *Eur.Phys.J.* **C72** (2012) 2120, [arXiv:1201.5873].

[49] M. Jezabek and J. H. Kuhn, *QCD Corrections to Semileptonic Decays of Heavy Quarks*, *Nucl.Phys.* **B314** (1989) 1.

[50] A. Denner and T. Sack, *The Top width*, *Nucl.Phys.* **B358** (1991) 46–58.

[51] G. Eilam, R. Mendel, R. Migneron, and A. Soni, *Radiative corrections to top quark decay*, *Phys.Rev.Lett.* **66** (1991) 3105–3108.

[52] M. Jezabek and J. H. Kuhn, *The Top width: Theoretical update*, *Phys.Rev.* **D48** (1993) 1910–1913, [hep-ph/9302295].

[53] A. Czarnecki and K. Melnikov, *Two loop QCD corrections to top quark width*, *Nucl.Phys.* **B544** (1999) 520–531, [hep-ph/9806244].

[54] K. Chetyrkin, R. Harlander, T. Seidensticker, and M. Steinhauser, *Second order QCD corrections to Gamma(t $\to$ W b)*, *Phys.Rev.* **D60** (1999) 114015, [hep-ph/9906273].

[55] M. Brucherseifer, F. Caola, and K. Melnikov, *$\mathcal{O}(\alpha_s^2)$ corrections to fully-differential top quark decays*, *JHEP* **1304** (2013) 059, [arXiv:1301.7133].

[56] C. Collaboration, *Measurement of the ratio B(t to Wb)/B(t to Wq)*, *Public Notes* (2012).

[57] U. Langenfeld, S. Moch, and P. Uwer, *Measuring the running top-quark mass*, *Phys.Rev.* **D80** (2009) 054009, [arXiv:0906.5273].

[58] M. Baak, M. Goebel, J. Haller, A. Hoecker, D. Kennedy, *et. al.*, *The Electroweak Fit of the Standard Model after the Discovery of a New Boson at the LHC*, *Eur.Phys.J.* **C72** (2012) 2205, [arXiv:1209.2716].

[59] M. Lindner, *Implications of Triviality for the Standard Model*, *Z.Phys.* **C31** (1986) 295.

[60] M. Sher, *Electroweak Higgs Potentials and Vacuum Stability*, *Phys.Rept.* **179** (1989) 273–418.

[61] G. Degrassi, S. Di Vita, J. Elias-Miro, J. R. Espinosa, G. F. Giudice, *et. al.*, *Higgs mass and vacuum stability in the Standard Model at NNLO*, *JHEP* **1208** (2012) 098, [arXiv:1205.6497].

[62] **ATLAS Collaboration**, G. Aad *et. al.*, *Measurement of the W boson polarization in top quark decays with the ATLAS detector*, *JHEP* **1206** (2012) 088, [arXiv:1205.2484].

[63] S. Glashow, J. Iliopoulos, and L. Maiani, *Weak Interactions with Lepton-Hadron Symmetry*, *Phys.Rev.* **D2** (1970) 1285–1292.

[64] A. Onofre, *Searches for new physics in top decays at the LHC*, arXiv:1212.6898.

[65] **D0 Collaboration**, V. Abazov *et. al.*, *Evidence for production of single top quarks and first direct measurement of —Vtb—*, *Phys.Rev.Lett.* **98** (2007) 181802, [hep-ex/0612052].

[66] **D0 Collaboration**, V. Abazov *et. al.*, *Observation of Single Top Quark Production*, *Phys.Rev.Lett.* **103** (2009) 092001, [arXiv:0903.0850].

[67] **CDF Collaboration**, T. Aaltonen *et. al.*, *First Observation of Electroweak Single Top Quark Production*, *Phys.Rev.Lett.* **103** (2009) 092002, [arXiv:0903.0885].

[68] B. Harris, E. Laenen, L. Phaf, Z. Sullivan, and S. Weinzierl, *The Fully differential single top quark cross-section in next to leading order QCD*, *Phys.Rev.* **D66** (2002) 054024, [hep-ph/0207055].

[69] Z. Sullivan, *Understanding single-top-quark production and jets at hadron colliders*, *Phys.Rev.* **D70** (2004) 114012, [hep-ph/0408049].

[70] N. Kidonakis, *Single top production at the Tevatron: Threshold resummation and finite-order soft gluon corrections*, *Phys.Rev.* **D74** (2006) 114012, [hep-ph/0609287].

[71] N. Kidonakis, *Higher-order soft gluon corrections in single top quark production at the LHC*, *Phys.Rev.* **D75** (2007) 071501, [hep-ph/0701080].

[72] E. Boos, V. Bunichev, L. Dudko, and M. Perfilov, *Interference between W' and W in single-top quark production processes*, *Phys.Lett.* **B655** (2007) 245–250, [hep-ph/0610080].

[73] F. Maltoni, K. Paul, T. Stelzer, and S. Willenbrock, *Associated production of Higgs and single top at hadron colliders*, *Phys.Rev.* **D64** (2001) 094023, [hep-ph/0106293].

[74] J. Cao, G. Eilam, M. Frank, K. Hikasa, G. Liu, *et. al.*, *SUSY-induced FCNC top-quark processes at the large hadron collider*, *Phys.Rev.* **D75** (2007) 075021, [hep-ph/0702264].

[75] V. Ahrens, A. Ferroglia, M. Neubert, B. Pecjak, and L. Yang, *Top-Quark Pair Production Beyond Next-to-Leading Order*, *Nucl.Phys.Proc.Suppl.* **205-206** (2010) 48–53, [arXiv:1006.4682].

[76] V. Ahrens, A. Ferroglia, M. Neubert, B. D. Pecjak, and L. L. Yang, *Renormalization-Group Improved Predictions for Top-Quark Pair Production at Hadron Colliders*, *JHEP* **1009** (2010) 097, [arXiv:1003.5827].

[77] N. Kidonakis, *Next-to-next-to-leading soft-gluon corrections for the top quark cross section and transverse momentum distribution*, *Phys.Rev.* **D82** (2010) 114030, [arXiv:1009.4935].

[78] M. Beneke, P. Falgari, S. Klein, and C. Schwinn, *Hadronic top-quark pair production with NNLL threshold resummation*, *Nucl.Phys.* **B855** (2012) 695–741, [arXiv:1109.1536].

[79] M. Cacciari, M. Czakon, M. Mangano, A. Mitov, and P. Nason, *Top-pair production at hadron colliders with next-to-next-to-leading logarithmic soft-gluon resummation*, *Phys.Lett.* **B710** (2012) 612–622, [arXiv:1111.5869].

[80] N. Kidonakis, *NNLL threshold resummation for top-pair and single-top production*, arXiv:1210.7813.

[81] M. Beneke, P. Falgari, S. Klein, J. Piclum, and C. Schwinn, *NNLL Threshold Resummation for the Total Top-Pair Production Cross Section*, arXiv:1205.0988.

[82] M. Beneke, M. Czakon, P. Falgari, A. Mitov, and C. Schwinn, *Threshold expansion of the gg(qq-bar) →gt; QQ-bar + X cross section at $\mathcal{O}(\alpha_s^4)$*, *Phys.Lett.* **B690** (2010) 483–490, [arXiv:0911.5166].

[83] V. Ahrens, A. Ferroglia, M. Neubert, B. D. Pecjak, and L. L. Yang, *Precision predictions for the $t\bar{t}$ production cross section at hadron colliders*, *Phys.Lett.* **B703** (2011) 135–141, [arXiv:1105.5824].

[84] P. Baernreuther, M. Czakon, and A. Mitov, *Percent Level Precision Physics at the Tevatron: First Genuine NNLO QCD Corrections to $q\bar{q} \to t\bar{t} + X$*, *Phys.Rev.Lett.* **109** (2012) 132001, [arXiv:1204.5201].

[85] M. Czakon and A. Mitov, *NNLO corrections to top pair production at hadron colliders: the quark-gluon reaction*, *JHEP* **1301** (2013) 080, [arXiv:1210.6832].

[86] M. Czakon, P. Fiedler, and A. Mitov, *The total top quark pair production cross-section at hadron colliders through $\mathcal{O}(alpha_S^4)$*, arXiv:1303.6254.

[87] K. Melnikov and M. Schulze, *NLO QCD corrections to top quark pair production and decay at hadron colliders*, *JHEP* **0908** (2009) 049, [arXiv:0907.3090].

[88] J. M. Campbell and R. K. Ellis, *Top-quark processes at NLO in production and decay*, arXiv:1204.1513.

[89] W. Beenakker, F. A. Berends, and A. Chapovsky, *One loop QCD interconnection effects in pair production of top quarks*, *Phys.Lett.* **B454** (1999) 129–136, [hep-ph/9902304].

[90] G. Bevilacqua, M. Czakon, A. van Hameren, C. G. Papadopoulos, and M. Worek, *Complete off-shell effects in top quark pair hadroproduction with leptonic decay at next-to-leading order*, *JHEP* **1102** (2011) 083, [arXiv:1012.4230].

[91] A. Denner, S. Dittmaier, S. Kallweit, and S. Pozzorini, *NLO QCD corrections to off-shell top-antitop production with leptonic decays at hadron colliders*, *JHEP* **1210** (2012) 110, [arXiv:1207.5018].

[92] W. Beenakker, A. Denner, W. Hollik, R. Mertig, T. Sack, *et. al.*, *Electroweak one loop contributions to top pair production in hadron colliders*, *Nucl.Phys.* **B411** (1994) 343–380.

[93] J. H. Kuhn, A. Scharf, and P. Uwer, *Electroweak effects in top-quark pair production at hadron colliders*, *Eur.Phys.J.* **C51** (2007) 37–53, [hep-ph/0610335].

[94] W. Bernreuther, M. Fuecker, and Z.-G. Si, *Weak interaction corrections to hadronic top quark pair production*, *Phys.Rev.* **D74** (2006) 113005, [hep-ph/0610334].

[95] W. Hollik and M. Kollar, *NLO QED contributions to top-pair production at hadron collider*, *Phys.Rev.* **D77** (2008) 014008, [arXiv:0708.1697].

[96] W. Bernreuther and Z.-G. Si, *Distributions and correlations for top quark pair production and decay at the Tevatron and LHC.*, *Nucl.Phys.* **B837** (2010) 90–121, [arXiv:1003.3926].

[97] D. Pagani, *The electroweak contribution to top quark pair production: cross sections and asymmetries*, arXiv:1212.0808.

[98] J. Kuehn, A. Scharf, and P. Uwer, *Weak Interactions in Top-Quark Pair Production at Hadron Colliders: An Update*, arXiv:1305.5773.

[99] **ATLAS Collaboration**, G. Aad *et. al.*, *Measurements of top quark pair relative differential cross-sections with ATLAS in pp collisions at* $\sqrt{s} = 7$ *TeV*, *Eur.Phys.J.* **C73** (2013) 2261, [arXiv:1207.5644].

[100] A. Martin, R. Roberts, W. Stirling, and R. Thorne, *Parton distributions incorporating QED contributions*, *Eur.Phys.J.* **C39** (2005) 155–161, [hep-ph/0411040].

[101] S. Carrazza, *Towards an unbiased determination of parton distributions with QED corrections*, arXiv:1305.4179.

[102] **ATLAS Collaboration**, G. Aad *et. al.*, *Search for resonances decaying into top-quark pairs using fully hadronic decays in pp collisions with ATLAS at* $\sqrt{s} = 7$ *TeV*, *JHEP* **1301** (2013) 116, [arXiv:1211.2202].

[103] **ATLAS Collaboration**, G. Aad *et. al.*, *A search for* $t\bar{t}$ *resonances in the lepton plus jets final state with ATLAS using 4.7* fb^{-1} *of pp collisions at* $\sqrt{s} = 7$ *TeV*, arXiv:1305.2756.

[104] G. Rodrigo, *The ttbar asymmetry in the Standard Model and beyond*, arXiv:1207.0331.

[105] **ATLAS Collaboration, CDF Collaboration, CMS Collaboration, D0 Collaboration**, Y. Peters, *Top anti-top Asymmetries at the Tevatron and the LHC*, arXiv:1211.6028.

[106] G. Rodrigo, *Tevatron anomalies and LHC cross-checks*, *PoS* **EPS-HEP2011** (2011) 214, [arXiv:1112.6106].

[107] D. Pagani, *Top quark forward-backward asymmetry at the Tevatron: the electroweak contribution*, *PoS* **CORFU2011** (2011) 027, [arXiv:1205.6182].

[108] A. Martin, W. Stirling, R. Thorne, and G. Watt, *Parton distributions for the LHC*, *Eur.Phys.J.* **C63** (2009) 189–285, [arXiv:0901.0002].

[109] R. D. Ball, L. Del Debbio, S. Forte, A. Guffanti, J. I. Latorre, *et. al.*, *A first unbiased global NLO determination of parton distributions and their uncertainties*, *Nucl.Phys.* **B838** (2010) 136–206, [arXiv:1002.4407].

[110] M. Gluck, J. Owens, and E. Reya, *Gluon Contribution to Hadronic J/psi Production*, *Phys.Rev.* **D17** (1978) 2324.

[111] B. Combridge, *Associated Production of Heavy Flavor States in p p and anti-p p Interactions: Some QCD Estimates*, *Nucl.Phys.* **B151** (1979) 429.

[112] J. Babcock, D. W. Sivers, and S. Wolfram, *QCD Estimates for Heavy Particle Production*, *Phys.Rev.* **D18** (1978) 162.

[113] K. Hagiwara and T. Yoshino, *Hadroproduction of Heavy Quark Flavors in QCD*, *Phys.Lett.* **B80** (1979) 282.

[114] L. Jones and H. Wyld, *On Hadronic Charm Production by Gluon Fusion*, *Phys.Rev.* **D17** (1978) 1782.

[115] H. Georgi, S. Glashow, M. Machacek, and D. V. Nanopoulos, *Charmed Particles from two - Gluon Annihilation in Proton Proton Collisions*, *Annals Phys.* **114** (1978) 273.

[116] P. Nason, S. Dawson, and R. Ellis, *The Total Cross-Section for the Production of Heavy Quarks in Hadronic Collisions*, *Nucl.Phys.* **B303** (1988) 607.

[117] G. Altarelli, M. Diemoz, G. Martinelli, and P. Nason, *Total Cross-Sections for Heavy Flavor Production in Hadronic Collisions and QCD*, *Nucl.Phys.* **B308** (1988) 724.

[118] W. Beenakker, H. Kuijf, W. van Neerven, and J. Smith, *QCD Corrections to Heavy Quark Production in p anti-p Collisions*, *Phys.Rev.* **D40** (1989) 54–82.

[119] V. Ahrens, A. Ferroglia, M. Neubert, B. D. Pecjak, and L.-L. Yang, *RG-improved single-particle inclusive cross sections and forward-backward asymmetry in $t\bar{t}$ production at hadron colliders*, *JHEP* **1109** (2011) 070, [arXiv:1103.0550].

[120] V. Ahrens, A. Ferroglia, M. Neubert, B. D. Pecjak, and L. L. Yang, *The top-pair forward-backward asymmetry beyond NLO*, *Phys.Rev.* **D84** (2011) 074004, [arXiv:1106.6051].

[121] N. Kidonakis and B. D. Pecjak, *Top-quark production and QCD*, *Eur.Phys.J.* **C72** (2012) 2084, [arXiv:1108.6063].

[122] T. Hahn, *Generating Feynman diagrams and amplitudes with FeynArts 3*, *Comput.Phys.Commun.* **140** (2001) 418–431, [hep-ph/0012260].

[123] T. Hahn and M. Perez-Victoria, *Automatized one-loop calculations in four and D dimensions*, *Comput. Phys. Commun.* **118** (1999) 153–165, [hep-ph/9807565].

[124] A. Denner, *Techniques for calculation of electroweak radiative corrections at the one loop level and results for W physics at LEP-200*, *Fortschr. Phys.* **41** (1993) 307–420, [arXiv:0709.1075].

[125] A. Martin, R. Roberts, W. Stirling, and R. Thorne, *NNLO global parton analysis*, *Phys.Lett.* **B531** (2002) 216–224, [hep-ph/0201127].

[126] **Particle Data Group**, K. Nakamura *et. al.*, *Review of particle physics*, *J. Phys.* **G37** (2010) 075021.

[127] J. H. Kuhn and G. Rodrigo, *Charge asymmetries of top quarks at hadron colliders revisited*, *JHEP* **1201** (2012) 063, [arXiv:1109.6830].

[128] A. Martin, R. Roberts, W. Stirling, and R. Thorne, *Physical gluons and high E(T) jets*, *Phys.Lett.* **B604** (2004) 61–68, [hep-ph/0410230].

[129] W. Bernreuther and Z.-G. Si, *Top quark and leptonic charge asymmetries for the Tevatron and LHC*, *Phys.Rev.* **D86** (2012) 034026, [arXiv:1205.6580].

[130] J. Aguilar-Saavedra and A. Juste, *Collider-independent t tbar forward-backward asymmetries*, *Phys.Rev.Lett.* **109** (2012) 211804, [arXiv:1205.1898].

[131] J. Aguilar-Saavedra, W. Bernreuther, and Z. Si, *Collider-independent top quark forward-backward asymmetries: standard model predictions*, *Phys.Rev.* **D86** (2012) 115020, [arXiv:1209.6352].

[132] J. F. Kamenik, J. Shu, and J. Zupan, *Review of New Physics Effects in t-tbar Production*, *Eur.Phys.J.* **C72** (2012) 2102, [arXiv:1107.5257].

[133] J. Aguilar-Saavedra and M. Perez-Victoria, *t tbar charge asymmetry, family and friends*, arXiv:1302.6618.

[134] J. Drobnak, J. F. Kamenik, and J. Zupan, *Flipping t tbar Asymmetries at the Tevatron and the LHC*, *Phys.Rev.* **D86** (2012) 054022, [arXiv:1205.4721].

[135] R. Haag, J. T. Lopuszanski, and M. Sohnius, *All Possible Generators of Supersymmetries of the s Matrix*, *Nucl.Phys.* **B88** (1975) 257.

[136] S. R. Coleman and J. Mandula, *ALL POSSIBLE SYMMETRIES OF THE S MATRIX*, *Phys.Rev.* **159** (1967) 1251–1256.

[137] S. P. Martin, *A Supersymmetry primer*, `hep-ph/9709356`.

[138] M. Drees, R. Godbole, and P. Roy, *Theory and phenomenology of sparticles: An account of four-dimensional N=1 supersymmetry in high energy physics*, .

[139] J. R. Ellis, S. Kelley, and D. V. Nanopoulos, *Probing the desert using gauge coupling unification*, *Phys.Lett.* **B260** (1991) 131–137.

[140] U. Amaldi, W. de Boer, and H. Furstenau, *Comparison of grand unified theories with electroweak and strong coupling constants measured at LEP*, *Phys.Lett.* **B260** (1991) 447–455.

[141] P. Langacker and M.-x. Luo, *Implications of precision electroweak experiments for M_t, ρ_0, $\sin^2\theta_W$ and grand unification*, *Phys.Rev.* **D44** (1991) 817–822.

[142] C. Giunti, C. Kim, and U. Lee, *Running coupling constants and grand unification models*, *Mod.Phys.Lett.* **A6** (1991) 1745–1755.

[143] W. Beenakker, S. Brensing, M. Kramer, A. Kulesza, E. Laenen, *et. al.*, *Squark and Gluino Hadroproduction*, *Int.J.Mod.Phys.* **A26** (2011) 2637–2664, [`arXiv:1105.1110`].

[144] P. M. Nadolsky, H.-L. Lai, Q.-H. Cao, J. Huston, J. Pumplin, *et. al.*, *Implications of CTEQ global analysis for collider observables*, *Phys.Rev.* **D78** (2008) 013004, [`arXiv:0802.0007`].

[145] **CMS Collaboration**, V. Khachatryan *et. al.*, *Search for Supersymmetry in pp Collisions at 7 TeV in Events with Jets and Missing Transverse Energy*, *Phys.Lett.* **B698** (2011) 196–218, [`arXiv:1101.1628`].

[146] L. Randall and D. Tucker-Smith, *Dijet Searches for Supersymmetry at the LHC*, *Phys. Rev. Lett.* **101** (2008) 221803, [`arXiv:0806.1049`].

[147] B. C. Allanach, *Impact of CMS Multi-jets and Missing Energy Search on CMSSM Fits*, *Phys. Rev.* **D83** (2011) 095019, [`arXiv:1102.3149`].

[148] C. Rogan, *Kinematical variables towards new dynamics at the LHC*, `arXiv:1006.2727`.

[149] **CMS Collaboration**, S. Chatrchyan *et. al.*, *Inclusive search for squarks and gluinos in pp collisions at $\sqrt{s} = 7$ TeV*, *Phys.Rev.* **D85** (2012) 012004, [`arXiv:1107.1279`].

[150] **CMS Collaboration**, S. Chatrchyan *et. al.*, *Inclusive search for supersymmetry using the razor variables in pp collisions at $\sqrt{s} = 7$ TeV*, `arXiv:1212.6961`.

[151] C. Lester and D. Summers, *Measuring masses of semiinvisibly decaying particles pair produced at hadron colliders*, *Phys.Lett.* **B463** (1999) 99–103, [`hep-ph/9906349`].

[152] A. Barr, C. Lester, and P. Stephens, *m(T2): The Truth behind the glamour*, *J.Phys.* **G29** (2003) 2343–2363, [`hep-ph/0304226`].

[153] **CMS Collaboration**, S. Chatrchyan *et. al.*, *Search for supersymmetry in hadronic final states using MT2 in pp collisions at $\sqrt{s} = 7$ TeV*, *JHEP* **1210** (2012) 018, [`arXiv:1207.1798`].

[154] T. J. LeCompte and S. P. Martin, *Compressed supersymmetry after 1/fb at the Large Hadron Collider*, *Phys. Rev.* **D85** (2012) 035023, [`arXiv:1111.6897`].

[155] M. Asano, T. Bringmann, and C. Weniger, *Indirect dark matter searches as a probe of degenerate particle spectra*, *Phys. Lett.* **B709** (2012) 128–132, [`arXiv:1112.5158`].

[156] A. Strubig, S. Caron, and M. Rammensee, *Constraints on the pMSSM from searches for squarks and gluinos by ATLAS*, *JHEP* **05** (2012) 150, [`arXiv:1202.6244`].

[157] **ATLAS Collaboration**, G. Aad *et. al.*, *Search for supersymmetry in pp collisions at $\sqrt{s} = 7$ TeV in final states with missing transverse momentum and b^- jets with the ATLAS detector*, *Phys.Rev.* **D85** (2012) 112006, [arXiv:1203.6193].

[158] **ATLAS Collaboration**, G. Aad *et. al.*, *Search for scalar top quark pair production in natural gauge mediated supersymmetry models with the ATLAS detector in pp collisions at $\sqrt{s} = 7$ TeV*, *Phys.Lett.* **B715** (2012) 44–60, [arXiv:1204.6736].

[159] **ATLAS Collaboration**, G. Aad *et. al.*, *Search for a supersymmetric partner to the top quark in final states with jets and missing transverse momentum at $\sqrt{s} = 7$ TeV with the ATLAS detector*, *Phys.Rev.Lett.* **109** (2012) 211802, [arXiv:1208.1447].

[160] **ATLAS Collaboration**, G. Aad *et. al.*, *Search for direct top squark pair production in final states with one isolated lepton, jets, and missing transverse momentum in $\sqrt{s} = 7$ TeV pp collisions using 4.7 fb^{-1} of ATLAS data*, *Phys.Rev.Lett.* **109** (2012) 211803, [arXiv:1208.2590].

[161] **ATLAS Collaboration**, G. Aad *et. al.*, *Search for light scalar top quark pair production in final states with two leptons with the ATLAS detector in $\sqrt{s} = 7$ TeV proton-proton collisions*, *Eur.Phys.J.* **C72** (2012) 2237, [arXiv:1208.4305].

[162] **ATLAS Collaboration**, G. Aad *et. al.*, *Search for light top squark pair production in final states with leptons and b^- jets with the ATLAS detector in $\sqrt{s} = 7$ TeV proton-proton collisions*, *Phys.Lett.* **B720** (2013) 13–31, [arXiv:1209.2102].

[163] **ATLAS Collaboration**, G. Aad *et. al.*, *Search for a heavy top-quark partner in final states with two leptons with the ATLAS detector at the LHC*, *JHEP* **1211** (2012) 094, [arXiv:1209.4186].

[164] **ATLAS Collaboration**, G. Aad *et. al.*, *Search for scalar bottom pair production with the ATLAS detector in pp Collisions at $\sqrt{s} = 7$ TeV*, *Phys.Rev.Lett.* **108** (2012) 181802, [arXiv:1112.3832].

[165] **ATLAS Collaboration**, G. Aad *et. al.*, *Search for direct chargino production in anomaly-mediated supersymmetry breaking models based on a disappearing-track signature in pp collisions at $\sqrt{s} = 7$ TeV with the ATLAS detector*, *JHEP* **1301** (2013) 131, [arXiv:1210.2852].

[166] **ATLAS Collaboration**, G. Aad *et. al.*, *Searches for heavy long-lived sleptons and R-Hadrons with the ATLAS detector in pp collisions at $\sqrt{s} = 7$ TeV*, *Phys.Lett.* **B720** (2013) 277–308, [arXiv:1211.1597].

[167] **ATLAS Collaboration**, G. Aad *et. al.*, *Search for direct production of charginos and neutralinos in events with three leptons and missing transverse momentum in $\sqrt{s} = 7$ TeV pp collisions with the ATLAS detector*, *Phys.Lett.* **B718** (2013) 841–859, [arXiv:1208.3144].

[168] **ATLAS Collaboration**, G. Aad *et. al.*, *Search for direct slepton and gaugino production in final states with two leptons and missing transverse momentum with the ATLAS detector in pp collisions at $\sqrt{s} = 7$ TeV*, *Phys.Lett.* **B718** (2013) 879–901, [arXiv:1208.2884].

[169] **ATLAS Collaboration**, G. Aad *et. al.*, *Search for supersymmetry in events with three leptons and missing transverse momentum in $\sqrt{s} = 7$ TeV pp collisions with the ATLAS detector*, *Phys.Rev.Lett.* **108** (2012) 261804, [arXiv:1204.5638].

[170] **CMS Collaboration**, S. Chatrchyan *et. al.*, *Search for electroweak production of charginos and neutralinos using leptonic final states in pp collisions at $\sqrt{s} = 7$ TeV*, *JHEP* **1211** (2012) 147, [arXiv:1209.6620].

[171] **CMS Collaboration**, S. Chatrchyan *et. al.*, *Search for supersymmetry in events with b-quark jets and missing transverse energy in pp collisions at 7 TeV*, *Phys.Rev.* **D86** (2012) 072010, [arXiv:1208.4859].

[172] N. Arkani-Hamed, G. L. Kane, J. Thaler, and L.-T. Wang, *Supersymmetry and the LHC inverse problem*, *JHEP* **0608** (2006) 070, [hep-ph/0512190].

[173] N. Bornhauser and M. Drees, *Mitigation of the LHC Inverse Problem*, *Phys.Rev.* **D86** (2012) 015025, [arXiv:1205.6080].

[174] J. Hubisz, J. Lykken, M. Pierini, and M. Spiropulu, *Missing energy look-alikes with 100 pb^{-1} at the LHC*, *Phys.Rev.* **D78** (2008) 075008, [arXiv:0805.2398].

[175] A. J. Barr and C. G. Lester, *A Review of the Mass Measurement Techniques proposed for the Large Hadron Collider*, *J. Phys.* **G37** (2010) 123001, [arXiv:1004.2732].

[176] I. Hinchliffe, F. Paige, M. Shapiro, J. Soderqvist, and W. Yao, *Precision SUSY measurements at CERN LHC*, *Phys.Rev.* **D55** (1997) 5520–5540, [hep-ph/9610544].

[177] H. Bachacou, I. Hinchliffe, and F. E. Paige, *Measurements of masses in SUGRA models at CERN LHC*, *Phys.Rev.* **D62** (2000) 015009, [hep-ph/9907518].

[178] B. Allanach, C. Lester, M. A. Parker, and B. Webber, *Measuring sparticle masses in nonuniversal string inspired models at the LHC*, *JHEP* **0009** (2000) 004, [hep-ph/0007009].

[179] **LHC/LC Study Group**, G. Weiglein *et. al.*, *Physics interplay of the LHC and the ILC*, *Phys.Rept.* **426** (2006) 47–358, [hep-ph/0410364].

[180] B. K. Gjelsten, D. J. Miller, and P. Osland, *Measurement of SUSY masses via cascade decays for SPS 1a*, *JHEP* **0412** (2004) 003, [hep-ph/0410303].

[181] D. Miller, P. Osland, and A. Raklev, *Invariant mass distributions in cascade decays*, *JHEP* **0603** (2006) 034, [hep-ph/0510356].

[182] C. G. Lester, *Constrained invariant mass distributions in cascade decays: The Shape of the 'm(qll)-threshold' and similar distributions*, *Phys.Lett.* **B655** (2007) 39–44, [hep-ph/0603171].

[183] M. Bisset, R. Lu, and N. Kersting, *Improving SUSY Spectrum Determinations at the LHC with Wedgebox Technique*, *JHEP* **1105** (2011) 095, [arXiv:0806.2492].

[184] D. Costanzo and D. R. Tovey, *Supersymmetric particle mass measurement with invariant mass correlations*, *JHEP* **0904** (2009) 084, [arXiv:0902.2331].

[185] G. Polesello and D. R. Tovey, *Supersymmetric particle mass measurement with the boost-corrected contransverse mass*, *JHEP* **1003** (2010) 030, [arXiv:0910.0174].

[186] K. T. Matchev and M. Park, *A General method for determining the masses of semi-invisibly decaying particles at hadron colliders*, *Phys.Rev.Lett.* **107** (2011) 061801, [arXiv:0910.1584].

[187] K. T. Matchev, F. Moortgat, L. Pape, and M. Park, *Precise reconstruction of sparticle masses without ambiguities*, *JHEP* **0908** (2009) 104, [arXiv:0906.2417].

[188] H.-C. Cheng, J. F. Gunion, Z. Han, and B. McElrath, *Accurate Mass Determinations in Decay Chains with Missing Energy. II*, *Phys.Rev.* **D80** (2009) 035020, [arXiv:0905.1344].

[189] L. Edelhauser, W. Porod, and R. K. Singh, *Spin Discrimination in Three-Body Decays*, *JHEP* **1008** (2010) 053, [arXiv:1005.3720].

[190] K. Agashe, D. Kim, M. Toharia, and D. G. Walker, *Distinguishing Dark Matter Stabilization Symmetries Using Multiple Kinematic Edges and Cusps*, *Phys.Rev.* **D82** (2010) 015007, [arXiv:1003.0899].

[191] M. M. Nojiri and K. Sakurai, *Controlling ISR in sparticle mass reconstruction*, *Phys.Rev.* **D82** (2010) 115026, [arXiv:1008.1813].

[192] A. Barr, T. Khoo, P. Konar, K. Kong, C. Lester, *et. al.*, *Guide to transverse projections and mass-constraining variables*, *Phys.Rev.* **D84** (2011) 095031, [arXiv:1105.2977].

[193] C.-Y. Chen and A. Freitas, *General analysis of decay chains with three-body decays involving missing energy*, *JHEP* **1201** (2012) 124, [arXiv:1110.6192].

[194] K. Choi, D. Guadagnoli, and C. B. Park, *Reducing combinatorial uncertainties: A new technique based on MT2 variables*, *JHEP* **1111** (2011) 117, [arXiv:1109.2201].

[195] B. K. Gjelsten, D. J. Miller, P. Osland, and A. R. Raklev, *Mass Determination in Cascade Decays Using Shape Formulas*, *AIP Conf.Proc.* **903** (2007) 257–260, [hep-ph/0611259].

[196] A. Barr, *Determining the spin of supersymmetric particles at the LHC using lepton charge asymmetry*, *Phys.Lett.* **B596** (2004) 205–212, [hep-ph/0405052].

[197] J. M. Smillie and B. R. Webber, *Distinguishing Spins in Supersymmetric and Universal Extra Dimension Models at the Large Hadron Collider*, *JHEP* **10** (2005) 069, [hep-ph/0507170].

[198] C. Athanasiou, C. G. Lester, J. M. Smillie, and B. R. Webber, *Distinguishing Spins in Decay Chains at the Large Hadron Collider*, *JHEP* **0608** (2006) 055, [hep-ph/0605286].

[199] M. Battaglia, A. K. Datta, A. De Roeck, K. Kong, and K. T. Matchev, *Contrasting supersymmetry and universal extra dimensions at colliders*, *eConf* **C050318** (2005) 0302, [hep-ph/0507284].

[200] A. Datta, K. Kong, and K. T. Matchev, *Discrimination of supersymmetry and universal extra dimensions at hadron colliders*, *Phys.Rev.* **D72** (2005) 096006, [hep-ph/0509246].

[201] L.-T. Wang and I. Yavin, *Spin measurements in cascade decays at the LHC*, *JHEP* **0704** (2007) 032, [hep-ph/0605296].

[202] S. Choi, K. Hagiwara, H.-U. Martyn, K. Mawatari, and P. Zerwas, *Spin Analysis of Supersymmetric Particles*, *Eur.Phys.J.* **C51** (2007) 753–774, [hep-ph/0612301].

[203] C. Kilic, L.-T. Wang, and I. Yavin, *On the existence of angular correlations in decays with heavy matter partners*, *JHEP* **0705** (2007) 052, [hep-ph/0703085].

[204] L.-T. Wang and I. Yavin, *A Review of Spin Determination at the LHC*, *Int.J.Mod.Phys.* **A23** (2008) 4647–4668, [arXiv:0802.2726].

[205] S. Choi, M. Drees, A. Freitas, and P. Zerwas, *Testing the Majorana Nature of Gluinos and Neutralinos*, *Phys.Rev.* **D78** (2008) 095007, [arXiv:0808.2410].

[206] M. Burns, K. Kong, K. T. Matchev, and M. Park, *A General Method for Model-Independent Measurements of Particle Spins, Couplings and Mixing Angles in Cascade Decays with Missing Energy at Hadron Colliders*, *JHEP* **0810** (2008) 081, [arXiv:0808.2472].

[207] O. Gedalia, S. J. Lee, and G. Perez, *Spin Determination via Third Generation Cascade Decays*, *Phys.Rev.* **D80** (2009) 035012, [arXiv:0901.4438].

[208] W. Ehrenfeld, A. Freitas, A. Landwehr, and D. Wyler, *Distinguishing spins in decay chains with photons at the Large Hadron Collider*, *JHEP* **0907** (2009) 056, [arXiv:0904.1293].

[209] N. Srimanobhas and B. Asavapibhop, *A review of the spin determination of supersymmetric decay chain via neutralino at the LHC*, *J.Phys.* **G38** (2011) 075001.

[210] G. L. Kane and J. P. Leveille, *Experimental Constraints on Gluino Masses and Supersymmetric Theories*, *Phys. Lett.* **B112** (1982) 227.

[211] P. R. Harrison and C. H. Llewellyn Smith, *Hadroproduction of Supersymmetric Particles*, *Nucl. Phys.* **B213** (1983) 223. [ERRATUM-ibid.B223:542,1983].

[212] E. Reya and D. P. Roy, *Supersymmetric particle production at p anti-p collider energies*, *Phys. Rev.* **D32** (1985) 645.

[213] S. Dawson, E. Eichten, and C. Quigg, *Search for Supersymmetric Particles in Hadron - Hadron Collisions*, *Phys. Rev.* **D31** (1985) 1581.

[214] H. Baer and X. Tata, *Component formulae for hadroproduction of left-handed and right-handed squarks*, *Phys. Lett.* **B160** (1985) 159.

[215] W. Beenakker, R. Hopker, M. Spira, and P. M. Zerwas, *Squark production at the Tevatron*, *Phys. Rev. Lett.* **74** (1995) 2905–2908, [hep-ph/9412272].

[216] W. Beenakker, R. Hopker, M. Spira, and P. M. Zerwas, *Gluino pair production at the Tevatron*, *Z. Phys.* **C69** (1995) 163–166, [hep-ph/9505416].

[217] W. Beenakker, M. Kramer, T. Plehn, M. Spira, and P. M. Zerwas, *Stop production at hadron colliders*, *Nucl. Phys.* **B515** (1998) 3–14, [hep-ph/9710451].

[218] W. Beenakker, R. Hopker, and M. Spira, *PROSPINO: A program for the PROduction of Supersymmetric Particles In Next-to-leading Order QCD*, hep-ph/9611232.

[219] D. Goncalves-Netto, D. Lopez-Val, K. Mawatari, T. Plehn, and I. Wigmore, *Automated Squark and Gluino Production to Next-to-Leading Order*, *Phys.Rev.* **D87** (2013) 014002, [arXiv:1211.0286].

[220] M. Kramer *et. al.*, *Supersymmetry production cross sections in pp collisions at sqrts = 7 TeV*, arXiv:1206.2892.

[221] U. Langenfeld and S.-O. Moch, *Higher-order soft corrections to squark hadro- production*, *Phys. Lett.* **B675** (2009) 210–221, [arXiv:0901.0802].

[222] A. Kulesza and L. Motyka, *Threshold resummation for squark-antisquark and gluino- pair production at the LHC*, *Phys. Rev. Lett.* **102** (2009) 111802, [arXiv:0807.2405].

[223] A. Kulesza and L. Motyka, *Soft gluon resummation for the production of gluino-gluino and squark-antisquark pairs at the LHC*, *Phys. Rev.* **D80** (2009) 095004, [arXiv:0905.4749].

[224] W. Beenakker *et. al.*, *Soft-gluon resummation for squark and gluino hadroproduction*, *JHEP* **12** (2009) 041, [arXiv:0909.4418].

[225] W. Beenakker *et. al.*, *Supersymmetric top and bottom squark production at hadron colliders*, *JHEP* **08** (2010) 098, [arXiv:1006.4771].

[226] M. Beneke, P. Falgari, and C. Schwinn, *Threshold resummation for pair production of coloured heavy (s)particles at hadron colliders*, *Nucl. Phys.* **B842** (2011) 414–474, [arXiv:1007.5414].

[227] W. Beenakker *et. al.*, *NNLL resummation for squark-antisquark pair production at the LHC*, *JHEP* **01** (2012) 076, [arXiv:1110.2446].

[228] P. Falgari, C. Schwinn, and C. Wever, *NLL soft and Coulomb resummation for squark and gluino production at the LHC*, *JHEP* **06** (2012) 052, [arXiv:1202.2260].

[229] P. Falgari, C. Schwinn, and C. Wever, *Finite-width effects on threshold corrections to squark and gluino production*, *JHEP* **1301** (2013) 085, [arXiv:1211.3408].

[230] T. Plehn, D. Rainwater, and P. Z. Skands, *Squark and gluino production with jets*, *Phys. Lett.* **B645** (2007) 217–221, [hep-ph/0510144].

[231] J. Alwall, S. de Visscher, and F. Maltoni, *QCD radiation in the production of heavy colored particles at the LHC*, *JHEP* **02** (2009) 017, [arXiv:0810.5350].

[232] R. Gavin, C. Hangst, M. Kraemer, M. Muehlleitner, M. Pellen, *et. al.*, *Matching Squark Pair Production at NLO with Parton Showers*, arXiv:1305.4061.

[233] P. Nason, *A New method for combining NLO QCD with shower Monte Carlo algorithms*, *JHEP* **0411** (2004) 040, [hep-ph/0409146].

[234] S. Frixione, P. Nason, and C. Oleari, *Matching NLO QCD computations with Parton Shower simulations: the POWHEG method*, *JHEP* **0711** (2007) 070, [arXiv:0709.2092].

[235] S. Alioli, P. Nason, C. Oleari, and E. Re, *A general framework for implementing NLO calculations in shower Monte Carlo programs: the POWHEG BOX*, *JHEP* **1006** (2010) 043, [arXiv:1002.2581].

[236] S. Bornhauser, M. Drees, H. K. Dreiner, and J. S. Kim, *Electroweak Contributions to Squark Pair Production at the LHC*, *Phys. Rev.* **D76** (2007) 095020, [arXiv:0709.2544].

[237] A. Arhrib, R. Benbrik, K. Cheung, and T.-C. Yuan, *Higgs boson enhancement effects on squark-pair production at the LHC*, *JHEP* **02** (2010) 048, [arXiv:0911.1820].

[238] W. Hollik, M. Kollar, and M. K. Trenkel, *Hadronic production of top-squark pairs with electroweak NLO contributions*, *JHEP* **02** (2008) 018, [arXiv:0712.0287].

[239] W. Hollik and E. Mirabella, *Squark anti-squark pair production at the LHC: the electroweak contribution*, *JHEP* **12** (2008) 087, [arXiv:0806.1433].

[240] W. Hollik, E. Mirabella, and M. K. Trenkel, *Electroweak contributions to squark–gluino production at the LHC*, *JHEP* **02** (2009) 002, [arXiv:0810.1044].

[241] M. Beccaria, G. Macorini, L. Panizzi, F. M. Renard, and C. Verzegnassi, *Stop-antistop and sbottom-antisbottom production at LHC: a one-loop search for model parameters dependence*, *Int. J. Mod. Phys.* **A23** (2008) 4779–4810, [arXiv:0804.1252].

[242] E. Mirabella, *NLO electroweak contributions to gluino pair production at hadron colliders*, *JHEP* **12** (2009) 012, [arXiv:0908.3318].

[243] J. Germer, W. Hollik, E. Mirabella, and M. K. Trenkel, *Hadronic production of squark-squark pairs: The electroweak contributions*, *JHEP* **08** (2010) 023, [arXiv:1004.2621].

[244] J. Germer, W. Hollik, and E. Mirabella, *Hadronic production of bottom-squark pairs with electroweak contributions*, *JHEP* **05** (2011) 068, [arXiv:1103.1258].

[245] K.-i. Hikasa and Y. Nakamura, *Soft breaking correction to hard supersymmetric relations: QCD corrections to squark decay*, *Z. Phys.* **C70** (1996) 139–144, [hep-ph/9501382]. [ERRATUM-ibid.C71:356,1996].

[246] S. Kraml, H. Eberl, A. Bartl, W. Majerotto, and W. Porod, *SUSY-QCD corrections to scalar quark decays into charginos and neutralinos*, *Phys. Lett.* **B386** (1996) 175–182, [hep-ph/9605412].

[247] A. Bartl, W. Majerotto, and W. Porod, *Squark and gluino decays for large tan beta*, *Z. Phys.* **C64** (1994) 499–508. [ERRATUM-ibid.C68:518,1995].

[248] A. Bartl *et. al.*, *Bosonic decays of stop(2) and sbottom(2)*, *Phys. Lett.* **B435** (1998) 118–124, [hep-ph/9804265].

[249] A. Bartl *et. al.*, *SUSY-QCD corrections to stop and sbottom decays into W+- and Z0 bosons*, *Phys. Lett.* **B419** (1998) 243–252, [hep-ph/9710286].

[250] A. Arhrib, A. Djouadi, W. Hollik, and C. Junger, *SUSY Higgs boson decays into scalar quarks: QCD corrections*, *Phys. Rev.* **D57** (1998) 5860–5870, [hep-ph/9702426].

[251] A. Bartl *et. al.*, *SUSY - QCD corrections to top and bottom squark decays into Higgs bosons*, *Phys. Rev.* **D59** (1999) 115007, [hep-ph/9806299].

[252] W. Beenakker, R. Hopker, and P. M. Zerwas, *SUSY QCD decays of squarks and gluinos*, *Phys. Lett.* **B378** (1996) 159–166, [hep-ph/9602378].

[253] W. Beenakker, R. Hopker, T. Plehn, and P. M. Zerwas, *Stop decays in SUSY-QCD*, *Z. Phys.* **C75** (1997) 349–356, [hep-ph/9610313].

[254] M. Muhlleitner, A. Djouadi, and Y. Mambrini, *SDECAY: A Fortran code for the decays of the supersymmetric particles in the MSSM*, *Comput. Phys. Commun.* **168** (2005) 46–70, [hep-ph/0311167].

[255] A. Djouadi, M. M. Muhlleitner, and M. Spira, *Decays of Supersymmetric Particles: the program SUSY-HIT (SUspect-SdecaY-Hdecay-InTerface)*, *Acta Phys. Polon.* **B38** (2007) 635–644, [hep-ph/0609292].

[256] J. Guasch, J. Sola, and W. Hollik, *Yukawa coupling corrections to scalar quark decays*, *Phys. Lett.* **B437** (1998) 88–99, [hep-ph/9802329].

[257] J. Guasch, W. Hollik, and J. Sola, *Fermionic decays of sfermions: A complete discussion at one-loop order*, *JHEP* **10** (2002) 040, [hep-ph/0207364].

[258] A. Arhrib and R. Benbrik, *Third generation sfermions decays into Z and W gauge bosons: Full one-loop analysis*, *Phys. Rev.* **D71** (2005) 095001, [hep-ph/0412349].

[259] A. Arhrib and R. Benbrik, *Complete one-loop analysis to stop and sbottom decays into Z and W+- bosons*, *Afr. J. Math. Phys.* **3** (2006) 85–91, [hep-ph/0511116].

[260] Q. Li, L. G. Jin, and C. S. Li, *Supersymmetric electroweak corrections to heavier top squark decay into lighter top squark and neutral Higgs boson*, *Phys. Rev.* **D66** (2002) 115008, [hep-ph/0207363].

[261] C. Weber, K. Kovarik, H. Eberl, and W. Majerotto, *Complete one-loop corrections to decays of charged and CP- even neutral Higgs bosons into sfermions*, *Nucl. Phys.* **B776** (2007) 138–169, [hep-ph/0701134].

[262] M. Drees, W. Hollik, and Q. Xu, *One-loop calculations of the decay of the next-to-lightest neutralino in the MSSM*, *JHEP* **02** (2007) 032, [hep-ph/0610267].

[263] G. Hallenbeck, M. Perelstein, C. Spethmann, J. Thom, and J. Vaughan, *Model Discrimination with the CMS Detector: a Case Study*, *Phys. Rev.* **D79** (2009) 075024, [arXiv:0812.3135].

[264] G. Corcella, I. Knowles, G. Marchesini, S. Moretti, K. Odagiri, *et. al.*, *HERWIG 6.5 release note*, hep-ph/0210213.

[265] S. Moretti, K. Odagiri, P. Richardson, M. H. Seymour, and B. R. Webber, *Implementation of supersymmetric processes in the HERWIG event generator*, *JHEP* **0204** (2002) 028, [hep-ph/0204123].

[266] T. Sjostrand, S. Mrenna, and P. Z. Skands, *PYTHIA 6.4 Physics and Manual*, *JHEP* **0605** (2006) 026, [hep-ph/0603175].

[267] T. Sjostrand, S. Mrenna, and P. Z. Skands, *A Brief Introduction to PYTHIA 8.1*, *Comput.Phys.Commun.* **178** (2008) 852–867, [arXiv:0710.3820].

[268] S. Mrenna, *A Closer Look at the 2011 cMSSM Results from CMS*, arXiv:1110.4078.

[269] **CMS Collaboration**, S. Chatrchyan *et. al.*, *Search for new physics in events with opposite-sign leptons, jets, and missing transverse energy in pp collisions at* $\sqrt{s} = 7$ *TeV*, *Phys.Lett.* **B718** (2013) 815–840, [arXiv:1206.3949].

[270] **ATLAS Collaboration**, G. Aad *et. al.*, *Search for an excess of events with an identical flavour lepton pair and significant missing transverse momentum in* $\sqrt{s} = 7$ *TeV proton-proton collisions with the ATLAS detector*, *Eur.Phys.J.* **C71** (2011) 1647, [arXiv:1103.6208].

[271] R. Boughezal and M. Schulze, *Precise predictions for top quark plus missing energy signatures at the LHC*, arXiv:1212.0898.

[272] T. Hahn and C. Schappacher, *The implementation of the minimal supersymmetric standard model in FeynArts and FormCalc*, *Comput. Phys. Commun.* **143** (2002) 54–68, [hep-ph/0105349].

[273] W. Hollik and D. Stockinger, *Regularization and supersymmetry-restoring counterterms in supersymmetric QCD*, *Eur. Phys. J.* **C20** (2001) 105–119, [hep-ph/0103009].

[274] G. 't Hooft and M. Veltman, *Scalar One Loop Integrals*, *Nucl.Phys.* **B153** (1979) 365–401.

[275] U. Baur, S. Keller, and D. Wackeroth, *Electroweak radiative corrections to W boson production in hadronic collisions*, *Phys. Rev.* **D59** (1999) 013002, [hep-ph/9807417].

[276] S. Frixione, E. Laenen, P. Motylinski, B. R. Webber, and C. D. White, *Single-top hadroproduction in association with a W boson*, *JHEP* **0807** (2008) 029, [arXiv:0805.3067].

[277] T. Binoth *et. al.*, *Automized Squark-Neutralino Production to Next-to-Leading Order*, *Phys. Rev.* **D84** (2011) 075005, [arXiv:1108.1250].

[278] K.-P. Diener, S. Dittmaier, and W. Hollik, *Electroweak higher-order effects and theoretical uncertainties in deep-inelastic neutrino scattering*, *Phys.Rev.* **D72** (2005) 093002, [hep-ph/0509084].

[279] M. R. Whalley, D. Bourilkov, and R. C. Group, *The Les Houches Accord PDFs (LHAPDF) and Lhaglue*, hep-ph/0508110.

[280] B. C. Allanach *et. al.*, *The Snowmass points and slopes: Benchmarks for SUSY searches*, *Eur. Phys. J.* **C25** (2002) 113–123, [hep-ph/0202233].

[281] **CMS Collaboration**, S. Chatrchyan *et. al.*, *Search for Supersymmetry at the LHC in Events with Jets and Missing Transverse Energy*, *Phys.Rev.Lett.* **107** (2011) 221804, [arXiv:1109.2352].

[282] **ATLAS Collaboration**, G. Aad *et. al.*, *Search for squarks and gluinos using final states with jets and missing transverse momentum with the ATLAS detector in sqrt(s) = 7 TeV proton-proton collisions*, *Phys.Lett.* **B710** (2012) 67–85, [arXiv:1109.6572].

[283] M. J. Dolan, D. Grellscheid, J. Jaeckel, V. V. Khoze, and P. Richardson, *New Constraints on Gauge Mediation and Beyond from LHC SUSY Searches at 7 TeV*, *JHEP* **1106** (2011) 095, [arXiv:1104.0585].

[284] S. AbdusSalam, B. Allanach, H. Dreiner, J. Ellis, U. Ellwanger, *et. al.*, *Benchmark Models, Planes, Lines and Points for Future SUSY Searches at the LHC*, *Eur.Phys.J.* **C71** (2011) 1835, [arXiv:1109.3859].

[285] B. C. Allanach, *SOFTSUSY: a program for calculating supersymmetric spectra*, *Comput. Phys. Commun.* **143** (2002) 305–331, [hep-ph/0104145].

[286] M. Cacciari and G. P. Salam, *Dispelling the* N^3 *myth for the* k_t *jet-finder*, *Phys.Lett.* **B641** (2006) 57–61, [hep-ph/0512210].

[287] M. Cacciari, G. P. Salam, and G. Soyez, *FastJet user manual*, *Eur. Phys. J.* **C72** (2012) 1896, [arXiv:1111.6097].

[288] G. Moortgat-Pick, K. Rolbiecki, and J. Tattersall, *Early spin determination at the LHC?*, *Phys. Lett.* **B699** (2011) 158–163, [arXiv:1102.0293].

[289] J. Alwall, M. Herquet, F. Maltoni, O. Mattelaer, and T. Stelzer, *MadGraph 5 : Going Beyond*, *JHEP* **1106** (2011) 128, [arXiv:1106.0522].

[290] Z. Usubov, *Looking for Squark Pair Production in the Early LHC Data*, arXiv:1005.5062.

[291] H.-C. Cheng, J. F. Gunion, Z. Han, G. Marandella, and B. McElrath, *Mass determination in SUSY-like events with missing energy*, *JHEP* **0712** (2007) 076, [arXiv:0707.0030].

[292] H. Baer, C.-h. Chen, F. Paige, and X. Tata, *Signals for minimal supergravity at the CERN large hadron collider: Multi - jet plus missing energy channel*, *Phys.Rev.* **D52** (1995) 2746–2759, [hep-ph/9503271].

[293] **CMS Collaboration**, G. Bayatian *et. al.*, *CMS technical design report, volume II: Physics performance*, *J.Phys.* **G34** (2007) 995–1579.

[294] M. M. Nojiri, Y. Shimizu, S. Okada, and K. Kawagoe, *Inclusive transverse mass analysis for squark and gluino mass determination*, *JHEP* **0806** (2008) 035, [arXiv:0802.2412].

[295] H. K. Dreiner, M. Kramer, J. M. Lindert, and B. O'Leary, *SUSY parameter determination at the LHC using cross sections and kinematic edges*, *JHEP* **04** (2010) 109, [arXiv:1003.2648].

[296] A. Denner, S. Dittmaier, and M. Roth, *Nonfactorizable photonic corrections to e+ e- →gt; W W →gt; four fermions*, *Nucl.Phys.* **B519** (1998) 39–84, [hep-ph/9710521].

[297] A. Denner, S. Dittmaier, M. Roth, and D. Wackeroth, *Electroweak radiative corrections to e+ e- ⟶ gt; W W ⟶ gt; 4 fermions in double pole approximation: The RACOONWW approach*, *Nucl.Phys.* **B587** (2000) 67–117, [hep-ph/0006307].

[298] W. Beenakker, A. Chapovsky, and F. A. Berends, *Nonfactorizable corrections to W pair production: Methods and analytic results*, *Nucl.Phys.* **B508** (1997) 17–63, [hep-ph/9707326].

[299] W. Beenakker, A. Chapovsky, and F. A. Berends, *Nonfactorizable corrections to W pair production*, *Phys.Lett.* **B411** (1997) 203–210, [hep-ph/9706339].

[300] W. Beenakker, F. A. Berends, and A. Chapovsky, *Radiative corrections to pair production of unstable particles: results for e+ e- ⟶ gt; four fermions*, *Nucl.Phys.* **B548** (1999) 3–59, [hep-ph/9811481].

[301] D. Wackeroth and W. Hollik, *Electroweak radiative corrections to resonant charged gauge boson production*, *Phys.Rev.* **D55** (1997) 6788–6818, [hep-ph/9606398].

[302] A. Denner, H. Eck, O. Hahn, and J. Kublbeck, *Compact Feynman rules for Majorana fermions*, *Phys.Lett.* **B291** (1992) 278–280.

[303] S. Heinemeyer, W. Hollik, H. Rzehak, and G. Weiglein, *High-precision predictions for the MSSM Higgs sector at O(alpha(b) alpha(s))*, *Eur.Phys.J.* **C39** (2005) 465–481, [hep-ph/0411114].

[304] W. Hollik and H. Rzehak, *The Sfermion mass spectrum of the MSSM at the one loop level*, *Eur.Phys.J.* **C32** (2003) 127–133, [hep-ph/0305328].

[305] D. Berdine, N. Kauer, and D. Rainwater, *Breakdown of the Narrow Width Approximation for New Physics*, *Phys.Rev.Lett.* **99** (2007) 111601, [hep-ph/0703058].

Acknowledgements

First of all, I want to thank my supervisor Prof. Wolfgang Hollik for the support during the entire period of PhD studies and in particular during the writing of the thesis.

A special thank goes to my good friend Jonas Lindert for proofreading parts of the thesis and especially for the stimulating and fruitful collaboration during the last two years.

I am also indebted to Peter Graf and Irene Tamborra for proofreading parts of the thesis and to my office mates Sophia Borowka and Tiziano Peraro for many interesting and useful discussions and their moral support.

Many thanks go also to all friends here in Munich and to Andrea, who continuously encouraged me during all the phases of the thesis.

Last but not least, I want to thank my parents Mimmi and Walter for the continuos help and support, especially during these years spent in Munich.